



HAL
open science

Remote sensing of atmospheric trace gases by optical correlation spectroscopy and lidar

Benjamin Thomas

► **To cite this version:**

Benjamin Thomas. Remote sensing of atmospheric trace gases by optical correlation spectroscopy and lidar. Physics [physics]. Université Claude Bernard - Lyon I, 2013. English. NNT : 2013LYO10180 . tel-01285049

HAL Id: tel-01285049

<https://theses.hal.science/tel-01285049>

Submitted on 10 Mar 2016

HAL is a multi-disciplinary open access archive for the deposit and dissemination of scientific research documents, whether they are published or not. The documents may come from teaching and research institutions in France or abroad, or from public or private research centers.

L'archive ouverte pluridisciplinaire **HAL**, est destinée au dépôt et à la diffusion de documents scientifiques de niveau recherche, publiés ou non, émanant des établissements d'enseignement et de recherche français ou étrangers, des laboratoires publics ou privés.

N° d'ordre: 180 - 2013

CLAUDE BERNARD LYON 1 UNIVERSITY

PHYSICS AND ASTROPHYSICS DOCTORAL SCHOOL

To obtain the
DEGREE OF DOCTOR OF PHILOSOPHY

**REMOTE SENSING OF ATMOSPHERIC TRACE GASES BY
OPTICAL CORRELATION SPECTROSCOPY AND LIDAR**

by
THOMAS BENJAMIN

23 October 2013

Doctoral advisor:
Patrick RAIROUX

JURY:

President: M. DUGOURD Philippe
Reviewers: M. KASPARIAN Jérôme
M. SVANBERG Sune
Examiners: M. BOUDON Vincent
M. CARIOU Jean-Pierre
M. MIFFRE Alain
M. ORPHAL Johannes
M. RAIROUX Patrick

Résumé de thèse

Ce travail présente une nouvelle méthode de télédétection à distance de la concentration d'un gaz trace dans l'atmosphère. Cette méthode est basée sur le couplage de la méthode spectroscopique de corrélation optique (Optical Correlation Spectroscopy, OCS) et la technologie de télédétection lidar dans lequel une source laser de large étendue spectrale est considérée. Dans ce travail, le formalisme de cette nouvelle méthode nommée OCS-lidar ainsi qu'un modèle numérique sont présentés. De plus, la première preuve expérimentale montrant que l'OCS-lidar est une méthode robuste permettant la mesure de gaz trace dans l'atmosphère à des fins environnementales, industrielles ou agricoles a été réalisée. En complément à ce travail, plusieurs études ont été effectuées sur les propriétés optiques de particules atmosphériques au moyen d'un lidar UV-VIS sensible en polarisation. Ces travaux ont permis d'aborder l'étude de la physique et chimie de l'atmosphère donnant lieu à la découverte d'une nouvelle voie de génération de centres de nucléation dans l'atmosphère.

Les premiers travaux furent consacrés au développement d'un nouveau formalisme pour estimer la concentration d'un gaz trace dans l'atmosphère à partir des signaux OCS-lidar. Pour évaluer les performances d'une telle méthode, un modèle numérique simulant des signaux OCS-lidar pour la mesure de la concentration de méthane et de vapeur d'eau a été réalisé. Les sources d'erreurs statistiques et systématiques ont pu être ainsi évaluées et discutées. L'influence de la pression et la température sur les propriétés spectroscopiques de ces gaz sur les mesures de concentration a également été étudiée. On a ainsi mis en évidence que la méthode OCS-lidar est faiblement sensible aux variations de pression de l'atmosphère et aux variations des forces de raies. L'influence des gradients de températures est également évaluée et discutée. En plus de ce travail théorique, la première démonstration expérimentale de l'OCS-lidar est présentée en utilisant un lidar basé sur une source laser femtoseconde. Les mesures OCS-lidar ont été réalisées au moyen d'un nouveau système expérimental entièrement élaboré et construit pendant cette thèse. Pour réaliser les mesures consacrées à la teneur en vapeur d'eau de l'atmosphère, la bande d'absorption de la molécule de H_2O 4ν à 720 nm a été utilisée. Ainsi les résultats obtenus ont montré le potentiel de la méthode OCS-

lidar pour mesurer la concentration de vapeur d'eau dans la couche limite atmosphérique. Deux configurations expérimentales différentes ont été évaluées, l'une où la modulation d'amplitude servant à la spectroscopie de corrélation est réalisée à l'émission par un modulateur d'amplitude actif, l'autre où la modulation est effectuée par des filtres passifs à la réception de la lumière rétrodiffusée. Par la suite, le développement de la méthodologie OCS-lidar dédiée à la mesure à distance de la concentration du méthane est présenté. Dans cette démarche, la bande d'absorption $2\nu_3$ à $1,66 \mu\text{m}$ est exploitée et les premières mesures des signaux lidar sont exposées. Ce travail se termine par la présentation des possibles perspectives d'évolution.

Thesis abstract

In this thesis, a new active remote sensing methodology is proposed to evaluate the content of atmospheric trace gases. The new methodology is based on laser spectroscopy and consists in coupling a spectrally broadband lidar with optical correlation spectroscopy (OCS-lidar). Theoretical and numerical studies have been performed and the first experimental proof has been achieved showing that OCS-lidar is a robust measurement methodology allowing trace gases surveys for environmental, agricultural and industrial plants. In addition, several studies have been achieved on the optical properties of atmospheric particles by using a UV-VIS polarization lidar with emphasis given on atmospheric physical and chemical processes.

As a first step, a new formalism has been developed to remotely evaluate the target gas concentration from the OCS-lidar signals. To evaluate the performance of this new methodology, a numerical model simulating OSC-lidar signals for methane and water vapor measurement has been developed. There, sources of statistical and systematic errors have been evaluated and discussed. Moreover, the influence of the absorption spectroscopic line parameters, such as atmospheric pressure and temperature, on the retrieved gas mixing ratio has been assessed within the OCS-lidar methodology. A key point is that, when using the OCS-lidar methodology, retrieved mixing ratios are weakly sensitive to the pressure broadening of the absorption line and to the statistical variation of the absorption line strength. Influences of temperature gradients are also evaluated and discussed. In addition to this theoretical work, the first experimental demonstration of the OCS-lidar methodology has been performed using a femtosecond lidar system. The latter has been entirely designed, developed and implemented in the framework of this thesis. Results show the ability of the OCS-lidar methodology to monitor the water vapor in the planetary boundary layer using the 4v 720 nm absorption band. Moreover, two different experimental configurations have been proposed, depending on whether the amplitude modulation is operated on the laser pulse or on the backscattered light, i.e. at the emission, with an active amplitude modulator or at the reception, with passive optical filters. The advances in developing the corresponding infrared OCS-lidar system for methane mixing ratios measurements are described and possible outlooks are given.

List of variables

A	Coefficient of the OCS third order polynomial
B	Constant associated to a molecule geometry and mass
B_D	Bandwidth of the detector
c	Speed of light
$C_i(\mathbf{r})$	Concentration of the i-species
$C_{TG}(\mathbf{r})$	Target gas concentration
$C_{TG,ref}$	Target gas concentration in the reference cell
$C_{TG,meas}$	Target gas concentration in the measurement cell
C_{H_2O}	Water vapor concentration
D	Photodetector
D_C	Photodetector of the correlated channel in AMR configuration
D_{NC}	Photodetector of the non-correlated channel in AMR configuration
e	Elementary charge
E_{vib}	Vibrational transition energy
E_{photon}	Photon energy
E_I	Electric field of the idler pulse
E_P	Electric field of the pump pulse
E_S	Electric field of the signal pulse
G	Gaussian function
g_k	Line shape profile
g_C	Line shape profile due to the collision effect
g_D	Line shape profile due to the Doppler effect
g_N	Line shape profile due to the natural broadening effect
h	Planck constant
i	Molecular species subscript
i_0	Dark current value
I	Detector current
$I_0(\nu)$	Intensity emitted by a broadband light source
I_1	Intensity measured by the detector with the optical source 1
I_2	Intensity measured by the detector with the optical source 2
J	Rotational quantum number
K	Constant of the lidar equation
k_b	Boltzmann's constant
k	Ro-vibrational line subscript
L_{ref}	Length of the reference cell
L_{meas}	Length of the measurement cell
L1	Diverging lens in the telescope
m	Modulation factor
m_{mol}	Molecule mass
$M_C(\lambda)$	Correlated amplitude modulation function
$M_{NC}(\lambda)$	Non-correlated amplitude modulation function
$M(\lambda_M, \lambda)$	Gaussian amplitude modulation function
n	Altitude range subscript
N	Number of photons
N_a	Number of atom in the molecule
N_e	Electron population of the excited state

N_e'	Electron population of the ground state
N_{LS}	Number of laser shots
$N_m(r)$	Number of molecule per volume
$N_p(r)$	Number of particle per volume
$O(r)$	Lidar overlap Function
OD_{CH_4}	Methane optical depth
$P(r)$	Signal Lidar
$P_0(\lambda)$	Power spectral density
$\overline{P_0}$	Laser power
P_N	Noise power
P_{atm}	Atmospheric pressure
P_{ref}	Reference pressure
P_C	Correlated OCS-lidar signal
P_{NC}	Non-correlated OCS-lidar signal
r	Range
R	Detector optical responsivity
R_D	Detector resistance
S_k	Line Strength
S_1	Power spectral density for the optical source 1
S_2	Power spectral density for the optical source 2
$T(r)$	Total atmospheric optical transmission
T_{mol}	Optical transmission due to molecules
T_{TG}	Optical transmission due to the target gas
T_{og}	Optical transmission due to the interfering species
T_{aer}	Optical transmission due to aerosols
T_{atm}	Atmospheric temperature
T_{ref}	Reference temperature
T_D	Detector temperature
$T_{eff}(\lambda)$	Effective transmission of an interference filter
$T_{IF}(\lambda, \theta_{IF})$	Effective transmission of an interference filter as a function of the AOI
$T_C(\lambda_0)$	Transmitted laser light through M_C as a function of the laser central wavelength
$T_{NC}(\lambda_0)$	Transmitted laser light through M_{NC} as a function of the laser central wavelength
v	Vibrational quantum number
$\alpha(r)$	Total extinction coefficient
$\alpha_p(r)$	Particle extinction coefficient
$\alpha_m(r)$	Molecular extinction coefficient
$\beta(r)$	Total atmospheric backscattering coefficient
$\beta_p(r)$	Particle backscattering coefficient
$\beta_m(r)$	Molecule backscattering coefficient
$\beta_0(v)$	Optical coefficient
Γ_N	FWHM for a Lorentz function associated to the natural broadening effect
Γ_C	FWHM for a Lorentz function associated to the collision effect
Γ_D	FWHM for a Gaussian function associated to the Doppler effect
ΔE	Uncertainty on the energy level
Δt	Time interval
Δv	Frequency width
θ	Angle of incidence in the OPA nonlinear crystal
θ_{IF}	Angle of incidence in the interference filter
θ_{max}	Maximum angle of incidence in the interference filter

σ	Absorption cross-section of molecule in the gas phase
$\sigma_{a,m}(f)$	Molecular extinction cross-section
$\sigma_{a,p}(r)$	Particle extinction cross-section
σ_{CH_4}	Methane absorption cross-section
$\sigma_{TG}(\lambda)$	Target gas absorption cross-section
$\sigma_i(\lambda)$	Absorption cross-section for molecular species i
σ_B	Standard deviation of the Gaussian function for the background noise
σ_D	Standard deviation of the Gaussian function for the detector noise
σ_{DC}	Standard deviation of the Gaussian function for the laser fluctuation noise
σ_L	Laser spectral bandwidth ($\sigma_L = FWHM / (2\sqrt{2\ln 2})$)
σ_{LF}	Standard deviation of the Gaussian function for the laser fluctuation noise
σ_N	Standard deviation of the Gaussian function for the total noise
σ_{SN}	Current standard deviation due to the shot noise
σ_T	Standard deviation of the Gaussian function for the laser fluctuation noise
$\eta(\lambda)$	Detector quantum efficiency
ℓ	Intensity measured by a detector
λ	Wavelength
λ_0	Central wavelength of the laser pulse
λ_M	Central wavelength of the modulation function M
ω_p	Angular frequency of the input laser pump in the OPA
ω_S	Angular frequency of the signal emitted by the OPA
ω_I	Angular frequency of the idler emitted by the OPA

List of acronyms

AOI	Angle of incidence
AOPDF	Acousto optic programmable dispersive filter
AME	Amplitude modulation at the emission
AMR	Amplitude modulation at the reception
CPA	Chirped pulse amplification
DIAL	Differential absorption lidar
DOAS	Differential optical absorption spectroscopy
FTIR	Fourier transform infrared spectroscopy
FWHM	Full width half maximum
HITRAN	High resolution transmission
LIDAR	Light detection and ranging
NEP	Noise-equivalent power
OCS	Optical correlation spectroscopy
OPA	Optical parametric amplifier
PBL	Planet boundary layer
PM	Particle matter
RH	Relative humidity
RSL	Raman scattering lidar
SNR	Signal to noise ratio
VOC	Volatile organic compounds
WLC	White light continuum in the OPA

Contents

Résumé de thèse.....	4
Thesis abstract.....	6
List of variables	7
List of acronyms	9
 Chapter 1:	
Introduction	15
1.1 General introduction.....	15
1.2 Atmospheric aerosols	18
1.3 Atmospheric trace gases.....	23
1.3.1 Introduction	23
1.3.2 Methane.....	27
1.3.3 Water vapor	28
1.4 Outline of this thesis.....	29
 Chapter 2:	
Methane and water vapor spectroscopy.....	31
2.1 Basics of spectroscopy and notations.....	32
2.1.1 Vibrational spectroscopy	33
2.1.2 Rotational spectroscopy	34
2.1.3 Ro-vibrational spectroscopy.....	34
2.2 Line, temperature and pressure broadening	36

2.2.1 Natural Broadening	37
2.2.2 Temperature broadening	38
2.2.3 Pressure broadening	39
2.2.4 Line shape profile	40
2.3 The case of spectrally integrated optical measurements	42
2.4 Spectroscopic data for water vapor and methane	44
2.4.1 The HITRAN Database	44
2.4.2 Spectrum of the CH ₄ absorption cross-section	45
2.4.2 Spectrum of the H ₂ O absorption cross-section	48

Chapter 3:

Optical Correlation Spectroscopy and Lidar	53
3.1 Optical correlation spectroscopy (OCS).....	55
3.1.1 An introduction to the OCS-methodology	55
3.1.2 The OCS-formalism	57
3.1.3 OCS numerical simulation	60
3.2 Light detection and ranging (lidar).....	62
3.2.1 Introduction	62
3.2.2 Elastic lidar formalism	64
3.2.3 Experimental set-up and measurements	69
3.3 Optical correlation spectroscopy coupled with lidar	74
3.3.1 OCS-lidar principle	75
3.3.2 The OCS-lidar formalism.....	76
3.3.3 Complementary material: The OCS-lidar algorithm using transmission product... 80	

Chapter 4:

The OCS-lidar numerical model.....	83
4.1 Numerical model of OCS-lidar signals	86
4.1.1 Numerical model for the atmosphere	86
4.1.2 Numerical simulation of the laser source	87
4.1.3 The amplitude modulation functions.....	89
4.1.4 The detection system.....	91
4.1.5 Output numerical OCS-lidar signals	95
4.2 Statistical errors on the retrieved concentration	99
4.2.1 Introduction	99
4.2.2 Laser fluctuations	101
4.2.3 Photodetector noise	102
4.2.4 Sky and light background noise	104
4.2.5 Experimental evaluation of σ_N	106
4.3 Systematic errors on the retrieved concentration	107
4.3.1 The OCS-lidar model bias.....	107
4.3.2 Temperature and pressure biases.....	110
4.3.3 HITRAN uncertainty bias	114
4.3.4 Interfering species bias	114
4.3.5 Aerosols and molecular contributions.....	118
4.4 Optimization of the OCS-lidar parameters.....	120
4.4.1 Optimization of the amplitude modulation functions	121
4.4.2 Optimization of the laser source.....	123

Chapter 5:

Experimental Set-ups and first OCS-lidar measurement	127
5.1 The laser source.....	128
5.1.1 The broadband laser source.....	129
5.1.2 The optical parametric amplifier	134
5.2 The amplitude modulation	139
5.2.1 Amplitude modulation in the AME-configuration.....	140
5.2.2 Amplitude modulation in the AMR-configuration.....	145
5.3 The lidar detection system.....	151
5.3.1 The telescope.....	151
5.3.2 The detection and the acquisition system.....	153
5.4 Experimental results in the visible spectral range.....	156
5.4.1 Water vapor mixing-ratio measurements in the AME-configuration	156
5.4.2 Water vapor mixing-ratio measurements in the AMR-configuration	159
5.4.3 Discussion	161
5.5 Preliminary results in the infrared spectral range.....	162
5.5.1 Experimental set up for methane mixing ratios retrieval with OCS-lidar.....	162
5.5.2 First infrared lidar signals	164
5.5.3 Amplitude modulation in the infrared spectral range.....	166

Chapter 6:

Conclusion and outlooks.....	171
List of personal publications	177
References	178

Chapter 1

Introduction

1.1 General introduction

This work is dedicated to the development of a new methodology to remotely study the composition of the atmosphere using optical instruments. As underlined in the IPCC report [IPCC 2007], there is a need for determining the spatial and temporal distribution of the atmospheric constituents, such as trace gases and particles. Both are considered as major actors in climate change processes and health effects through air pollution [Bond et al. 2013, IPCC 2007].

The Earth's climate, usually described in terms of the mean and variability of temperature, precipitation and wind, evolves in time under the influence of natural phenomena such as volcanic eruptions [McCormick et al. 1995] and solar cycles [Grandpierre et al. 2004], as well as human-induced changes on the atmospheric composition [National Research Council

2010]. In turn, climate directly responds to such changes, as well as indirectly, through a variety of feedback mechanisms [Cox et al. 2000, IPCC 2007].

The Earth's radiation budget is mainly governed by three factors:

The first one is the incoming solar radiation, equal to approximately 1370 Watts per meter square facing the Sun, which represents 342 Watts per meter square over the entire Earth's surface. This value changes by about 0.1 % as a function of the solar activity which follows an 11-years cycle [Grandpierre et al. 2004]. This first factor is extremely important in the estimation of the Earth's radiative budget, however since mankind has no influence on the solar activity, it can be hardly used to control or limit climate change.

Secondly, the fraction of the Sun radiation that is reflected, called the albedo, reaches an approximate value of 30 % for the Earth. This factor varies as a function of the cloud cover, the atmospheric particles load (including volcanic particles) and the surface reflectivity, which may greatly differ if highly reflective surfaces such as snow or absorbing vegetation are encountered [Charlson et al. 1987]. By adding particles, or suspended particulate matter (PM), in the atmosphere, human activity such as the coal industry, has significantly influenced the Earth's albedo [Spracklen et al. 2008]. Moreover, the atmospheric aerosols load (ensemble of particles suspended in air) greatly influences the cloud cover since these particles may act as condensation nuclei [Fletcher 1966].

The last major factor affecting the Earth's radiative budget is the greenhouse effect, which by absorbing the long wave radiations from the Earth's surface, keeps a significant amount of energy from getting lost in space. Greenhouse gas concentrations greatly impact the Earth's climate [Karl et al. 2003] despite their concentrations are relatively low, a few parts/million or less. For example, carbon dioxide (CO₂), known as the second most potent greenhouse gas after water vapor, has an atmospheric concentration below 400 ppm, while methane (CH₄), the third greenhouse gas, only reaches 1.7 ppm. For this reason, these gases are often referred to as trace gases. More precisely, a trace gas is a gas which makes up less than 1 % by volume of the Earth's atmosphere. Such extremely low concentrations explain why even small emissions of a trace gas in the atmosphere may easily double or triple their concentrations, and thus their effects on the Earth's radiative budget.

Both aerosols and trace gases also influence the human health. Fine particles, defined as particles smaller than 2.5 micrometers [Seinfeld 1998], are related to the most serious health effects, including lung cancer [Raaschou-Nielsen et al. 2013], and other cardiopulmonary

mortality [Cohen et al. 2005]. Recent studies [Mokdad et al. 2004, EEA 2009] show that particle matter suspended in air is responsible for 370 000 premature deaths every year in Europe. Particles larger than 10 micrometers are usually filtered by our nose and our throat, but smaller particles may penetrate, depending on their size, deeper in the lungs, and then cause health problems such as asthma, lung cancer, cardiovascular issues, respiratory diseases, birth defects and premature deaths. Extremely fine particles, under 100 nanometers in diameter, can even reach other organs by passing through the lungs, being then even more dangerous for the cardiovascular system [Hsieh et al. 2013].

The influence of atmospheric trace gases and particles on the Earth's climate and human health is governed by complex processes [Dupart et al. 2012, Kulmala et al. 2012]. To this, we can add the difficulties encountered when quantitatively evaluating their concentration in the Earth's atmosphere, as well as their optical and chemical properties. As for example, atmospheric CO₂, which is well mixed in the Earth's atmosphere, requires to be determined with a precision of less than 1 % on its concentration with a high spatial resolution over the Earth's surface to estimate properly its sources and sinks [Abshire et al. 2012]

In this context, there is an obvious need for characterizing these compounds. How are such atmospheric trace gases and particles spatially distributed? How do their concentrations evolve in time? What are the chemical, morphological and optical properties of these atmospheric compounds? This knowledge is of prime importance to better understand their influence on complex mechanisms such as the Earth's climate and the human health.

For this purpose, numerous methodologies and technical solutions have been developed, mostly since the second half of 20th century and up to now. Atmospheric aerosols and trace gases have extremely different properties, such as their size or their shape. Consequently, instruments to measure their spatial and temporal distribution are not necessarily similar. For this reason, the two following sections of this introduction will treat separately the study of aerosols and trace gases.

1.2 Atmospheric aerosols

As mentioned above, atmospheric aerosols play a key role in the Earth's atmosphere radiative balance both directly, by light extinction, and indirectly, through complex processes involving physical and chemical properties of aerosols [Twomey 1974]. Figure 1.1 presents four examples of such particles showing their diversity in shape and size.

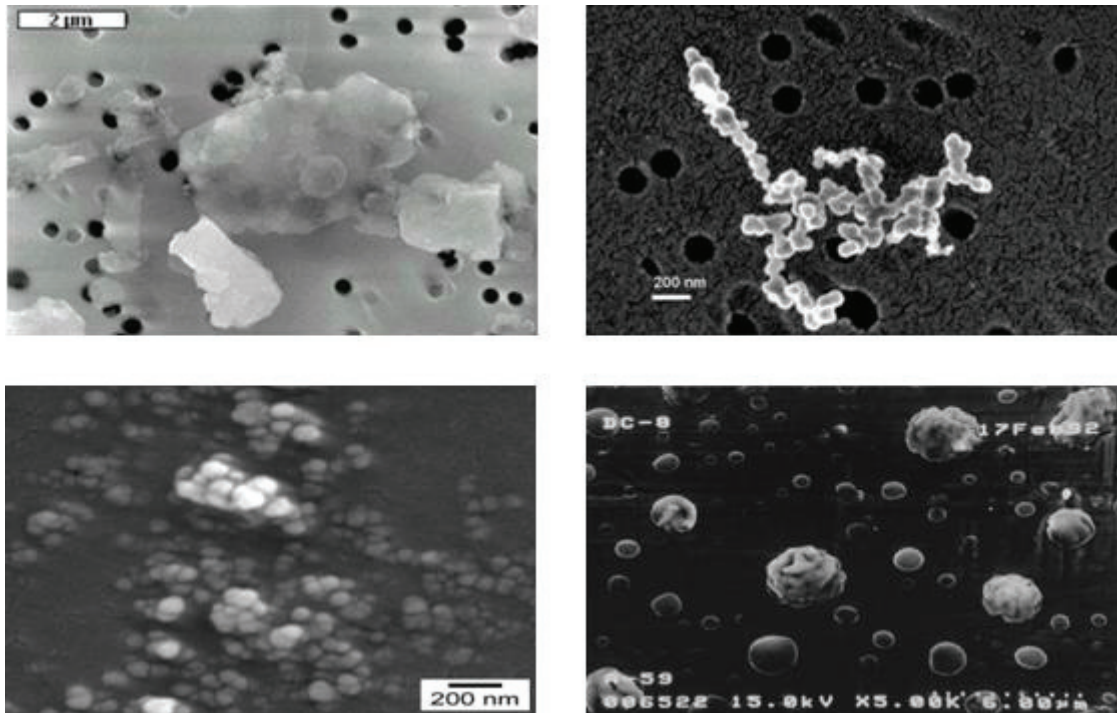


Fig. 1.1: Examples of atmospheric particles. TiO_2 particles (top left), single soot particle (top right), ensemble of soot particles from combustion (bottom left), ensemble of atmospheric particles in the free troposphere, including sulfate, nitrate, SiO_2 (bottom right) [Delmas et al, 2005]

In the troposphere, a review of the radiative forcing due to tropospheric aerosols has been proposed by Haywood and Boucher [Haywood et al. 2000]. Tropospheric particles affect hydrometeor formation by acting as condensation nuclei [Gunthe et al. 2011]. Recent studies have shown that natural and anthropogenic PM may also modify the physical and chemical properties of the atmospheric planetary boundary layer (PBL), especially in urban polluted areas, through surface photo-catalytic reactions [Nicolas et al. 2009] and formation of secondary aerosols [Haddad et al. 2011, Frosh et al. 2011]. In addition, biomass burning can be a main concern in urban polluted areas [Favez et al. 2010] and further oxidation processes

by ozone can occur [Baduel et al. 2011]. For climate forcing assessments, the indirect role of particles on the radiative properties of atmospheric particles must be quantitatively estimated. This task is very difficult since a complete physical and chemical PM characterization is not yet achieved [IPCC 2007] even if recent studies are promising [Andrew et al. 2011]. In particular, there is a need for measuring spatial and temporal variations of PM-concentrations in the mixed layer above urban polluted areas.

To perform these measurements, different techniques exist. For example, high volume air samplers are used to measure pollution levels in the atmosphere by collecting particles on a filter paper. The particles load can be assessed by measuring the air stream and by weighing the filter [Pityn et al. 2013]. In addition, optical techniques, such as the analysis of the light scattered or absorbed by particles in the air, are also commonly used. For example, the Aethalometer [Trompeter et al. 2013, Gianini et al. 2013] is an instrument that uses optical analysis to determine the mass concentration of soot particles, also called black carbon, collected from an air stream passing through a filter. The Sun photometer can also be mentioned as it is used in numerous measurement campaigns [Zhao et al. 2013, Nakata et al. 2013] to retrieve the aerosol load in urban areas. One of the major limitations when studying atmospheric aerosols originates from the lack of detailed knowledge on the optical properties of atmospheric aerosols, which induces large uncertainties. To face such a complexity, laser spectroscopy is of prime importance since PM light scattering and extinction are nowadays the main applied optical properties to evaluate the PM-atmospheric content. Several optical properties can be addressed by laser spectroscopy, as for example the scattering phase function [Gayet et al. 1997]. Laser spectroscopy can be applied to address the chemical composition of atmospheric particles, by studying their refractive index wavelength dependency [Lang-Yona et al. 2009]. Laser-induced fluorescence is another methodology to access to the PM chemical composition [Kasparian et al. 2012a,b], also used to characterize organic and biogenic atmospheric particles [Mejean et al. 2004, Mei et al. 2012]. Finally, laser based technologies are also used to remotely study the atmosphere composition. These techniques are called lidar, acronym for LIght Detection And Ranging. The work presented in this thesis is mostly based on the lidar technique.

The lidar is a very efficient tool to remotely provide range-resolved measurements of the optical properties, such as absorption and scattering [Measures 1992, Weitkamp 2005, Fujii 2005]. The lidar principle is based on a pulsed laser beam that is sent into the atmosphere, where it is scattered and absorbed by atmospheric molecules and aerosols. The backscattered

light is collected with a receiving telescope and converted to an electrical signal and digitized for further analysis. This instrument can be used to study the aerosol load in the atmosphere, such as urban particles [Yan et al. 2013, Miffre et al. 2010], volcanic ash particles [Sassen et al. 2007, Miffre et al. 2011, 2012a, b] and desert dust particles [Ansmann et al. 2011, Dupart et al. 2012, David et al. 2013] but can also be specific to other components in the atmosphere as it will be seen in the following section, such as trace gases [Gheusi et al. 2001], or water vapor [Whiteman et al. 2011]. Laser active remote sensing is particularly interesting as it provides fast and range-resolved access to the optical properties of an ensemble of atmospheric particles, under in situ atmospheric conditions of temperature and humidity [Kacenelenbogen et al. 2011, Veselovskii et al. 2010]. The laser excitation wavelength λ can be chosen in the visible (VIS) [David et al. 2012, David et al. 2013], infrared (IR) [Mejean et al. 2004, Kacenelenbogen et al. 2011, Sugimoto et al. 2002] or ultraviolet (UV) spectral range [Reichardt et al. 2000, De Villiers et al. 2010, Freudenthaler et al. 2009, Miffre et al. 2011]. In the meantime, atmospheric particles present a three-modal size distribution with an ultra-fine mode (in the nanometer scale), a fine mode (in the range of a few hundreds of nanometers) and a coarse mode (in the micrometer size range). While coarse particles experience sedimentation processes and ultra-fine particles encounter aggregation and condensation processes, in urban polluted areas, fine particles, whose main emissions are sometimes local, experience the longest lifetime. Hence, most observed atmospheric particles are fine, and in urban polluted areas the number of fine particles can exceed $1000 \text{ part.cm}^{-3}$ [Favez et al. 2010]. To address highly concentrated fine particles with laser remote sensing, it is interesting to choose a laser excitation wavelength in the UV spectral range, where particles size parameters ($2\pi r/\lambda$ for an r equivalent sphere radius) often lead to scattering efficiency enhancements [Mishchenko et al. 2002]. This is, however, challenging since in the UV spectral range, molecular scattering may overcome particles scattering.

Among the major uncertainties involved in climate change modeling, the lack of knowledge on the atmospheric particles shape is an essential point, especially in urban polluted areas, where atmospheric aerosols may present a wide range of size and shape. Hence, applying the century-old Lorenz–Mie formalism to tropospheric particles may lead to significant errors in climate change modeling [Kahnert et al. 2005], as non-spherical particles scatter light differently from volume- or surface-equivalent spheres. In particular, orientation averaging over an ensemble of non-spherical particles does not lead to the same scattering pattern as for spheres [Nousiainen et al. 2009]. Hence, non-spherical particles are difficult to address since

no general analytical solution is available, except for some specific geometry far away from the observed highly-irregular shape of atmospheric particles [Mishchenko et al. 2002]. However, the polarization of the phase function is unequivocally sensitive to particles shape modifications [Mishchenko et al. 2002], which makes the detection of this property attractive for laser remote sensing. For spherical particles, the polarization state of the laser is preserved during the scattering process. In contrast, scattering of light by an ensemble of randomly-oriented non-spherical particles modify the polarization state of the laser. More precisely, as this polarization state is analyzed at a far range compared to the particles size, randomly-oriented non-spherical particles exhibit a non-zero polarization change [Mishchenko et al. 2002], often called depolarization, whose magnitude (hereafter called the particles depolarization ratio) is a signature of the particles sphericity. Hence, polarization-sensitive lidar systems can be used as particle shape indicators.

A part of this thesis has been dedicated to the study of atmospheric aerosols by using a highly sensitive and accurate UV-VIS polarization lidar [David et al. 2012]. The next paragraphs briefly relate the work that has been achieved on atmospheric aerosols by using the UV-VIS polarization lidar. More detailed information can be found in the different published papers related to this specific topic [Dupart et al. 2012, David et al. 2012, 2013a,b, Miffre et al. 2011, 2012a,b].

The optical backscattering properties of atmospheric non-spherical particles have been analyzed thanks to a home-built 355 – 532 nm depolarization lidar system (usually referred to as $2\beta + 2\delta$ lidar system in the lidar community). More details on this system can be found in [David et al. 2012]. Using these sensitive UV-VIS polarization lidar measurements, a new methodology has been developed to retrieve, in a two or three component particle mixture, the backscattering coefficients specific to each particle component [David et al. 2013a].

In addition, new particle formation events have been studied in the atmosphere by using our UV-VIS polarization lidar which is new and opens new insights at the forefront with the state-of-the-art knowledge in atmospheric physics and chemistry [Dupart et al. 2012]. In such photochemistry, the dust particles surface acts as a sink for many gases, such as sulfur dioxide. Under most conditions, sulfur dioxide reacts on dust particle surfaces, leading to the production of sulfate ions. For specific atmospheric conditions, these observations provide evidence for an alternative pathway as depicted in Figure 1.2, in which a series of reactions under solar UV-light produces first gaseous sulfuric acid as an intermediate product before

surface-bound sulfate. Metal oxides present in mineral dust act as atmospheric photo-catalysts promoting the formation of gaseous OH-radicals, which initiate the conversion of SO_2 to H_2SO_4 in the vicinity of mineral dust particles. Under low dust conditions, this process may lead to nucleation events in the atmosphere. More details on this chemical process can be found elsewhere [Dupart et al. 2012].

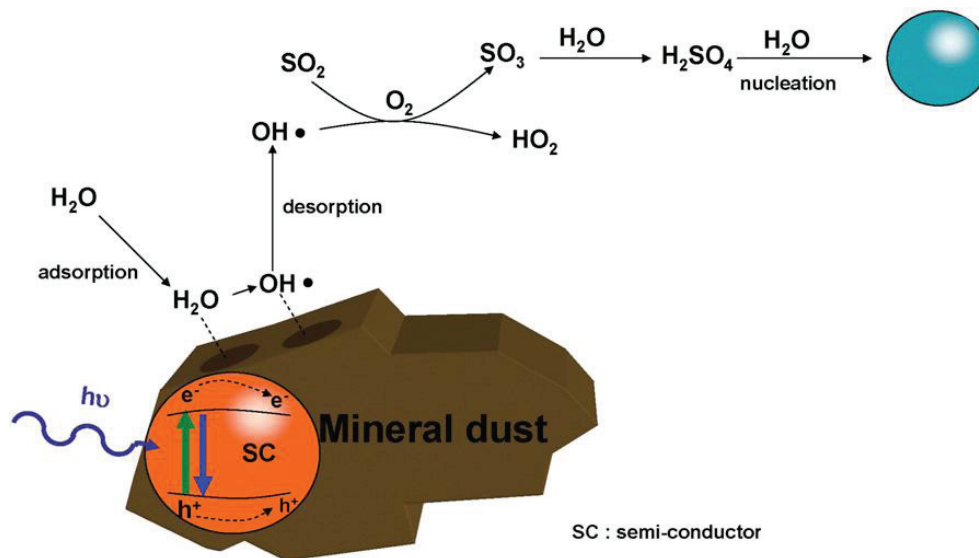


Fig. 1.2: Scheme of reaction mechanism. The semiconductor (SC) components of dust under UV irradiation are producing OH radicals that may desorb and react with SO_2 in the vicinity of the dust OH radicals oxidizing SO_2 in the vicinity of the surface. The produced sulfuric acid may then initiate nucleation events.

New particle formation events can be initiated by natural and anthropogenic phenomenon mainly involving sulfuric acid cluster and other atmospheric compounds. It is also interesting to note that recent works showed that new particle formation events can be artificially induced in the atmosphere by high power laser light involving nitrate and water compounds [Henin et al. 2011, Kasparian et al. 2012a, b], leading to the formation of hydrometeors in the laser beam.

1.3 Atmospheric trace gases

1.3.1 Introduction

Natural and anthropogenic atmospheric gases, such as CO₂, CH₄, volatile organic compounds (VOC) and water vapor, also play an important role in the Earth's radiative budget and in air pollution [IPCC 2007]. The detection and the measurement of gas concentrations are important for both understanding and monitoring a variety of phenomena from industrial processes to environmental change [Hodgkinson et al. 2013].

Hence, monitoring techniques have been developed to evaluate the atmospheric content of such trace gases. We can mention the use of media such as Teflon bags or sampling tubes to trap trace gases, laboratory analysis can then determine the composition of the atmosphere by using mass spectrometer or gas chromatography [Kuprov et al. 2011, Huang et al. 2013, Delmas 2005]. Also, absorption plates can trap pollutants, such as sulfur dioxide, on a reactive plate for measuring air contaminants concentrations [Delmas 2005]. In addition, optical spectroscopic techniques can also precisely assess atmospheric trace gas mixing ratios (dimensionless quantities), which are defined as the amount of a constituent divided by the total amount of all other constituents in a mixture. Nowadays, several optical methodologies stand as references; the next paragraphs present the most commonly used methodologies to perform trace gas concentration measurements. A global review on optical gas sensing can be found in [Hodgkinson et al. 2013]. In addition, the following paragraphs present (non-exhaustively) different optical methodologies for trace gases remote sensing

Differential optical absorption spectroscopy, also known as DOAS [Richter et al. 1999, Eisinger et al. 1997, Platt et al. 1994] is a methodology used to determine trace gases concentrations by measuring their specific narrow band absorption structures. As an example, NO₂ measurements were made as early as 1973 [Brewer 1973]. The main advantage of this technique is that it allows real-time measurements of several different trace-gas species with a single instrument [Platt et al. 1994]. Discussion of optimal DOAS instrument design characteristics can be found in [Plane et al. 1992].

Fourier transform infrared spectroscopy (FTIR) [Pieniniemi et al. 2010, Pongrácz et al. 2010] is another technique used to perform optical gas sensing based on a source emitting a broadband having different wavelengths in the infrared spectral range. In this case, the IR radiation goes through an interferometer, typically a Michelson interferometer, which

spectrally modulates the infrared radiation before going into a measurement gas cell. By data processing, Fourier Transform mathematics is used to turn an interferogram into an absorption spectrum. The absorption of infrared radiation at each wavelength is then quantitatively related to the number of absorbing molecules in the sample gas. This methodology can also be applied to perform long-path measurements of atmospheric trace gas concentrations [Gosz et al. 1988].

Laser-based remote sensing techniques have been used to retrieve atmospheric gas mixing ratios, in which absorption spectroscopy measurements were carried out. The lidar technique stands as a reference for trace gas concentration remote sensing over a long range, mostly using two different lidar methodologies, the differential absorption lidar and the Raman scattering lidar [Weitkamp 2005].

The differential absorption lidar (DIAL) relies on a differential return from two closely spaced laser wavelengths, one is strongly absorbed by the gas of interest, called the on line, while the off line is weakly absorbed. Figure 1.3 presents the principle of the concentration determination by differential absorption lidar from [Robinson et al. 2011]. The amplitude of the differential return signal at different distances along the laser beam path allows to evaluate the target gas concentration.

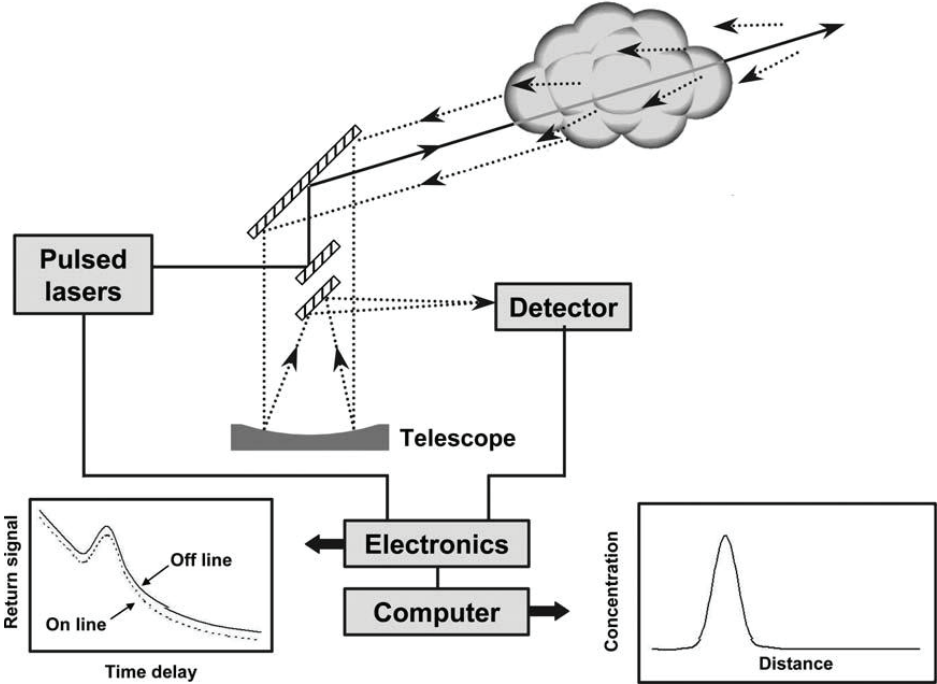


Fig. 1.3: DIAL operates by measuring the backscattered radiation from at least two laser pulses transmitted into the atmosphere. [Robinson et al. 2011]

Integrated [Riris et al. 2012, Ehret et al. 2008] or range-resolved trace gas concentrations have hence been assessed over a wide variety of ranges, within the PBL [Gaudio et al. 2012] up to global planetary measurements [Guo et al. 2012, Cogan et al. 2012, Kiemle et al. 2011, Ismail et al. 2008]. Gas mass flux measurements have also been achieved when combined with wind field measurements [Chambers et al. 2008]. In addition, safety measurements and leak localization for hazardous gases have been performed and are now commonly used [Fix et al. 2004].

However, to achieve accurate DIAL measurements, a tunable laser, having a narrow spectral line width is required combined with a high spectral resolution detector [Gibert et al. 2008]. Hence, when applying the DIAL-methodology, limitations may occur when the spectral width of the emission laser does not match the target gas absorption line. Examples of this situation are given by NO_3^* in the visible spectral range and by ozone (O_3) in the ultra-violet spectral range, as shown by V.D. Burlakov [Burlakov et al. 2010], who recently underlined that during ozone DIAL measurements, ozone absorption broad spectral lines (more than 10 nm width) lead to important corrections in the optical extinction coefficient. Conversely, when the absorption line width is in the same range as the laser spectral width (or even narrower than), effective absorption cross-sections should be taken into account. It follows that a correction is required, as for the detection of mercury (Hg) or nitric oxide (NO) [Guan et al. 2010] in the UV spectral range, or as for greenhouse gases such as water vapor (H_2O) [Wagner et al. 2013], methane (CH_4) [Ehret et al. 2008] or carbon dioxide (CO_2) [Ismail et al. 2010] in the mid-infrared spectral region.

The Raman scattering lidar (RSL) is based on the frequency ro-vibrational shift of the scattered radiation as a result of the inelastic optical interaction of photons with atmospheric molecules. As a consequence, the backscattered light wavelength differs from the laser source wavelength, and this shift is characteristic of the scattering molecule. For example, when excited with a 355 nm radiation, the nitrogen molecule emits light at 387 nm as a result of the Raman scattering while the water vapor emits at 407 nm [Whiteman et al. 2011]. However, Raman scattering cross-sections are weak, in a range of 10^3 lower than the elastic scattering ones [Inaba 1976]. Hence, this methodology is appropriate for active remote sensing of high concentration atmospheric trace gases or water vapor [Di Girolamo et al. 2009, Whiteman et al. 2011, Borg et al. 2011].

In the past fifteen years, laser technology improvement and new methodology development have been achieved. Other methodologies, based on a broadband emission laser, have hence been successfully studied [Faye et al. 2001] and applied [South et al. 1998, Rairoux et al. 2000, Geiko et al. 2010, Stepanov et al. 2010]. In the field of remote sensing using broadband lasers (a few nanometers) instead of a narrowband lasers (a few picometers), we may mention novel research achievements on identification of biological aerosols using fluorescence [Xu et al. 2007, Mejean et al. 2004] and remote sensing of greenhouse gases by broadband differential absorption lidar [Penchey et al. 2012, Georgieva et al. 2011, Minato et al. 1999].

In this thesis, we propose another methodology to remotely address atmospheric trace gases. This new methodology is based on coupling lidar remote sensing with optical correlation spectroscopy (OCS), hereafter called OCS-lidar. OCS is a known and robust methodology for in-situ gas sample concentration measurements [Dakin et al. 2003, Lou et al. 2012a, b, Lou et al. 2010]. Pioneering work in this field has been done by Ward and Zwick, who developed the so-called GASPEC instrument [Ward et al. 1975]. In a few words (further explanations are given in Chapter 3), the OCS instrument involves two broadband light sources with identical spectral distributions: one beam passes through a reference cell containing the gas of interest, before entering the cell where the measurement is achieved, while the second light beam only passes through the measurement cell. In this case, because it went through the reference cell, the first beam spectrum has been carved by the absorption cross-section of the target gas. After the measurement cell, the two output signals are used to evaluate the target gas concentration, based on the difference in extinction undergone by the two light beams. The target gas concentration can be retrieved from the calculated correlation by using one mathematical function (either the difference or the ratio between the two optical output signals). Hence, to estimate the amount of gas, the OCS methodology does not require spectrally-resolved optical measurements, which would make either the laser source or the detector (or even both of them) much more complex. The coupling of GASPEC with a lidar has been first proposed by Edner et al. [Edner et al. 1984], who performed a remote sensing experiment on a 70 m distant open-ended chamber, simulating a Hg-containing atmosphere. Laser pulses, emitted at the 253.7-nm wavelength Hg-absorption line, were retro-reflected by a solid target back to the lidar telescope, hence simulating backscattering from the atmosphere. The spectral correlation was then achieved by inserting a highly concentrated Hg-reference gas cell in the light pathway.

This thesis focuses on the study of the feasibility of this new methodology to measure a trace gas concentration, and more specifically water vapor and methane. These two gases have been chosen because water vapor usually presents a high atmospheric concentration in the range up to a few percent while methane has numerous and localized emission sources. In addition, they are, respectively, the first and third most potent greenhouse gases. The CO₂, second most potent greenhouse gas, has already been in the center of numerous studies [Etheridge et al. 1996, Berner et al. 2001]. Moreover, CO₂ is known to be well mixed in the troposphere and is therefore not the best candidate to test a new methodology since the spatial and temporal concentration variations are then harder to measure.

1.3.2 Methane

Methane greenhouse gas has a global warming potential 25 times higher than carbon dioxide due vibrations and rotations of the methane molecule that correspond to radiations in the infrared spectral range. Its mixing ratio was stable and equal to 700 ppb before the human industrial upheaval and nowadays reaches 1.7 ppm and is still increasing, as it can be seen in Figure 1.4. As a consequence, methane is, after carbon dioxide, the second most important anthropogenic greenhouse gas, directly contributing 0.48 W/m² to the total anthropogenic radiative forcing of 2.63 W/m² by well-mixed greenhouse gases [IPCC 2007]. Methane greenhouse gas contributes up to 20 % to the total radiative forcing of the Earth's.

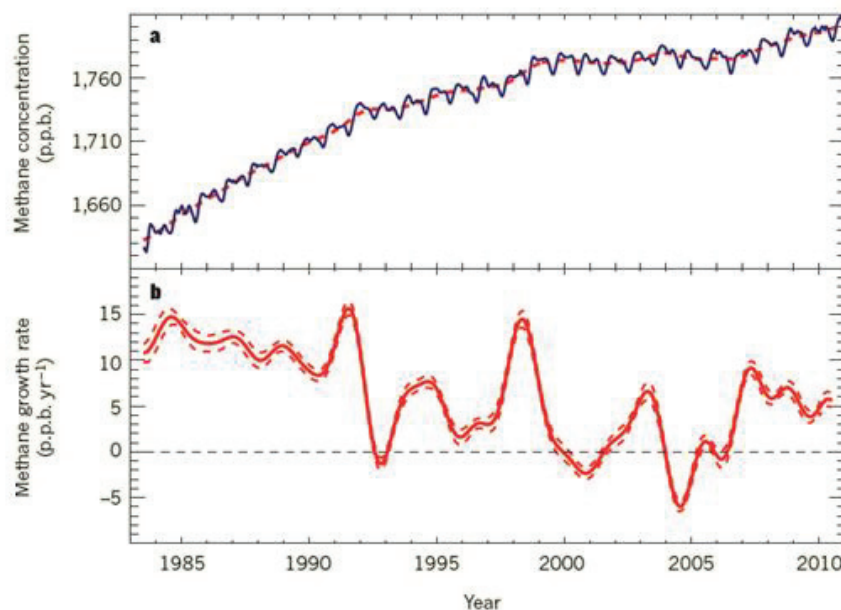


Fig. 1.4: Average methane concentration (top graph) and methane growth rate [Heimann 2011].

Methane spatial and temporal concentration variations are large. Background concentrations exhibit seasonal [Heiman 2011] and regional variations from wetlands, rice paddies, and permafrost [Shakhova 2010]. These variations are subject to large uncertainties due to the lack of observations at high latitude and to low-frequency observations [Kiemle et al. 2011, Heimann 2011]. Anthropogenic methane emissions from agriculture, waste, and refinery sources, which are local and coupled with high concentrations (up to the tens of ppm), represent 40 % of the global methane budget [Robinson et al. 2011]. The uncertainty in this value is large, due to inadequate emission inventory [Shakhova 2010].

1.3.3 Water vapor

Its concentration in the Earth's atmosphere can greatly vary since the maximum amount of water vapor in air radically changes with temperature. For example, air at 273 K can hold only 6 000 ppm of water vapor, while the maximum concentration before condensation in air at 300 K reaches 35 000 ppm. Therefore, concentrations in the Earth's atmosphere range from a few ppm for cold dry air up to 4 % in volume of the atmosphere for hot and humid air. For the same reasons, the water vapor spatial distribution is extremely variable; however, approximately 99 % of the water vapor is located within the troposphere. Moreover, the whole average concentration of water vapor is hard to evaluate since it is constantly depleted by precipitation and increased by evaporation from ocean, seas, lakes and rivers.

The condensation of water vapor to the liquid or ice phase is responsible for clouds, rain, snow, and other precipitation. Less obviously, the latent heat of vaporization, which is released to the atmosphere whenever condensation occurs, is one of the most important terms in the atmospheric energy budget on both local and global scales. Water vapor is also the most potent greenhouse gas owing to the presence of the hydroxyl bond which strongly absorbs in the infra-red region of the light spectrum, forming what is also called the water vapor absorption continuum.

Due to this continuum, water vapor is also known as an interfering species when measuring other atmospheric components. The induced bias can be significantly reduced if the water vapor concentration profile is known.

Despite water vapor is a well-known compound of the atmosphere, fundamental physico-chemical processes involving this greenhouse gas are presently under study [Kulmala et al. 2013]. In addition, climate change reinforces the need for H₂O spatial distribution measurements. This last decade shows a considerable relative increase of the water vapor amount in the tropopause [IPCC 2007] which in turn decreases the formation of precipitation cloud in the lower atmosphere.

1.4 Outline of this thesis

This manuscript reports the work done on a new methodology based on broadband differential lidar [Thomas et al. 2012, Thomas et al. 2013a, b]. It has been achieved at the Institute of Light and Matter (ILM) in the framework of a research and development program based on a patent [J. Kasparian, J.P. Wolf: FR2916849A1A1] and with the support of the Leosphere company. The manuscript is organized as follows.

The basics of molecular spectroscopy together with the presentation of the spectroscopic data used in this thesis are presented in Chapter 2. It includes a study which shows that, when using spectrally-integrated optical measurements, the spectral line shape is not a major concern in such measurements and that the measurement is mostly sensitive to the strength of the considered spectroscopic transitions. Finally, the absorption cross-section of atmospheric water vapor and methane is presented by using the HITRAN database.

Then, the OCS-lidar methodology is introduced in Chapter 3. The two techniques on which this methodology is based, namely the OCS and the lidar, are first introduced by giving importance on the principle of optical correlation spectroscopy then on the lidar technique. In this subsection, the lidar formalism as well as the first experimental lidar data built in the frame of this thesis are presented. Finally, the formalism of the OCS-lidar methodology is presented to show how the target gas concentration can be retrieved from the OCS-lidar signals.

The Chapter 4 is then dedicated to the numerical model that has been developed to evaluate the feasibility, the precision and the sensitivity of the new OCS-lidar methodology. As a first step, the numerical model simulating the OCS-lidar signal is presented, showing its

capabilities. From there, the statistical and systematic errors are evaluated and discussed, in two case studies, namely water vapor and methane. The last subsection of this chapter presents how the laser source and the amplitude modulator used to achieve the optical spectral correlation, have been optimized by using the here presented numerical model.

Finally, the first experimental OCS-lidar set-up and the first experimental results using the OCS-lidar methodology are presented in Chapter 5. It first describes the laser source, the amplitude modulation, and the detection system. The first results for water vapor concentration measurements in the visible range are then presented for two different experimental set-ups, depending on whether the amplitude modulation is applied before or after the atmospheric backscattering process. Also, the recent advance achieved in the methane measurement in the infrared is presented in this chapter. This manuscript ends with a conclusion and an outlook.

Chapter 2

Methane and water vapor spectroscopy

The work presented in this thesis is based on the absorption spectroscopy of light by methane and water vapor. An account on the absorption of electromagnetic radiation by molecules in the gas phase is given in this chapter by presenting the fundamental absorption mechanisms, which are first briefly recalled to fix our notations, together with the major sources of line broadening. As detailed in Chapter 3, this thesis proposes a new methodology to remotely retrieve trace gas concentrations. Because this methodology is based on spectrally-integrated optical measurements, it is necessary to discuss the influence of the line shape profile on such optical measurements. This key point is discussed in this chapter. Finally, the spectroscopic properties of methane and water vapor molecules are introduced and their respective absorption cross-section is presented, by using the spectroscopic HITRAN database.

2.1 Basics of spectroscopy and notations

The work presented in this thesis is based on molecular spectroscopy. For this reason, this section briefly presents the basics and introduces the notations used in this text. The knowledge presented here is based on several text books [Banwell et al. 1994, Hollas 1998, Biémont 2008].

Spectroscopy is the study of the interaction, such as absorption or emission, of electromagnetic radiation with matter. The state of a molecule is defined by its energy which can take discrete values, as described by quantum theory. These energy values are called energy levels. A molecule is most likely to absorb a photon having a frequency ν only if its energy $h\nu$ (h being the Planck constant) corresponds to the difference of energy between two energy levels of the molecule. When such absorption occurs, the molecule reaches a higher energy level. Similarly, when the molecule returns to a lower energy level, a photon is emitted with the corresponding energy, this is called an energy transition.

Each molecule can absorb or emit several discrete frequencies giving rise to the emission and absorption spectrum of the molecule. The total internal energy of a molecule is divided in different form of internal energy: electronic, vibrational and rotational which depend on the electronic configuration of the molecule as well as on its geometry, as detailed below. As a consequence, the absorption spectrum of the molecule is a signature of the molecule and this feature can be used for its identification, which constitutes the basic principle of molecular spectroscopy.

Electronic transitions are highly energetic, in the range of a few electron-volts, thus the emitted or absorbed radiations are in the ultra-violet spectral range or the high frequency part of the visible spectrum (blue). Vibrational and rotational transitions are less energetic and concern the low frequency part of the visible spectrum (red) and the infrared spectrum. The different energy levels are described by their quantum number, written v and J for vibrational and rotational levels respectively.

2.1.1 Vibrational spectroscopy

A molecular vibration occurs when atoms in a molecule are in periodic motion. The frequencies of molecular vibrations, hereafter noted ν_{vib} , typically range from less than 10^{12} to approximately 10^{14} Hz. Vibrations of a simple molecule such as diatomic molecules are well described by the harmonic oscillator theory. The vibrational energy level $E_{\text{vib}}(\nu)$ can be written as a function of the vibration frequency ν_{vib} and the quantum number ν :

$$E_{\text{vib}}(\nu) = h \cdot \nu_{\text{vib}} \cdot \left(\nu + \frac{1}{2} \right) \quad (2.1)$$

However, this expression is a first approximation since diatomic molecules are not perfect harmonic oscillators, so that Equation (2.1) is usually completed by adding anharmonic terms.

When considering a polyatomic molecule, many different molecular vibration modes are possible. As a result, several vibrational frequencies have to be considered. Figure 2.1 presents an example of possible vibration modes in the case of the water vapor molecule. The hydrogen atoms can move back and forth towards the oxygen atom (antisymmetric and symmetric stretch) or towards the other hydrogen atom (scissoring bend).

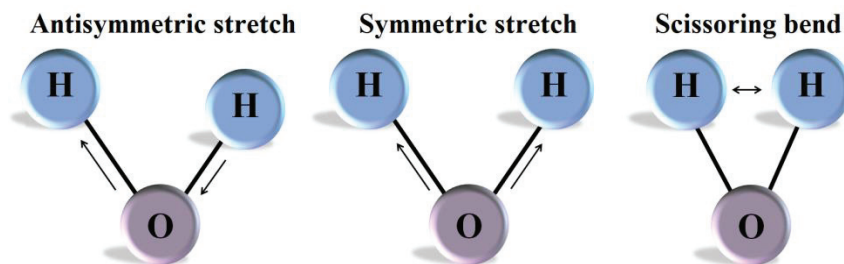


Fig. 2.1: Example of vibrational modes for the water molecule.

The number of possible modes depends on the geometry of the molecule. A linear molecule composed of N_a atoms has $3N_a - 5$ vibrational modes while polyatomic non-linear molecules have $3N_a - 6$ possible vibration modes. For example, methane (CH_4) has nine vibrational modes. However due to its spherical symmetry, only four of these modes are independent, so that the vibrational modes of the methane molecule are denoted ν_1 , ν_2 , ν_3 and ν_4 .

2.1.2 Rotational spectroscopy

In the gas phase, a molecule is also free to rotate due to the absence of intermolecular forces, as opposed to the liquid and solid thermodynamic phases. If we consider a diatomic molecule, the rotational energy levels E_{rot} depends on the rotational quantum number J and a constant B depending on the molecule moment of inertia:

$$E_{\text{rot}}(J) = h \cdot c \cdot B \cdot J \cdot (J + 1) \quad (2.2)$$

Here c is the speed of light. When considering polyatomic molecules, many more rotational modes have to be considered since there is more than one rotation axis. In this case, the rotational energy level E_{rot} analytical expression differs depending on the geometry of the molecule, symmetric or asymmetric, linear or not, number of atoms.

Moreover, some transitions between two rotational energy levels are not possible. The quantum theory related to rotational transitions implies selection rules. These selection rules depend on the dipolar momentum of the molecule. If it is parallel to the molecular axis, then the selection rule is given by $\Delta J = \pm 1$. If it is perpendicular, then $\Delta J = 0, \pm 1$.

2.1.3 Ro-vibrational spectroscopy

Vibrational and rotational transitions can simultaneously occur, and correspond to the transitions between an energy level characterized by its quantum numbers (v, J) to an energy level having (v', J') for ro-vibrational quantum numbers. These transitions are called ro-vibrational transitions. Since the difference in energy between two vibrational levels is larger than between two rotational levels, rotational transitions give a fine structure for each vibrational transition. The resulting spectrum involving vibrational transitions having the same rotational quantum number ($\Delta J = J' - J = 0$) in the ground (v, J) and excited (v', J') state is called the Q-branch. On the high frequency side of the Q-branch, the energy of rotational transitions is added to the energy of the vibrational transition. This is known as the R-branch of the spectrum for $\Delta J = +1$. The P-branch for $\Delta J = -1$ lies on the low wavenumber side of the Q-branch. Figure 2.2 presents a typical energy level diagram for ro-vibrational transitions

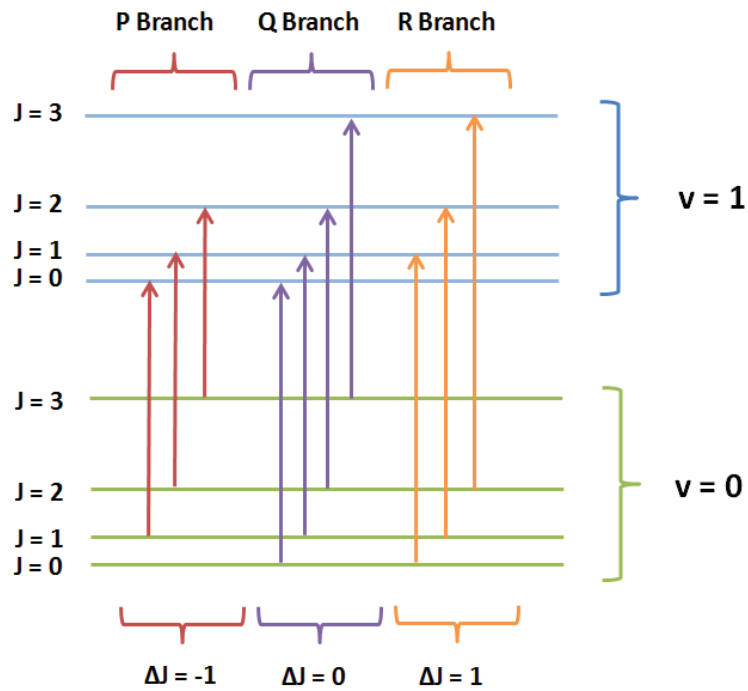


Fig. 2.2: Schematic ro-vibrational energy level diagram.

Thus, it is clear that each molecule has a set of absorption or emission lines associated with a frequency ν . However, each allowed transition is not equally probable: from quantum mechanics, each transition has a probability to absorb or emit radiation from which results the so-called line strength, hereafter noted S . The line strength S depends on the gas temperature and also on the number of molecules in the initial state but is pressure independent. As an example, Figure, 2.3 presents a line spectrum showing the P, Q and R-branch of the methane molecule due to the ν_3 ro-vibrational transition in the infrared spectral range. These lines, which correspond to a given vibrational transition, form a band. These data come from the HITRAN database, which is described and used later in this chapter.

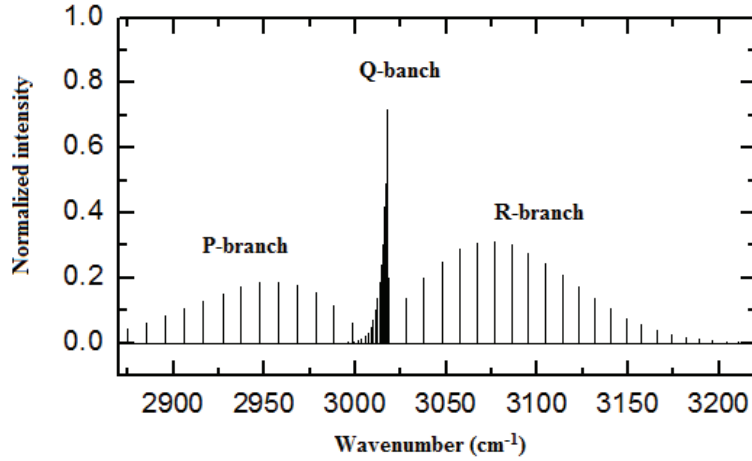


Fig.2.3: The line spectrum of the methane ν_3 ro-vibrational band around 3000 cm^{-1} wavenumber ($3.3 \text{ }\mu\text{m}$ wavelength).

2.2 Line, temperature and pressure broadening

The energy transition process described in the previous section implies that each molecule has an absorption line spectrum. Hence, to each spectral line, hereafter noted k , corresponds a unique frequency and a strength, written as $\nu_{0,k}$ and S_k respectively. However, these absorption lines are not infinitely thin but have a spectral width. This spectral width is described by the line shape profile g_k which depends on the considered transition line and on the atmospheric temperature and the atmospheric pressure.

For a given frequency ν , the probability of absorption is given by the absorption cross-section, expressed in m^2 , which is defined as:

$$\sigma(T_{atm}, P_{atm}, \nu) = \sum_k S_k(T_{atm}) \cdot g_k(T_{atm}, P_{atm}, \nu - \nu_{0,k}) \quad (2.3)$$

where the line shape profile g_k is function of the atmospheric temperature T_{atm} and pressure P_{atm} . This function is normalized so that:

$$\int_0^\infty g_k(T_{atm}, P_{atm}, \nu - \nu_{0,k}) \cdot d\nu = 1 \quad (2.4)$$

The next subsections focus on the line shape profile by recalling the different sources of broadening.

2.2.1 Natural Broadening

Ro-vibrational energy transitions have a natural broadening due to the Heisenberg uncertainty principle relating the lifetime of the excited state to the uncertainty on its energy. A short lifetime Δt will lead a large energy uncertainty ΔE and therefore a broad emission. This natural broadening results in a Lorentzian line shape profile written g_N as shown in Figure 2.4. The spectral line shape g_N due to the natural broadening is in this case expressed as a function of the frequency ν_0 as follows:

$$g_N(\nu - \nu_0) = \frac{\Gamma_N}{2\pi \cdot \left((\nu - \nu_0)^2 + \left(\frac{\Gamma_N}{2} \right)^2 \right)} \quad (2.5)$$

where Γ_n is the FWHM of the Lorentz function and function of ΔE .

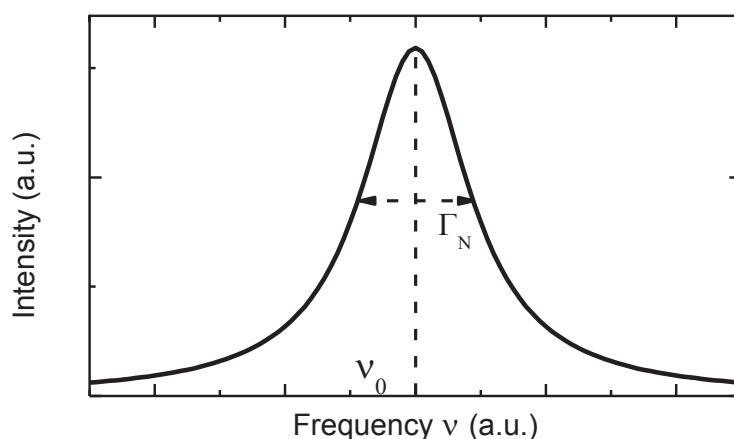


Fig. 2.4: Line shape profile as a Lorentz function centered on ν_0 with Γ_n the FWHM.

In the infrared spectral region, the typical life time for molecular vibrational transitions to occur is quite long, in the range of 10^{-3} s, leading to narrow spectral lines, with a natural broadening in the range of 100 Hz. When actually measured, a gas absorption cross-section

presents broader absorption lines than expected by natural broadening due to the spectral broadening that occurs from the gas temperature and pressure, as detailed below.

2.2.2 Temperature broadening

Since the rotational and vibrational state distribution in the electronic ground state changes with temperature, the absorption line strength varies with the gas temperature, assumed in our case to be equal to the atmospheric temperature T_{atm} at local thermal equilibrium. As expressed by the Maxwell-Boltzmann statistic, the temperature T_{atm} and the difference of energy between the two levels $E_2 - E_1$ defines the population ratio N_2 / N_1 , which is related to the line strength:

$$\frac{N_2}{N_1} = \exp\left(-\frac{E_2 - E_1}{k_B \cdot T_{\text{atm}}}\right) \quad (2.6)$$

As a consequence, the absolute width of the absorption line changes with the strength, in agreement with Equation (2.3).

Moreover, when considering an ensemble of molecules in the gas phase, the distribution of the velocity of each molecule induces a Doppler effect. The higher the temperature of the gas is, the wider the distribution of the velocity gets. If one assumes that each molecule moves in a random direction, the Doppler shift is seen as a broadening effect. The latter is described by a Gaussian line shape profile that gets broader when the temperature increases, in this case, the line shape profile due to the Doppler effect g_D is expressed as follows:

$$g_D(\nu - \nu_0) = \frac{1}{\Gamma_D} \sqrt{\frac{4 \cdot \ln 2}{\pi}} \cdot \exp\left(-4 \cdot \ln 2 \cdot \left(\frac{\nu - \nu_0}{\Gamma_D}\right)^2\right) \quad (2.7)$$

with Γ_D the FWHM of the Gaussian function defined as:

$$\Gamma_D = \frac{2 \cdot \nu_0}{c} \cdot \sqrt{\frac{2 \cdot \ln 2 \cdot k_B \cdot T_{atm}}{m_{mol}}} \quad (2.8)$$

Where m_{mol} is the mass molecule and k_B the Boltzmann constant.

We observe that the Gaussian broadening, displayed in Figure 2.5, due to the Doppler effect is a function of the temperature T_{atm} , the frequency of the line transition ν_0 and the molecule mass m_{mol} .

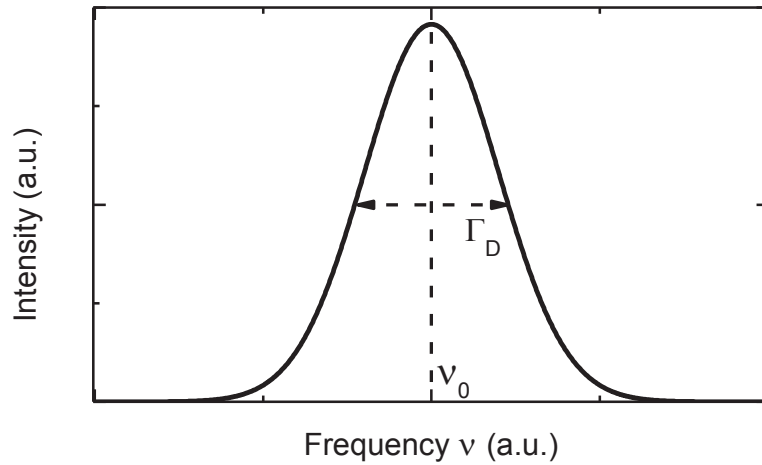


Fig. 2.5: Line shape profile as a Gaussian function centered on ν_0 with Γ_D the FWHM.

At 300 K, the Doppler broadening leads to a rovibrational transition line shape profile that has a width in the range of 100 MHz, i.e. 10^6 times higher than the natural broadening effect.

2.2.3 Pressure broadening

The line strength S_k of the absorption spectral line k does not depend on the atmospheric pressure P . However, the presence of nearby molecules will affect the absorption cross-section of an individual molecule through its line shape profile $g_k(T_{atm}, P_{atm})$. When the pressure increases, the collisions between the molecules are more frequent. The kinetic energy brought during the collision process causes electrons in an excited state to drop down to a lower energy level, as in the stimulated emission process. Therefore the characteristic life time of the excited state becomes shorter. As for natural broadening, this shorter life time

increases the uncertainty in the emitted energy. As a consequence, the pressure of the atmosphere and the partial pressure of the dedicated gas cause a line broadening described by a Lorentzian profile.

$$g_C(\nu - \nu_0) = \frac{\Gamma_C}{2\pi \cdot \left((\nu - \nu_0)^2 + \left(\frac{\Gamma_C}{2} \right)^2 \right)} \quad (2.9)$$

where Γ_C is the FWHM of the Lorentzian function.

The probability for a transition to a lower energy to occur through a collision is also of course related to the nature of the molecules involved. The broadening of the line shape profile described by Γ_C is therefore function of the gas chemical composition:

$$\Gamma_C = \sum_i \gamma_i \cdot P_{p,i} \quad (2.10)$$

where γ_i is the broadening coefficient associated to the chemical species i and $P_{p,i}$ is the partial pressure of this species. In the case of atmospheric spectroscopy, the partial pressure of trace gases being extremely low, only two terms related to O_2 and N_2 are taken into account in the sum introduced in Equation (2.11). For a standard atmosphere (21 % oxygen and 79 % nitrogen), Γ_C is equal to:

$$\Gamma_C = \gamma_{O_2} \cdot 0.21 \cdot P_{atm} + \gamma_{N_2} \cdot 0.79 \cdot P_{atm} \quad (2.11)$$

where γ_{O_2} and γ_{N_2} are respectively the oxygen and nitrogen broadening coefficient and P_{atm} the atmospheric pressure. Typical collision broadening can reach width in the range of 500 MHz at ground level.

2.2.4 Line shape profile

The actual line shape profile g_k of the ro-vibrational transition k is the convolution of the spectral shape profiles due to the natural broadening g_N , the Doppler effect g_D and the collision effect g_C . As mentioned in the previous paragraphs, the natural broadening effect is

significantly smaller than the Doppler and collisional effect, leading to the assumption that $g_N(\nu - \nu_0)$ can be seen as a Dirac delta function, so that the line shape profile g_k can be expressed as:

$$g_k(\nu - \nu_0) = g_D(\nu - \nu_0) * g_C(\nu - \nu_0) \quad (2.12)$$

The resulting line shape profile is the convolution of a Lorentzian and a Gaussian profile, also known as a Voigt profile. Depending on the atmospheric pressure and temperature, the parameters Γ_D and Γ_C may strongly vary. The resulting line shape profile, presented in Figure 2.6, can therefore be:

- a Gaussian profile, when the pressure broadening is low compared with the temperature broadening.
- a Voigt profile, when the pressure and temperature broadening are in the same range.
- a Lorentzian profile, when the temperature broadening becomes negligible at sufficiently high pressures.

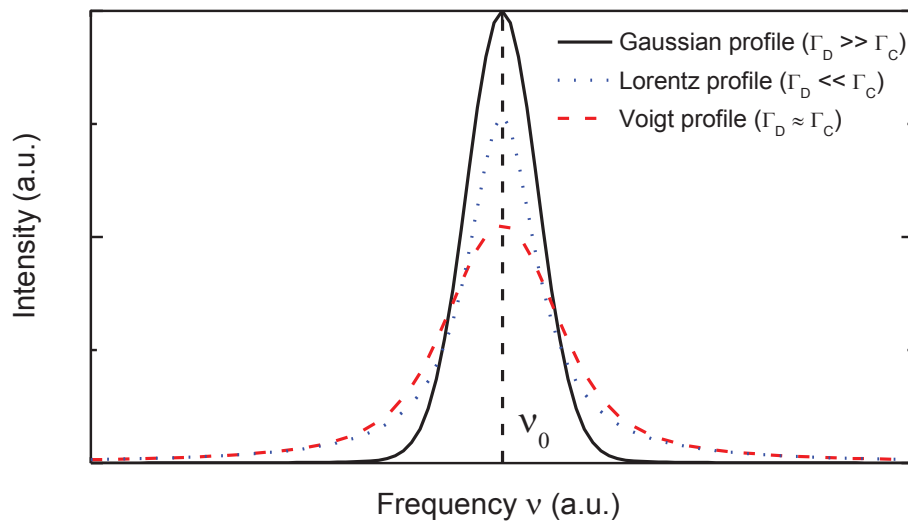


Fig. 2.6: Gaussian, Lorentzian and Voigt functions can be used as a line shape profile depending on the pressure and temperature conditions. The three function have been normalized

2.3 The case of spectrally integrated optical measurements

The work presented in this thesis relies on measurements that are performed with a spectrally broadband light source and a non-spectrally resolved detector. A non-spectrally resolved detector is to be understood as a detector that delivers a signal that is not resolved in terms of frequency, within its operational spectral range. This section accounts for the spectral line shape when such spectrally-integrated measurements are performed. It is shown that the spectral line shape is not a major concern in such measurements and that the measurement is mostly sensitive to the strength of the considered spectroscopic transitions.

In this section, we assume an optical signal, noted ℓ , resulting from an initial incoming light beam, having an intensity $I_0(\nu)$, that undergoes the optical transmission $T(\nu)$ and a backscattering or reflection coefficient noted $\beta_0(\nu)$, measured by a non-spectrally resolved detector, having a quantum efficiency $\eta(\nu)$. The ℓ -signal can then be expressed as follows if one assumes a homogenous medium:

$$\ell = \int_0^{\infty} I_0(\nu) \cdot \beta_0(\nu) \cdot T(\nu) \cdot \eta(\nu) \cdot d\nu \quad (2.13)$$

If we consider a gas cell filled with a single molecule species with the associated concentration C_i and an absorption cross-section $\sigma_i(\nu)$, the optical transmission T can be developed by following the Beer-Lambert law so that we get for the ℓ -signal:

$$\ell = \int_0^{\infty} I_0(\nu) \cdot \beta_0(\nu) \cdot \eta(\nu) \cdot \exp(-l \cdot C_i \cdot \sigma_i(\nu)) \cdot d\nu \quad (2.14)$$

where l is the length of the optical path.

We now assume that the emission spectrum $I_0(\nu)$, the detector quantum efficiency $\eta(\nu)$ and the $\beta_0(\lambda)$ coefficient are frequency independent over a spectral width $\Delta\nu$ covering the considered absorption lines. This assumption can be made since $I_0(\nu)$, $\eta(\nu)$, and $\beta_0(\lambda)$ are relatively flat compared with the absorption lines. In this case, the optical signal can be assumed to be proportional to the optical transmission integrated over $\Delta\nu$:

$$\ell \propto \int_{\Delta\nu} \exp(-l \cdot C_i \cdot \sigma_i(\nu)) \cdot d\nu \quad (2.15)$$

Then by using the first order Taylor expansion of the exponential law $\exp(x) \approx 1+x$, we obtain:

$$\ell \propto - \int_{\Delta\nu} \sigma_i(\nu) \cdot d\nu \quad (2.16)$$

Using Equation (2.3) we then obtain:

$$\ell \propto - \int_{\Delta\nu} \sum_k S_k(T_{atm}) \cdot g_k(T_{atm}, P_{atm}, \nu - \nu_0) \cdot d\nu \quad (2.17)$$

Since S_k is not a function of ν , Equation (2.17) becomes:

$$\ell \propto - \sum_k S_k(T_{atm}) \cdot \int_{\Delta\nu} g_k(T_{atm}, P_{atm}, \nu - \nu_0) \cdot d\nu \quad (2.18)$$

Then, if we assume that the absolute spectral line-width is low compared with the considered spectral range, i.e. $\Delta\nu \gg \Gamma_D + \Gamma_C$, we get:

$$\int_{\Delta\nu} g_k(\nu - \nu_0) \cdot d\nu \approx \int_0^{\infty} g_k(\nu - \nu_0) \cdot d\nu = 1 \quad (2.19)$$

By combining Equations (2.18) and (2.19), we obtain the final result:

$$\ell \propto - \sum_k S_k(T_{atm}) \quad (2.20)$$

As a conclusion, the optical signal received by a non-spectrally resolved detector only depends on the line strength of the involved spectroscopic transitions, provided that the light source and the detector have a significantly larger spectral width than the absorption cross-

section spectral line width. A major consequence of this result is that the influence of the pressure dependence of the absorption cross-section is greatly reduced, since the line strength is pressure independent. This point will be used in Chapter 4 where a precise computation has been performed for OCS-lidar signals by using a numerical model.

2.4 Spectroscopic data for water vapor and methane

As mentioned in the introduction, the new methodology which is presented in the following chapters is tested and evaluated by using methane and water vapor as case studies. In this subsection, we hence present the methane and water vapor spectral properties. As a first step, we present the HITRAN database [Rothman et al. 2009] from which our spectral data originates. Then, after a brief review on the molecules themselves, the methane and water vapor absorption cross-section spectra are described.

2.4.1 The HITRAN Database

The HITRAN database [Rothman et al. 2009], for HIgh resolution TRANsmission, stands as a worldwide standard for calculating the absorption cross-section of common trace gases in the atmosphere, including their most recurring isotopologues, from the ultraviolet up to the far infrared spectral regions. The latest version (2012) contains 7,400,447 spectral lines for 47 different molecules, incorporating 120 isotopologues. It was at first developed by the Air Force Cambridge Research Laboratories in the 60's and is now maintained and developed at the Harvard-Smithsonian Center for Astrophysics, Cambridge, USA.

At present, theoretical models are not able to predict the variation of the absorption cross-section with temperature and pressure with sufficient precision, mostly due to the complexity of choosing the appropriate line shape profile for given atmospheric conditions. For each molecule, the absorption cross-sections have been experimentally measured at different temperatures and pressures. These data have been completed by empirical models to interpolate these cross-sections to obtain the missing intermediate temperatures and pressures, as published by [Orphal et al. 2003]. Therefore, the data are a compilation of measured or simulated spectroscopic absorption data, gathered in 19 parameters. The parameters, which

are used to calculate the absorption cross-section spectrum for each energy transition of each molecule and isotope, are listed below:

- Transition wavenumber in vacuum
- Line strength
- Einstein A-coefficient
- Air-broadened width
- Self-broadened width
- Lower-state energy
- Temperature dependence
- Air-pressure shift

Then, a home-made computer code is used to retrieve the absorption cross-section from these parameters. The absorption cross-section can be retrieved with a high spectral resolution ($< 0.01 \text{ cm}^{-1}$) under determined atmospheric conditions of temperature and pressure.

The GEISA database (Gestion et Etude des Informations Spectroscopiques Atmosphériques: Management and Study of Spectroscopic Information) [Jacquinet-Husson et al. 2011] has also been used for verification and control in the framework of this thesis: in the considered spectral bands, no significant difference in the resulting absorption cross-section spectra have been noted.

2.4.2 Spectrum of the CH₄ absorption cross-section

The work presented here has a special interest for methane in the gas phase in the Earth's atmosphere. This section presents the methane molecule and its absorption spectrum in the near infrared spectral region.

Methane is the simplest alkane with chemical formula CH₄. Figure 2.7 presents a 3D-view of the methane molecule. It is a tetrahedral molecule with four equivalent C-H bonds, the equilibrium distance between carbon and hydrogen atoms is 108.70 pm with a 109.5° angle between each H-C-H. At room temperature and standard pressure, methane is a colorless and odorless gas.

Methane

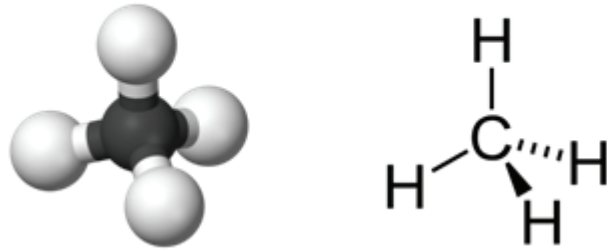


Fig. 2.7: 3D-view of the methane (left: ball and stick, right: skeletal formula).

As already mentioned in Section 2.1, the methane molecule has 5 atoms, leading to 9 possible vibration modes. Its spherical geometry induces the degeneracy of some of these modes, which means that some of the 9 vibrational modes correspond to the same vibration frequency. As a consequence, the methane has four vibrational modes presented in Table 2.1.

Mode	Type	Degenerated	Wavelength (μm)
ν_1	Stretching mode	Non-degenerated	3.43
ν_2	Bending mode	Two times	6.52
ν_3	Stretching mode	Two times	3.31
ν_4	Bending mode	Three times	7.63

Table 2.1: Vibrational modes of the CH_4 molecule.

These are the fundamental modes. However, numerous harmonic modes and combinations between these modes are possible, in addition to the rotational lines. As a result, the methane molecule has a complex absorption spectrum as can be seen in Figure 2.8, where the methane absorption cross-section between 1 and 4 μm is presented, computed from the HITRAN database spectral parameters at a 293 K temperature and 1 atm atmospheric pressure using a Voigt profile. The works presented in the following chapters use the methane ro-vibrational transitions (P, Q and R-branch) at the second harmonic of the ν_3 vibrational band, written $2\nu_3$ around the 1665 nm wavelength, located inside an infrared Earth's atmospheric window [Frankenberg et al. 2008].

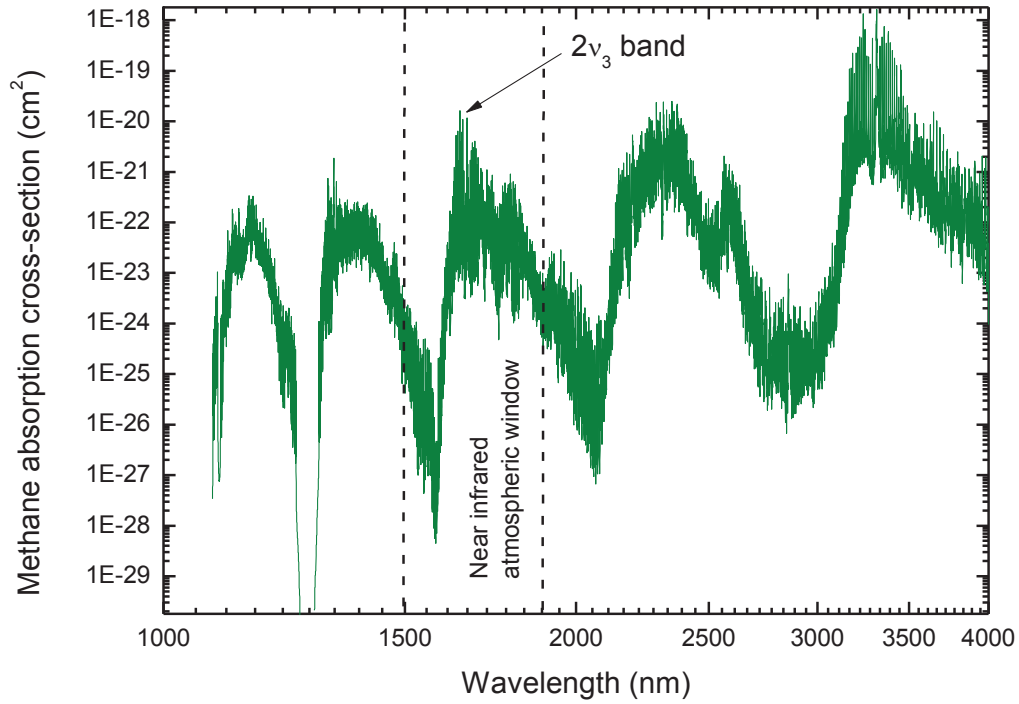


Fig. 2.8: HITRAN methane absorption cross-section at a 293 K temperature under atmospheric pressure, showing the absorption bands in the wavelength range (1000-4000 nm) of the spectrum, as well as the $2\nu_3$ absorption band and the atmospheric window.

The $2\nu_3$ absorption band and the corresponding methane absorption cross-section σ_{CH_4} calculated at 293 K and 1 atm are depicted in Figure 2.9.

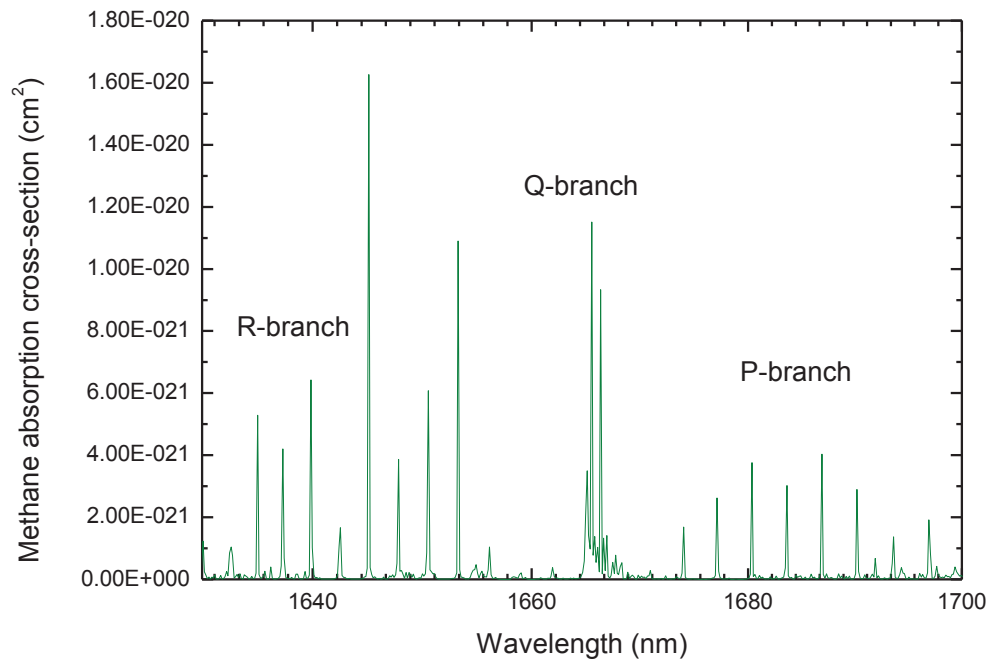


Fig. 2.9: The methane $2v_3$ vibrational band around the 1665 nanometers wavelength computed with the HITRAN database at a 293 K temperature and 1 atm atmospheric pressure, using a Voigt profile.

This spectrum is typical for a spherical top molecule [Champion et al. 1992] such as methane (or SCl_6 , SiH_4 , Ca_4 for example), with a strong Q-branch composed of many transitions. These absorption lines cannot be resolved because their spectral broadening is larger than the gap between each spectral line. Absorption lines in the P and R-branch are extremely narrow and well defined. Depending on the temperature and pressure, the bandwidth of such lines is in the range of the picometer.

2.4.2 Spectrum of the H_2O absorption cross-section

The second gas used in the thesis is water vapor. This section briefly introduces the water molecule and presents its absorption spectrum in the near infrared spectral region.

Water vapor is the most abundant compound on Earth's surface and is composed of two hydrogen atoms covalently bonded to a single oxygen atom. As shown in Figure 2.10, the molecule presents a 104.45° angle and an equilibrium distance between the hydrogen and the

oxygen atoms of 95.84 pm. It is in dynamic equilibrium between the liquid and gas states at standard temperature and pressure

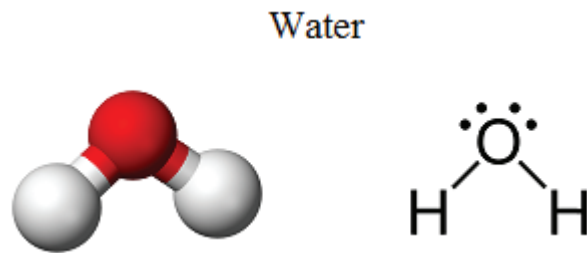


Fig. 2.10: 3D-view of the water molecule (left: ball and stick, right: skeletal formula).

Due to the presence of the hydroxyl bond, water vapor has strong absorption bands in the infrared spectral region. The water vapor molecule has three main vibrational modes as presented in Table 2.2.

Mode	Type	Wavelength (μm)
ν_1	Stretching mode	2.73
ν_2	Bending mode	6.27
ν_3	Stretching mode	2.66

Table 2.2: Vibrational modes of the H_2O molecule.

The water vapor absorption spectrum is extremely complex due to the numerous combinations of movement of the covalent bonds [Bernath et al. 2002], giving rise to tens of thousands to millions of absorption lines. In addition to these spectral lines, water vapor possesses a continuum absorption band in the entire IR spectrum and microwave spectral regions, which varies relatively slowly with wavelength. Sophisticated ab-initio [Tvorogov et al. 1994, Ma et al. 1999, Ma et al. 2002] and semi-empirical [Clough et al. 1989, Clough et al. 1995, Mlawer et al. 1999] line shape models have been developed, which describe quite well this continuum. The dominating role of the far wings of water vapor lines in the continuum absorption, especially in atmospheric conditions, is most commonly accepted today.

On the other hand, water dimers, consisting of two water molecules loosely bound by a hydrogen bond, have been and are being often discussed as a possible component of the water self-continuum absorption [Vigasin et al. 1989, 2000; Cormier et al. 2005].

Thus, a controversy on the nature of the water vapor continuum still remains unsolved. As a response, the atmospheric science community has largely adopted a pragmatic approach. Most

radiative transfer codes now used in climate modeling, numerical weather prediction and remote sensing, run with a semi-empirical formulation of the continuum [Clough et al. 1989].

Using the HITRAN spectroscopic database, we calculated the absorption cross-section as presented in Figure 2.11 in the visible and near infrared region at a 293 K temperature under atmospheric pressure. The water vapor absorption cross-section is strongly dependent on the wavelength: it goes from 10^{-32} cm² in the UV spectral range up to 10^{-19} cm² at a 4 μm wavelength. Compared with other trace gas, the water vapor cross-section is not particularly strong, as for example CO₂ which reaches 10^{-17} cm² at 4.2 μm. However its concentration can be up to 100 times higher than CO₂, which explains why water vapor is predominant on the Earth's radiative budget.

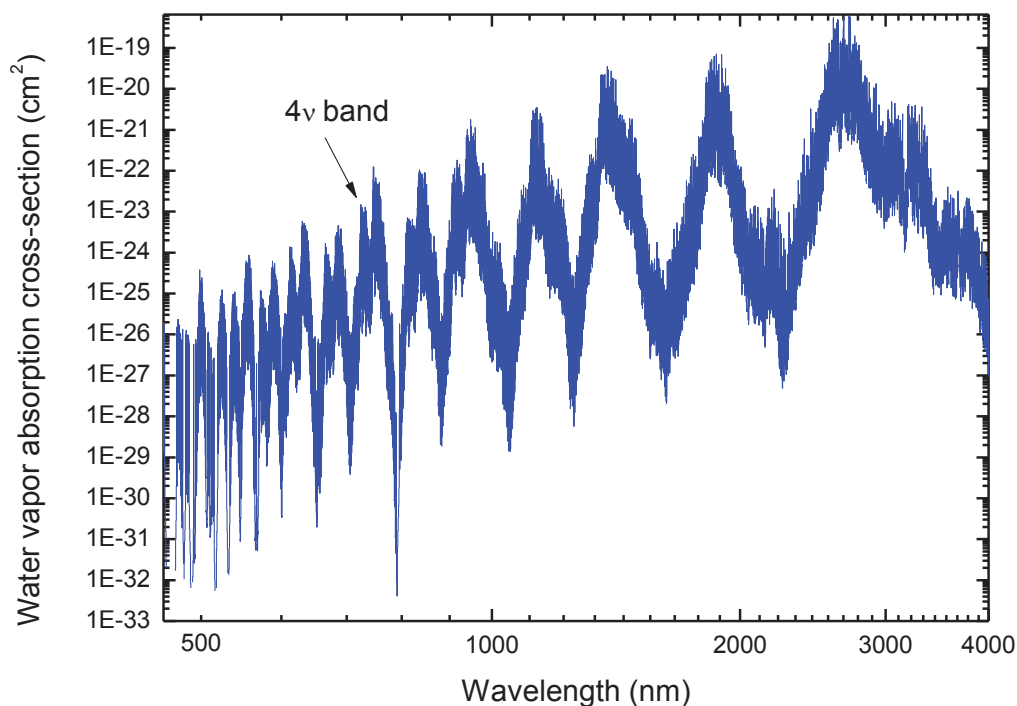


Fig. 2.11: HITRAN water vapor absorption cross-section at a 293 K temperature under atmospheric pressure, showing the absorption bands in the wavelength range (400-4000 nm) of the spectrum as well as the 4v absorption band discussed below.

In this thesis, special interest has been given to the 4v 720 nm water vapor absorption band, presented in Figure 2.12, which is a combination of the ν_1 and ν_3 vibrational modes having 67 ro-vibrational lines [Browell et al. 1991]. This spectral range has been chosen because it corresponds to an absorption spectral band, available to the laser emission and also to the light

detector spectral range used in the experiment presented in Chapter 5. Moreover, around 720 nm, in the PBL, other atmospheric gases will not significantly absorb the laser light, so that the influence of possible interfering species will be negligible. However, H₂O remote sensing using lidar is also achieved at different absorption spectral bands in the near-infrared, such as the 815 nm absorption band [Ismail et al. 2010].

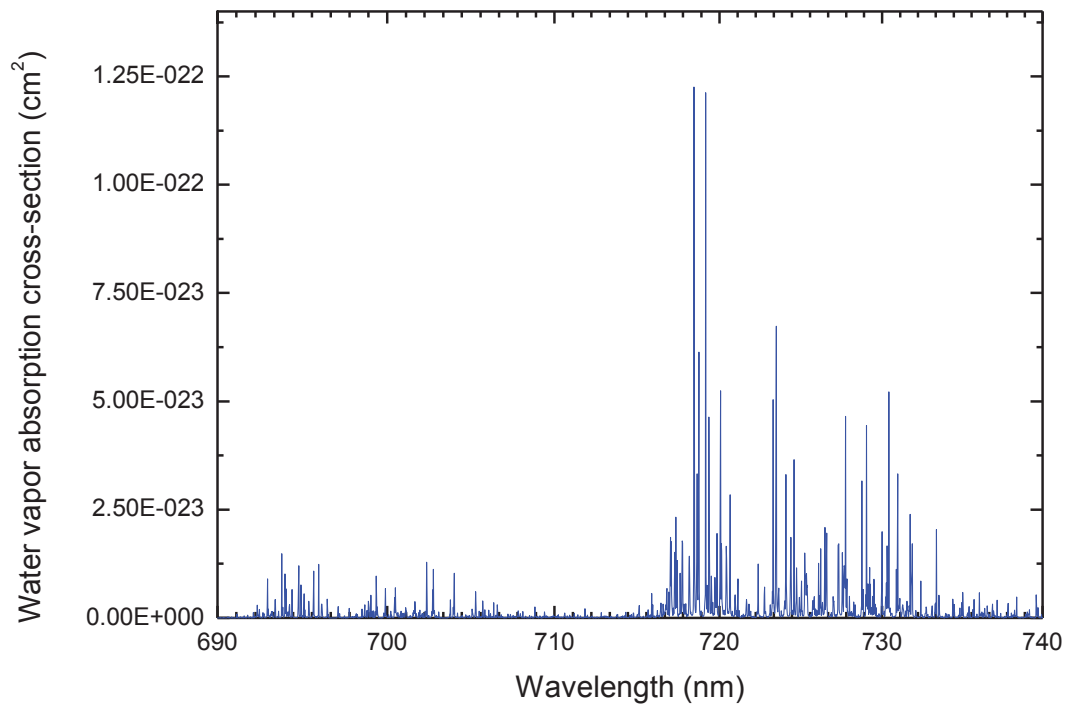


Fig. 2.12: The 4 ν 720 nm water vapor absorption band.

In addition, when measuring the methane concentration, water vapor may act as a possible interfering species. Its influence will be discussed in Chapter 4. Figure 2.13 presents the water vapor absorption cross-section in the infrared range near the methane 2 ν_3 vibrational band.

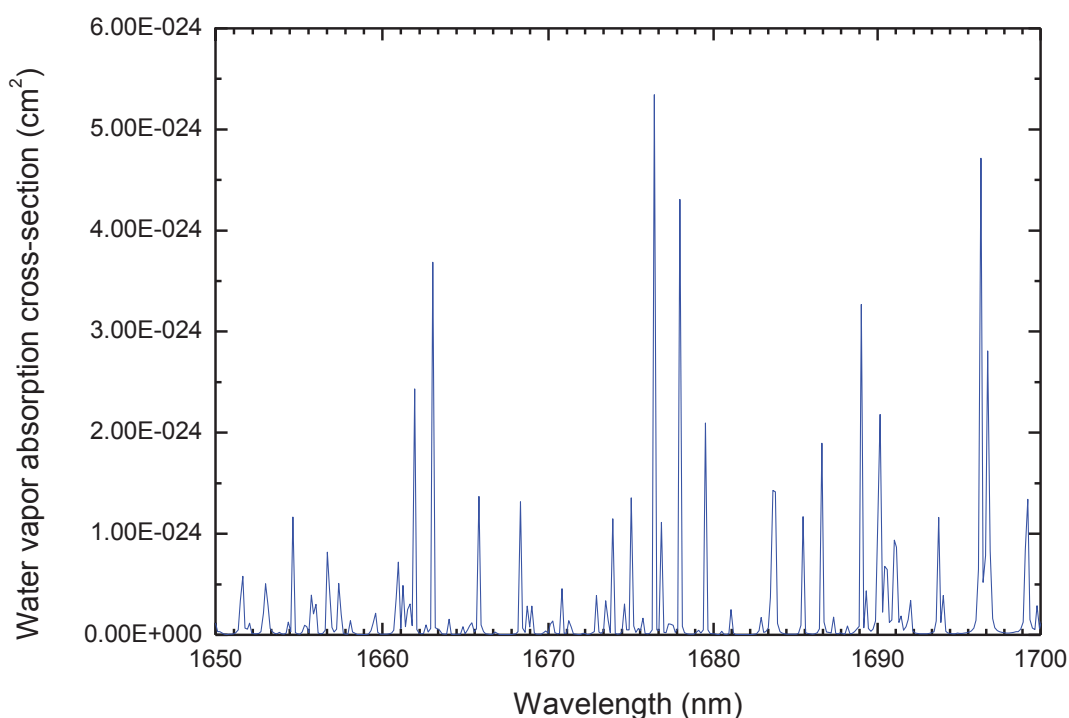


Fig. 2.13: Water vapor absorption cross section near the methane $2\nu_3$ vibrational band.

Since the work presented in the manuscript is based on molecular spectroscopy, this second chapter introduces the fundamentals of absorption spectroscopy that will be used in the following chapters. Firstly, a brief review on ro-vibrational spectroscopy is given with emphasis on the line shape profile. The atmospheric temperature and pressure influence the absorption cross-section through the broadening of the line shape profile, which is presented. We demonstrated that spectrally-integrated optical measurements are mostly sensitive to the line strength leading to a low dependency on the atmospheric pressure. This result is of prime importance for the forthcoming chapters. Since this work is focused on the study of methane and water vapor, the spectral properties of both gases have been discussed by using the HITRAN spectroscopic database. The following chapter will present how, based on these spectral properties, optical measurements can be performed to retrieve the concentration of such gases and will introduce the new methodology developed in this thesis.

Chapter 3

Optical Correlation Spectroscopy and Lidar

This chapter reviews the principle and the formalism of the Optical Correlation Spectroscopy Lidar, called OCS-lidar. This new methodology allows to remotely evaluate the content of a trace gas in the atmosphere by combining two existing methods, the optical correlation spectroscopy (OCS) and the light detection and ranging (lidar). As detailed in this chapter, the OCS-lidar methodology relies on laser spectroscopy, both the laser and the detector are spectrally broad which allows to retrieve the trace gas concentration by spectrally modulating the broadband laser over a trace gas absorption band. The OCS-lidar differs from the conventional wavelength modulation spectroscopy (WMS) technique [Schilt et al. 2003] because after laser pulse shaping, the trace gas absorption line is spectrally-resolved while OCS-lidar does not require a spectrally-resolved detector. The OCS-lidar methodology also differs from the DIAL technique, since trace gas concentrations are retrieved in the DIAL technique from the evaluation of a spectrally-resolved differential absorption on a specific absorption line.

As a first step, Section 3.1 presents the physical basis of the optical correlation spectroscopy used for trace gas concentration measurements. The background related to this methodology is reviewed as well as the corresponding formalism. As an example, a numerical simulation is presented for methane concentration measurements by using this methodology. Then, Section 3.2 presents the lidar technique. Firstly, the equations commonly used in the lidar formalism are presented and are then extended to a spectrally broadband laser source. Then, the lidar system built in the framework of this PhD thesis is described and the first measurements are presented. Lidar measurements showing desert dust particles, originating from the Sahara region, in the atmosphere above Lyon are presented. The obtained lidar signals are then compared with those of an existing and validated lidar system [David et al. 2012] while atmospheric 7-days air mass back-trajectories are also used as a complementary tool to validate the new lidar system.

Finally, based on the two previous sections, we present a new methodology combining the benefits of both the OCS and the lidar methodologies to remotely evaluate atmospheric trace gas concentrations. The coupling of the optical correlation spectroscopy and the lidar is presented, giving rise to the optical correlation spectroscopy lidar. In a few words, the optical correlation spectroscopy is achieved between two lidar signals, obtained by propagating two different laser pulses into the atmosphere. Both signals are obtained by spectrally shaping a broadband pulsed laser source, emitting around the target gas absorption line: a broadband laser pulse, spectrally shaped around target gas absorption lines (called the correlated signal), and a broadband laser pulse shaped outside these target gas absorption lines (called the non-correlated signal). To perform the spectral shaping, several optical methods can be applied as for example the Fabry-Perot interferometer method [Vargas-Rodríguez et al. 2007] or the 4F-grating pulse shaper method [Weiner et al. 2000]. In this work, the initial laser pulse is spectrally shaped with an Acoustic Optical Programmable Dispersive Filter (AOPDF) [Kaplan et al. 2002], which to our knowledge is new in the lidar community. Hence, the optical correlation is achieved by setting the AOPDF filter parameters, as a function of the target gas absorption spectrum, which can hence be faithfully carved to perform sensitive and accurate trace gas concentrations measurements.

3.1 Optical correlation spectroscopy (OCS)

3.1.1 An introduction to the OCS-methodology

Optical correlation spectroscopy is a methodology based on absorption spectroscopy for selectively detecting a target gas of interest or measuring its concentration. Its main advantage is that measurements can be performed in a complex mixture of gases and particles, as often encountered in the Earth's atmosphere, using a simple broadband light source. This section proposes a review of the different methodologies developed along the 20th century that led to the present OCS-methodology.

Spectroscopic techniques to remotely evaluate trace gas concentrations in the atmosphere have appeared in the 20's. Gordon Dobson, a British physicist and meteorologist, created the first instrument in 1924 to measure the atmospheric ozone concentration from the ground. The instrument is based on a spectroscopic differential measurement [Dobson 1968]. His instrument, called the Dobson Ozone Spectrophotometer, measures the total ozone column by differential absorption of the UV-light emitted by the Sun. By comparing the light intensity at two wavelengths that are strongly or weakly absorbed by ozone, the average concentration of ozone in the atmosphere can be retrieved. This instrument has been used for ozone measurements since 1925 and has provided valuable data for understanding ozone changes over the 20th century. The Dobson's methodology appears to be the oldest ancestor of what is nowadays called optical correlation spectroscopy.

Measurement of trace gases by using optical correlation spectroscopy expanded with the increasing awareness of complex processes involved in environmental phenomena, such as pollution and climate change, leading to a closer examination of the behavior of trace gases in the atmosphere during the 70's. At the same time, many instruments were developed [Hodgkinson et al. 2013], which took advantage of the recent advances in laser technology and optical spectroscopy techniques, initiated by major oil and mining companies who were in need for such technologies for exploration purposes. Measurements using gas correlation spectroscopy have then been studied in [Herget et al. 1976] where atmospheric gaseous pollutants concentration measurements in 1976 using Gas Filter Correlation are reported. There, a light beam was transmitted through a "correlation cell" filled with a known

concentration of a target gas, then through a measurement cell and eventually measured on an optical detector, as presented in Figure 3.1. A second measurement was operated by replacing the correlation cell by a neutral density filter. The density was chosen so that the optical extinction was similar when interchanging the correlation cell with the neutral density filter. From the difference in intensity measured when the correlation cell and the neutral density filter were switched, the gas concentration was retrieved.

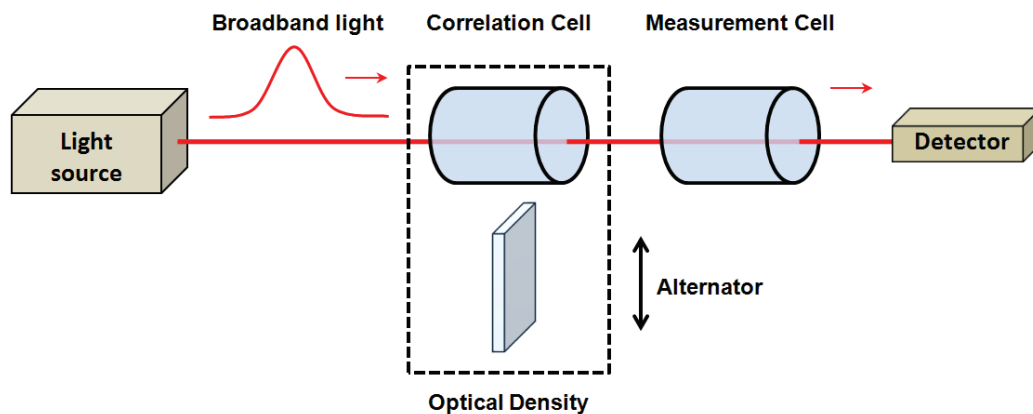


Fig. 3.1: Simplified gas filter correlation instrument. A broadband light source passes alternatively through a correlation cell or a neutral optical density and then through the measurement cell. The difference in intensity measured when the correlation cell and the neutral density are switched allows to retrieve the gas concentration in the measurement cell.

Based on a similar methodology, instruments such as GASPEC (Gas Spectroscopy) [Ward et al. 1975] or COSPEC (Correlation Spectroscopy) [Sandroni et al. 1977] are dedicated to the remote sensing of trace gas in the atmosphere using gas filter correlation. In these instruments, the measurement cell is replaced by a long optical pathway to reach sufficient optical extinction, thus the average concentration of pollutants such as sulfur dioxide could be estimated.

Later in 2000, Keabian et al. [Keabian et al. 2000] measured nitrogen dioxide in the 400-500 nm spectral region by using gas correlation spectroscopy. Based on the same methodology as Herget et al., their experimental set-up was improved using multimode fibers and two blue emitting diodes, allowing the optical paths to be switched electronically, rather than mechanically, as done previously. This new system reached 1 ppm.m sensitivity with negligible bias when interfering species CO_2 and SO_2 were added to the measurement cell.

In 2005, Cheung et al. [2005, 2006] investigated this methodology for measuring acetylene C_2H_2 with a minimum detectable concentration of 0.15 ppm.m. The experimental set-up was improved by using a single light source with a delay line between the two optical paths, avoiding the use of two light sources that may have different spectral properties as in Keabian's experiment [Keabian et al. 2000]. Also, it is the first time to my knowledge that the name "Optical Correlation Spectroscopy" was used to describe this methodology. At the same time, J.P. Dakin et al, [Dakin et al. 2003] studied gas correlation spectroscopy showing theoretical results for quantitative detection of O_2 , CO , and CO_2 . J. P. Dakin's PhD student, P. Chambers, dedicated his thesis to the study of the correlation spectroscopy gas detection method [Chambers 2005]. Comparisons between simulations and experiments have been performed as well as a close study on the interfering species and pressure dependence.

Lastly, Lou et al. [2009] performed measurements on sulfur dioxide in the UV spectral range by using the gas correlation technique. The light source is based on a light-emitting diode having a 15 nm wide emission spectrum (FWHM), showing that this kind of low-cost light sources can be used for such measurements. Results show a sensitivity of 0.08 ppm.m for a 60-s integration time achieved with a compact and cost-effective experimental set-up, ideal for industrial emission controls.

Optical correlation spectroscopy uses spectrally broadband light sources, and therefore includes several absorption lines. As a consequence, measurements using the OCS technique are immune to interfering species since a different gas would have the same influence on the correlated and non-correlated signals. However, since it is broadband, the contrast between the two signals required by the OCS-technique is not as strong as when using spectrally narrow light sources or spectrally-resolved detectors where a single on and off absorption line can be addressed.

3.1.2 The OCS-formalism

This section presents the formalism of the OCS-methodology. It shows how the target gas concentration can be retrieved from the two optical measurements performed in the OCS experiment. Optical Correlation Spectroscopy involves two spectrally broadband optical sources, labeled "Optical Source 1" and "Optical Source 2" having a respective power density

spectrum $S_1(\lambda)$ and $S_2(\lambda)$, used on and off alternatively with a given switching frequency ensuring that when S_1 is on, S_2 is off and vice versa. The two optical sources are assumed to be identical in terms of normalized power spectral density, as written in Equation (3.1):

$$\frac{S_1(\lambda)}{\int_0^\infty S_1(\lambda) \cdot d\lambda} = \frac{S_2(\lambda)}{\int_0^\infty S_2(\lambda) \cdot d\lambda} \quad (3.1)$$

Figure 3.2 presents the experimental set-up proposed by P. Chambers in his thesis. The optical source 1 is directed through a cell containing the target gas only, hence called the reference cell. Due to the optical extinction caused by the target gas absorption cross-section $\sigma_{TG}(\lambda)$, the output spectrum acquires the characteristic absorption spectrum of the target gas. There, the optical source 2 is combined with the output of the reference cell. The intensity of the two light sources is set so that it is equal to the intensity of the light transmitted by the reference cell, as written in Equation (3.2), so that:

$$\int_0^\infty S_1(\lambda) \cdot \exp(-C_{TG,ref} \cdot \sigma_{TG}(\lambda) \cdot L_{ref}) \cdot d\lambda = \int_0^\infty S_2(\lambda) \cdot d\lambda \quad (3.2)$$

where $C_{TG,ref}$ and L_{ref} are the concentration of the target gas and the length of the reference cell respectively. The condition, expressed in Equation (3.2), is experimentally verified by using an optical detector, called the “Input Signal Detector” in P. Chambers’s figure. Finally, the target gas concentration $C_{TG,meas}$ is measured by passing the two light beams through a measurement cell having a length L_{meas} and eventually measured by a second optical detector, called the “Measurement Signal Detector”.

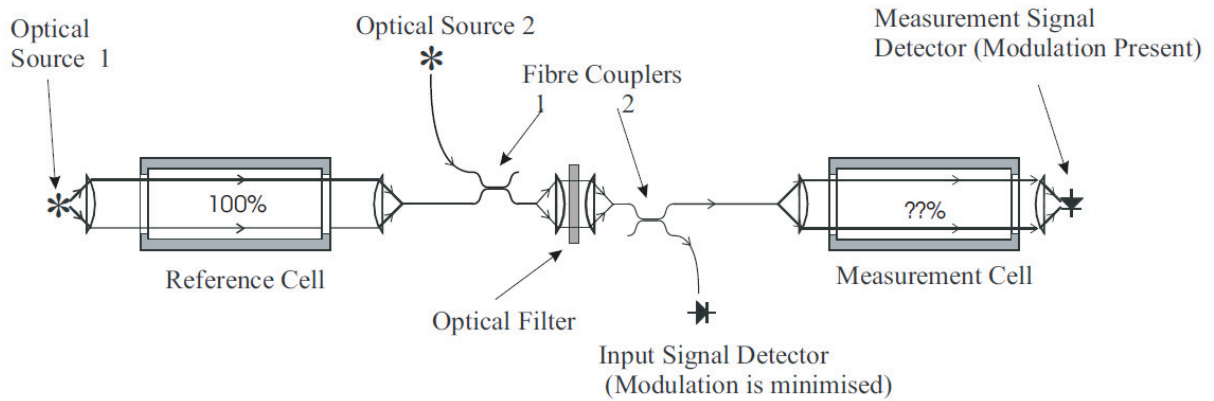


Fig. 3.2: Example of an Optical Correlation Spectroscopy system, as presented in P. Chambers’s thesis.

When the condition expressed in Equation (3.2) is fulfilled, it is clear that the signal measured by the Input Signal Detector is constant despite the two light sources are turned on and off alternatively. When they pass through the measurement cell for retrieving the target gas concentration, the two light beams have similar intensities but present different spectral power densities. Finally, the measurement signal detector measures the intensity transmitted through the measurement cell. When the optical source 1 is on, the intensity measured by the detector can be written as:

$$I_1 = \int_0^{\infty} S_1(\lambda) \cdot \exp(-C_{TG,ref} \cdot \sigma_{TG}(\lambda) \cdot L_{ref}) \cdot \exp(-C_{TG,meas} \cdot \sigma_{TG}(\lambda) \cdot L_{meas}) \cdot d\lambda \quad (3.3)$$

Then, when the optical source 2 is on, the intensity measured by the measurement signal detector is:

$$I_2 = \int_0^{\infty} S_2(\lambda) \cdot \exp(-C_{TG,meas} \cdot \sigma_{TG}(\lambda) \cdot L_{meas}) \cdot d\lambda \quad (3.4)$$

In the last two equations Equation (3.3) and (3.4), the quantum efficiencies of the two detectors have been assumed to be equal to 1. The light emitted by the optical source 1 undergoes a lower extinction while going through the measurement cell since its spectral component corresponding to the absorption band of the target gas has been already dimmed within the reference cell. Therefore if $C_{TG,meas} > 0$, then $I_1 > I_2$. Thus, the measurement signal detector measures an intensity modulation whose frequency is equal to the on/off switching frequency. In turn, a modulation function m can be defined as the difference between I_1 and I_2 divided by their mean value, as written in Equation (3.5).

$$m = 2 \cdot \left(\frac{I_1 - I_2}{I_1 + I_2} \right) \quad (3.5)$$

Finally, the m -value can be associated to the target gas concentration by using a calibration function. In P. Chambers thesis, this calibration function is retrieved by using gas sample with known concentration from 0 to 100 % with a 20 % steps.

3.1.3 OCS numerical simulation

The sensitivity of the OCS-methodology depends on the trace gas absorption cross-section, on the length of the gas cells, on the detector noise equivalent power and on the quality of the calibration. Such a complete study is beyond the scope of this thesis as it can be found elsewhere [Chambers 2005]. In this section, a numerical simulation is presented to illustrate the OCS-methodology for methane concentration measurements. The $2\nu_3$ Q-branch transition in the 1665 nm infrared region, as presented in Chapter 2, has been used to apply the OCS methodology. As an input, we have chosen a 1 meter long reference cell, assumed to be filled with methane at a temperature of 20 °C under atmospheric pressure. Finally, the two optical sources are assumed to be spectrally Gaussian.

Figure 3.3 shows the simulated power density spectrum $S_1(\lambda)$ of the optical source 1, before (black) and after transmission through the reference cell (green), in which case the plotted signal becomes $S_1 \times T_{ref}$. The latter has been computed using Equation (3.6), which describes the optical transmission $T_{ref}(\lambda)$ of the reference cell:

$$T_{ref}(\lambda) = \exp(-C_{TG,ref} \cdot \sigma_{TG}(\lambda) \cdot L_{ref}) \quad (3.6)$$

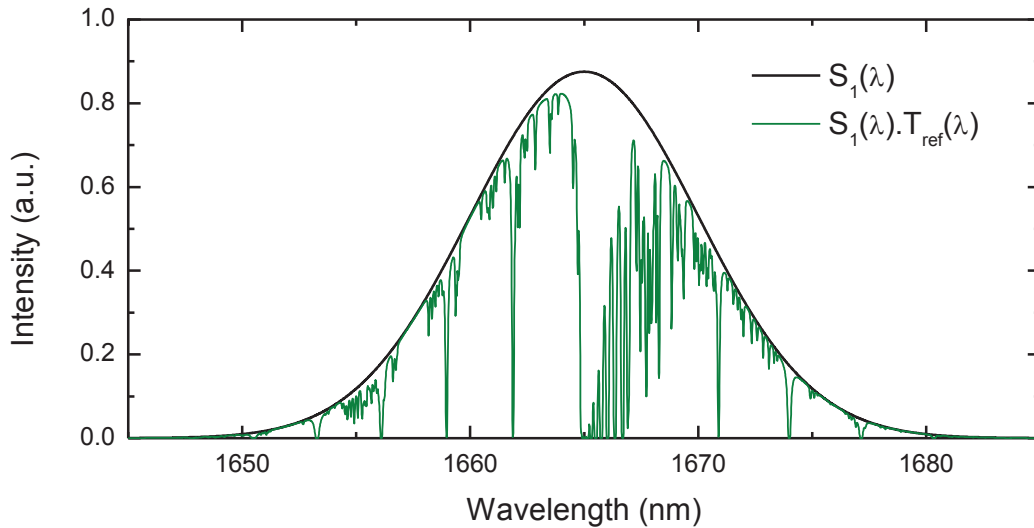


Fig. 3.3: Power spectral density $S_1(\lambda)$ of the optical source 1 (black) and the power spectral density after the reference cell (green). The methane absorption spectrum is faithfully carved in the spectrum of the transmitted light. The methane absorption cross-section has been computed by using the HITRAN database.

For the here proposed input parameters, 28 % of intensity of the optical source 1 has been absorbed by the methane hold in the reference cell. The intensity of the optical source 2 is then set so that the condition described in Equation (3.2) be fulfilled.

For a given concentration C_{meas} , Figure 3.4 shows the on and off modulation of the two optical sources (see graph a), together with the intensity measured by the Input Signal Detector and the Measurement Signal Detector, (see graph b).

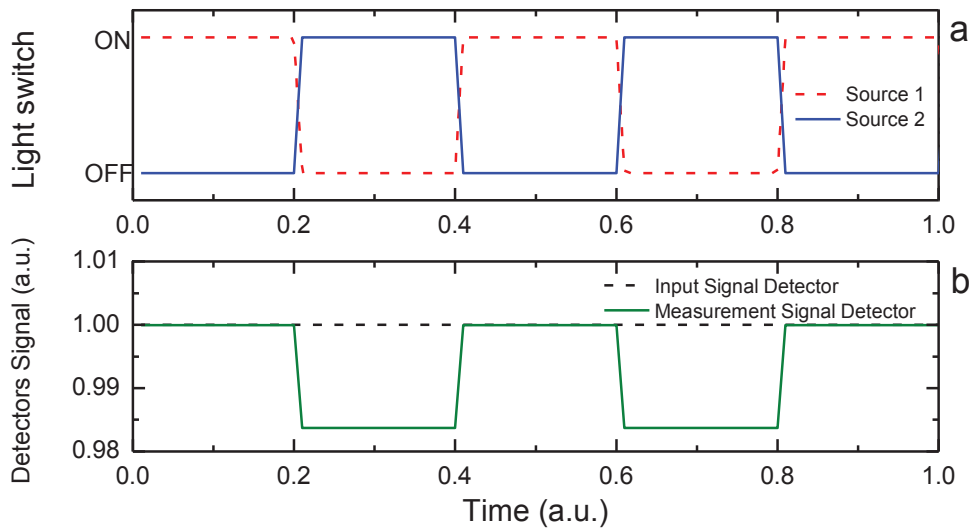


Fig. 3.4: (a) On and off modulation of the two optical sources 1 and 2 as a function of time (b) Intensity measured by the input signal detector (black) and the measurement signal detector (green) as a function of the time. The input signal is constant regardless which optical source is on while the measurement signal is modulated by the on and off frequency.

The modulation factor m can then be computed by using Equation (3.5) and the signals I_1 and I_2 , measured by the measurement signal detector, as detailed in Equations (3.3) and (3.4). For a given set-up, the gas concentration in the measurement cell can then be related to the modulation factor as shown on Figure 3.5.

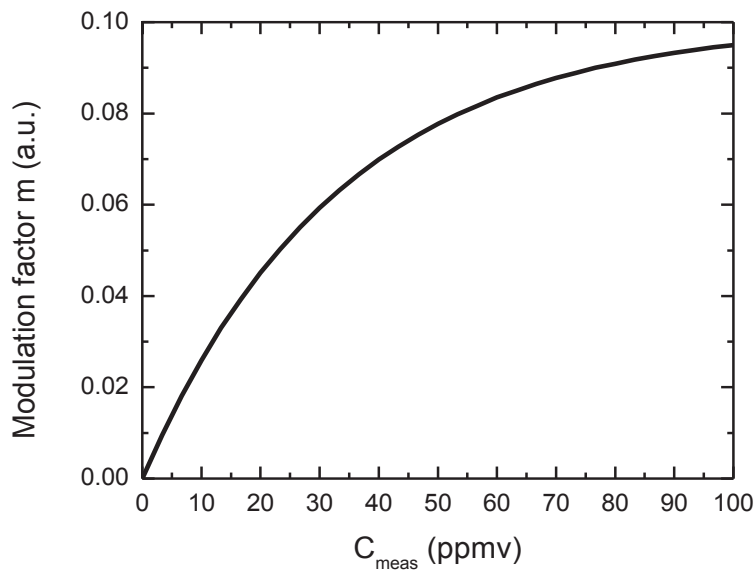


Fig. 3.5: Modulation factor m as a function of the methane concentration in the measurement cell C_{meas} .

3.2 Light detection and ranging (lidar)

3.2.1 Introduction

The acronym lidar stands for Light Detection and Ranging. It is a remote sensing technology that uses a laser light source to illuminate a target in order to measure and analyze the absorbed and backscattered light. Since its invention in 1961 [Fiocco et al. 1963], lidar systems have been widely used in numerous applications in various fields, such as physics, astronomy, laser altimetry, contour mapping, military, robotic, law enforcement, spaceflight, forestry [Weitkamp 2005, Measures 1992]. When applied for atmospheric purposes, lidar systems rely on the scattering and on the absorption of radiation from a pulsed laser source by atmospheric components such as aerosols and molecules. The measurement of the backscattered light, synchronized with the laser pulse, enables to study the spatial and temporal distribution of the atmospheric compounds over several kilometers with a range resolution of a few meters. This method is widely used for studying atmospheric processes. Among these processes, we may mention the remote sensing of aerosols concentrations [Schumann et al. 2011, Sugimoto et al. 2011, Miffre et al. 2011, 2012a] and the study of their

optical properties using polarization sensitive lidar [David et al. 2012]. Measurements of trace gas spatio-temporal distributions have also been performed on CO₂ [Abshire et al. 2012], CH₄ [Ehret 2008], O₃ [Kuang et al. 2013], H₂O [Whiteman et al. 2011], and also on volatile organic compounds (VOC) [Robinson et al. 2011]. Lidar is also used for wind field measurements [R. Frehlich et al. 2013], but also to study the PBL height [Griffiths et al. 2013], and to perform cloud measurements [Delanoe et al. 2013]. Due to these capabilities, the lidar technology has become a major tool for studying the change in the chemical composition of the Earth's atmosphere and to evaluate the induced implications on the climate.

Reviews on the lidar technique are given in the reference books of Inaba [1976], Measures [1992] and in Weitkamp [2005]. The principle of a lidar is to use the scattering and the absorption of the radiation from a pulsed laser source as it propagates through the atmosphere. A well-known phenomenon is the one observed in Figure 3.6, where the laser beam is visible at night because of the scattering by atmospheric molecules and particles.



Fig. 3.6: Picture of the laser pulse propagating into the atmosphere at Lyon, France (color enhanced).

The light scattered in the direction of the telescope, defined as the backscattered light, is focused on a light detection system, and the generated electric signal is then sampled by a

transient recorder, as displayed in Figure 3.7. The detector can be composed of several optical components: a parallelizing lens, and a band-pass filter are often used to reduce the sky background contribution. The distance at which the light has been scattered is determined by the time delay between the laser pulse emission and the signal reception.

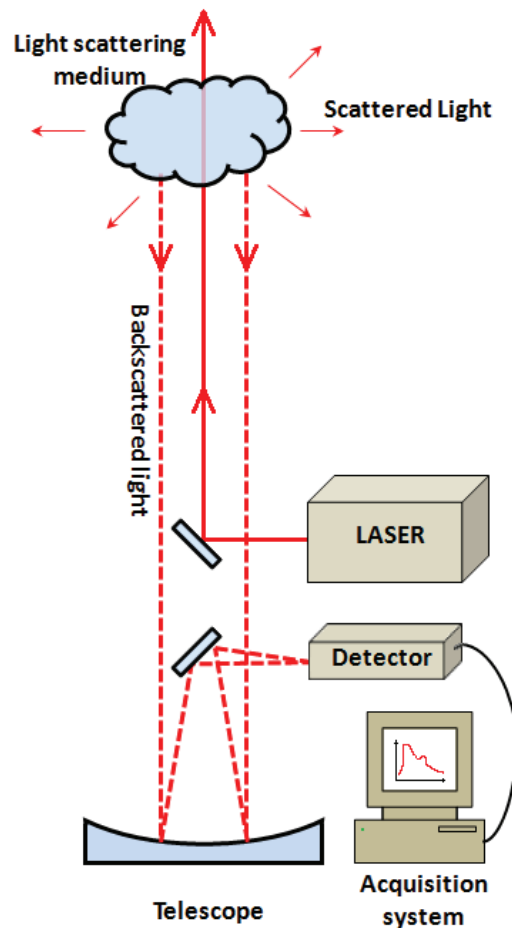


Fig. 3.7: Principle of a lidar system. A laser pulse is emitted into the atmosphere, the light backscattered by atmospheric particles and molecules is collected by a telescope and focused on a light detector. The resulting signal is then recorded by the acquisition system.

3.2.2 Elastic lidar formalism

For an initial laser pulse having an optical power P_0 , the backscattered power $P(r)$ received at a range r from the lidar source is expressed by the lidar Equation (3.7). This equation may be used as a basis for the lidar formalism and can be more developed depending on the type of lidar. As an example, the interested reader can find in [Hayman et al. 2012, David et al. 2012]

the modification of the lidar equation when polarization experiments are carried out. A single wavelength elastic lidar system can be described by the following equation:

$$P(r) = \frac{K}{r^2} \cdot O(r) \cdot P_0 \cdot \beta(r) \cdot T^2(r) \cdot \eta + P_N \quad (3.7)$$

$O(r)$ represents the overlap function between the telescope field of view and the laser beam as a function of the range r . η represents the optical efficiency of the detection system which includes the detector quantum efficiency of the photo-detector and possible interference filters introduced in the detection system. K is a constant depending on the lidar system parameters such as the telescope mirror diameter, the speed of light or the pulse duration. Statistical fluctuations due to the photons and the statistical fluctuations of the signal are represented by the random function P_N centered on 0. The atmospheric volume backscattering coefficient $\beta(r)$, to be described in the following paragraph, is range-dependent with its unit being $\text{m}^{-1} \cdot \text{sr}^{-1}$. $T(r)$ corresponds to the atmospheric optical transmission derived from the Beer-Lambert law as expressed in Equation (3.8):

$$T(r) = \exp\left(-\int_0^r \alpha(r') \cdot dr'\right) \quad (3.8)$$

where $\alpha(r)$ is the optical extinction coefficient depending on the range expressed in m^{-1} . $\alpha(r)$ and $\beta(r)$ are the two most important terms in the lidar equation since they are directly related to the atmospheric molecules and particles content in the probed atmospheric column. The two following sections are meant to present these two coefficients.

a) The atmospheric volume backscattering coefficient β

Because it is additive, the atmospheric backscattering coefficient β is the sum of its molecular (m) and particles (p) contributions at range r :

$$\beta(r) = \beta_m(r) + \beta_p(r) \quad (3.9)$$

The backscattering coefficient β_p and β_m are function of the concentrations of particles written $N_p(r)$, or molecules written $N_m(r)$, and the differential backscattering cross-section (averaged

on the particle size distribution) written $\frac{d\bar{\sigma}}{d\Omega}$ with under-script p or m, as in the Equation (3.10a) and (3.10b):

$$\beta_m(r) = N_m(r) \cdot \frac{d\bar{\sigma}_m}{d\Omega} \quad (3.10a)$$

$$\beta_p(r) = N_p(r) \cdot \frac{d\bar{\sigma}_p}{d\Omega} \quad (3.10b)$$

As an example, Figure 3.8a presents the molecular backscattering coefficient β_m , simulated by assuming an adiabatic atmospheric model. In addition, Figure 3.8b shows an example of the particles backscattering coefficient β_p measured with a lidar system running at 355 nm wavelength. Graph (b) has been retrieved by applying the Klett algorithm [Klett 1985].

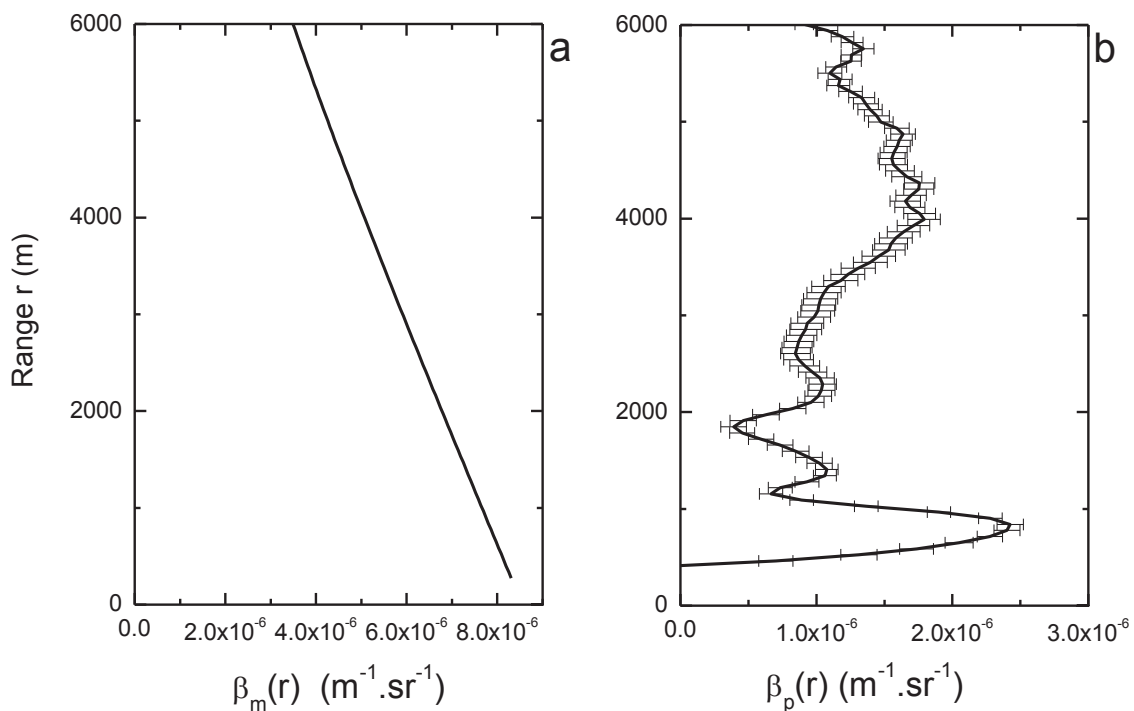


Fig. 3.8: Molecular backscattering coefficient (simulated) and particles backscattering coefficient as a function of the range at wavelength 355 nm measured during this thesis the 9th of July 2010 in the city of Lyon.

The wavelength dependency of the particle backscattering cross-section is described by the Mie scattering [Bohren et al. 2004, Miles et al. 2001] and tends to decrease with the wavelength. On the other side, molecular scattering is at first order described by Rayleigh

theory, which is an extension of the Mie theory for particles greatly smaller than the wavelength of the radiation. The strong wavelength dependency of the molecular scattering, following a λ^{-4} law, means that the molecular contribution to the backscattering coefficient is predominant in the UV spectral range while it is negligible in the near infrared spectral range, when compared to the particle contribution.

b) The atmospheric extinction coefficient α

As for the backscattering coefficient, the extinction coefficient $\alpha(r)$ can be written as the sum of its molecular and particles contributions:

$$\alpha(r) = \alpha_m(r) + \alpha_p(r) \quad (3.11)$$

The extinction coefficients $\alpha_m(r)$ and $\alpha_p(r)$ can be written as a function of the atmospheric absorption cross-sections (averaged on the particle size distribution) $\bar{\sigma}_{a,m}$ and $\bar{\sigma}_{a,p}$ for respectively molecules and particles:

$$\alpha_m(r) = N_m(r) \cdot \bar{\sigma}_{a,m} \quad (3.12a)$$

$$\alpha_p(r) = N_p(r) \cdot \bar{\sigma}_{a,p} \quad (3.12b)$$

Figure 3.9 shows the extinction coefficient of urban particles measured with a nitrogen Raman lidar operating at 387 nm and the simulated molecular extinction coefficient using an adiabatic atmospheric model.

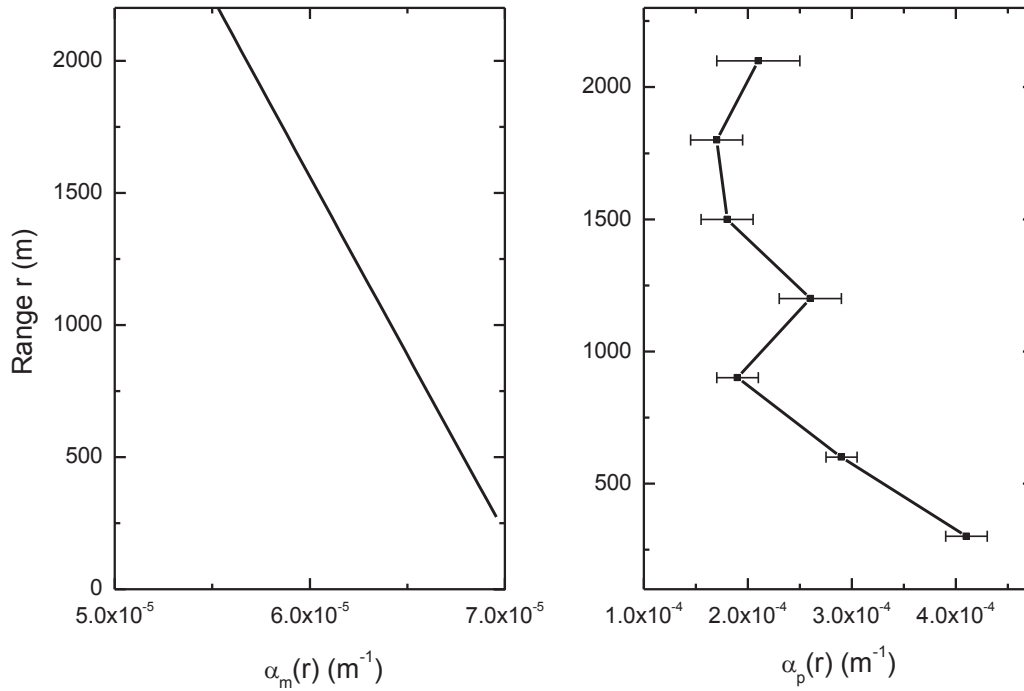


Fig. 3.9: The molecular extinction coefficient (simulated) and the particles extinction coefficient measured during this thesis with a nitrogen Raman lidar (387 nm) as a function of the range the 9th of July 2010 in Lyon.

Each term used in this section is described without any wavelength dependency since we set Equations (3.7) for a single wavelength lidar system, based on a monochromatic laser pulse P_0 . This assumption is often made in lidar systems using a laser source with very low spectral width. As an example, the Nd:YAG laser has a spectral width in the range of a few picometers. Therefore, with such a spectrally narrow laser source, it is generally considered that each term of the lidar equation is wavelength independent. This assumption greatly simplifies the lidar equation.

As described in the forthcoming Section 3.3, the OCS-lidar methodology requires a spectrally broadband laser source. Therefore, the lidar formalism has to be extended to broadband laser sources.

When assuming a non-monochromatic laser source, the power spectral density $P_0(\lambda)$ of the laser becomes wavelength dependent, as for the other terms present in the lidar Equation (3.7). However, if we assume a non-spectrally resolved detector, the lidar signal $P(r)$ is not a function of the wavelength λ as the backscattered light has been integrated over the wavelength during detection. In this case, the previous formalism has to be changed by adding

the wavelength dependency for each term and the integral over the wavelength from 0 to infinity:

$$P(r) = \frac{1}{r^2} \cdot \int_0^{\infty} K(\lambda) \cdot O(r, \lambda) \cdot P_0(\lambda) \cdot \beta(r, \lambda) \cdot T^2(r, \lambda) \cdot \eta(\lambda) \cdot d\lambda + P_N \quad (3.13)$$

Terms are similar to those in Equation (3.7) but the spectral dependence has been added as well as the integration performed by the detector.

3.2.3 Experimental set-up and measurements

As a first step for the OCS-lidar development, a new aerosol lidar using a spectrally broadband laser source has been entirely designed, built and aligned in the frame of this PhD project. This section briefly presents the experimental set-up and shows the first lidar measurements achieved with this new lidar system. The resulting lidar signals are compared with an existing lidar system as a proof of its correct functioning. These first experimental results show that the lidar system based on a spectrally broadband fs-laser is operational and can be used as a basis for the development of the OCS-lidar methodology described in the following section.

The new lidar system is based on a titanium-sapphire laser source operating at the 785 nm wavelength with a 110 femtosecond pulse duration, 4 mJ per pulse and a 1 kHz repetition rate. The power spectral density $P_0(\lambda)$ is presented in Figure 3.10.

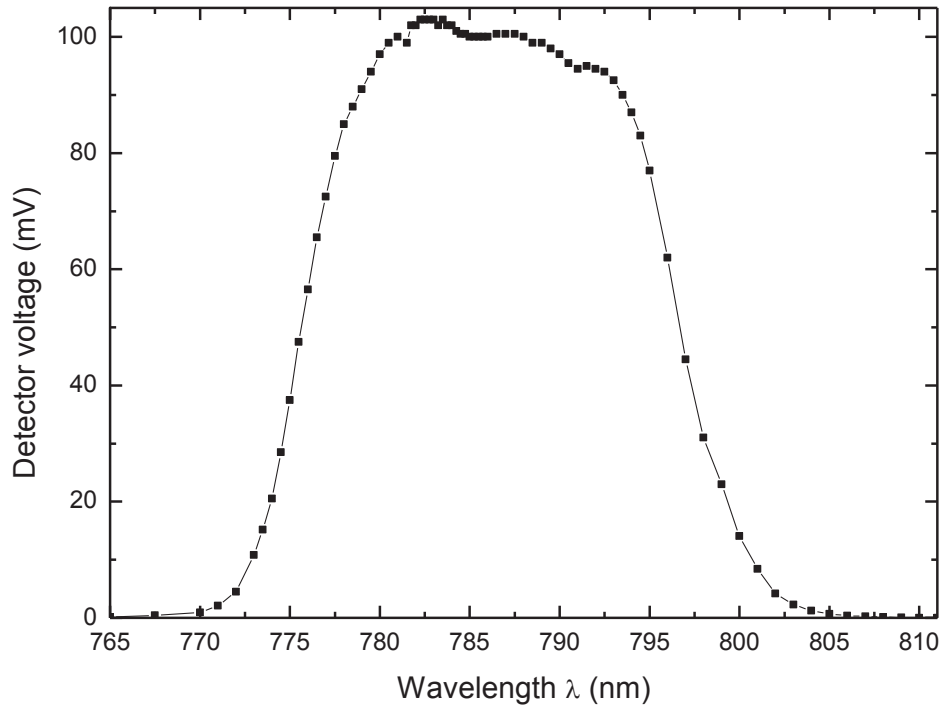


Fig. 3.10: Laser power spectral density $P_0(\lambda)$ measured at the output of the femtosecond laser source.

The backscattered photons are collected with a 30 cm diameter $f/4$ Newtonian telescope (to be more precisely described in Chapter 5), and are focused on a Hamamatsu photomultiplier tube R7400-U20. Signals are sampled by a Licel, 12 bits, Transient Recorder at a 40 MHz sample rate.

Using this new lidar system, measurements of Saharan dust particles backscattering have been performed on the 18th and 19th of July 2012 between 3500 and 5500 meters above Lyon. Figure 3.11 shows the obtained range-corrected lidar signals at the 785 nm wavelength. In order to corroborate the proper functioning of this new lidar, measurements with a second lidar system, operating at 355 nm, have also been performed. The 355-nm lidar has been already used and validated during several lidar particles outbreaks [Miffre et al. 2011, David et al. 2012]. The signal at 355 nm presented here has been taken 40 minutes after the signal at 785 nm. The 355-nm signal presented here arises from the depolarization channel, in this way the strong molecular contribution in the UV range is limited. Hence, both signals are more sensitive to the particles load than to the molecular load, and are therefore more comparable with each other. The output lidar signals are multiplied by the range squared r^2 in order to ease the reading, and are referred to as range-corrected lidar signals.

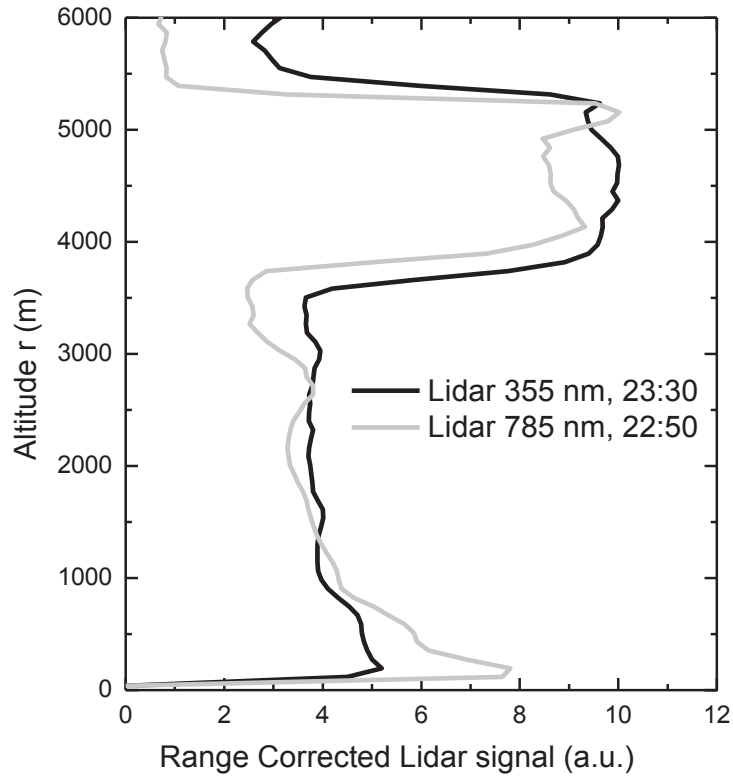


Fig. 3.11: Range corrected lidar signals at 785 nm (red) and at 355 nm on the depolarization channel (blue).

In both lidar experiments, we observe the presence of a high backscattering coefficient between 3500 and 5500 meters altitude, which confirms that the observations made on the new lidar system are relevant. However, the two signals are not quite similar, mostly for two reasons. Firstly, they operate at different wavelengths, therefore the 355 nm lidar is more sensitive to small particles (radius ≈ 500 nm) while the 785 nm lidar is sensitive to bigger particles (radius ≈ 1 μm) particle size as explained by the scattering theory [Mishchenko et al, 2002]. Secondly, the signals are not recorded simultaneously but with 40 minutes delay.

The time-altitude colored map displayed in Figure 3.12 represents a continuous measurement performed at 785 nm with a temporal resolution of 20 seconds during the same Saharan dust outbreak. The great stability of the dust layer over 40 minutes is observed with our new lidar instrument.

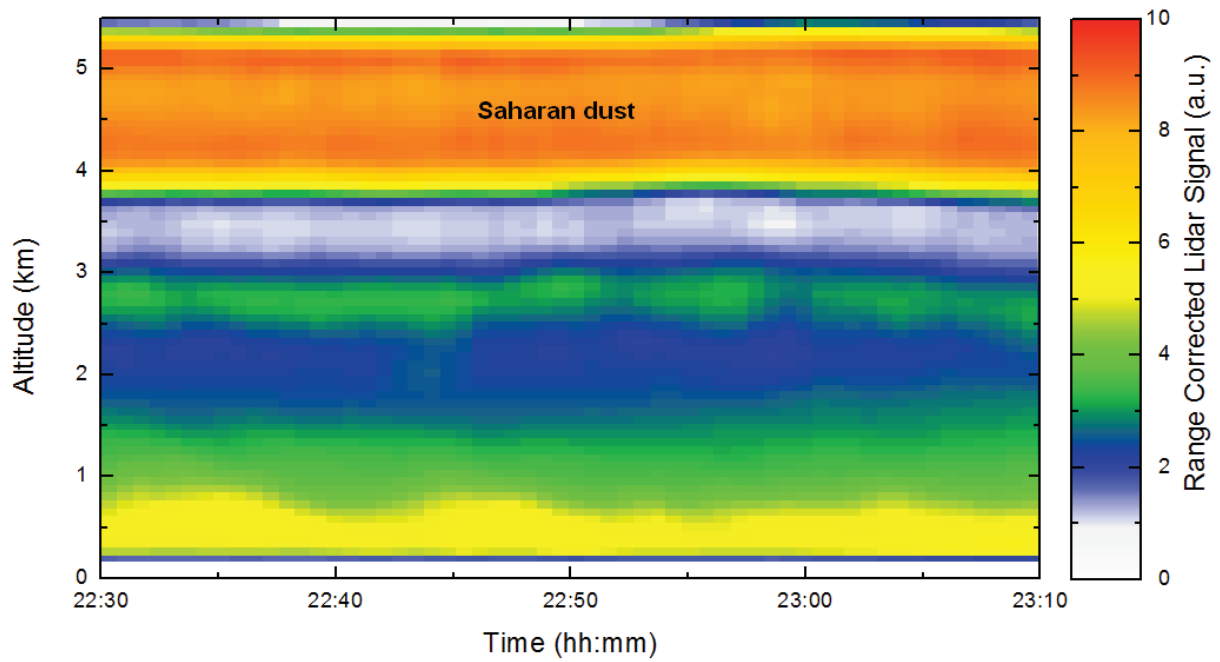


Fig. 3.12: Time altitude map of the range corrected 785-nm lidar signals during the Saharan dust event the 18th of July from 22:30 to 23:10 (local time).

Figure 3.13 shows the time altitude map after the dust event with 10 measurements every hour during 11 hours. The colors scale has been changed in order to show the planetary boundary layer height as well as clouds, including cirrus clouds located at 10 000 meters altitude.

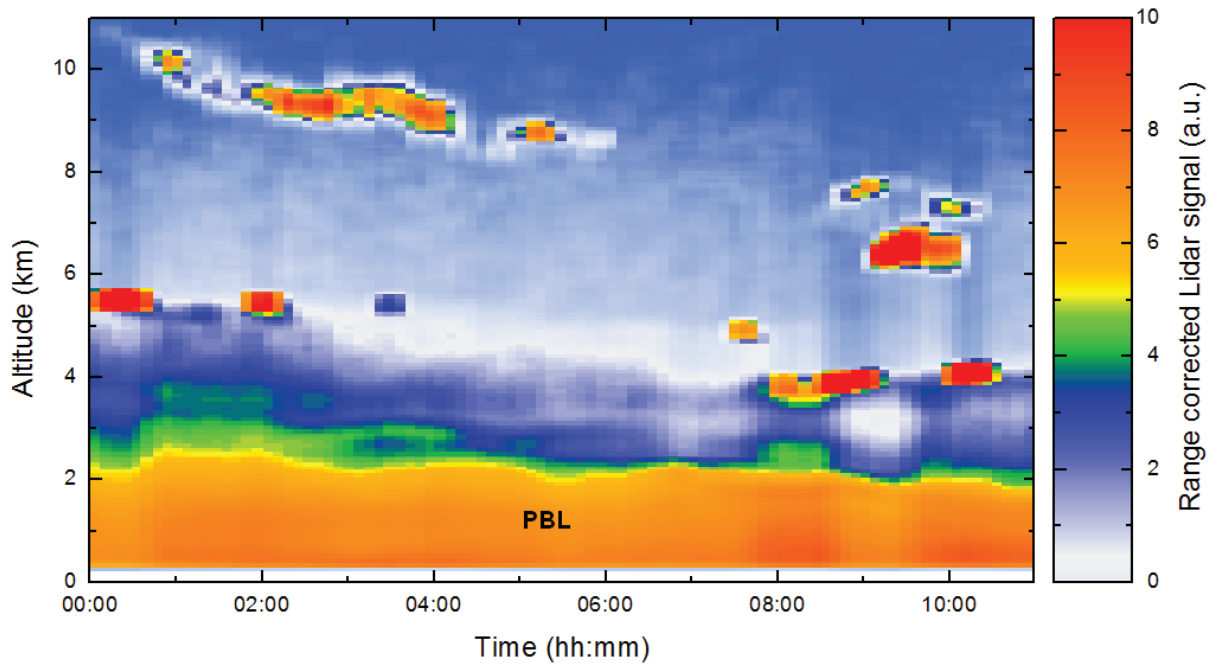


Fig. 3.13: Time altitude map of the range corrected lidar signals after the Saharan dust event the 19th of July from 00:00 to 11:00 (local time).

Back-trajectories can be used to confirm the origin of these air masses. They present the history of air masses, retracing its position through time and space based on meteorology. The 7-days air mass back-trajectories arriving at Lyon, displayed in Figure 3.14, confirm that the air mass arriving at a 5000 meters altitude above Lyon at 23:00 the 18th of July comes from the Sahara region before going above the Atlantic Ocean and in France by the west. The air mass at 3000 meters comes from the Ocean, as well as the air masses at 3000 and 5000 meters altitude 6 hours later, which corroborate the 3.12 and 3.13 color maps.

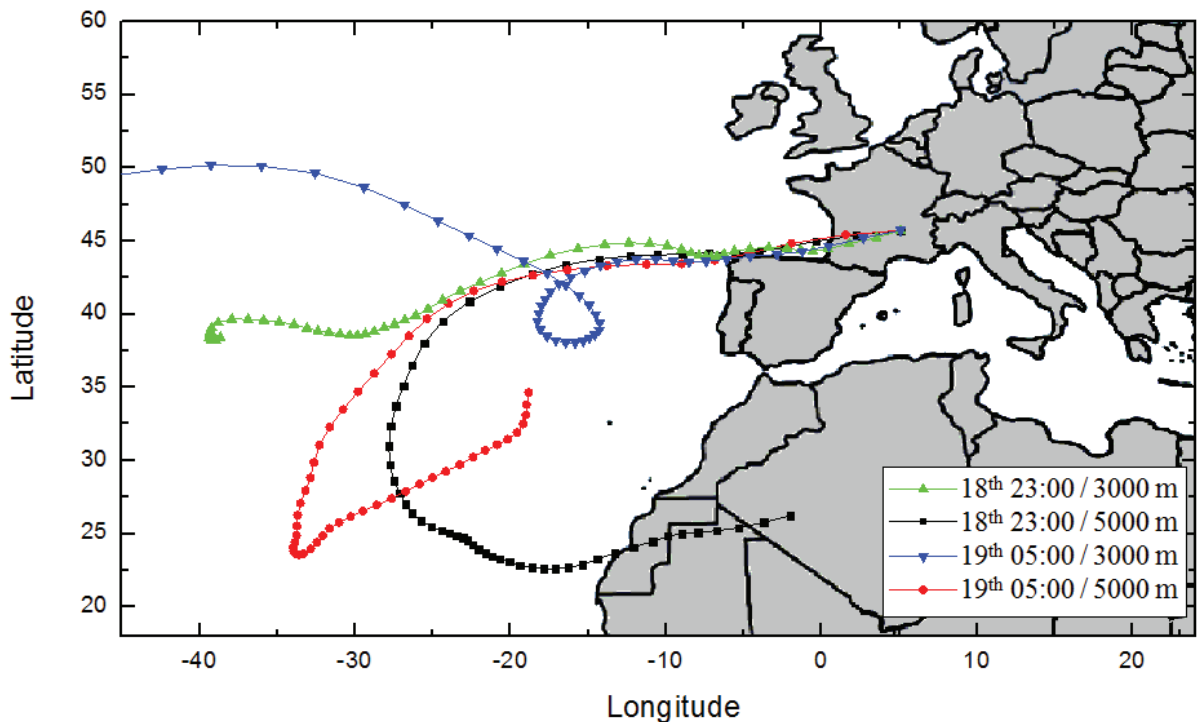


Fig. 3.14: Seven days air mass back trajectories arriving at Lyon at 3000 m altitude (green and blue) or 5000 m altitude (black and red) at 23:00 the 18th of July and at 05:00 the 19th (local time).

These first measurements performed with our new broadband lidar system appear to be consistent with another validated lidar instrument but also with geophysics. This broadband lidar system is hence operational and can be therefore be used as a basis for the development of the OCS-lidar methodology described in the following section.

3.3 Optical correlation spectroscopy coupled with lidar

Based on the OCS methodology and the lidar technique described in the previous sections, we here describe the new OCS-lidar methodology. It is a new differential absorption spectroscopy methodology inspired by a pioneer work performed on gas correlation lidar.

Gas correlation lidar has been introduced by [Edner et al. 1984] where preliminary experiments on atomic mercury were reported by using a differential absorption lidar (DIAL) coupled with a gas filter correlation technique. In contrast with the OCS and gas filter correlation techniques, the amplitude modulation to achieve the gas correlation is here

obtained by using an active amplitude modulator at the emission, instead of at the reception. This optical device allows us to achieve pulse shaping with great versatility and avoids the use of a gas cell, which required precise pressure and temperature control. The principle of this new methodology is here described and a new formalism explaining how the gas concentration is retrieved without the need of a permanent calibration procedure is presented.

3.3.1 OCS-lidar principle

This new methodology combines the capacity of the OCS technique to retrieve a gas concentration with the capacity of the lidar technique to perform long range measurements by using the light backscattered by the atmosphere. This section more precisely presents its principle.

The OCS-lidar principle is described in Figure 3.15 for a trace gas having an absorption line centered at a wavelength λ_0 . As in the conventional lidar technique, recalled in Section 3.2, a laser source is used to generate pulses having sufficient power density $P_0(\lambda)$ to achieve backscattering range-resolved measurements. The laser line width is chosen to be spectrally broad to cover one or several absorption lines of the trace gas absorption spectrum. Then, as for the OCS-methodology, a correlated (respectively non-correlated) signal is generated by applying an amplitude modulation $M_C(\lambda)$ (respectively $M_{NC}(\lambda)$) on the power density spectrum $P_0(\lambda)$ through an amplitude modulator (previously a reference gas cell in the OCS methodology). The non-correlated signal serves as a reference signal, following the OCS-principle described in Section 3.1. Then, after backscattering from the atmosphere due to molecules and aerosols, both the correlated and the non-correlated signals are collected with a telescope, and then directed towards the detector D to obtain two output OCS-lidar signals $P_C(r)$ and $P_{NC}(r)$, which are range-resolved. From an experimental point of view, an alternative acquisition of $P_C(r)$ and $P_{NC}(r)$, performed with a unique detector D, renders the optical signal acquisition and evaluation more robust. Hence, $P_C(r)$ and $P_{NC}(r)$ are alternatively gathered into a specific electronic buffer. The modulations M_C and M_{NC} are also alternatively generated by the amplitude modulator.

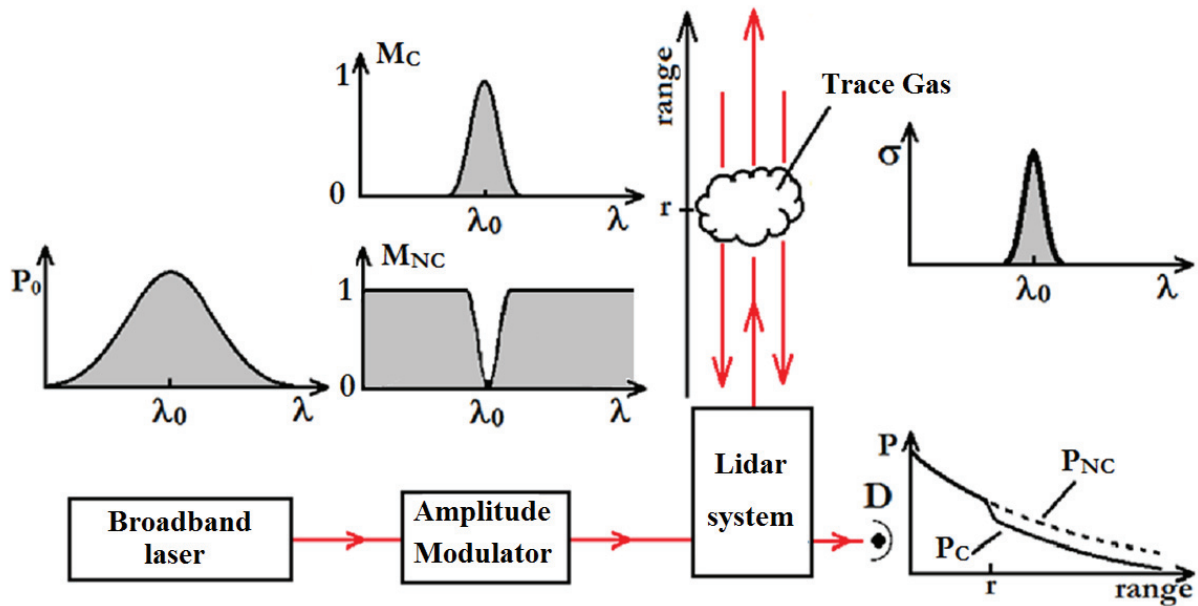


Fig. 3.15: Principle of the OCS-lidar methodology. A spectrally broadband laser pulse is shaped by an amplitude modulator. Two different laser pulses are alternatively generated, one is correlated and one is non-correlated to the trace gas absorption cross-section. Using a lidar system, the difference of extinction seen on the OCS-lidar signals P_C and P_{NC} allows to retrieve the trace gas concentration.

The trace gas concentration is then retrieved from $P_C(r)$ and $P_{NC}(r)$ by applying a methodology to be detailed in the following Section 3.3.2. As in the OCS-methodology, the difference between $P_C(r)$ and $P_{NC}(r)$ is a signature of the presence of the studied trace gas in the atmosphere, since absorption of the gas along the optical pathway only occurs for the correlated signal. The accuracy in the retrieved concentration depends on the difference in absorption between the two signals (which is driven by the SNR of the lidar signals, the gas amount, its absorption cross-section, the amplitude modulation and the possible presence of interfering species), and, as in conventional lidar, on the required range resolution and on the detector random noise. These points are discussed in Chapter 4. The wavelength λ_0 is determined by the spectral properties of the trace gas as to be seen in Section 4.4.2.

3.3.2 The OCS-lidar formalism

In this section, we detail the derivation of the gas concentration from the two output OCS-lidar signals $P_C(r)$ and $P_{NC}(r)$. The formalism to retrieve the target gas concentration is also

referred to as the OCS-lidar retrieval algorithm when used in the numerical model presented in Chapter 4.

At a range r from the lidar source, the initial laser pulse, with power density spectrum $P_0(\lambda)$, is related to the output OCS-lidar signal $P_C(r)$ and $P_{NC}(r)$ by Equations (3.14a) and (3.14b), called OCS-lidar equations. These latter are similar to Equation (3.13) except that the correlated or non-correlated amplitude modulation terms, respectively M_C and M_{NC} , are added in the equation.

$$P_C(r) = \frac{1}{r^2} \cdot \int_0^{\infty} K(\lambda) \cdot O(r, \lambda) \cdot P_0(\lambda) \cdot M_C(\lambda) \cdot \beta(r, \lambda) \cdot T^2(r, \lambda) \cdot \eta(\lambda) \cdot d\lambda + P_N \quad (3.14a)$$

$$P_{NC}(r) = \frac{1}{r^2} \cdot \int_0^{\infty} K(\lambda) \cdot O(r, \lambda) \cdot P_0(\lambda) \cdot M_{NC}(\lambda) \cdot \beta(r, \lambda) \cdot T^2(r, \lambda) \cdot \eta(\lambda) \cdot d\lambda + P_N \quad (3.14b)$$

Hence, in the specific case of the OCS-lidar methodology, the output power P_C (or P_{NC}) is related to the initial laser pulse power density spectrum $P_0(\lambda)$ through a modulation function $M_C(\lambda)$ (respectively M_{NC}). The atmospheric transmission $T(r, \lambda)$ can be expressed as follows:

$$T(r, \lambda) = \exp\left(-\sum_i \int_0^r \sigma_i(r', \lambda) \cdot C_i(r') \cdot dr'\right) \quad (3.15)$$

where $C_i(r)$ is the volume concentration (in molecules cm^{-3}) of the atmospheric compound i participating in laser light extinction through its absorption cross-section $\sigma_i(r, \lambda)$. The absorption cross-section is temperature and pressure dependent, which in the OCS-lidar equation may be interpreted as a range dependency. The i compounds are the atmospheric molecules N_2 and O_2 (transmission T_{mol}), the target gas (transmission T_{TG}), the other trace gases such as water vapor (transmission T_{og}), and the aerosols (transmission T_{aer}). Hence, the atmosphere transmission $T(r, \lambda)$ can be expressed as:

$$T(r, \lambda) = T_{\text{TG}}(r, \lambda) \cdot T_{\text{og}}(r, \lambda) \cdot T_{\text{mol}}(r, \lambda) \cdot T_{\text{aer}}(r, \lambda) \quad (3.16)$$

To evaluate the target gas concentration at range r , we use the OCS-lidar Equation (3.14a) and (3.14b). These two equations have more than two unknowns. However, it is possible by using the ratio P_C/P_{NC} to make some of these unknowns vanish. The last part of this chapter presents how to retrieve the target gas concentration from OCS-lidar equation.

Using Equation (3.14a) and (3.14b), we set the equation of the ratio P_C/P_{NC} in Equation (3.17). P_N being a random function centered on 0, it has been written separately out of the ratio.

$$\frac{P_C(r)}{P_{NC}(r)} = \frac{\int_0^{\infty} K(\lambda) \cdot O(r, \lambda) \cdot P_0(\lambda) \cdot M_C(\lambda) \cdot \beta(r, \lambda) \cdot T^2(r, \lambda) \cdot \eta(\lambda) \cdot d\lambda}{\int_0^{\infty} K(\lambda) \cdot O(r, \lambda) \cdot P_0(\lambda) \cdot M_{NC}(\lambda) \cdot \beta(r, \lambda) \cdot T^2(r, \lambda) \cdot \eta(\lambda) \cdot d\lambda} + P_N \quad (3.17)$$

In order to continue the analysis, the following assumptions are made:

- The telescope and the associated optical components are achromatic, $K(\lambda)$ and $O(r, \lambda)$ can be assumed as wavelength independent.
- The $\sigma_{TG}(\lambda)$ cross-section is assumed to be range independent, variations of the atmospheric temperature and pressure are not taken into account. The $\sigma_{TG}(r, \lambda)$ range dependency will be taken into account in the second part of this development. This assumption is discussed in Section 4.3.2.
- As a first step, we may assume that there is no interfering species within the considered spectral interval so that $T_{og} = 1$. This assumption is discussed in Section 4.3.4.
- The backscattering coefficient $\beta(r, \lambda)$ as well as the aerosol transmission $T_{aer}(r, \lambda)$ are also assumed to be wavelength independent over the considered wavelength interval. This assumption is discussed in Section 4.3.5.
- To ease the reading, the quantum efficiency of the detector $\eta(\lambda)$ can be seen as an amplitude modulation function applied by the detector and can be merged with the amplitude modulation function M_C and M_{NC} .

Considering all these assumptions, K , $O(r)$ and $\beta(r)$ can be moved out of the integral and therefore vanished as shown in Equation (3.18):

$$\frac{P_C(r)}{P_{NC}(r)} = \frac{\int_0^{\infty} P_0(\lambda) \cdot M_C(\lambda) \cdot T^2(r, \lambda) \cdot d\lambda}{\int_0^{\infty} P_0(\lambda) \cdot M_{NC}(\lambda) \cdot T^2(r, \lambda) \cdot d\lambda} \quad (3.18)$$

We then approximate the target gas transmission by a Taylor expansion of the exponential function up to third order in terms of the laser light extinction coefficient (assumption discussed in Section 4.3.1):

$$T_{TG}^2(r, \lambda) = 1 - 2 \cdot \sigma(\lambda) \cdot CC(r) + \frac{(-2 \cdot \sigma(\lambda) \cdot CC(r))^2}{2} + \frac{(-2 \cdot \sigma(\lambda) \cdot CC(r))^3}{6} + O^4 \quad (3.19)$$

where O^4 stands for the fourth order error term as a function of laser light extinction while $CC(r)$ is the path-integrated target gas concentration, or cumulative concentration, defined as

$$CC(r) = \int_0^r C_{TG}(r') \cdot dr' \quad (3.20)$$

Hence, the target gas concentration $C_{TG}(r)$ can be retrieved at range r from $CC(r)$ by derivation with respect to r . Determination of $CC(r)$ is feasible by noting that $CC(r)$ is the solution of a third order polynomial equation, deduced from Equation (3.18) and (3.19). After a few calculations, we get

$$A_3(r) \cdot CC(r)^3 + A_2(r) \cdot CC(r)^2 + A_1(r) \cdot CC(r) + A_0(r) = 0 \quad (3.21)$$

where the A-coefficients are expressed as :

$$A_3(r) = \frac{4}{3} \int_{\Delta\lambda} P_0(\lambda) \cdot T_{mol}^2(r, \lambda) \cdot \sigma_{TG}^3(\lambda) \cdot (P_{NC}(r) \cdot M_C(\lambda) - P_C(r) \cdot M_{NC}(\lambda)) \cdot d\lambda \quad (3.22a)$$

$$A_2(r) = -2 \int_{\Delta\lambda} P_0(\lambda) \cdot T_{mol}^2(r, \lambda) \cdot \sigma_{TG}^2(\lambda) \cdot (P_{NC}(r) \cdot M_C(\lambda) - P_C(r) \cdot M_{NC}(\lambda)) \cdot d\lambda \quad (3.22b)$$

$$A_1(r) = 2 \int_{\Delta\lambda} P_0(\lambda) \cdot T_{mol}^2(r, \lambda) \cdot \sigma_{TG}(\lambda) \cdot (P_{NC}(r) \cdot M_C(\lambda) - P_C(r) \cdot M_{NC}(\lambda)) \cdot d\lambda \quad (3.22c)$$

$$A_0(r) = -(1 + O^4) \cdot \int_{\Delta\lambda} P_0(\lambda) \cdot T_{mol}^2(r, \lambda) \cdot (P_{NC}(r) \cdot M_C(\lambda) - P_C(r) \cdot M_{NC}(\lambda)) \cdot d\lambda \quad (3.22d)$$

To solve Equation (3.21), each term hold in the A-coefficients has to be assessed. The P_C and P_{NC} terms, as well as the power spectral density $P_0(\lambda)$ are experimentally measured. The absorption cross-section of the target gas is computed from the HITRAN database as detailed in Chapter 2. The amplitude modulation functions M_C and M_{NC} are programmed on the amplitude modulator. Finally, theoretical models are used for the molecular backscattering cross-section coefficient as well as for the atmospheric molecular transmission.

Equation (3.21) has hence an analytical solution if one assumes that the O^4 term, present in the A_0 weighting coefficient, is zero. This assumption is discussed in Section 4.3.1.

3.3.3 Complementary material: The OCS-lidar algorithm using transmission product

The previous development assumes the target gas cross-section to be range independent. This assumption is necessary if one wants to establish the 3rd order polynomial expressed in Equation (3.21), otherwise Equation (3.18) cannot be solved for the cumulative concentration $CC(r)$. However, the target gas transmission $T_{TG}(r, \lambda)$ can be divided along the range axis in several transmission factors for a given altitude interval Δr . Thus, T_{TG} can be expressed as the multiplication of the transmission between the range $n \cdot \Delta r$ and $(n+1) \cdot \Delta r$

$$T_{TG}(r, \lambda) = \prod_{n=0}^{n=r/\Delta r} T_{TG}(n \cdot \Delta r, \lambda) \quad (3.23)$$

$$T_{TG}(r, \lambda) = \prod_{n=0}^{n=r/\Delta r} \exp\left(-\int_{n \cdot \Delta r}^{(n+1) \cdot \Delta r} \sigma_{TG}(r', \lambda) \cdot CC(r') \cdot dr'\right) \quad (3.24)$$

For a sufficiently small altitude interval Δr , the temperature and the pressure can be assumed as constant. Therefore, the target gas absorption cross-section can also be considered as constant with the range r within this interval. In this way, the absorption cross-section can be different for each atmospheric layer included between $n \cdot \Delta r$ and $(n+1) \cdot \Delta r$. Equation (3.24) then becomes:

$$T_{TG}(r, \lambda) = \prod_{n=0}^{n=r/\Delta r} \exp\left(-\sigma_{TG}(\lambda, n) \cdot \int_{n \cdot \Delta r}^{(n+1) \cdot \Delta r} CC(r') \cdot dr'\right) \quad (3.25)$$

To retrieve the concentration $C_{TG}(r)$, an iterative procedure is applied, the concentration near the ground is retrieved as previously with the 3rd order polynomial. Concentrations above this point are retrieved by including the target gas transmission retrieved at lower range in the A-coefficients. Using this methodology, the absorption cross-section variations with temperature or pressure can be considered.

The difference between these two retrieval algorithms are presented in Section 4.3.1 where a numerical model is used to assess the bias induced by the assumptions made in this section.

This chapter has presented the principle and the formalism of a new methodology called OCS-lidar to remotely retrieve the concentration of an atmospheric trace gas. The latter is based on the combination of two existing methodologies, the optical correlation spectroscopy (OCS) and the lidar.

First, the OCS-methodology is depicted, its historical background is reviewed together with a presentation of its formalism and a numerical computation for methane measurements. Then, the lidar technique is presented where the principle and formalism are also described. Moreover, a lidar system based on a spectrally broadband laser has been developed in the framework of this thesis. The first experimental measurements are here presented where a Saharan dust outbreak has been observed above the city of Lyon, showing that this lidar system is operational and can be used for the OCS-lidar methodology.

Finally, the coupling of both methodologies is presented. The OCS-lidar combines the capacity of the OCS methodology to retrieve a target gas concentration using a broadband light source, with the capacity of the lidar to perform long-range measurements using the backscattered light of a laser pulse transmitted in the atmosphere. The last section sets the OCS-lidar equations and shows how to retrieve the target gas concentration from a third order polynomial.

Chapter 4

The OCS-lidar numerical model

This chapter presents the numerical model that has been developed to assess the performance of our trace gas concentration retrieval methodology. The purpose of such a numerical model is twofold. As it is new, the OCS-lidar methodology has for the first time been studied through this numerical model. We ensured to properly assess the feasibility of the methodology by running realistic simulations. By this means, the different sources of statistical and systematic errors, related to the OCS-lidar formalism described in Section 3.3, have been evaluated. Secondly, the numerical model has been used to improve the performance of this methodology. Numerous parameters detailed in this chapter, such as the amplitude modulation functions or the laser central wavelength, greatly influence the precision and the sensitivity of this methodology. By allowing to test different sets of parameters, this numerical model allows to significantly improve the accuracy of the retrieved gas concentration of the OCS-lidar experiment presented in Chapter 5.

This fourth chapter is organized as follows. First, the numerical model generating the OCS-lidar signals is described by taking into account a realistic modeling of the noise sources. Each simulated element is detailed: the atmosphere, the laser source, the amplitude

modulation functions and the detection system. The OCS-lidar signals have been simulated for two case studies:

- In the visible spectral range (VIS) for water vapor concentration measurements. We consider in this case the $4\nu_2$ 720 nm water vapor absorption band, as described in Chapter 2.
- In the near infrared spectral range (NIR) for methane concentration measurements. In this case, we consider the $2\nu_3$ vibrational band around the 1665 nanometers wavelength, also described in Chapter 2.

To evaluate the sensitivity and the accuracy of the OCS-lidar methodology, different input gas (methane and water vapor) concentration profiles are considered and the corresponding mixing ratios are retrieved by using the OCS-lidar methodology developed in Section 3.3. The inherent assumptions of the OCS-lidar methodology are then discussed in the next subsections. Statistical errors due to the detector noise, the background shot-noise and the laser fluctuations are detailed in Section 4.2 and their influence on the retrieved concentration is discussed. Section 4.3 presents the systematic errors, the contribution to the relative error due to the model, the atmospheric conditions (temperature and pressure), the aerosols and molecular contributions, the uncertainties on the spectral data and the possible presence of interfering species are evaluated. Finally, this chapter ends with the presentation of the achieved optimization processes that are needed to properly choose the amplitude modulations functions and the laser settings. The work performed in this chapter has been published in B. Thomas et al. [2012, 2013a, b].

To ease the reading, Figure 4.1 shows the diagram of the OCS-lidar numerical model. It presents the input needed to compute the OCS-lidar signals. Then, from these signals, the target gas concentration can be retrieved by using the OCS-lidar retrieval algorithm. The retrieved concentration can be compared with the input concentration in order to evaluate the relative error. Hence, the influence of each parameter on the retrieved gas concentration can be studied.

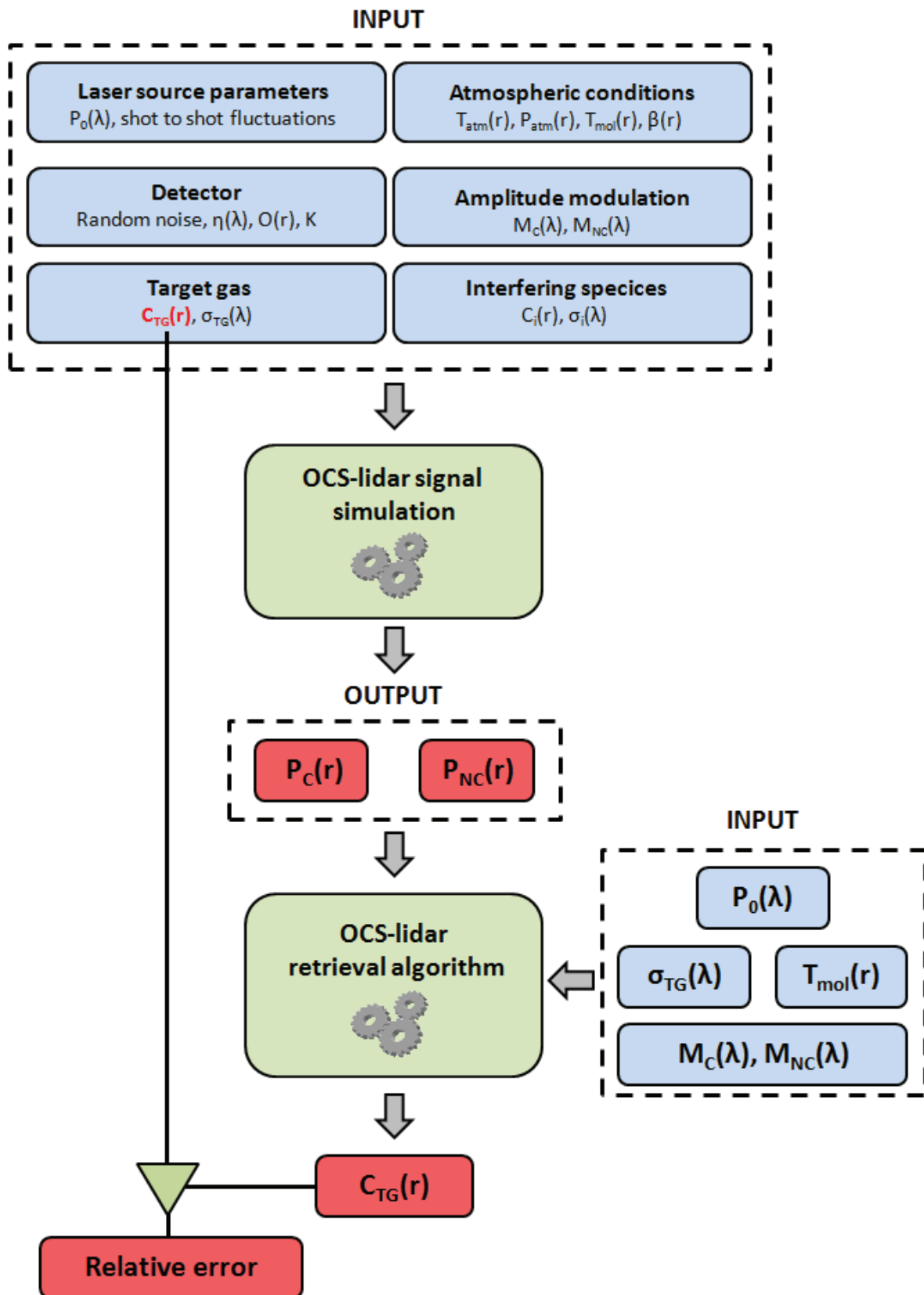


Fig. 4.1: Diagram of the OCS-lidar numerical model.

4.1 Numerical model of OCS-lidar signals

This section presents the different inputs to the numerical model. It describes how the atmosphere, the laser source, the amplitude modulation and the detection system are modeled. Finally, the resulting OCS-lidar signals $P_C(r)$ and $P_{NC}(r)$ are presented.

4.1.1 Numerical model for the atmosphere

To perform appropriate numerical simulations, the atmospheric conditions are based on a standard urban atmosphere, as defined by J. H. Seinfeld [Seinfeld, 1998]. The temperature and pressure profiles as well as the molecular backscattering coefficients are set in order to simulate either vertical or horizontal trace gas concentration profile measurements. Figure 4.2 shows the molecular and particles backscattering coefficients together with the vertical profile for the atmospheric temperature T_{atm} , and the pressure P_{atm} . The pressure is based on the exponential decay model with ground pressure equal to 1 atm, and the temperature profile is based on the adiabatic model with a temperature gradient of 0.01 K.m^{-1} . The molecular backscattering coefficient $\beta_m(r,\lambda)$ is computed by using the Rayleigh scattering formalism. In our model, the particles backscattering coefficient $\beta_p(r,\lambda)$ is assumed to be constant for both vertical and horizontal pointing directions, this parameter influences the SNR of the OCS-lidar signals but has no direct influence on the retrieved concentration. The β_p -values are set at $10^{-7} \text{ m}^{-1}.\text{sr}^{-1}$ in the near infrared spectral range ($1.6 \mu\text{m}$) and $2 \times 10^{-7} \text{ m}^{-1}.\text{sr}^{-1}$ in the visible region (700 nm). These values are in the range of typical values for urban particles backscattering coefficients but are rather low to avoid overestimating the sensitivity of the methodology.

For horizontal measurements, the value of each parameter (P_{atm} , T_{atm} , β_m and β_p) is assumed to be constant with the range and equal to the value taken at ground level (i.e. at range $r = 0$).

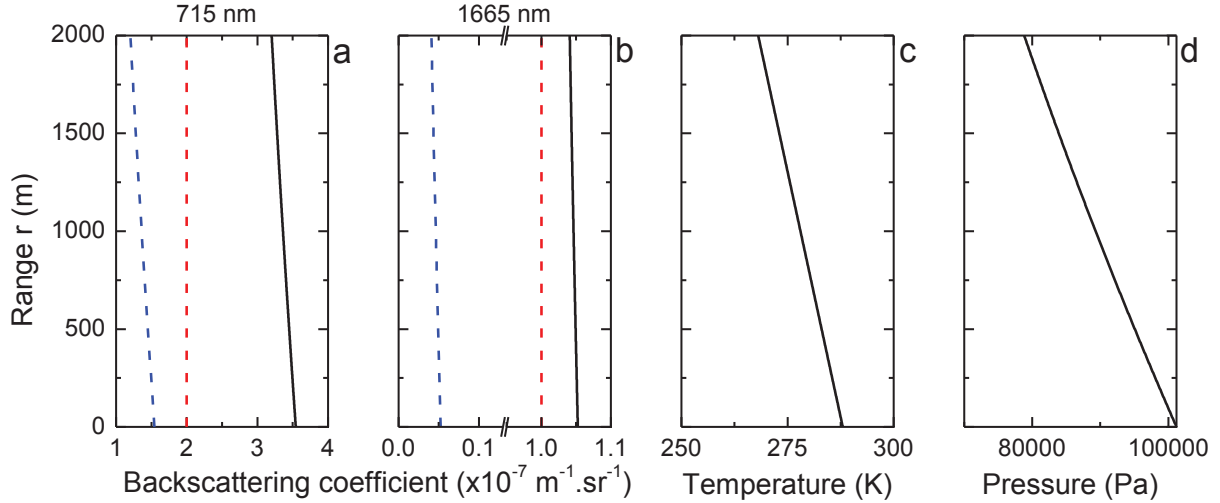


Fig. 4.2: Molecular backscattering coefficient $\beta_m(r,\lambda)$ (blue dashed lines), particle backscattering coefficient $\beta_p(r,\lambda)$ (red dashed lines), and total backscattering coefficient $\beta(r,\lambda) = \beta_m(r,\lambda) + \beta_p(r,\lambda)$ (black lines) at wavelengths $\lambda = 715 \text{ nm}$ (a) and $\lambda = 1665 \text{ nm}$ (b) as set in the numerical model for vertical measurement simulations. The temperature profile (c) is set on an adiabatic model, while the pressure profile (d) follows an exponential decay with a 101 200 Pa ground pressure.

4.1.2 Numerical simulation of the laser source

The OCS-lidar laser source simulated in this numerical model must fulfill the requirements for the OCS-lidar methodology. Apart from its high power density (to achieve range resolved backscattering measurements) and its spectrally broad emission line (to match one or several absorption lines of the target gas absorption spectrum), high pulse-to-pulse energy and spectral stability is required (typically in the 1 % range), depending on the expected concentration accuracy and sensitivity. Several broadband laser sources can hence be used, such as a high power Fabry-Pérot diode laser, a white-light fiber laser or an OPA pumped by an ultra-short femtosecond laser. Femtosecond broadband laser sources can be considered as spectrally stable light sources which is crucial for accurate absorption spectroscopy measurements, as to be seen in Section 4.2.3. In this numerical simulation, an OPA (Optical Parametric Amplifier) pumped by ultra-short femtosecond laser has been considered. The laser pulse characteristics are given in Table 4. 1.

Laser source	Near infrared	Visible
Pulse energy	250 μ J	100 μ J
Pulse duration	100 fs	100 fs
Pulse spectral shape	Gaussian	Gaussian
Central wavelength λ_0	1665 nm	714 nm
Spectral width (FWHM)	20 nm	15 nm
Pulse repetition rate	1 kHz	1 kHz
Laser beam divergence	0.1 mrad	0.1 mrad

Table 4.1: Laser source specifications

The power spectral density $P_0(\lambda)$ of the emitted laser pulse is assumed to be Gaussian and computed by using the following equation:

$$P_0(\lambda) = \overline{P}_0 \cdot G(\lambda_0, \sigma_L) \quad (4.1)$$

where \overline{P}_0 is the output power and $\sigma_L = \text{FWHM} / (2\sqrt{2\ln 2})$ is the standard deviation of the normalized Gaussian function G centered at wavelength λ_0 . Figure 4.3 shows the simulated Gaussian pulse in the NIR (a) and VIS (b) spectral ranges used for OCS-lidar to detect methane and water vapor respectively. Unlike the central wavelength λ_0 , the spectral width of the laser pulse is not tunable and is equal to $\sigma_L = 6.3$ nm (15 nm FWHM).

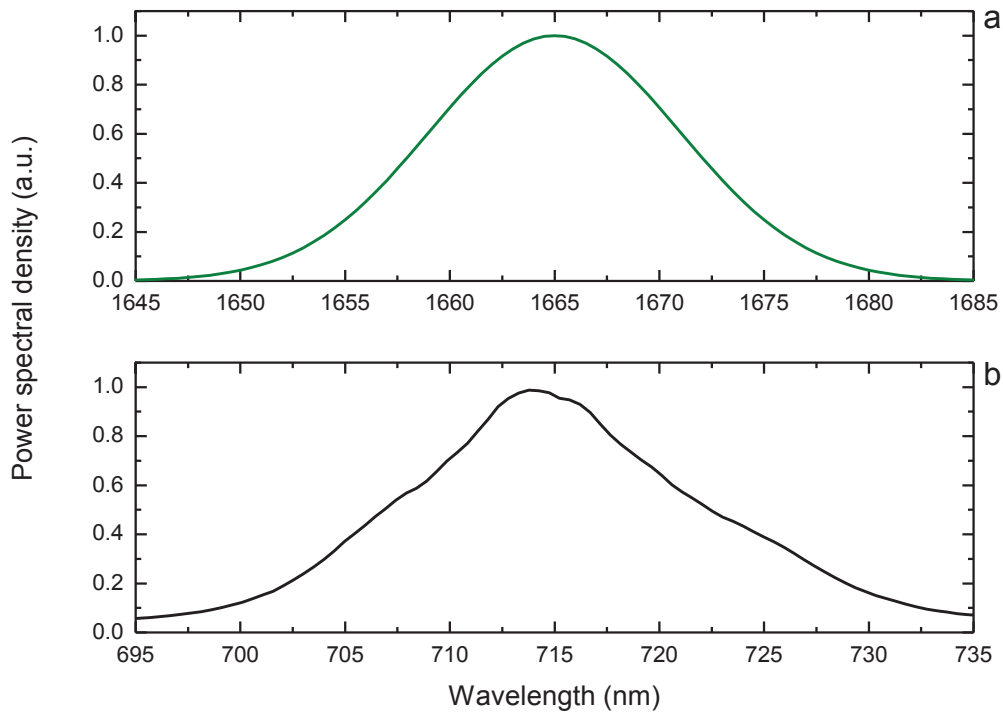


Fig. 4.3: Laser power spectral density $P_0(\lambda)$ in the NIR (a) based on a Gaussian centered at $\lambda_0 = 1665$ nm and 15 nm FWHM spectral width. The power spectral density $P_0(\lambda)$ in the VIS (b) is based on actual measurement of the OPA spectrum, centered at 714 nm with 15 nm FWHM spectral width.

4.1.3 The amplitude modulation functions

As described in Section 3.1, in conventional OCS experiments, the laser pulse is spectrally shaped by using a reference cell. However, as previously mentioned in Section 3.3, in the OCS-lidar methodology, the amplitude modulation can be performed by using an Acousto Optic Programmable Dispersive Filter (AOPDF). Such an optical component ensures an amplitude modulation of the initial femtosecond laser pulse by providing the amplitude modulations functions $M_C(\lambda)$ and $M_{NC}(\lambda)$, respectively, correlated and non-correlated with the target gas absorption bands. These amplitude modulation functions used in the numerical model have to be simulated with respect to the AOPDF specifications and technical limitations. The measured maximum spectral resolution in the visible region reaches 0.5 nm and 1.1 nm in the infrared region with a maximum transmission of 60 %.

Possible AOPDF modulator transmissions $M_C(\lambda)$ and $M_{NC}(\lambda)$ are shown in Figures 4.4 and 4.5 in the NIR and visible spectral range together with the methane and water vapor

absorption cross-sections. These amplitude modulations result from the optimization procedure, to be described in Section 4.4.

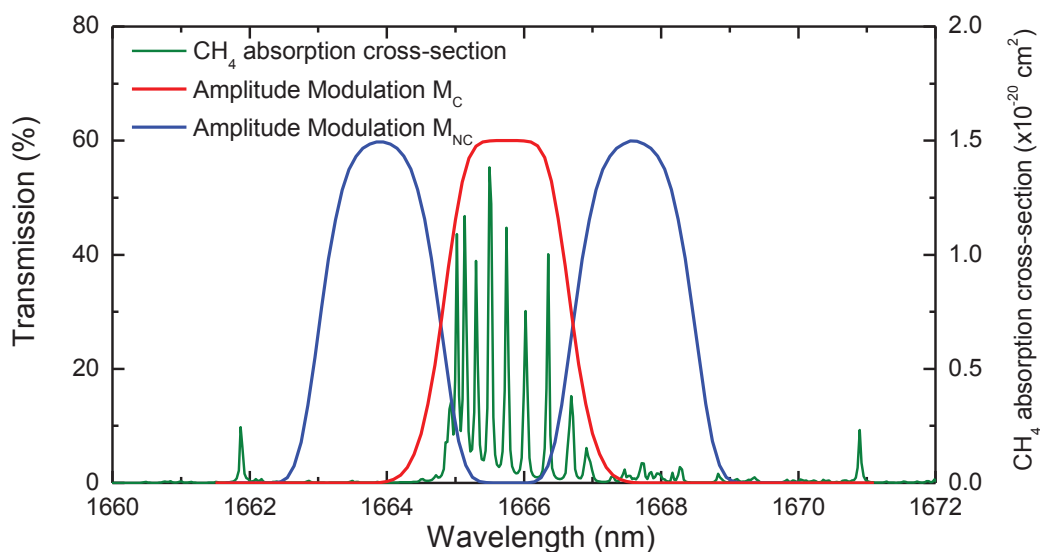


Fig. 4.4: Amplitude modulation functions $M_C(\lambda)$ (red) and $M_{NC}(\lambda)$ (blue) generated by the AOPDF in the infrared spectral range together with the methane absorption cross-section (green) derived from the HITRAN spectroscopic database (see Chapter 2).

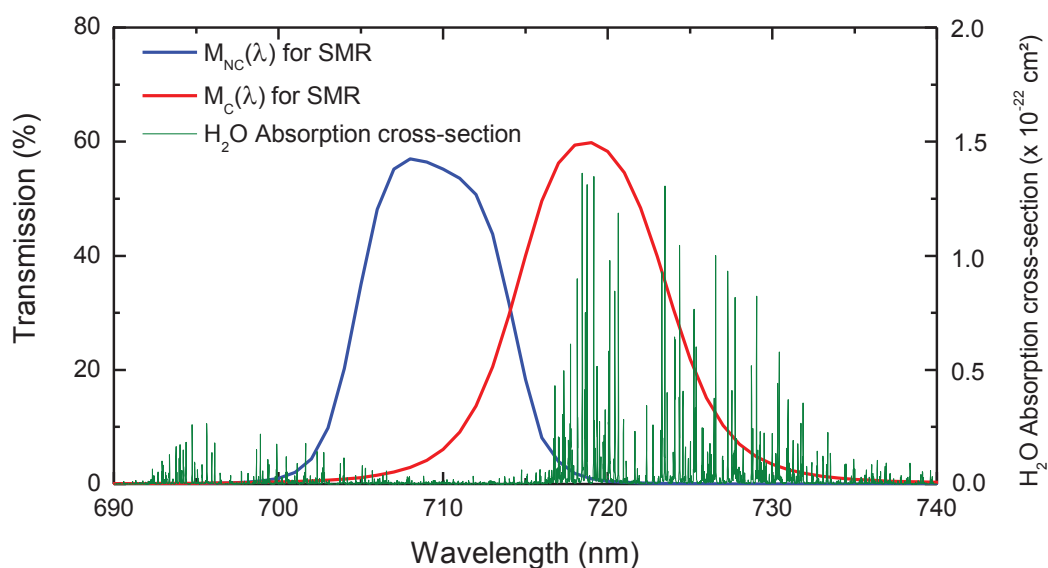


Fig. 4.5: $M_C(\lambda)$ (red) and $M_{NC}(\lambda)$ (blue) generated by the AOPDF in the visible spectral range together with the water vapor absorption cross-section (green) derived from the HITRAN spectroscopic database (see Chapter 2).

4.1.4 The detection system

The detection system is composed of all optical and electric components used to collect and to focus the backscattered photons on the photo-detector and then record the corresponding electrical signal. This includes the receiving optics (telescope in a Newton-configuration), a parallelizing lens, all possible interference filters used to limit the background contribution, a converging lens, the photo-detector and the acquisition system recording the electric signal delivered by the detector. The overlap function $O(r)$, the detection system efficiency $\eta(\lambda)$ and the noise P_N related to the photo-detector are discussed in this section.

The overlap function $O(r)$ has been simulated for a 30 cm diameter $f/4$ Newtonian telescope with a 3 mm-pinhole inserted at the telescope focus. As shown in Figure 4.6, the overlap function of the telescope is higher than 0.9 above a 120 meters range. Due to the secondary mirror (diameter = 5 cm), the maximum does not exceed 0.97.

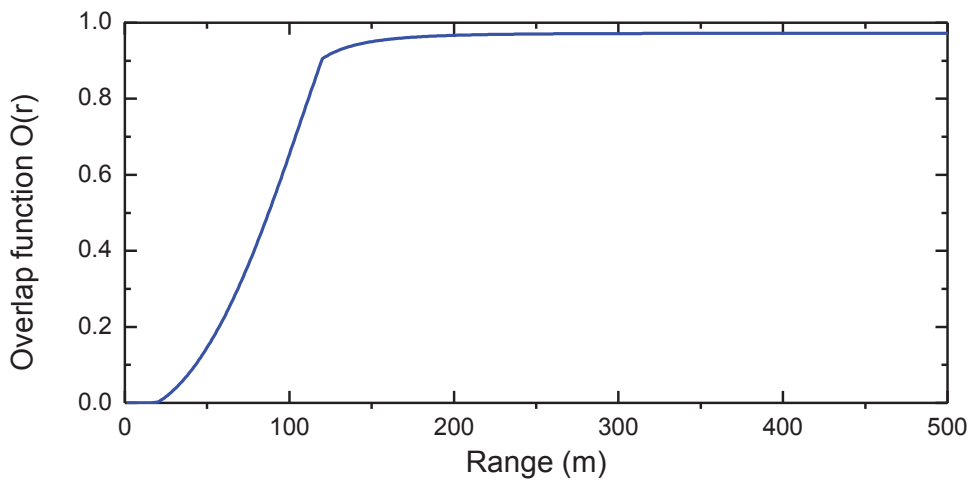


Fig. 4.6: Overlap function $O(r)$ of a 30 cm diameter $f/4$ Newtonian telescope with a 3 mm pinhole inserted at the telescope's focus.

The optical efficiency $\eta(\lambda)$ of the detection system (see Section 3.2.2) is defined by the transmission coefficient of each lens, and the quantum efficiency of the photodetector. In the case of this numerical model, the lens transmission coefficients are assumed to be wavelength independent within the considered spectral range. Therefore, the optical efficiency is proportional to the quantum efficiency of the photodetector.

Since our methodology is based on absorption spectroscopy, $\eta(\lambda)$ has been measured in order to precisely know the spectral detector response. To do so, the experimental set-up presented in Figure 4.7 has been achieved. The wavelength-tunable OPA system is used to generate a spectrally broadband laser pulse which is then sent through the AOPDF. The latter acts as a tunable spectral filter with a 0.5 nm bandwidth corresponding to its maximum spectral resolution. By this means, only the selected part of the power density spectrum is transmitted. Then, the broadband laser pulse passes through a 50/50 beam splitter before being measured by the photodetector on one side and a wavelength calibrated powermeter on the other side.

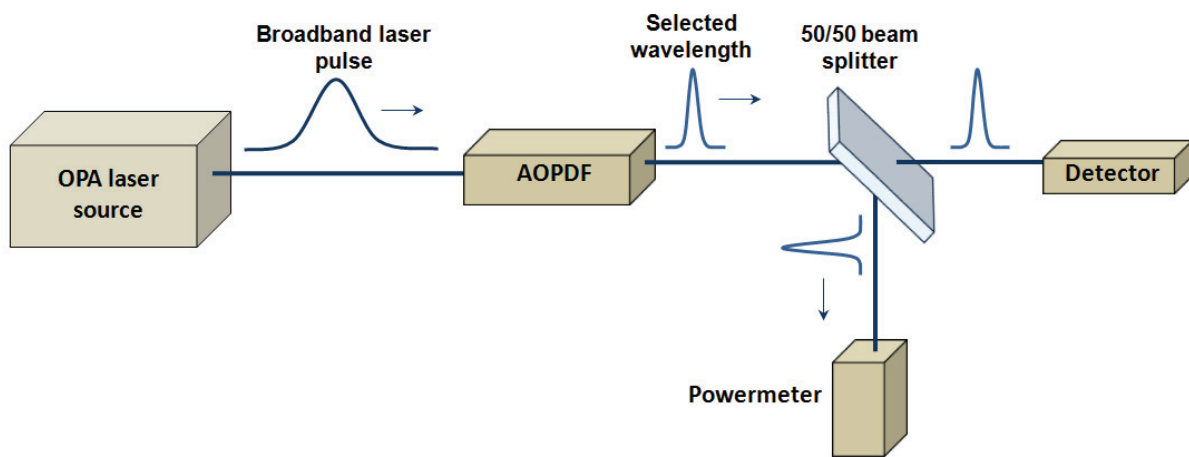


Fig. 4.7: Photodetector quantum efficiency measurement setup. The AOPDF acts as a tunable spectral filter with 0.5 nm spectral resolution. Only a part of the broadband power spectral density is transmitted by the AOPDF before being sent to a wavelength-calibrated powermeter and the detector. Measurements are repeated for different selected wavelengths, then the detector signal is normalized by the laser power measurement to retrieve the detector quantum efficiency.

The quantum efficiency of the photodetector is then retrieved by changing the selected wavelength with the AOPDF and the OPA system. The signal measured by the photodetector is normalized thanks to the pulse power measurement. Figure 4.8a shows the results obtained for two “similar” photomultiplier tubes in the visible range, showing the need for measuring $\eta(\lambda)$. Figure 4.8b presents the normalized quantum efficiency given by the constructor of the APD InGaAs infrared detector.

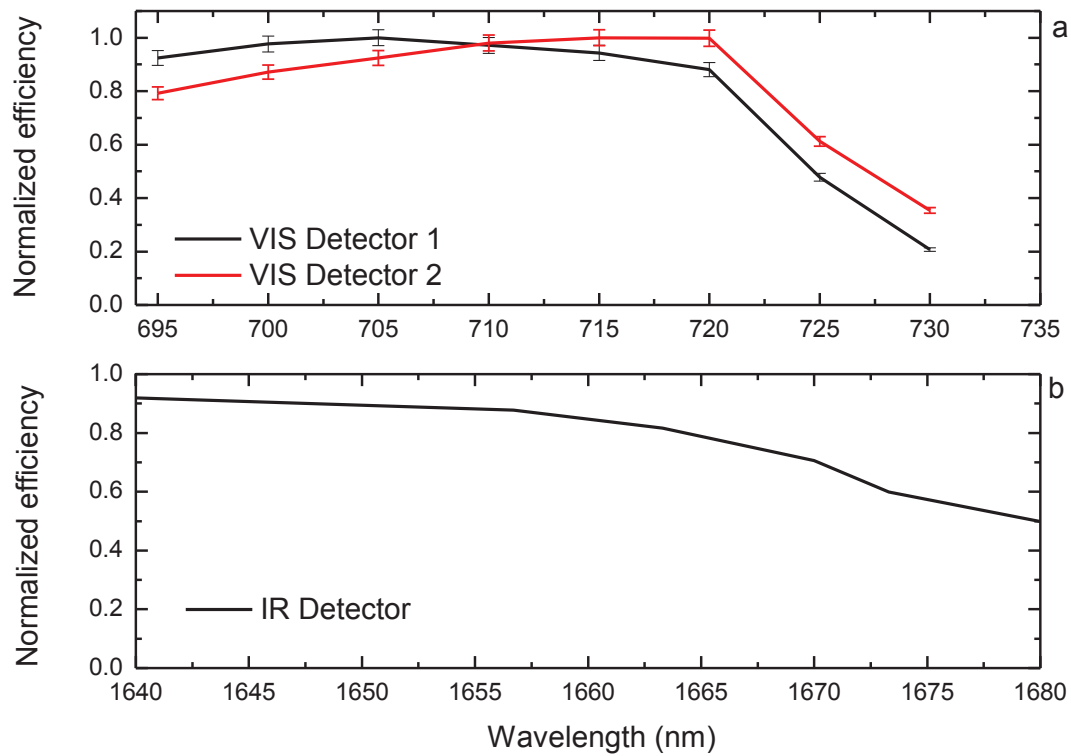


Fig. 4.8: Normalized quantum efficiency of two photomultiplier tubes in the visible spectral range (a) measured by the experimental set-up presented in Figure 4.7. Normalized quantum efficiency of the APD InGaAs detector given by the constructor (b).

Since the simulations are operated at different spectral ranges, infrared at 1665 nm and visible at 720 nm (for methane and water vapor respectively), two sets of detector parameters have been considered (as shown in Table 4.2). In the case of the NIR simulation, the photodetector parameters are based on the InGaAs APD. The detector operating in the visible range is based on the Hamamatsu photomultiplier tube R7400-U20.

In both spectral ranges, VIS and NIR, the acquisition system is based on a Transient Recorder Licel, 12 bits, and 40 MHz sample rate. Therefore, signals $P_C(r)$ and $P_{NC}(r)$ are sampled with a spatial resolution of $\Delta r = 3.75$ meters corresponding to the 40 MHz frequency sample rate.

Figure 4.9 represents the successive steps to simulate an OCS-lidar signal with random noise. The continuous signal generated from the OCS-lidar equation is computed for discrete values of the range $r = n \times \Delta r$, where n is a positive integer. In order to simulate the statistical fluctuation undergone by the signals $P_C(r)$ and $P_{NC}(r)$, each discrete value of the signal is summed with a value $P_N(r)$. $P_N(r)$ is defined as a statistical function with random fluctuation

following a Gaussian statistical distribution centered at zero and with a standard deviation σ_N whose value is discussed below in Section 4.2.1.

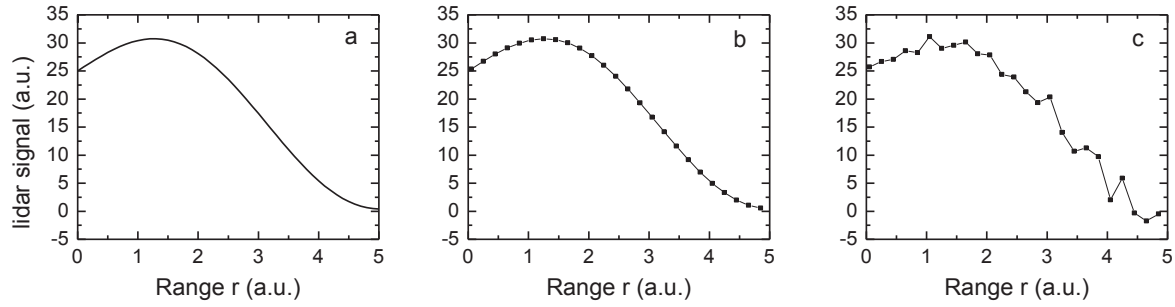


Fig. 4.9: Sequences of the OCS-lidar simulation. (a): Simulation of OCS-lidar signal using a the continuous function described in Equation (3.14) (b): Discrete values of the OCS-lidar signal are considered in order to simulate the spatial resolution of the detector. (c): The signal is summed with the random function P_F which follows a Gaussian statistical distribution.

Table 4.2 presents a summary of the different inputs given to the numerical model.

Laser source	Near infrared	Visible
Pulse energy	250 μ J	100 μ J
Pulse duration	100 fs	100 fs
Pulse spectral shape	Gaussian	Gaussian
Central wavelength λ_0	1665 nm	714 nm
Spectral width (FWHM)	20 nm	15 nm
Pulse repetition rate	1 kHz	1 kHz
Laser beam divergence	0.1 mrad	0.1 mrad
Modulator (AOPDF)		
Spectral resolution	1.1 nm	0.5 nm
Spectral width	6 nm	25 nm
Maximum transmission	60 %	60 %
Minimum transmission	10^{-2} %	10^{-2} %
Telescope		
Diameter	200 mm	300 mm
Primary mirror focal length	600 mm	1200 mm
Field of view (full angle)	0.3 mrad	0.3 mrad

Detector (D)		
Type	InGaAs (APD)	Photomultiplier tube
Responsivity (R)	5 A.W ⁻¹ at 1 665.7 nm	4.10 ⁴ A.W ⁻¹ at 715 nm
Electrical response bandwidth	10 MHz	350 MHz
Detector diameter	200 μm	6 mm
Detector temperature	252 K	Room temperature
Noise Equivalent Power	570 fW.Hz ^{-1/2}	/
Atmosphere		
Molecular volume backscattering coefficient	based on a Standard Atmosphere	based on a Standard Atmosphere
Aerosol backscattering coefficient	10 ⁻⁷ m ⁻¹ sr ⁻¹	2.10 ⁻⁷ m ⁻¹ sr ⁻¹
Input methane mixing ratios	1 ppm – 400 ppm	/
Water vapor (RH)	0 % – 95 %	0 % – 95 %

Table 4.2: OCS-lidar numerical model parameters used for the numerical OCS-lidar signals simulation NIR (for methane) and in the visible spectral range (for water vapor). The laser source, the amplitude modulator (AOPDF) and the detection system parameters are detailed for a standard atmosphere containing methane mixing ratio from 1 to 400 ppm, RH-values from 0 to 95 %, atmospheric aerosols and molecules (N₂ and O₂).

4.1.5 Output numerical OCS-lidar signals

Based on the numerical model depicted in the previous sections, OCS-lidar signals are simulated for different methane or water vapor input concentration profiles by applying Equation (3.14). Four input atmospheric concentration profiles are here studied and presented:

- A low methane concentration profile, 1.5 and 3 ppm, as usually observed in urban areas [Vinogradova, 2006].
- A methane concentration profile in the range from 2 to 10 ppm, typical for industrial sites. [Chambers et al. 2008].
- A high methane concentration profile in the range of hundreds of ppm, representative of methane leakages [Chambers et al. 2008].
- A water vapor profile of a constant 6000 ppm, representative of low water vapor concentration near the ground (relative humidity of 50 % at 283 K).

The concentration profile can be retrieved from these signals, using the OCS-lidar retrieval algorithm based on the formalism written in Section 3.3. The 3rd order polynomial (Equation (3.21)) is solved for $CC(r)$, before deriving numerically this function to retrieve $C(r)$. $CC(r)$ is numerically smoothed and its spatial resolution is reduced to lower the statistical fluctuations.

The resulting OCS-lidar output signals P_C and P_{NC} are presented in Figures 4.10, 4.11, 4.12 and 4.13 (top panel) for each input methane or water vapor profile and for different acquisition times, to improve signal-to-noise ratios. This ensures reliable concentrations to be retrieved, as detailed in Section 4.2, where statistical and systematic errors on the retrieved mixing ratio are discussed.

Figure 4.10 shows the infrared OCS-signals and the input and retrieved concentration profiles for a methane mixing ratio that oscillates between 1.5 and 3 ppm. This case simulates typical methane concentration variations observed in urban areas [Vinogradova et al. 2006]. The results presented simulate measurements operated in the minute range.

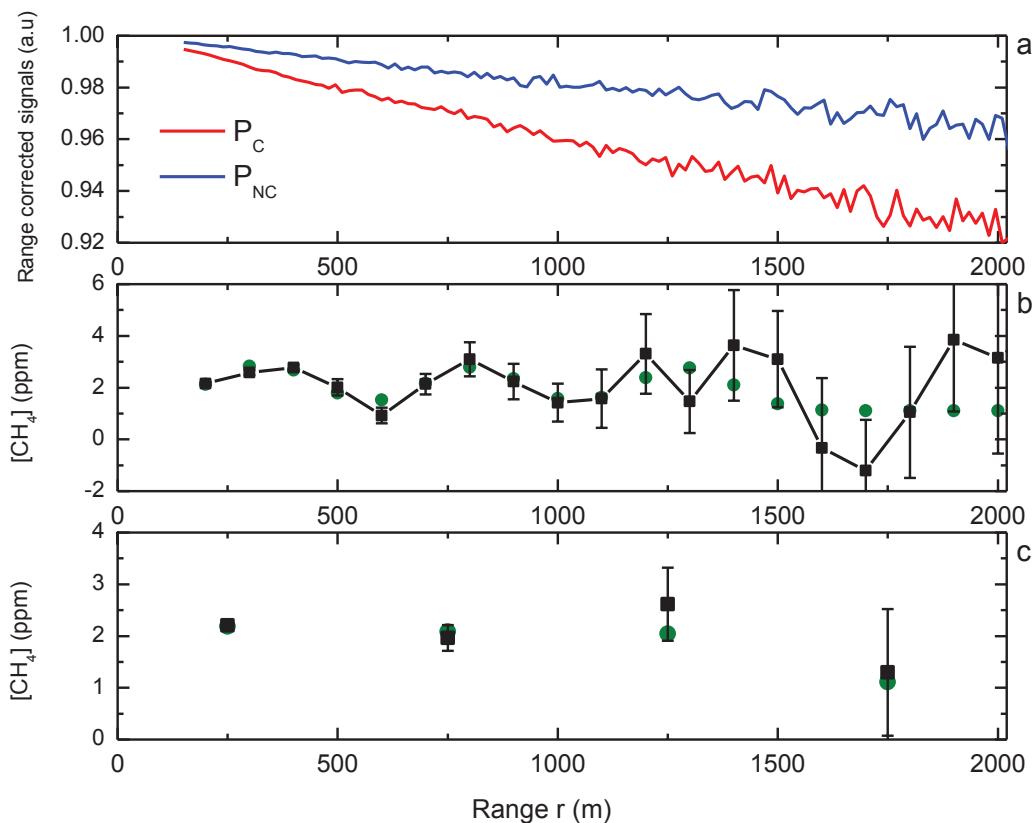


Fig. 4.10: Low methane concentration input (green, 1.5 to 3 ppm) and retrieved (black) OCS-lidar methane mixing ratio (in ppm) as a function of range r (in meters) with two different spatial resolutions (b and c) together with the corresponding range-corrected correlated OCS-lidar signal P_C (in red) and non-correlated OCS-lidar signal P_{NC} (in blue) as a function of range r (a).

The plotted error bars, which indicate the statistical error on the retrieved mixing ratio, are discussed in the following section. Figure 4.10 shows that, for urban areas, the statistical error on the retrieved methane mixing ratios remains below 20 % up to a one kilometer range. This error increases with range and reaches 100 % at a two kilometers range. This statistical error can be reduced by range and time averaging to reach higher accuracy on the retrieved methane mixing ratio. Further, the retrieved methane mixing ratio has also been plotted for a range resolution of 500 meters (see Figure 4.10). A further increased accuracy can be obtained by limiting the range resolution even more: for a 1000 meters range resolution, the averaged methane mixing ratio is 2.1 ppm and the relative error between the input and simulated mixing ratio falls down to 6 %.

Figure 4.11 presents a simulation for arbitrary methane mixing ratio fluctuations in the range from 2 to 10 ppm, typical for industrial sites working with methane [Chambers et al. 2008]. The range-resolved mixing ratio has a 100 meters range resolution with an increased accuracy than for lower concentrations. Statistical errors are found to be below 25 % up to a 1 500 meters range.

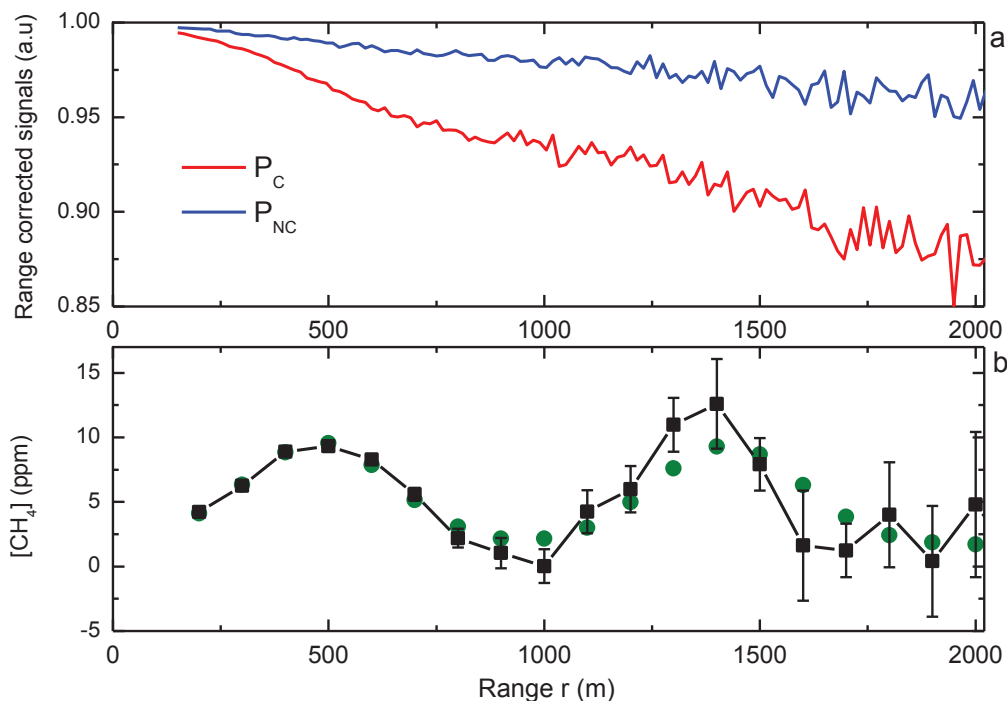


Fig. 4.11: Methane concentration input (green, 1.7 to 10 ppm) and retrieved (black) OCS-lidar methane mixing ratio (in ppm) as a function of range r (b) together with the corresponding range-corrected correlated OCS-lidar signal P_C (in red) and non-correlated OCS-lidar signal P_{NC} (in blue) as a function of range r (a).

Figure 4.12 is related to important methane mixing ratios, up to 400 ppm, measured with a 15 meters spatial resolution and measured in the second range. This configuration is ideal to localize high methane concentrations, representative of methane leakages.

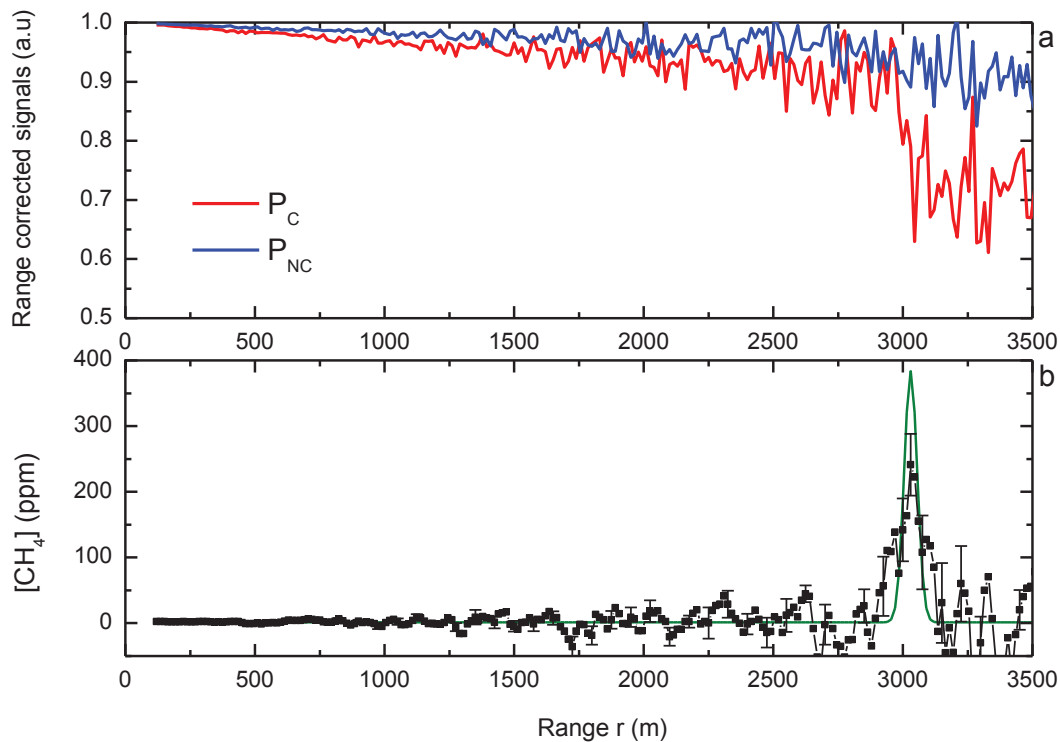


Fig. 4.12: Methane concentration input (green, 400 ppm peak at 3000 m) and retrieved (black) OCS-lidar methane mixing ratio (in ppm) as a function of range r (b) together with the corresponding range-corrected correlated OCS-lidar signal P_C (in red) and non-correlated OCS-lidar signal P_{NC} (in blue) as a function of range r (a).

Finally, a simulation for water vapor measurement is presented in Figure 4.13 for a typical relative humidity during winter. For an input water vapor mixing ratio of 6000 ppm (50 % relative humidity at 283 K, green squares), our OCS-lidar numerical simulation shows that the difference in extinction between the two OCS-lidar signals $P_C(r)$ and $P_{NC}(r)$ reaches 10 % for a 4000 meters lidar optical pathway (i.e at a 2000 meters range).

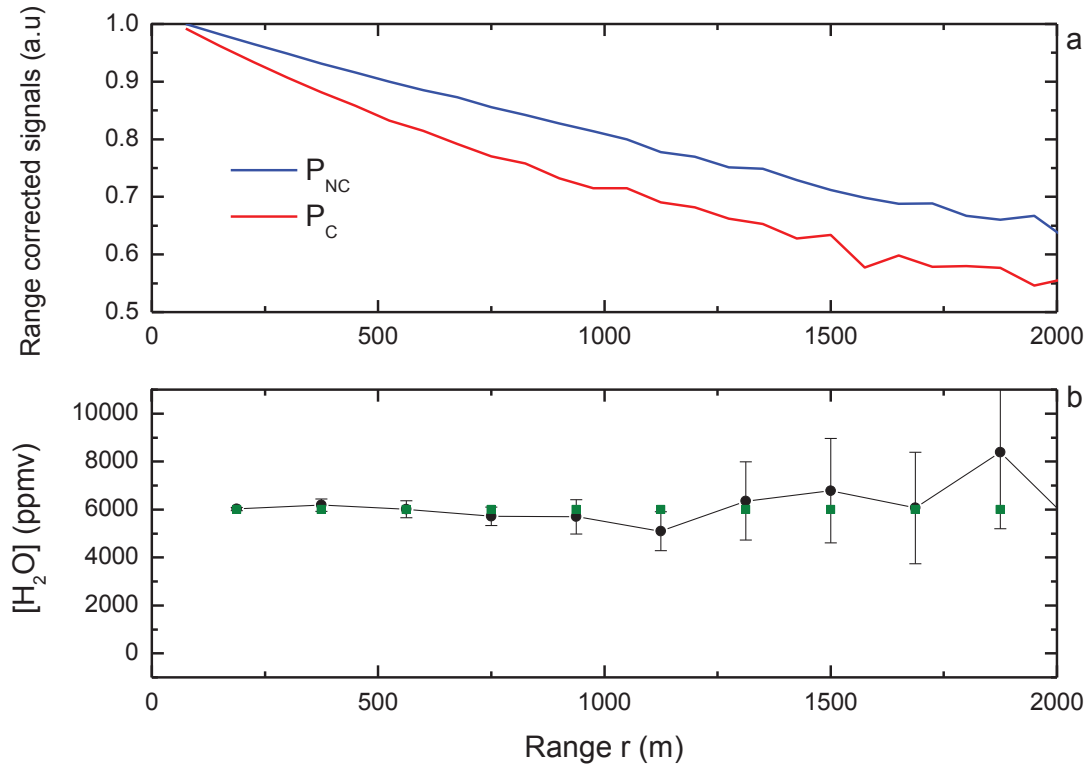


Fig. 4.13: Water vapor concentration input (green, 6000 ppm constant corresponding to RH = 50 % at 10 °C) and retrieved (black) OCS-lidar methane mixing ratio (in ppm) as a function of range r (b). The corresponding range-corrected correlated OCS-lidar signal P_C (in red) and non-correlated OCS-lidar signal P_{NC} (in blue) are plotted in graph (a) as a function of range r .

4.2 Statistical errors on the retrieved concentration

This section describes the different sources of statistical fluctuations that have been studied thanks to the OCS-lidar numerical model. We first introduce how the random noise is simulated in our numerical model. Then, the three main sources of statistical fluctuation, namely the laser fluctuation, the detector noise and the background light noise, are described. Finally, this section ends by proposing a methodology to experimentally evaluate the noise influencing the OCS-lidar signals.

4.2.1 Introduction

The influence of random noise has been estimated by applying a Monte-Carlo simulation algorithm. As mentioned in Section 4.1.4, the statistical fluctuation of the OCS-lidar signals is

simulated by a Gaussian statistical distribution. The optical power received on the detector surface, defined by the OCS-lidar equation (Equation (3.14)) is converted into a current through the responsivity R , expressed in A/W . A numerical value is generated by a random function following the Gaussian statistical distribution with standard deviation σ_N and is summed with the current generated by the backscattered photons (see Figure 4.9). For a given number of laser shots N_{LS} , the resulting OCS-lidar signal is the average of each signal. Within the electronic bandwidth of the detector, the different sources of noise are assumed to be independent. Since the random noise follows a Gaussian distribution, it is equivalent to average each signal with a statistical fluctuation of standard deviation equal to σ_N or to simulate a single signal with a statistical fluctuation of standard deviation equal to $\sigma_N / \sqrt{N_{LS}}$.

The evaluation of σ_N can be performed either by following a theoretical or an experimental approach. For the near infrared simulation, σ_N has been assessed by using a theoretical approach while σ_N in the visible spectral range has been assessed by using experimental data.

In the near infrared, the detector noise and background photons are assumed to follow a Gaussian statistical distribution associated with their standard deviation σ_D and σ_B respectively, as presented in Sections 4.2.3 and 4.2.4. Therefore, the root mean square σ_N is equal to the quadratic sum of each root mean square as expressed in the following equation:

$$\sigma_N^2 = \sigma_D^2 + \sigma_B^2 \quad (4.2)$$

The statistical error in the retrieved methane concentration due to the laser fluctuations is treated differently, since the statistical fluctuation of the laser does not simply add to the OCS-lidar signal, as it is the case for the detector noise and for the background light noise. Therefore, Section 4.2.2 presents how this source of statistical error has been evaluated by using the Monte-Carlo simulation.

Finally, the last Section 4.2.5, is dedicated to the evaluation of σ_N by using experimental data collected with the 715 nm lidar system. This methodology has been applied to the water vapor simulation.

4.2.2 Laser fluctuations

As detailed in Chapter 3, the OCS-lidar methodology is based on the spectral properties of the laser light. Hence, the laser power density fluctuations are of prime importance for accurate trace gas mixing ratio retrievals. Consequently, the influence of statistical fluctuation of $P_0(\lambda)$ has been studied through our numerical model in the infrared region. We hence assumed a Gaussian spectral profile for the laser source, defined by its central wavelength λ_0 , its spectral width σ_L , and its power \overline{P}_0 being the integration over λ of the spectral density $P_0(\lambda)$. For each of these terms, λ_0 , σ_L , \overline{P}_0 , statistical fluctuations have been simulated with a Gaussian distribution with standard deviation noted $\Delta\lambda_0$, $\Delta\sigma_L$, $\Delta\overline{P}_0$ respectively.

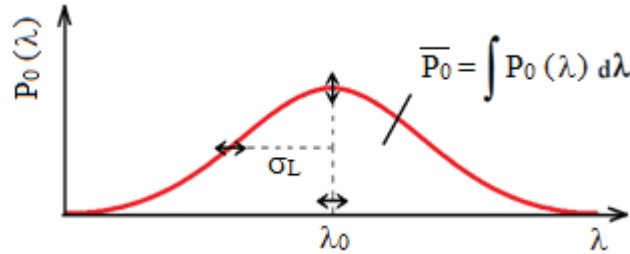


Fig. 4.14: Laser power spectral density of the simulated Gaussian laser pulse. Such a shape undergoes Gaussian fluctuations centered at a wavelength λ_0 , with a standard deviation σ_L and a total power \overline{P}_0 .

To illustrate this statistical variation from pulse-to-pulse, three pulsed light sources have been simulated with different $\Delta\lambda_0$, $\Delta\sigma_L$, $\Delta\overline{P}_0$ as sum-up in Table 4.3.

Set-up	λ_0 (nm)	$\Delta\lambda_0$ (nm)	σ_L (nm)	$\Delta\sigma_L$ (nm)	\overline{P}_0 (μJ)	$\Delta\overline{P}_0$ (μJ)
(1)	1665	0.1	10	0.1	250	12.5 (5 %)
(2)	1665	1	10	1	250	25 (10 %)
(3)	1665	2	10	2	250	50 (20 %)

Table 4.3: Characteristics of the different chosen broadened laser sources: fs laser source and two free running diode lasers.

For each set-up, numerical simulations have been performed for methane and the corresponding methane concentration has hence been retrieved. Figure 4.15 presents the

relative error on the retrieved methane concentration as a function of the input concentration for the three different setups.

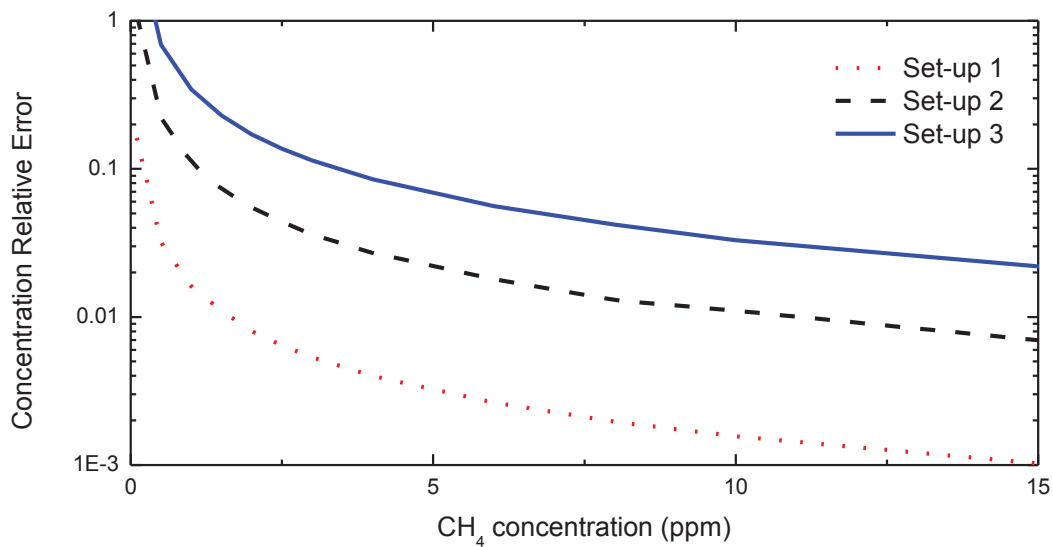


Fig. 4.15: Methane concentration relative error due to the pulsed broadband light source instability depending of the methane concentration for Table 4.3 light sources.

For concentration below 2 ppm, the light source stability induces a significant relative error on the retrieved concentration, broadband pulsed sources (2) and (3) reach 10 % or more. Set-up (1) leads to a relative error around 1 % for 1.7 ppm methane concentration (world average methane concentration). At higher methane mixing ratios, the relative error induced by the laser imperfect stability rapidly becomes negligible (< 1 %) for the three light sources (30 ppm for (3), 10 ppm for (2) and 1.5 ppm for (1)).

4.2.3 Photodetector noise

The detector noise is a random fluctuation of the electrical signal produced by several different effects [Howard 2002]. In the case of a photo-detector, we can mention the shot noise, the thermal noise (also called Johnson or Nyquist noise) and the dark current.

a) The shot noise

Shot noise exists because light is made of discrete photons, it does not depend on the quality of the detector and it is unavoidable. However, the shot noise becomes a real issue when the number of photons is sufficiently small so that uncertainties due to the Poisson distribution,

which describes the occurrence of independent random events, are not negligible. This assumption can be made when the optical intensity is low, which is the case when measuring the backscattered light of a μJ -laser pulse. The standard deviation of the shot noise is given by the square root of the average number of photons N , therefore the signal-to-noise ratio SNR can be expressed as follows:

$$SNR = \frac{N}{\sqrt{N}} = \sqrt{N} \quad (4.3)$$

Since the shot noise is a Poissonian process, the standard deviation of the current due to the shot noise σ_{SN} can be expressed as a function of the spectral bandwidth B_D of the detector, the output current I and the elementary charge e as follows [Howard, 2002]:

$$\sigma_{SN} = \sqrt{2 \cdot e \cdot I \cdot B_D} \quad (4.4)$$

b) The thermal noise

The thermal noise is also an electrical noise generated by the thermal agitation of the electrons inside the electrical conductor, which happens even when no voltage is applied. The standard deviation is equal to [Howard, 2002]:

$$\sigma_T = \sqrt{\frac{4 \cdot k_B \cdot T_D \cdot B_D}{R_D}} \quad (4.5)$$

where k_B is the Boltzmann's constant, R_D is the load resistance of the photodetector and T_D is the photodetector temperature.

c) The dark current

The dark current, also called the reverse bias leakage current, is the constant response exhibited by a detector due to the random generation of electrons and holes within the depletion region of the photodetector. As for the shot noise, it can be modeled by a Poissonian distribution. The resulting fluctuation can be characterized by its standard deviation σ_{DC} [Howard, 2002]:

$$\sigma_{DC} = \sqrt{2 \cdot e \cdot i_0 \cdot B_D} \quad (4.6)$$

where i_0 is the current defined by the photodetector type, typically for InGaAs detector, its value ranges from 1 to 20 nA.

From there, the standard deviation σ_D can be evaluated by the following equation:

$$\sigma_D^2 = \sigma_{SN}^2 + \sigma_T^2 + \sigma_{DC}^2 \quad (4.7)$$

However, the noise generated by the detector can also be evaluated using its noise equivalent power (NEP) expressed in $W \cdot Hz^{-1/2}$. It measures the sensitivity of a photodetector and is defined as the signal power that gives a signal to noise ratio of one in a one Hertz output bandwidth. The standard deviation of the detector output current is given by the following equation:

$$\sigma_D = NEP \cdot R \cdot \sqrt{B_D} \quad (4.8)$$

In the case of the InGaAs detector from Licel, the NEP given by the constructor is equal to $570 \text{ fW}/\text{Hz}^{-1/2}$. If we assumed a responsivity $R = 5 \text{ A}/\text{W}$ and a bandwidth $B_D = 10 \text{ MHz}$, the standard deviation on the output current due to the detector noise would be equal to $\sigma_D = 9 \text{ nA}$.

4.2.4 Sky and light background noise

As well-known in lidar research [Measures 1992, David et al. 2013a], other sources of photons, such as the Sun, the Earth, the Moon or any light sources near the lidar receptor may be scattered by atmospheric molecules and particles and measured by the light detector. Such photons form an unwanted background signal on the measured lidar signal.

As an example, Figure 4.16 shows the measurement of the background over 2 days measured with a 5 mrad field of view Newtonian telescope and an interferential filter centered at 355 nm and 532 nm having a 0.35 nm bandwidth.

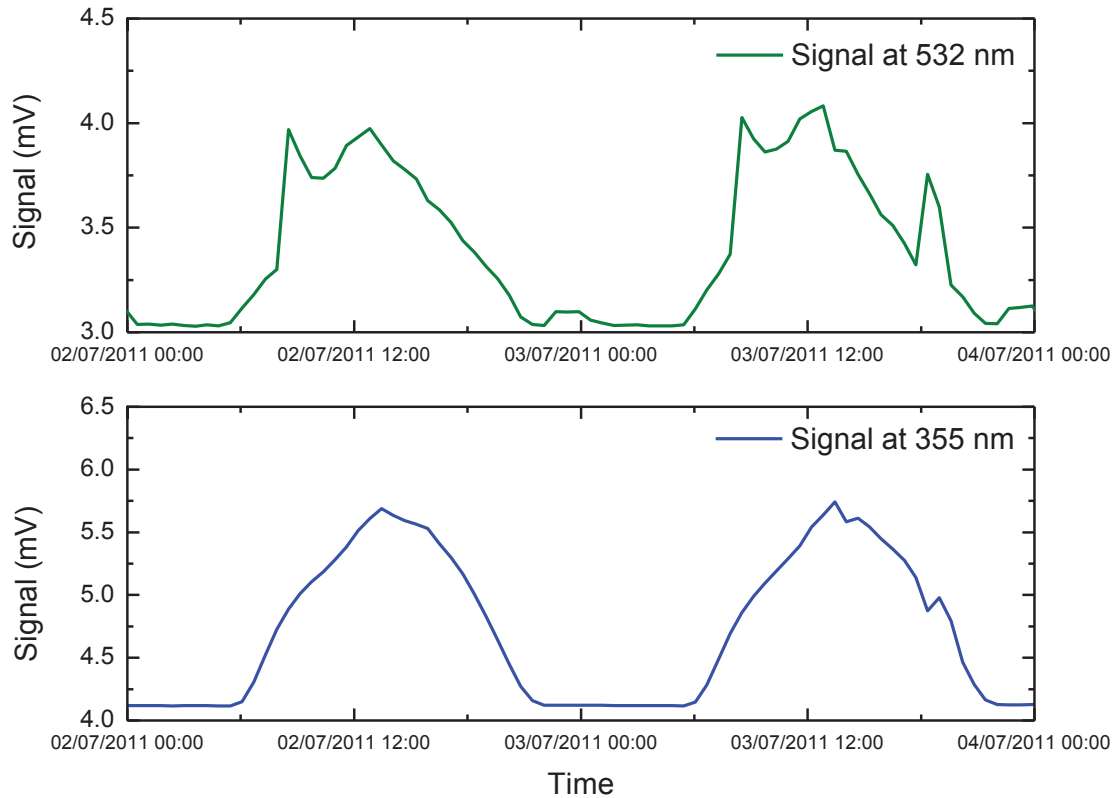


Fig. 4.16: Background measurement operated at 355 (blue) and 532 nm (green) during 2 days.

Lidar signals are sampled and averaged over less than one minute, the signal due to the background can be averaged and subtracted in order to only keep the signal due to the backscattered light from the laser source. However, the shot noise due to background photons generates random fluctuations that cannot be removed. As seen in Section 4.2.3, the standard deviation of the shot noise is equal to the square root of the number of photons, therefore in the case of the background light, the greater the average value of the background signals is, the stronger the statistical fluctuation will be.

In order to properly assess the shot noise due to the background, the software Libratran has been used. It is a collection of C and Fortran functions and programs for calculation of solar and thermal radiations in the Earth's atmosphere [Mayer et al. 2005]. In our case, we computed the received background radiation by using an urban aerosol model (mixture of water soluble and dust and soot-like particles [Settle et al. 1989]) and a mid-latitude summer season atmospheric model [Anderson et al. 1986].

When considering a 30 cm diameter telescope with a 3 mrad field of view over a 20 nm spectral bandwidth at 1.6 μm wavelength, the background optical power received by our

detector would be in the range of the micro watt. After a few calculations, the fluctuation in the detector current due to the shot noise of the background light is in the range of $\sigma_B = 10 \text{ nA}$ when considering the light at $1.6 \text{ }\mu\text{m}$ and a 40 MHz acquisition rate with a detector responsivity of 5 A/W .

4.2.5 Experimental evaluation of σ_N

The standard deviation of the noise σ_N used in our numerical simulation can also be assessed by using experimental data. In the visible range, the 715 nm -lidar system has been used to experimentally evaluate σ_N . Figure 4.17 presents data from the 715 nm -lidar system used for the measurement of water vapor.

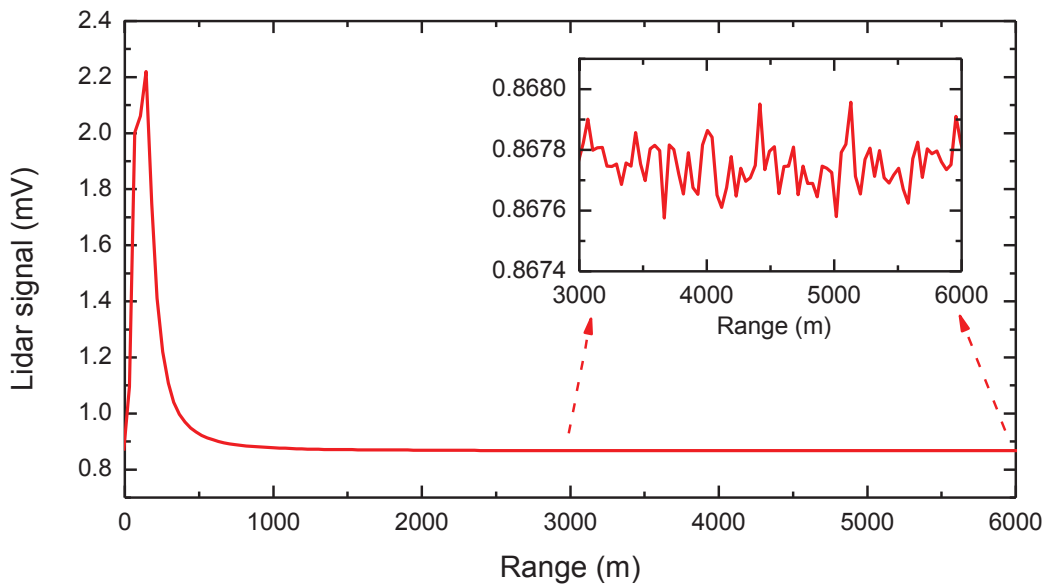


Fig. 4.17: Raw lidar signal measured with the VIS-lidar system with a zoom on the noise.

The noise measured at high altitude, above $3\,000$ meters, is used to compute the averaged background signal, written S_{Bckg} . Figure 4.18 shows the relative frequency count of the noise between $3\,000$ and $9\,000$ meters centered on S_{Bckg} . The noise statistical fluctuation follows a Gaussian distribution, the standard deviation σ_N can be assumed to be equal to the standard deviation of this Gaussian for a simulated lidar signal of similar amplitude. By using this methodology, the statistical fluctuations simulated in the numerical model are ensured to be realistic.

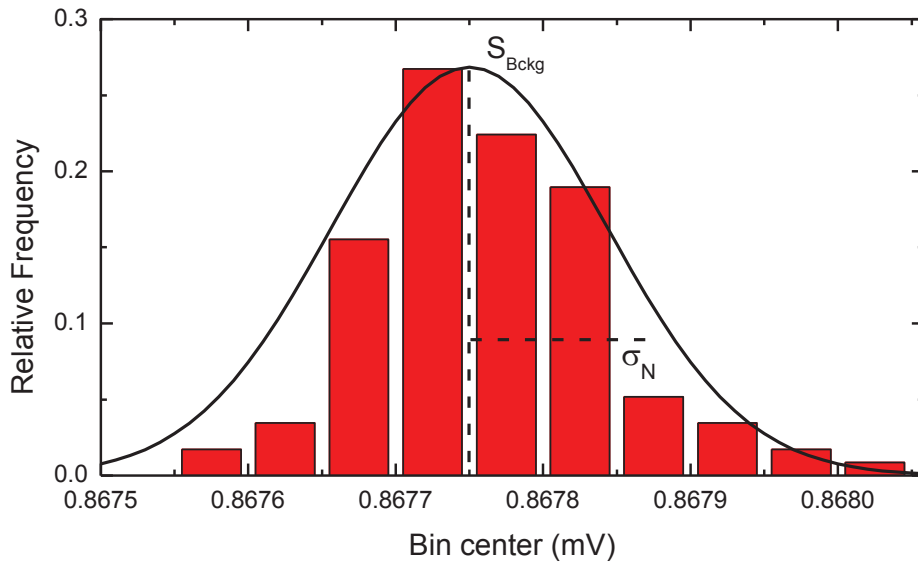


Fig. 4.18: Relative frequency count of the lidar signal statistical fluctuation centered on the average value of the background S_{Bckg} .

4.3 Systematic errors on the retrieved concentration

Main systematic errors originate from the concentration retrieval procedure (third-order approximation of the Beer-Lambert law), from the dependence of the gas absorption cross-sections with the range r , but also from the possible presence of interfering species and the contribution of aerosols and molecules to the retrieved mixing ratio. More precisely, this section presents the different sources of bias due to the OCS-lidar model, to the temperature and pressure variations, the spectral data uncertainties, the possible interfering species, and the aerosols and molecular contributions.

4.3.1 The OCS-lidar model bias

The third order approximation of the Beer-Lambert law used in Section 3.3.2 induces a systematic error on the retrieved methane mixing ratio. Mathematically, this systematic error originates from the assumption that O^4 is equal to zero in the A_0 coefficient when solving Equation (3.21). The approximation of the Beer-Lambert law works well (i.e. $O^4 \approx 0$) when the

optical extinction is low, however, for high target gas concentrations, or long optical paths, the optical depth reaches higher value and leads to a non-negligible bias (i.e. $O^4 > 0$).

To illustrate this bias, Figure 4.19 shows the induced systematic error, computed thanks to the numerical model in the near infrared region, as a function of the methane mean optical depth OD_{CH_4} . At a 15 % methane optical depth, the third order approximation of the Beer-Lambert law leads to a 20 % systematic error on the methane mixing ratio; methane mixing ratios are hence underestimated. Hence, if not corrected, this bias limits the use of the OCS-lidar methodology when the absorption of the studied gas is too high.

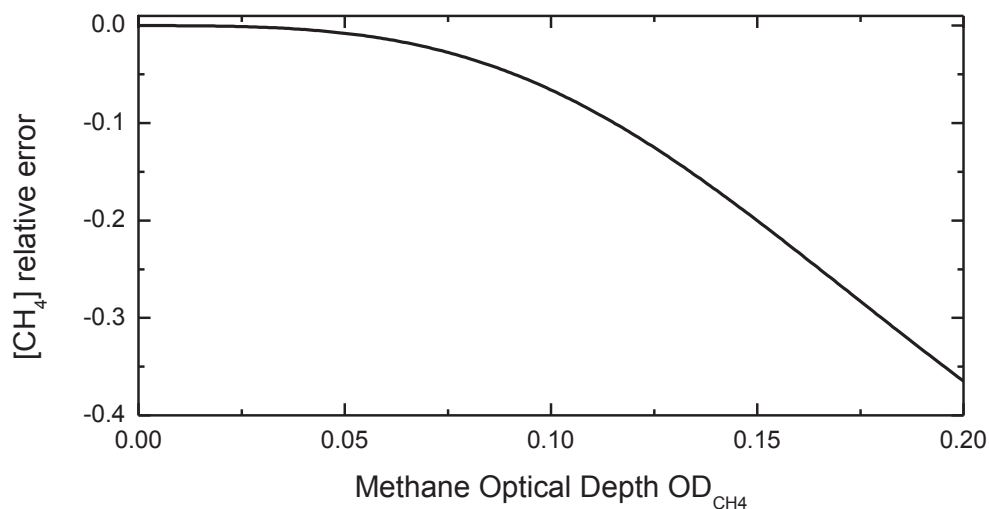


Fig. 4.19: Relative error on the methane mixing ratio as a function of the methane optical depth due to the third order approximation in the OCS-lidar model.

However, this bias can be greatly reduced by applying a correction on the retrieved cumulative concentration $CC(r)$. It is to note that the bias on the retrieved concentration is a function of the cumulative concentration $CC(r)$, i.e. whatever the concentration profile $C(r)$ is, the bias due to the model is the same for an equal value of $CC(r)$. As a result, it is possible to apply a correction to the retrieved $CC(r)$ before deriving for $C(r)$. In order to clarify this point, Figure 4.20a shows an example of two input methane concentration profiles, called input 1 and input 2, together with their retrieved profiles output 1 and output 2, obtained by applying the here developed OCS-lidar numerical simulation. As the two input profiles represent high methane concentrations, the retrieved profiles are significantly underestimated. The Figure 4.20b displays the corresponding cumulative concentration $CC(r)$.

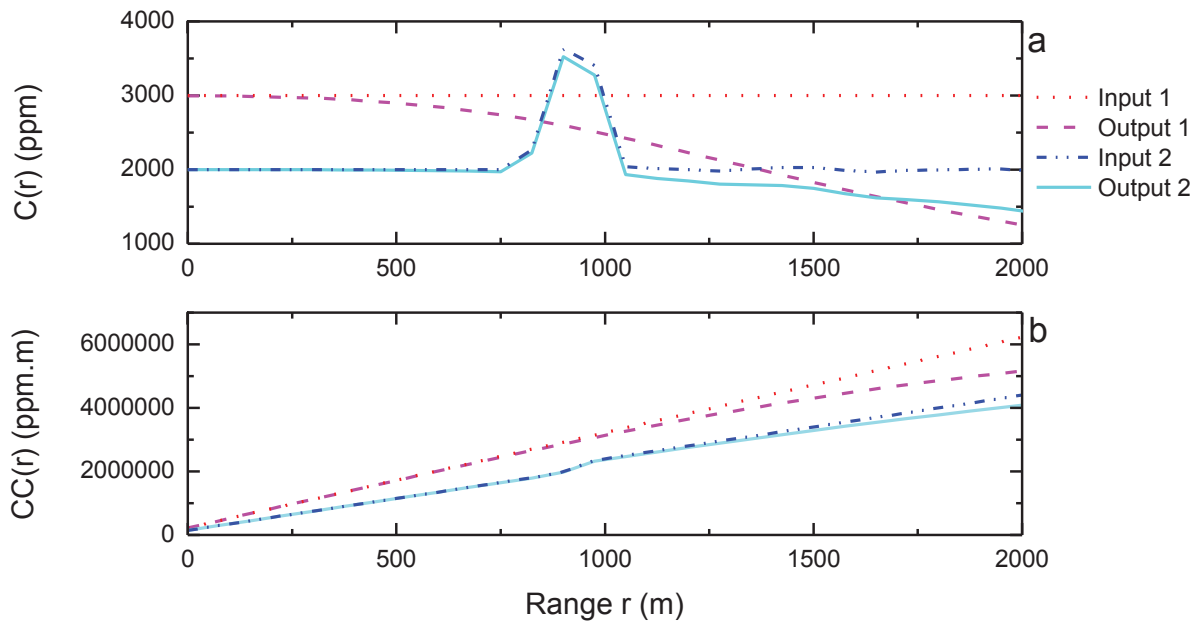


Fig. 4.20: Example of two input concentration profiles (graph a, red dots and blue double dots dash) together with their corresponding output profile retrieved by the algorithm (respectively magenta dashes and cyan full line). Graph b presents the cumulative profiles, i.e. the profile 1 and 2 integrated over the range, with the same color code. In both graphs, the retrieved outputs are underestimated due to the third order approximation of the Beer Lambert law.

Figure 4.21 shows the relative error CC_{input}/CC_{output} as a function of the CC_{output} . One can notice that the relative error is the same for both profiles. This function represents the correction to apply in order to reduce the bias due to the third order approximation.

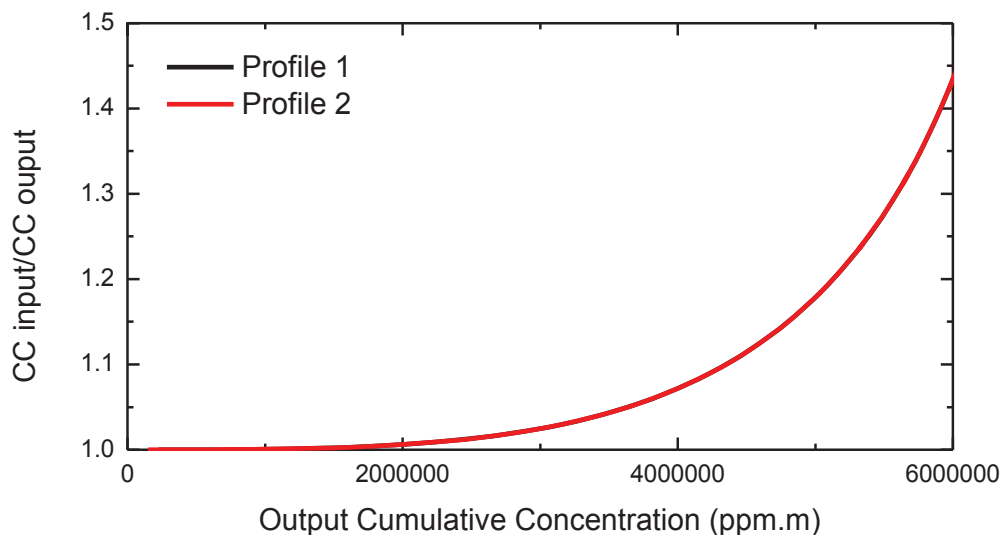


Fig. 4.21: Relative error CC_{input}/CC_{output} as a function of the CC_{output} . The relative error is function of the cumulative concentration $CC(r)$ but not of the concentration profile $C(r)$.

Once the correction is applied, the relative error on the methane concentration due to the model bias is lower than $5 \cdot 10^{-4}$. The residual error is due to numerical approximations performed by the computer, which creates arbitrary oscillations as shown on Figure 4.22.

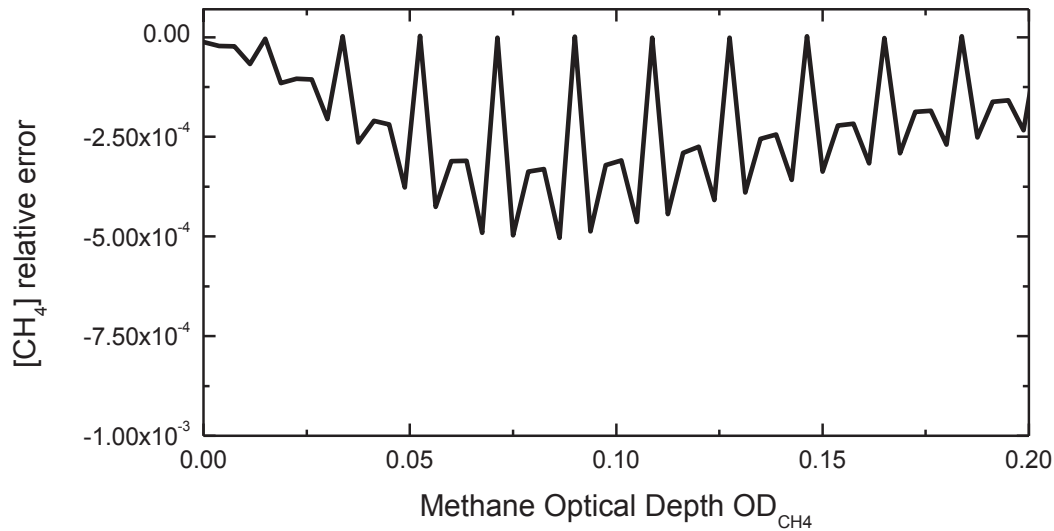


Fig. 4.22: Relative error on the methane mixing ratio as a function of the methane optical depth once the correction is applied.

When using the OCS-lidar algorithm using the transmission product (see Section 3.3.2), the bias due to the model does not need any correction, the systematic error on the retrieved concentration is lower than 10^{-6} . In this case, the approximation that O^4 is equal to zero in the A_0 coefficient is still made, but the optical path is limited by Δr . Therefore, even for high target gas concentrations, the optical depth hardly gets over 10^{-3} .

4.3.2 Temperature and pressure biases

As mentioned in Chapter 2, the atmospheric temperature T_{atm} and the atmospheric pressure P_{atm} will affect the precision on the retrieved concentration through the temperature and pressure dependence of the absorption cross-section. Remote sensing deals with strong environmental constraints in the Earth's atmosphere. As for example, methane diffuse emitters are subject to large temperature variations, from -40 up to $+50$ °C, as observed in gas pipelines in the Arctic region or in desert regions. For methane point source emitters, such

as open-air refinery burners or a power plant, the methane gas temperature can reach the kindling point (or auto-ignition point) of 537 °C. Systematic errors due to temperature and pressure variations are studied and estimated in this section.

Figure 4.23a shows an example of the methane absorption cross-section at temperature 230 and 500 K for a fixed 1 atm atmospheric pressure. One can observe in Figure 4.23a that each branch of the methane absorption cross-section has a specific behavior with temperature variations. Similarly, Figure 4.23b displays the methane absorption cross-section at pressure 0.1 and 1 atm at the fixed 290 K atmospheric temperature.

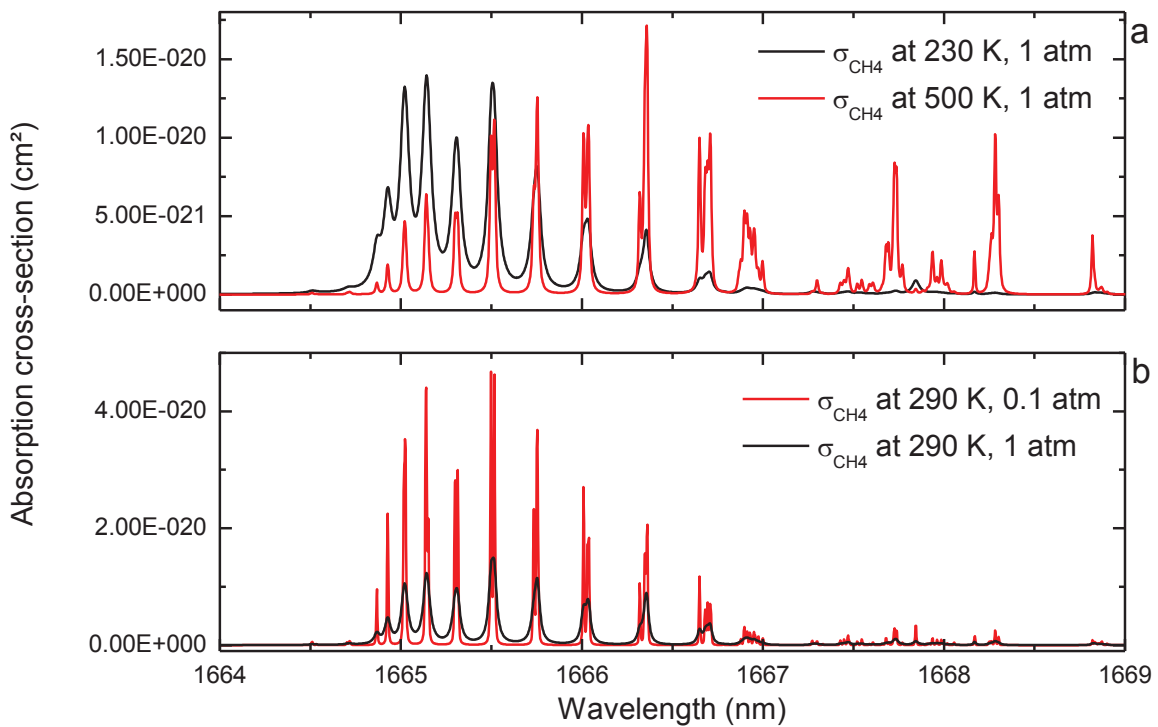


Fig. 4.23: Methane absorption cross-section σ_{CH_4} computed at temperature 230 and 500 K at 1 atm (graph a) and pressure 0.1 and 1 atm at 290 K (graph b).

OCS-lidar signals P_C and P_{NC} have been computed as a function of the atmospheric temperature T_{atm} and the atmospheric pressure P_{atm} , for methane measurements by using the Figure 4.4 amplitude modulation functions. The temperature and pressure ranges have been chosen to cover all possible values that can be reached in the troposphere as well as near ground level, under different climate conditions (arctic, desert, mountains). Our results are presented in Figure 4.24 in the form of a color map representing the OCS-lidar signals P_C and P_{NC} as a function of the atmospheric temperature T_{atm} and pressure P_{atm} . The observed P_C and P_{NC} variations with T_{atm} and P_{atm} originate from the methane absorption cross-section, which

appears in the transmission $T(r,\lambda)$ of the atmosphere. To highlight the P_C and P_{NC} dependence with T_{atm} and P_{atm} , relative variations of P_C and P_{NC} have been computed by following Equation (4.9) (written here for P_C) and are plotted in Figure 4.24, with respect to a reference OCS-lidar signal, simulated at the reference temperature T_{ref} and pressure P_{ref} .

$$\frac{\Delta P_C}{P_C} = \frac{|P_C(T_{atm}, P_{atm}) - P_C(T_{ref}, P_{ref})|}{P_C(T_{ref}, P_{ref})} \quad (4.9)$$

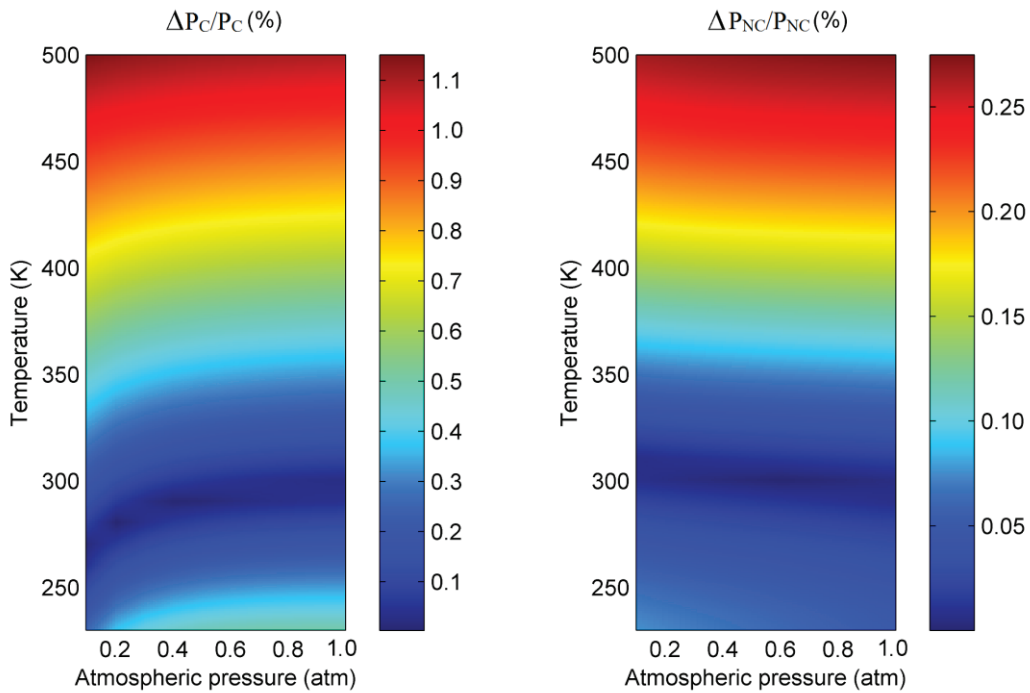


Fig. 4.24: OCS-lidar signals P_C and P_{NC} as a function of the atmospheric temperature T_{atm} and the atmospheric pressure P_{atm} , expressed in relative units with respect to the following reference temperature $T_{ref} = 296$ K and the reference pressure $P_{ref} = 1$ atm.

One striking feature of the OCS-lidar methodology is that strong atmospheric pressure variations along the laser beam propagation, from 0.2 up to 1 atm, induce less than 0.1 % relative variation in the OCS-lidar signals. However, the temperature variations more significantly affect the OCS-lidar signals: when it varies from 230 to 500 K, the signals P_C and P_{NC} respectively change by 1.15 % and 0.27 %. Such OCS-lidar variations must be considered as they induce a systematic error on the retrieved methane-mixing ratio, as shown in the next paragraph.

By solving Equation (3.21), the methane mixing ratio has been retrieved as a function of the atmospheric temperature T_{atm} and the atmospheric pressure P_{atm} . In Equation (3.22), the OCS-lidar signals P_C and P_{NC} appear in the A-coefficients of the third order polynomial equation. Hence, a change in the atmospheric temperature and pressure conditions induces a bias on the retrieved methane mixing ratio. Since pressure variations do not strongly affect the OCS-lidar signals (see Figure 4.24), only temperature changes are presented in the bias estimation. Figure 4.25 shows the systematic error on the retrieved methane mixing ratio as a function of the temperature difference $T_{\text{atm}} - T_{\text{ref}}$, for different T_{ref} values. As shown in Figure 4.25, the obtained curves are not symmetric with respect to the temperature difference, but the bias on the mixing ratio systematically increases when $|T_{\text{atm}} - T_{\text{ref}}|$ increases. For a -50 K temperature difference, the mixing ratio bias reaches 25 %. This behavior is not straightforward but can be explained if one considers that the OCS-lidar signals are obtained by integrating a spectral dependent function (see Section 2.3), corresponding mainly to the transmission $T(r, \lambda)$ of the atmosphere. Hence, OCS-lidar signals mainly depend on the absorption line strength, rather than on the spectral line broadening g_n which in turn limits the temperature and pressure dependence of the retrieved methane mixing ratio and favors the OCS-lidar methodology.

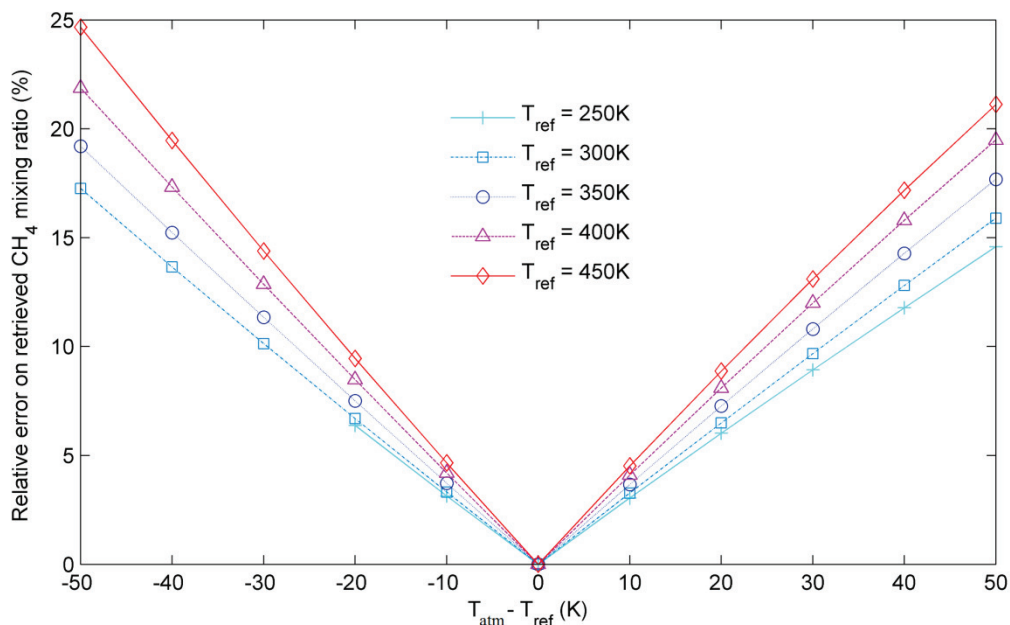


Fig. 4.25: Systematic error on the retrieved MMR as a function of the temperature difference $T_{\text{atm}} - T_{\text{ref}}$ for different T_{ref} values: 250 K (crosses), 300 K (squares), 350 K (circles), 400 K (triangles), 450 K (diamonds).

4.3.3 HITRAN uncertainty bias

The accuracy on the retrieved mixing ratio is also determined by the accuracy on the individual absorption line parameters, which are taken from the HITRAN spectroscopic database. As stated in Chapter 2, the accuracy on the line shape profiles $g_k(T_{atm}, P_{atm}, \nu - \nu_{k,0})$ does not significantly affect the retrieved mixing ratio since OCS-lidar signals are based on an integral performed over a broad spectral range. Hence, the accuracy on the retrieved mixing ratio depends on the absorption line strength S_k of each individual line k within the spectral interval, rather than on individual absorption line shape profiles. To evaluate the bias due to S_k -uncertainties, we used the absorption line strengths uncertainties proposed by C. Frankenberg [Frankenberg et al. 2008] in its supplementary material as a reference literature. In this paper, the line strength uncertainty corresponding to line k is given in the form of a $1 \sigma_k$ -error at the 296 K reference temperature. For each methane absorption line k , confidence bands, which correspond to $\pm 2\sigma_k$, have been used for an accurate evaluation of the line strength uncertainty. Then, to retrieve the mixing ratio uncertainty due to S_k -uncertainties, we considered the most pessimistic case, in which, the S_k -uncertainty of each absorption line k is either positive for all k -lines (and therefore equal to $+2\sigma_k$), or negative for all k -lines (equal to $-2\sigma_k$). In both cases, the numerical results were identical up to the fourth digit, and the relative error on the retrieved mixing ratio remained below half a percent. This is due to the high precision of the individual line strengths in the HITRAN database, which are known with better than 1 %-uncertainty.

4.3.4 Interfering species bias

For a more complete numerical model, we also included the possible role of interfering species. As detailed in Chapter 2, the HITRAN database [Rothman et al. 2009] is used to compute the absorption cross-section of the studied possible interfering trace gases. Figures 4.26 and 4.27 show the absorption cross-section of the traces gases available in the HITRAN database in the 1.6 μm wavelength range and in the 715 nm wavelength range. For each wavelength, the absorption cross-section of the interfering species is at least 10^3 times lower than the target gas absorption cross-section. However, in the near infrared spectral range,

water vapor may act as an interfering species since typical water vapor concentrations can be as high as 10^3 times that of methane concentration.

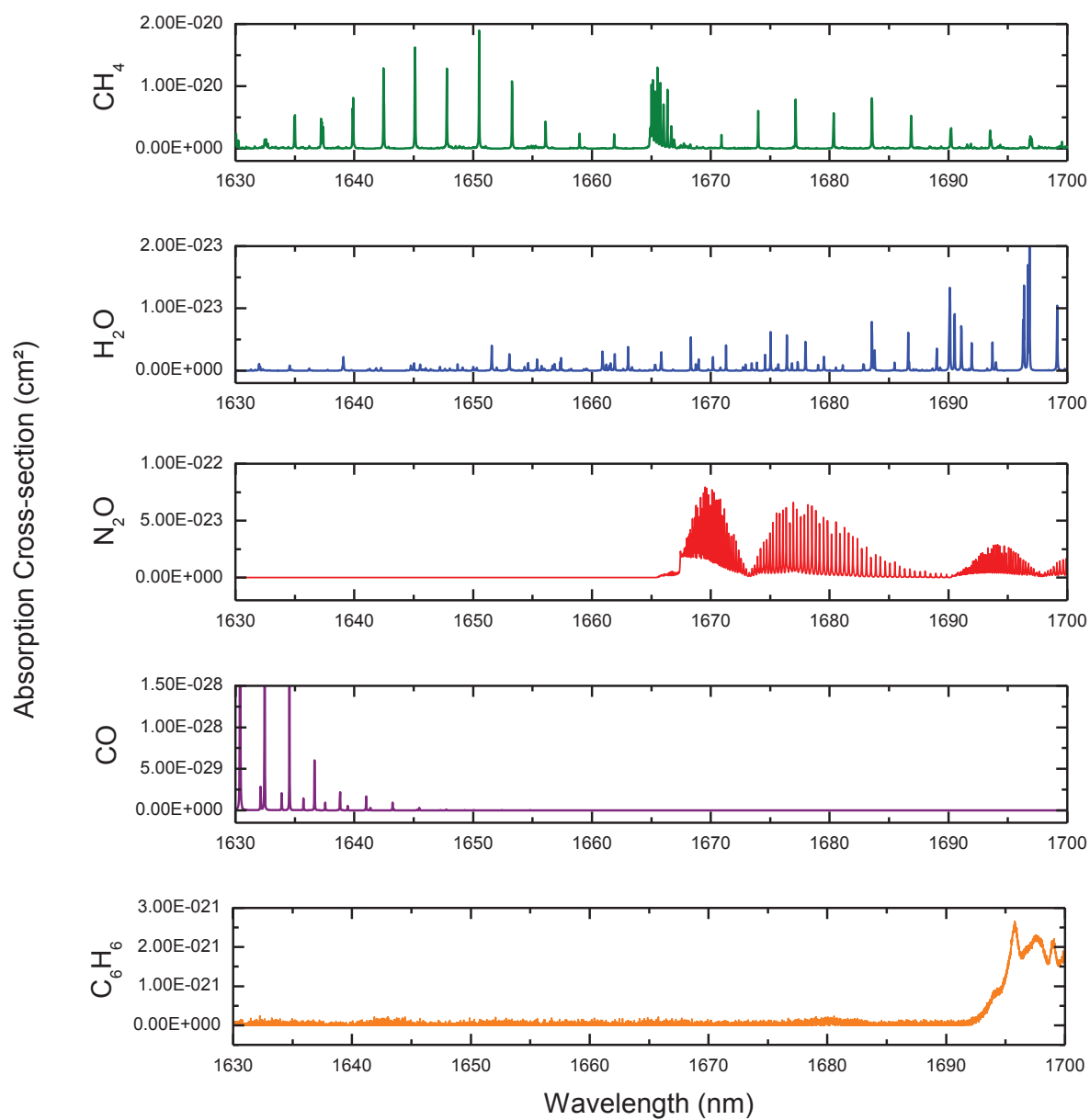


Fig. 4.26: Absorption cross-section computed from the HITRAN database in the near infrared wavelength region (1630-1700 nm).

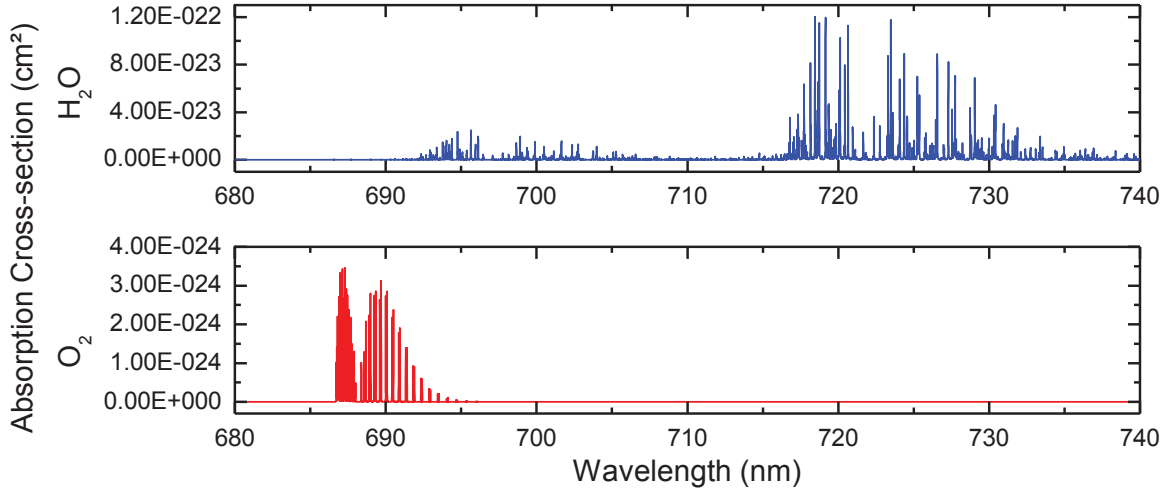


Fig. 4.27: Absorption cross-section computed from the HITRAN database in the visible region wavelength (680-740 nm).

Chemical species different from the target gas may contribute to the atmospheric transmission T , defined in Equation (3.16), due to their cross-section and their atmospheric concentration. Using the methane simulation, the bias due to the possible presence of interfering species in the infrared region has been evaluated. From the HITRAN database [Rothman et al. 2009], using a line-by-line simulation code, we computed absorption cross-sections for the following chemical species: H_2O , CO_2 , N_2O , CO , O_3 , NO , HO , HF , HCl , HBr , HI , C_2H_2 , C_6H_6 , CH_2O , and toluene. For methane OCS-lidar detection, we chose the methane spectral absorption band ($\lambda_0 = 1665.7 \pm 6.0$ nm) to minimize the contribution of such interfering species. In the selected spectral range, only water vapor has a non negligible optical extinction, in contrary to the above listed other chemical species, whose atmospheric extinction is at least 1000 times lower than that of methane for typical planetary boundary layer mixing ratios. Hence, the transmission $T_{og}(r, \lambda)$ from interfering species, introduced in Section 3.3.2, will be limited to the water vapor contribution, leading to:

$$T_{og}(r, \lambda) = \exp\left(-\sigma_{H_2O}(\lambda) \cdot \int_0^r C_{H_2O}(r') \cdot dr'\right) \quad (4.10)$$

In the considered spectral range, the water vapor absorption is in the same range than the methane absorption. As an example, Figure 4.28 shows methane and water vapor extinctions for respectively 1.7 ppm (background concentration) and 10 000 ppm (Relative humidity of 80 % at 293 K).

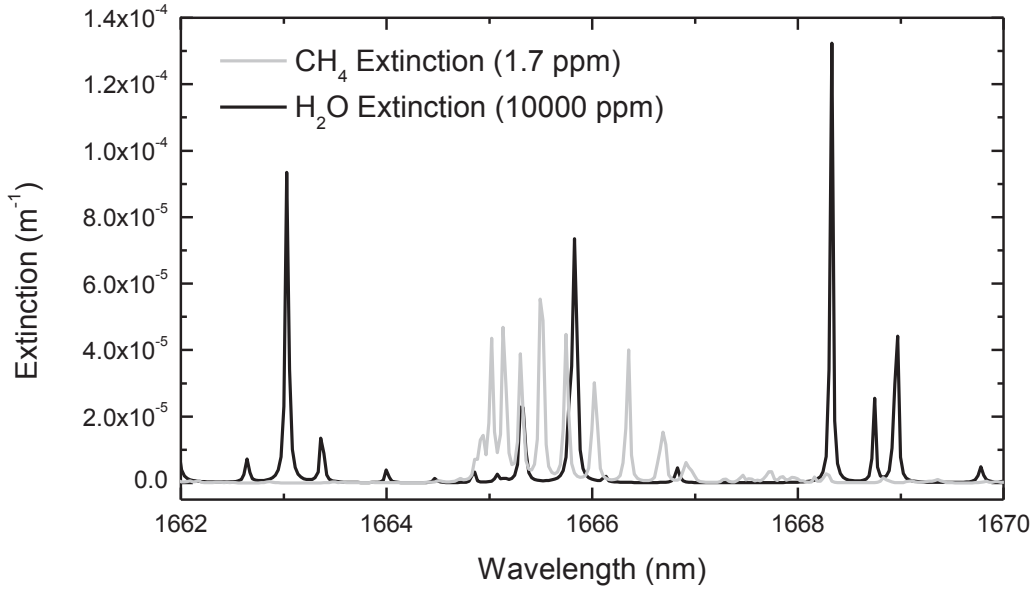


Fig. 4.28: Methane and water vapor extinction as a function of the wavelength computed for respectively 1.7 ppm (background concentration) and 10 000 ppm (relative humidity 80 % at 293 K).

To include this correction, $T_{og}(r,\lambda)$ is not assumed to be equal to 1 as in Section 3.3.2 and can be considered as a multiplicative term for the weighting A-coefficients introduced in the same section (Equation 3.22). These coefficients therefore become:

$$A_3(r) = \frac{4}{3} \int_{\Delta\lambda} P_0(\lambda) \cdot T_{mol}^2(r, \lambda) \cdot T_{og}^2(r, \lambda) \cdot \sigma_{TG}^3(\lambda) \cdot (P_{NC}(r) \cdot M_C(\lambda) - P_C(r) \cdot M_{NC}(\lambda)) \cdot d\lambda \quad (4.11a)$$

$$A_2(r) = -2 \int_{\Delta\lambda} P_0(\lambda) \cdot T_{mol}^2(r, \lambda) \cdot T_{og}^2(r, \lambda) \cdot \sigma_{TG}^2(\lambda) \cdot (P_{NC}(r) \cdot M_C(\lambda) - P_C(r) \cdot M_{NC}(\lambda)) \cdot d\lambda \quad (4.11b)$$

$$A_1(r) = 2 \int_{\Delta\lambda} P_0(\lambda) \cdot T_{mol}^2(r, \lambda) \cdot T_{og}^2(r, \lambda) \cdot \sigma_{TG}(\lambda) \cdot (P_{NC}(r) \cdot M_C(\lambda) - P_C(r) \cdot M_{NC}(\lambda)) \cdot d\lambda \quad (4.11c)$$

$$A_0(r) = -(1 + O^4) \cdot \int_{\Delta\lambda} P_0(\lambda) \cdot T_{mol}^2(r, \lambda) \cdot T_{og}^2(r, \lambda) \cdot (P_{NC}(r) \cdot M_C(\lambda) - P_C(r) \cdot M_{NC}(\lambda)) \cdot d\lambda \quad (4.11d)$$

Since the water vapor concentration profile $C_{H_2O}(r)$ along the optical path is unknown, the water vapor transmission can only be assessed by using either a reference water vapor profile or by directly using range-resolved water vapor measurements. As an example, $T_{og}(r,\lambda)$, used in the A-coefficients to retrieve the concentration, is computed for a 50 % constant relative humidity (RH) and for a 20 °C atmospheric temperature. On the other hand, OCS-lidar signals P_C and P_{NC} have been simulated using different RH values.

Figure 4.29 shows the corresponding relative error when RH-values are equal to 60, 70 and 90 %. For these three high RH-values, the presence of water vapor induces a positive bias in the retrieved methane mixing ratio, which appears to be negligible for methane mixing ratio above 10 ppm. At background methane mixing ratio (1 to 2 ppm), knowledge of the water vapor concentration profile is a necessity.

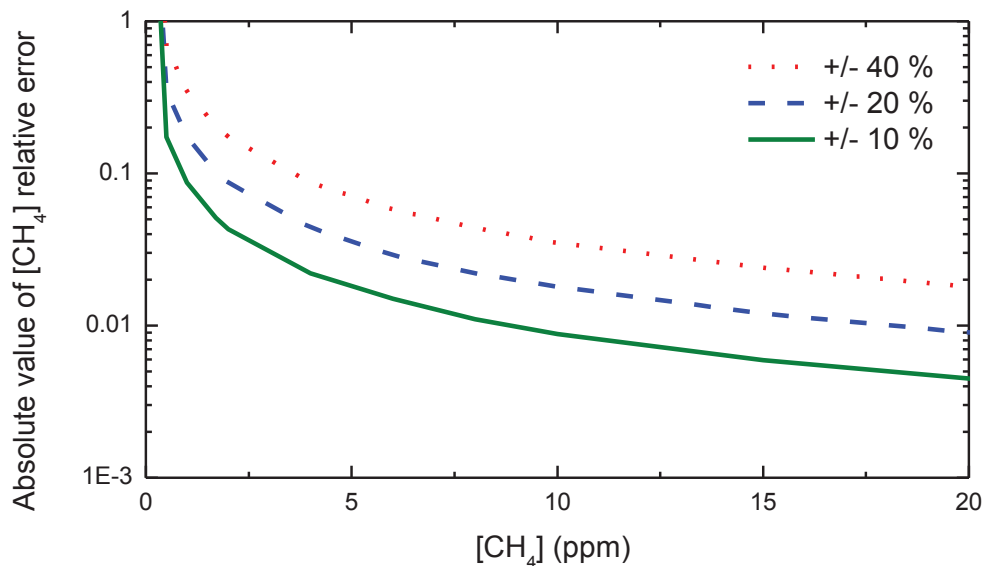


Fig. 4.29: Influence of water vapor on the methane mixing ratio retrieval. The systematic error on the methane mixing ratio is presented as a function of the methane mixing ratio at range 1 000 meters. The error is presented for RH \pm 10 % (green full line), RH \pm 20 % (blue dashed-line), and RH \pm 40 % (red dotted-line).

4.3.5 Aerosols and molecular contributions

Atmospheric molecular and aerosols scattering contributions to the methane mixing ratio evaluation have also been studied. In the near-IR spectral region, the atmospheric backscattering coefficient is mainly governed by the aerosol backscattering coefficient, which is typically 100 times higher than the molecular backscattering coefficient. In Section 3.3.2, we assumed the aerosol transmission $T_{\text{aer}}(r, \lambda)$ and backscattering coefficient $\beta(r, \lambda)$ to be wavelength independent over the considered spectral range. We explored the spectral dependency of the aerosol scattering coefficient by assuming a power law distribution for the wavelength dependency, using an Ångström coefficient [Sasano et al. 1989] equal to 1. In the selected spectral range ($\lambda_0 = 1665.7 \pm 6.0$ nm), the $T_{\text{aer}}(r, \lambda)$ relative variation is in the 10^{-4} range for an 10^{-4} m^{-1} aerosol extinction coefficient, integrated over a 2 kilometers range. A similar conclusion can be drawn for the aerosol backscattering coefficient, by assuming the

same power law wavelength dependency. Varying the Ångström coefficient from 0.5 to 2 does not change these conclusions. Figure 4.30 represents the corresponding relative error on the methane mixing ratio as a function of the methane optical depth, for aerosol transmission (top panel) and aerosol backscattering (bottom panel). The bias is low, below $6 \cdot 10^{-3}$, even at low methane optical depth.

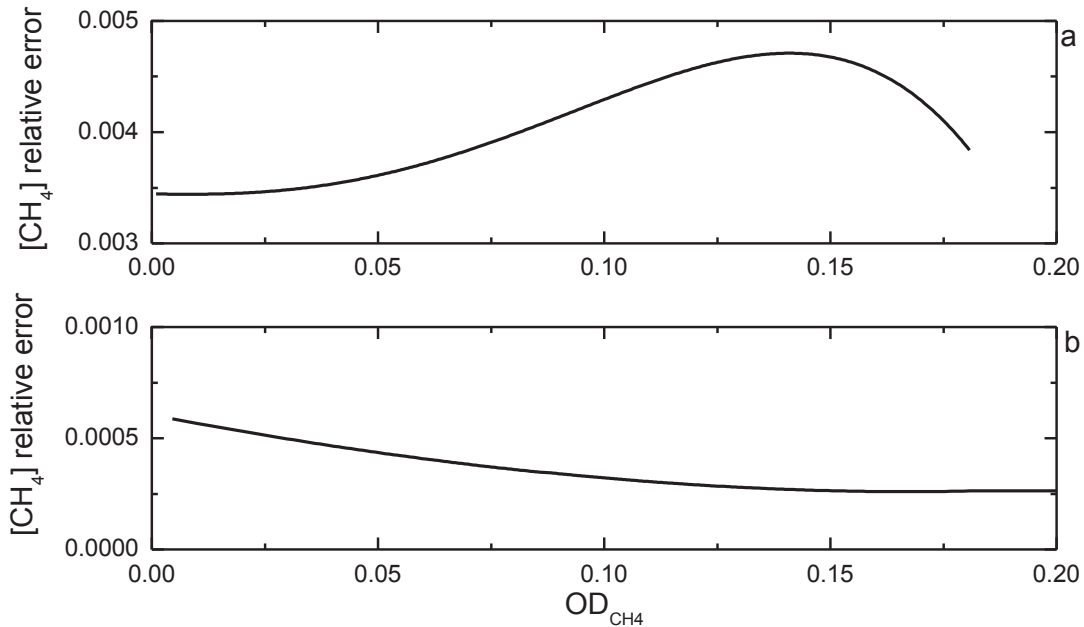


Fig. 4.30: Relative error on the methane mixing ratio due to the assumption that the aerosol transmission $T_{\text{aer}}(r, \lambda)$ (graph a) and the backscattering coefficient $\beta(r, \lambda)$ (graph b) are wavelength independent as a function of the methane optical depth.

To summarize the evaluation of the statistical and the systematic errors affecting the gas concentration measurement, Table 4.4 presents the error budget for a simulated methane concentration retrieval of 10 ppm at a 1000 meters range. As explained above, this error budget may change depending on the range, on the target gas concentration, on the NEP of the photodetector, on the time of the day (day or night), but also on the laser source spectral stability, and on the temperature shift and the presence of interfering species.

The main uncertainties on the retrieved concentration come from:

- the detection noise that can be improved by increasing the OCS-lidar signal SNR.
- the possible presence of interfering species, that can be limited by evaluating the concentration of such species and using appropriate modulation functions.
- the atmospheric temperature variations, that can be reduced by estimating the temperature profile.

Source of error	Uncertainty (%)
Statistical error (see Section 4.2)	13.2
Pulse-to-pulse power and spectral fluctuations	0.2
Detector noise and background light noise	13
Systematic errors (see Section 4.3)	6.3
Model bias	5×10^{-2}
Temperature bias (± 10 K)	3.4
Water vapor bias (± 20 %)	2.0
Spectral data uncertainties	0.5
Aerosol transmission wavelength independency	0.34
Aerosol backscattering wavelength independency	5×10^{-2}
Error on methane gas concentration	< 20 %

Table 4.4: OCS lidar error budget for simulated methane concentration retrieval of 10 ppm at a remote distance of 1000 meters with a 100 meters spatial resolution. The statistical error includes pulse-to-pulse fluctuations following specification of OPA fs-laser source. The detector noise results from a 10 minutes signal average time measurement during daylight. Systematic error includes the model bias, the HITRAN uncertainties, and temperature and water vapor biases from reference values of 285 K and RH=50 %.

4.4 Optimization of the OCS-lidar parameters

To improve the precision on the target gas retrieved concentration, the laser power density $P_0(\lambda)$ and the amplitude modulation functions $M_C(\lambda)$ and $M_{NC}(\lambda)$ have to be properly adjusted when using the OCS-lidar numerical model.

The central wavelength λ_0 of $P_0(\lambda)$ as well as the $M_C(\lambda)$ and $M_{NC}(\lambda)$ functions are set to maximize the difference in optical transmission due to the presence of the target gas between the two OCS-lidar signals, all while optimizing the signal-to-noise ratio for both signals. In order to do so, we use the numerical model to test and find the best parameters for each instrument. In this section, we first present how the amplitude modulation functions are set, and then how the laser central wavelength is determined.

4.4.1 Optimization of the amplitude modulation functions

As explained in Section 4.2, the statistical fluctuations generated by the detector, as well as the light background and the laser fluctuations, induce statistical fluctuation on the retrieved target gas concentration. However, these statistical fluctuations can be minimized by properly choosing the amplitude modulation functions $M_C(\lambda)$ and $M_{NC}(\lambda)$. On the contrary, when the amplitude modulation functions are not appropriately chosen, the statistical fluctuations on the retrieved concentration can be extremely high despite the fluctuation on the OCS-lidar signals remains very low. To illustrate this point, one can imagine what would happen if $M_C(\lambda) = M_{NC}(\lambda)$: since the correlated and non-correlated laser pulses would then have the same spectral components, they would both undergo the same light extinction when propagating through the atmosphere. Therefore, the two OCS-lidar signals P_C and P_{NC} measured by the detector would be equal, within their statistical fluctuations, and this independently of the presence of the target gas. The retrieved concentration would therefore be centered on 0 and would highly fluctuate due to the OCS-lidar signal noise. As soon as the amplitude modulation functions are chosen so that the two OCS-lidar signals are different, the concentration of the target gas can be retrieved. There, the greater the difference of extinction undergone by the two OCS-lidar signals is, the lower the statistical error on the retrieved concentration will be.

To optimize the two functions $M_C(\lambda)$ and $M_{NC}(\lambda)$, we use the normalized weighted transmission $T_{H_2O}(r, \lambda_M)$, defined in Equation (4.12), where λ_M is the central wavelength of a Gaussian amplitude modulation function $M(\lambda_M, \lambda)$:

$$T_{H_2O}(r, \lambda_M) = \frac{\int_{\Delta\lambda} P_0(\lambda) \cdot M(\lambda_M, \lambda) \cdot T(r, \lambda) \cdot d\lambda}{\int_{\Delta\lambda} P_0(\lambda) \cdot M(\lambda_M, \lambda) \cdot d\lambda} \quad (4.12)$$

Here $\Delta\lambda$ is the considered spectral region. The amplitude modulation function $M(\lambda_M, \lambda)$ is a function that is shifted along the wavelength axis through its λ_M -parameter, as illustrated in Figure 4.31. For each λ_M -value, the corresponding T_{H_2O} is calculated for a 1000 meters pathway.

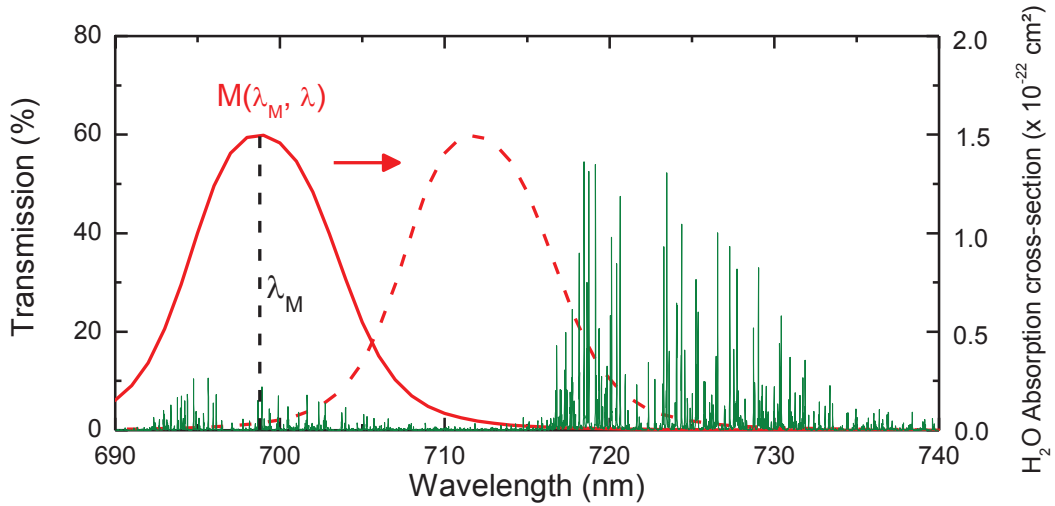


Fig. 4.31: Water vapor absorption cross-section (green) together with the amplitude modulation function $M(\lambda_M, \lambda)$ (red) which is shifted along the wavelength axis. For each value of λ_M , the corresponding value of T_{H_2O} is computed.

As an example of this optimization procedure, Figure 4.32 shows $T_{H_2O}(r, \lambda_M)$ resulting on a 4 000 meters optical pathway for a water vapor mixing ratio of 8 000 ppm as a function of λ_M . Since $T_{H_2O}(\lambda_M)$ depends on the water vapor absorption cross-section, over a given spectral width, the minimum value of $T_{H_2O}(\lambda_M)$ defines the optimized $M_C(\lambda)$ modulation function. Similarly, the local maximum defines the optimized $M_{NC}(\lambda)$ modulation function. Using similar procedures, we optimized the spectral width of $M_C(\lambda)$ and $M_{NC}(\lambda)$ functions.

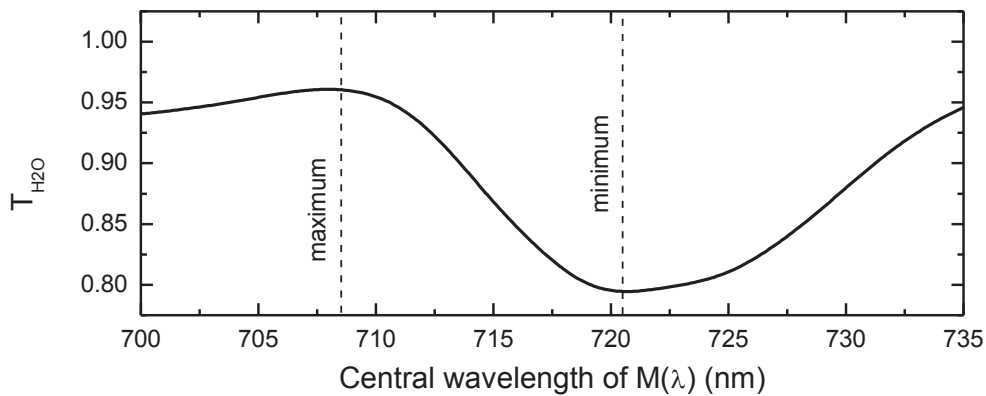


Fig. 4.32: Calculated normalized weighted water vapor transmission T_{H_2O} as a function of the central wavelength λ_M of the amplitude modulation function $M(\lambda_M, \lambda)$ and for a of 4000 meters optical pathway. As $M(\lambda_M, \lambda)$ is shifted towards higher wavelengths, $T_{H_2O}(\lambda_M)$ reaches a minimum because of higher values of the H_2O absorption cross-section in the 720 nm spectral region.

As a conclusion, both the central wavelength and the width of the amplitude modulations functions are hence determined.

4.4.2 Optimization of the laser source

In order to optimize the signal to noise ratio of the OCS-lidar signals, the central wavelength λ_0 of the laser power spectral density $P_0(\lambda, \lambda_0)$ has been adjusted. The light transmitted by the amplitude modulator depends on λ_0 , and for an amplitude modulation $M(\lambda_M, \lambda)$, the transmitted light would be maximum when $\lambda_M = \lambda_0$. However, the OCS-lidar methodology requires two amplitude modulation functions, the correlated one, and the non-correlated one. Therefore the laser central wavelength has to be chosen so that both OCS-lidar signals P_C and P_{NC} have an optimized signal to noise ratio. Figure 4.33 presents the transmitted laser light as a function of λ_0 through the two amplitude modulation functions M_C and M_{NC} as well as the sum of both T_{Total} as defined in the following equations:

$$T_C(\lambda_0) = \frac{\int_0^\infty P_0(\lambda, \lambda_0) \cdot M_C(\lambda) \cdot d\lambda}{\int_0^\infty P_0(\lambda, \lambda_0) \cdot d\lambda} \quad (4.13a)$$

$$T_{NC}(\lambda_0) = \frac{\int_0^\infty P_0(\lambda, \lambda_0) \cdot M_{NC}(\lambda) \cdot d\lambda}{\int_0^\infty P_0(\lambda, \lambda_0) \cdot d\lambda} \quad (4.13b)$$

$$T_{Total}(\lambda_0) = T_C(\lambda_0) + T_{NC}(\lambda_0) \quad (4.13c)$$

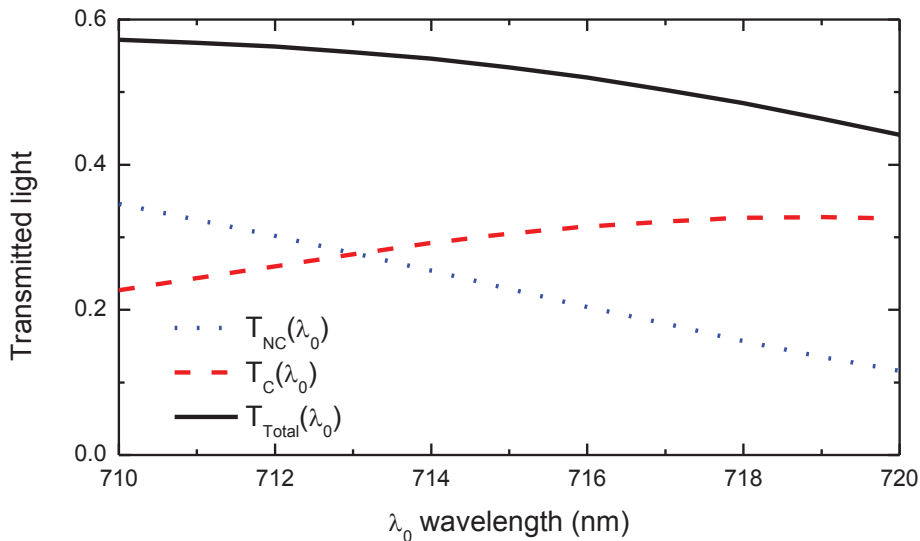


Fig. 4.33: Transmitted laser light through the amplitude modulator for M_C (red) and M_{NC} (blue) and the sum of both (black) as a function of the central wavelength λ_0 of the laser power spectral density $P_0(\lambda, \lambda_0)$.

The maximum total transmission T_{Total} reaches 60 % which is the amplitude modulator maximum transmission. T_C and T_{NC} reach a similar value, 29 %, for a central wavelength $\lambda_0 = 713$ nm. However, the correlated signal P_C undergoes a higher extinction due to the water vapor, which can be in the range of 10 % higher than for P_{NC} depending on the range and on the water vapor concentration. Therefore the central wavelength λ_0 is slightly shifted at 714 nm so that T_C is 10 % higher than T_{NC} , in this configuration, both OCS-lidar signals P_C and P_{NC} are expected to have similar signal-to-noise ratios.

In this chapter, the OCS-lidar numerical model has been presented. The purpose of this numerical model was to study the feasibility of the OCS-lidar methodology by evaluating the different sources of statistical and systematic errors, a key point for the forthcoming experiments detailed in Chapter 5.

Into more details, this chapter presented the numerical model, describing how the atmosphere, the laser source, the amplitude modulation and the detection system have been modeled. As case studies, simulations for methane and water vapor have been presented, showing that the OCS-lidar methodology can retrieve methane and water concentration profiles using a micro pulse laser (≈ 50 $\mu\text{J}/\text{pulse}$). In the case of methane, the numerical model shows that background mixing ratios may be measured up to 1 kilometer range with less than 20 % accuracy. Higher mixing ratio profiles can also be retrieved such as that of a methane leakage (hundred of ppm) at a 3 kilometer range with a 15 meters range resolution with time measurement in the second range. Our numerical model also shows that water vapor mixing ratio profiles can be retrieved in the PBL in the visible, and the following Chapter 5 presents the actual measurements for water vapor mixing ratio profiles.

Then, the sources of error related to the OCS-lidar methodology are presented. The statistical errors due to the laser fluctuations, the detector noise and the background light noise are described and evaluated. In addition, the bias on the retrieved concentration due to systematic errors is also studied. Such errors mostly originate from the OCS-lidar model, the temperature and pressure variations, the possible presence of interfering species, the uncertainties on the HITRAN spectral parameters and the aerosols and molecular contributions.

Finally, the OCS-lidar numerical model is used to improve the performances of the OCS-lidar methodology by optimizing the laser source central wavelength and the amplitude modulation

functions. In particular, the laser central wavelength and the amplitude modulation functions are set to minimize the relative error on the retrieved concentration. Such settings are then used in the OCS-lidar experiment, to be described in the following chapter.

Chapter 5

Experimental Set-ups and first OCS-lidar measurement

This chapter is dedicated to the OCS-lidar experiment, the presentation and the specification of its optical components. This experimental achievement is the first experimental proof of the Optical Correlation Spectroscopy lidar. The experiment described in this section has been entirely designed, developed and implemented in the framework of this thesis.

As a first step, the femtosecond laser source and the optical parametric amplifier used in this experiment are described together with their specifications. Then, two different experimental configurations, corresponding to two different experimental set-ups are proposed to achieve the amplitude modulation, related to the optical correlation spectroscopy. The amplitude modulation is operated either at the emission with an active amplitude modulator before the backscattering process, or with passive optical filters directly on the backscattered laser light. The optoelectronic detection system used to collect the backscattered photons and record the corresponding electrical signal is also described.

In both configurations, range-resolved gas concentration measurements, achieved with a 50 μJ ground-based OCS-lidar, are presented, followed by an extended discussion presenting the retrieved mixing ratio and the corresponding accuracy. This work has been recently published [Thomas et al., 2013].

5.1 The laser source

The use of a laser source to perform atom or molecular spectroscopy has considerably increased the knowledge on molecular spectroscopy constants, dynamics and also on the physical chemistry related to the molecules [Kaiser 1988, Bandrauk 2002]. Laser spectroscopy demands strong requirements on the light source. As an example, light absorption spectroscopy, which is based on the Beer Lambert's law, requires high intensity stability to reach low signal to noise ratio concentration measurements. When a high spectral resolution is needed, the spectral stability and purity also represents a strong requirement. Moreover, lasers having a short pulse duration greatly contributed to time-resolved spectroscopy [Kaiser 1988].

In this work, laser pulses, propagating in the atmosphere, are used to perform range, or time, resolved measurements using the well-known lidar arrangement. Because correlation spectroscopy is achieved, as detailed in Section 3.3, a spectrally broadband laser with a high stability in terms of intensity and spectrum is required. In this context, different light sources may be considered, such as pulsed diode lasers, pulsed optical parametric oscillators, fiber lasers, dye lasers or femtosecond laser sources. We believe that all these sources could be used with the OCS-lidar methodology, leading to different signal to noise ratios, retrieved concentration accuracy, maximum range, measurement duration and detection limit.

Because this PhD work is pioneer in this field, we choose an optical parametric amplifier (OPA) pumped with a femtosecond Ti-Sapphire laser. This laser source offers numerous advantages. First, its central wavelength is tunable via the OPA and covers a large spectral range allowing the study of different gases with a unique laser source. Secondly, the output intensity developed by this source is high enough to perform lidar measurements, in the range of several micro-joules. Moreover, the laser spectrum is significantly broader than the minimum spectral resolution of the amplitude modulator used in this experiment, so that the correlation spectroscopy can be achieved. Finally, the laser source stability, in terms of intensity and spectrum, is sufficient to perform trace gas concentration measurements, as those simulated in the previous chapter.

5.1.1 The broadband laser source

The laser source used in this experiment is based on a femtosecond titanium-doped sapphire laser. It is a solid-state laser capable of operating from 690 to 1080 nanometers which is crucial for the femtosecond laser pulse source generation, relatively to the necessity of a wide gain bandwidth. The broadband emission is amplified by using the chirped pulse amplification technique (CPA) [Cook 1960]. When using short laser pulses, in the range of hundred femtoseconds, the instantaneous intensity received by the gain medium reaches several gigawatts per square centimeters causing serious damage to the laser's components through non-linear processes such as self-focusing [Melnichuk 2010]. In order to limit these effects, the ultrashort laser pulses can be stretched in time so that the instantaneous intensity becomes sufficiently low compared with the initial intensity, avoiding possible damage. The CPA principle is depicted in Figure 5.1.

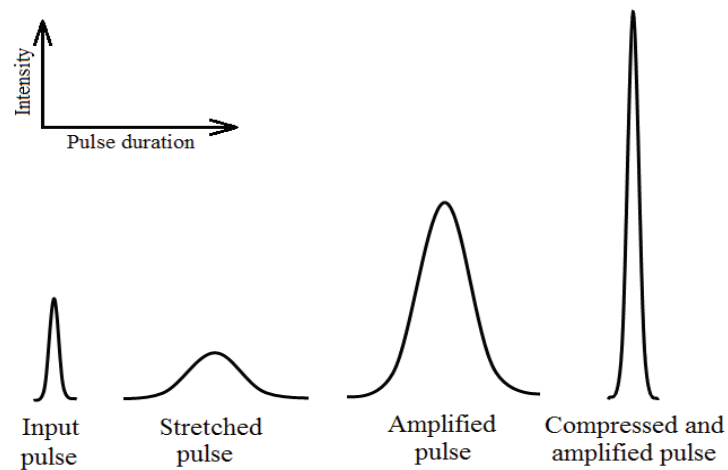


Fig. 5.1: Principle of the chirped pulse amplification. The initial pulse, having a pulse duration in the femtosecond range, is stretched so the pulse duration reaches a few picoseconds. Then the pulse is amplified, from micro-joule to milli-joule, before being compressed with a pulse duration back to the femtosecond range.

Table 5.1 presents the laser specifications.

Output characteristics	
Average power	4 W *
Repetition rate	1 kHz *
Energy per pulse	4 mJ *
Energy stability	1 % *
Pulse duration (FWHM)	80-130 fs
Instantaneous power	≈ 40 GW
Spectral specifications	
Central wavelength λ_0	788 nm *
Spectral width (FWHM)	22 nm *
Beam properties	
Laser beam divergence	0.1 mrad *
Beam diameter (FWHM)	7 mm *
Spatial mode	$M^2 < 1.3$ (TEM ₀₀)
Pointing Stability	< 30 μ rad

Table 5.1: Specifications of the Integra HE from Quantronix. The asterisk indicates when the value has been measured in the laboratory, other values are specified by the constructor.

The laser spectrum is presented in Figure 5.2 together with the power as a function of time, as a result of a measurement performed with a monochromator and a Hamamatsu photomultiplier tube R7400-U20.

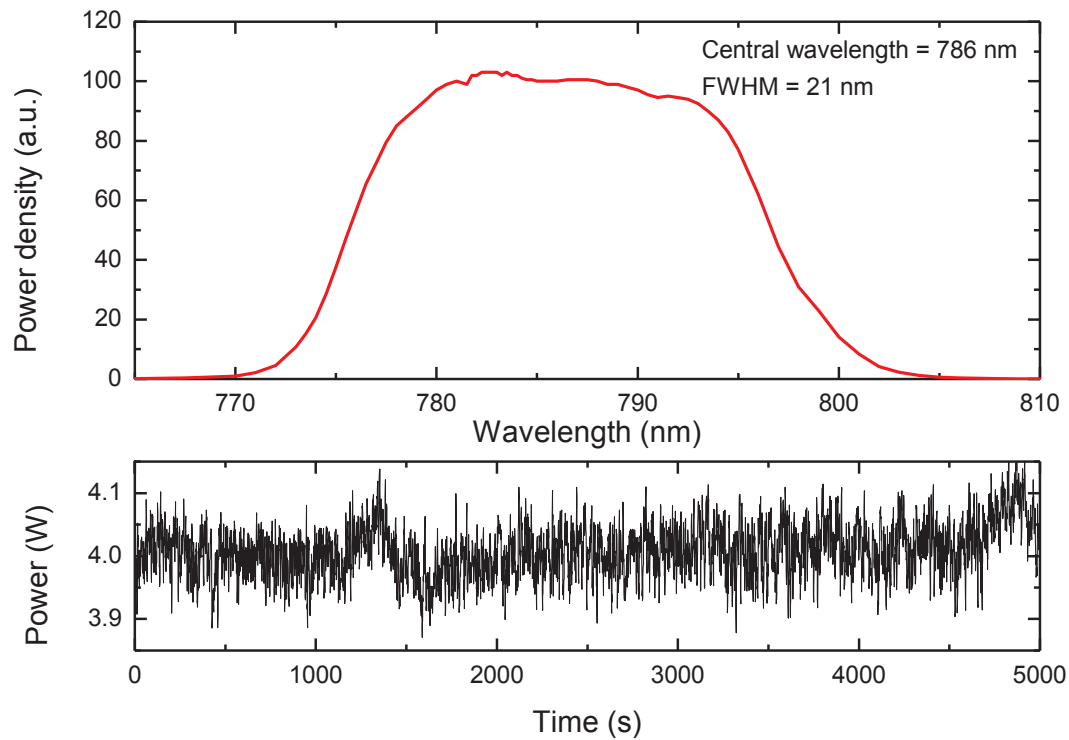
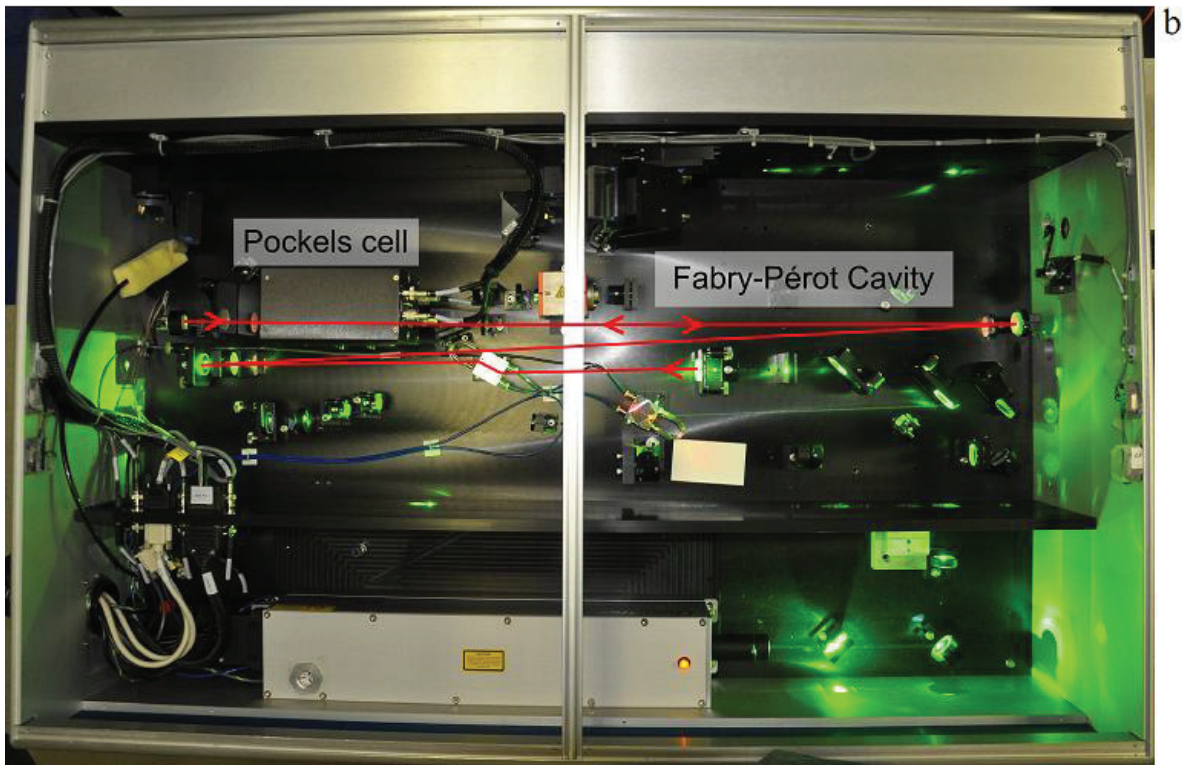
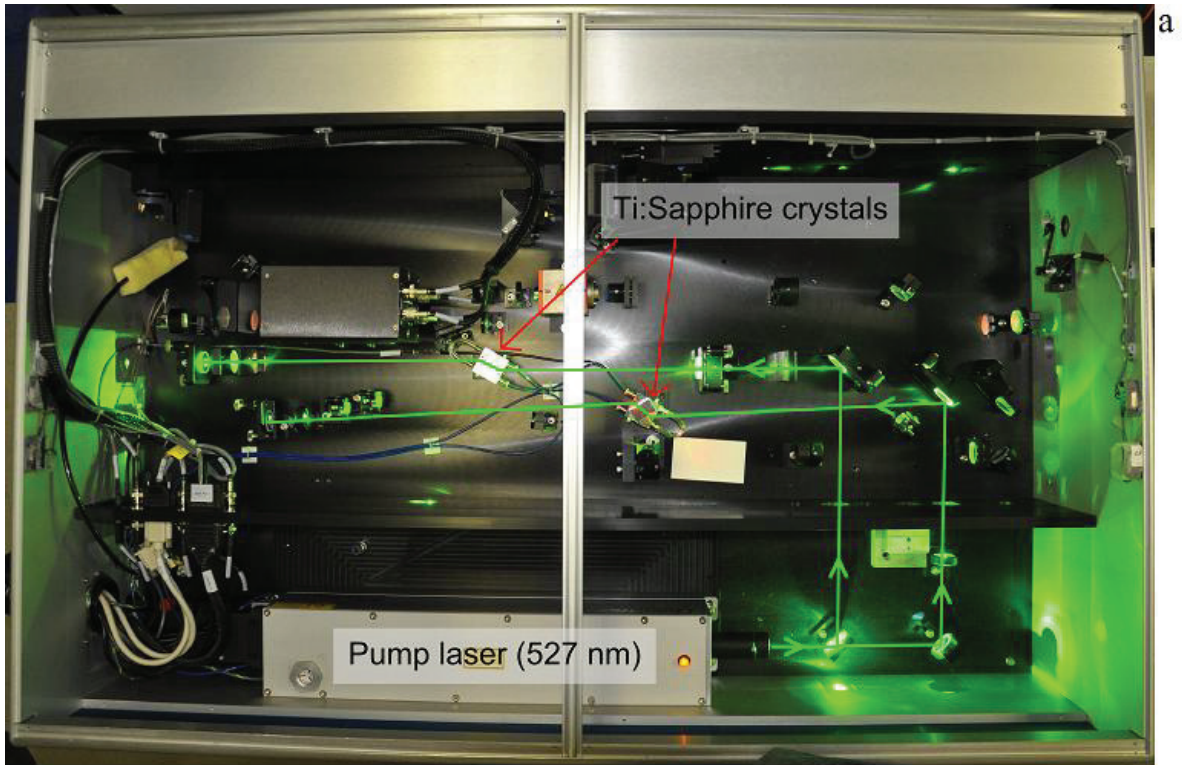


Fig. 5.2: Graph (a) presents the measured power density spectrum of the femtosecond laser while graph (b) shows the 200 shots-average of this power as a function of time.

Figure 5.3 shows the inside of the femtosecond laser and underlines the optical paths. The laser fits in a compact box whose dimensions are $1140 \times 750 \times 330$ mm. The pump laser is a frequency doubled neodymium-doped yttrium lithium fluoride (Nd:YLF) emitting 24 Watts at 527 nm. As shown in Figure 5.3a, the emitted laser beam is split into two laser beams so that, among the available 24 Watts, 9 of them are focused into a Ti-Sa crystal in a Fabry-Pérot cavity (Figure 5.3b) while the remaining 15 ones are used into the Ti-Sa crystal in the amplification stage (Figure 5.3c). Finally, the laser pulse, centered at 784 nm is recompressed so that the output laser pulse duration drops down to less than 130 femtoseconds.



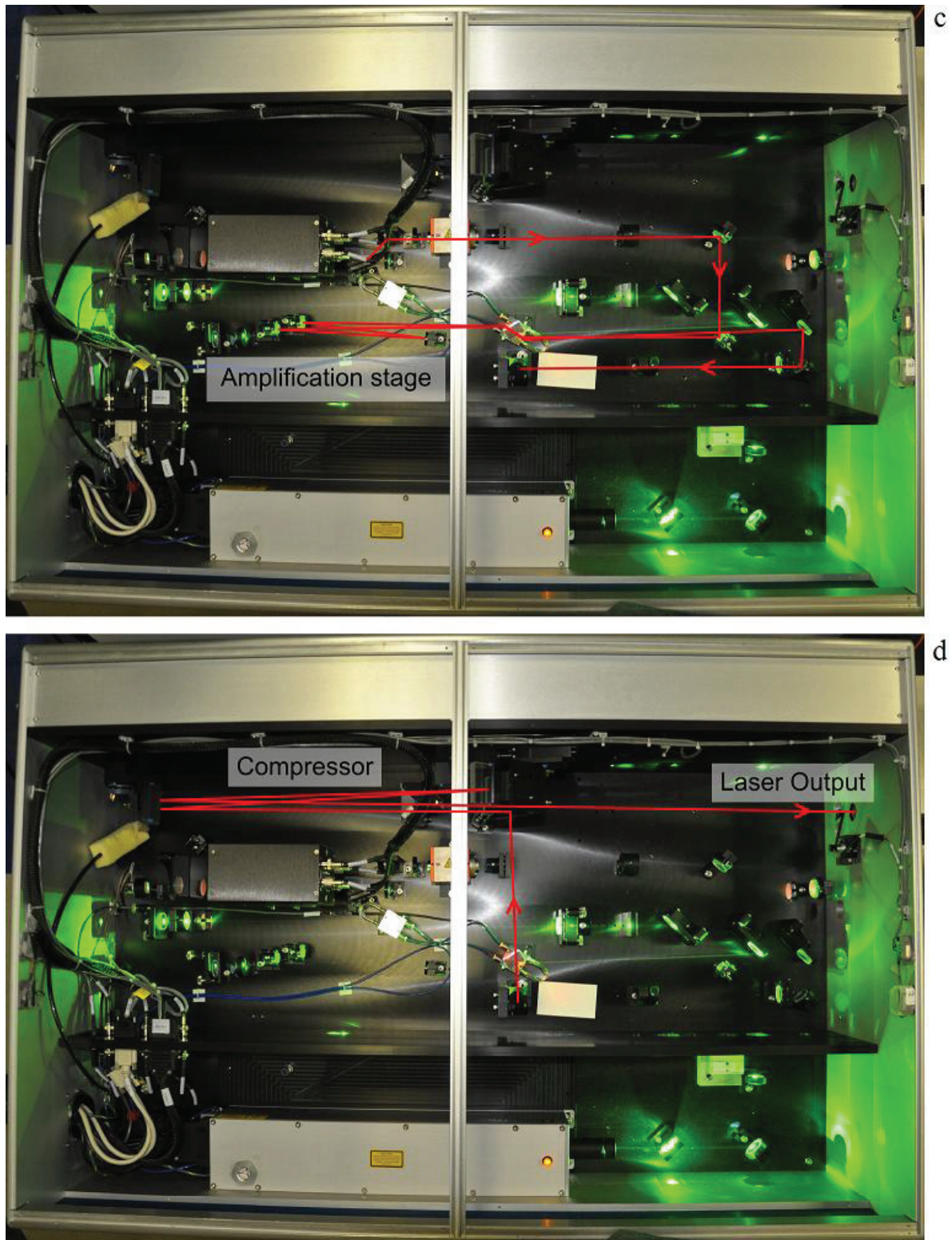


Fig. 5.3: Top view of the femtosecond laser presenting the layout of the optical components. The Nd:YLF pump laser (527 nm) is transmitted to the two Ti:Sa crystals (a) into the Fabry-Pérot cavity (b) and the amplification stage (c). Finally, the generated and amplified pulse is recompressed to 130 fs pulse duration (d).

5.1.2 The optical parametric amplifier

The femtosecond laser is used as a pump for the optical parametric amplifier (OPA, Palitra FS from Quantronix) [Armstrong et al. 1962, Dmitriev et al. 1997]. The latter is a light source that emits at tunable wavelengths using non-linear processes. Its central wavelength is tunable from the 300 to 2 000 nm, to account for possible studies of numerous trace gases, such as the following non-exhaustive list: CH₄, H₂O, CO₂, N₂O, CO, O₃, NO, HO, HF, HCl, HBr, HI, C₂H₂, C₆H₆. This section presents the OPA system used in the OCS-lidar experiment, together with its measured specifications.

The femtosecond laser depicted in Section 5.1.1, is used as the powerful optical wave which initiates the three-wave mixing process occurring in the optical parametric amplifier. When considering the femtosecond laser pulse duration, the nonlinear crystal where the three-wave interaction takes place (here a bismuth borate crystal, BIBO crystal, BiB₃O₆) is extremely thin, in the millimeter range. This crystal has advanced characteristics for nonlinear applications: its effective nonlinear coefficient is so large that the three-wave mixing efficiency is optimized; in addition, it also has a high damage threshold and is non-hygroscopic so it can resist to a powerful pump wave [Ghotbi et al. 2006, Tzankov et al. 2008].

The three-wave mixing process is governed by energy and momentum conservation laws. As a result, photons emitted from the femtosecond pump laser generate two other photons of equivalent energy. If ω_p , ω_s and ω_i represent the angular frequency of respectively the pump, the signal and the idler, ω_p can then be expressed as follows:

$$\omega_p = \omega_s + \omega_i \quad (5.1)$$

The signal and the idler frequency are regulated by the temporal and the spatial overlap between the pump and the signal, and also by the phase matching condition, which depends on the angle θ between the incident pump laser ray and the optical axis of the BIBO crystal. By changing the angle of incidence on the crystal, the signal and the idler signals can be tuned with respect to Equation (5.1) and according to the Sellmeier equations. Figure 5.4 summarizes the simplified geometry of the three-wave mixing process.

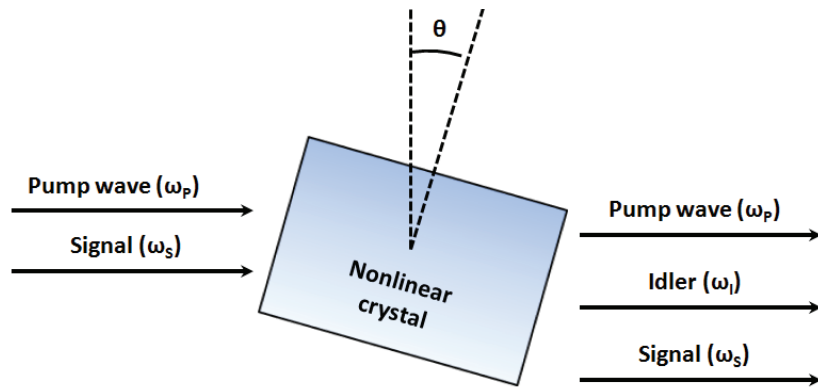


Fig. 5.4: Phase matching principle in the optical parametric amplifier. ω_p , ω_s and ω_i represent the angular frequency of respectively the pump, the signal and the idler while θ represents the angle of incidence in the crystal.

As it propagates through the crystal, the low-energy signal will increase due to the efficient power exchange with the pump. This effective amplification is the optical parametric amplification process. In our case, the signal originates from a white light continuum generated before the three-wave mixing. The white light continuum is produced by focusing a part of the pump in a transparent sapphire crystal. The polarization of the signal and of the idler depends on the polarization of the pump laser and on the type of the crystal used in the OPA. More precisely, different types of BIBO crystal, lead to either similar polarization between the signal and idler, commonly named as a type I-crystal, or orthogonal polarization, named as a type II-crystal. In the here performed experiment, we will use a type II-crystal so that the Idler and the signal have orthogonal polarizations, and can therefore be separated for example, by using one or several polarization beam splitter cubes.

The work presented here is based on correlation spectroscopy by spectrally shaping the laser pulse before it is sent into the atmosphere. In the literature, spectral shaping of broadband OPA laser source has been largely described, where an amplitude modulation is operated on the white light before the amplification stage occurs [Légaré et al. 2008]. Therefore, the question may rise if the amplitude modulation process could be operated on the white light continuum before the amplification process.

The OPA process can be described by the coupled wave equations [Akhmanov et al. 1992]. In particular, the generation of the idler pulse of electric field $E_I(\omega)$ in the frequency domain is described by [Tan et al. 2003]:

$$E_I(\omega) \propto \int_{-\infty}^{\infty} E_S(\omega') \cdot E_P(\omega' + \omega) \cdot d\omega' \quad (5.2)$$

where $E_S(\omega)$ and $E_P(\omega)$ are the signal and the pump electric fields in the frequency domain respectively. The shape of the generated idler pulse is a convolution between the pump and the signal pulse. In our configuration, the laser pump has a broadband emission and would therefore lead to severe limitations in resolution of the transferred pulse shape. In order to keep the resolution of the amplitude modulator, the pump laser would need to be a near delta function which would significantly reduce the energy of the source and hence reduce the efficiency of the non-linear process.

Figure 5.5 shows the layout of the optical components. The OPA is organized on a baseplate designed to provide a thermally stable platform (405 x 290 x 203 mm). It contains two optical parametric amplification stages, one to achieve the signal pre-amplification and another to perform the power amplification. The pump is divided through a beam splitter, 99 % of the pump energy is dedicated to the amplification stage, the remaining 1 % is split to achieve the signal preamplification on the one hand, then the white light continuum generation (WLC generation) on the other hand. When the signal and the idler are amplified, the remaining pump is separated from the signal and idler waves by a dichroic mirror (MD). Each stage includes a linear motorized stage (Delay 1 and Delay 2 in Figure 5.5) to achieve the temporal overlap between the signal and pump waves, and a BIBO crystal (BiBO 1 and BiBO 2) with a rotational motor is used to achieve the crystal phase-matching.

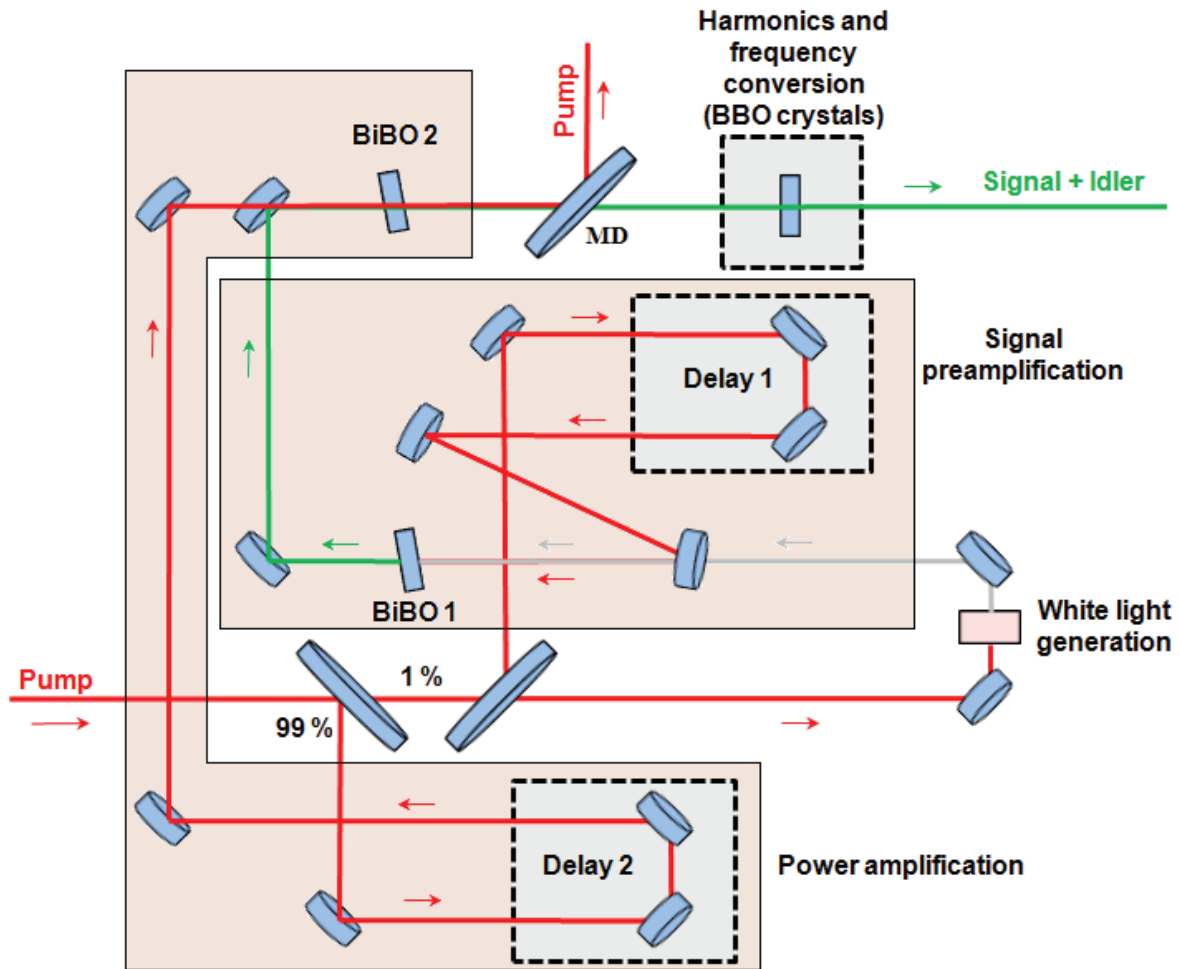


Fig. 5.5: Optical layout of the optical parametric amplifier.

Before the laser output, two barium borate crystals (BaB_2O_4 , also called BBO) are used to achieve frequency doubling or tripling so that the wavelength range of the OPA goes from 300 nm to 2 000 nm. The OPA conversion efficiency, defined as Output Signal energy/Pump energy, is presented in Figure 5.6, showing the efficiency for the signal + idler in the infrared and the efficiency for the 4 BBO crystals in the visible range and the UV spectral ranges.

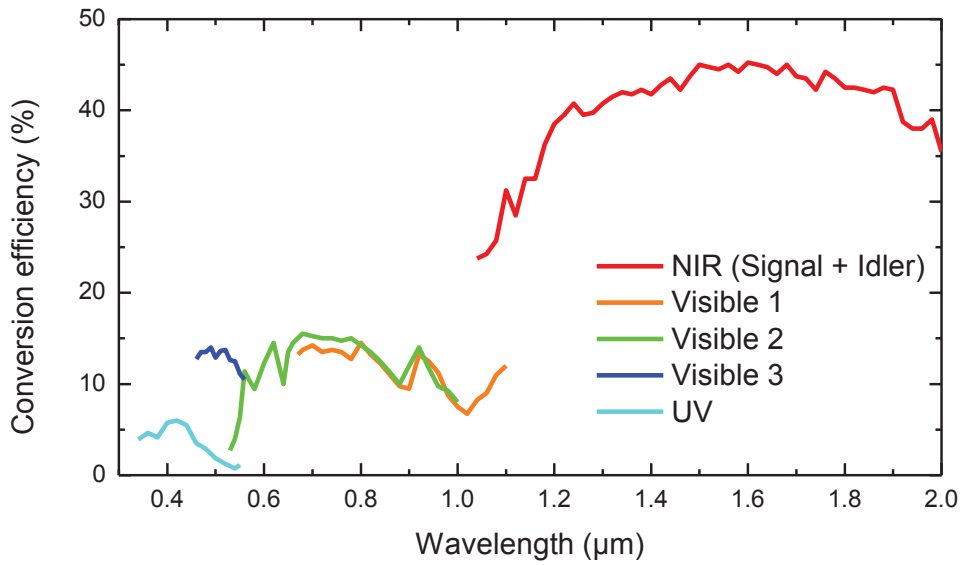


Fig. 5.6: Conversion efficiency of the OPA in the infrared (Signal + idler), in the visible (orange, green and dark blue) and in the UV (cyan). The conversion efficiency has been measured using a calibrated power meter, the initial laser energy is 4 W (4 mJ at 1 kHz repetition rate).

The pulse duration of the OPA is shorter than the laser pump, in the range of 60 fs. The measured power density spectrum of the signal emitted at 1500 nm by the OPA is presented in Figure 5.7.

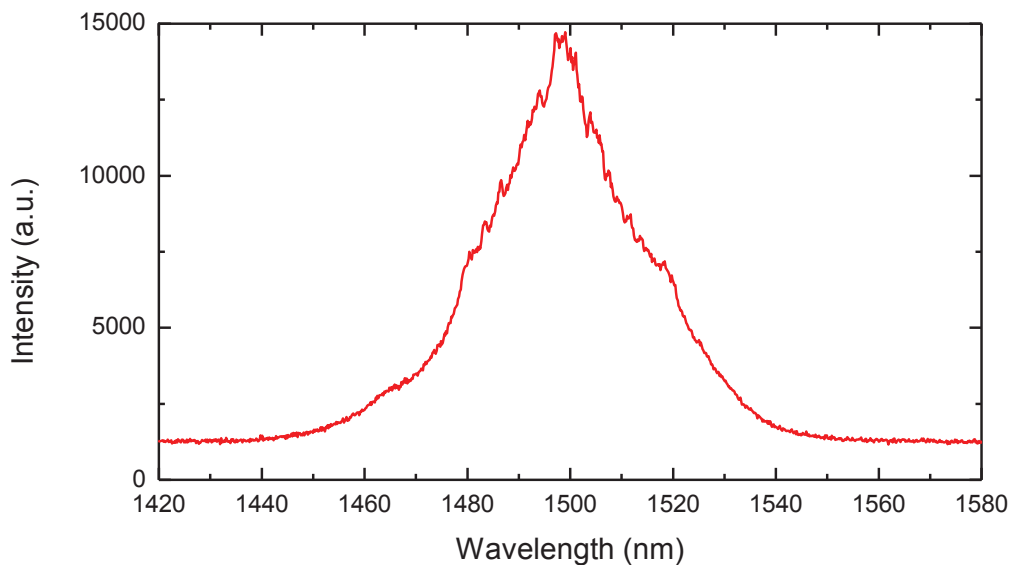


Fig. 5.7: The measured power density spectrum of the signal emitted at 1500 nm by the optical parametric amplifier.

Care should be taken when using ultra-short femtosecond laser pulses because they can suffer from group velocity dispersion when propagating through the atmosphere which is a spectrally dispersing medium [Shen 2003, Rairoux et al. 2000]. At 1 atm, the Earth's atmosphere has a group velocity dispersion of $20.05 \text{ fs}^2/\text{m}$ [Wrzesinski et al., 2011], which leads for a 60 fs laser pulse to an increase of the laser pulse duration equal to 900 fs/km. However, the power density of the laser pulse remains unchanged as long as no self-phase modulation, related to the Kerr effect, occurs. Self-focusing and other non-linear processes occur when pulse intensity exceeds $10^{10} \text{ W.cm}^{-2}$, well above the intensity required in this experiment (around 10^8 W.cm^{-2} at 50 m range). As a consequence, laser filamentation, of which the power threshold is 3.2 GW at 800 nm wavelength [Marburger 1975], should also not occur since its mechanism also requires self-focusing. In addition, temporal distortion of fs-laser pulses, which may rise from atmospheric turbulence [Extermann et al. 2008], should be considered in the case of a strong atmospheric temperature gradient (100 K.m^{-1}).

5.2 The amplitude modulation

This section presents how the amplitude modulation is performed in the OCS-lidar experiment. As it has been presented in Chapters 3 and 4, the amplitude modulation, or spectral shaping, is operated by using an amplitude modulator located after the output of the OPA system. However, a careful analysis of Equation (3.14) leads to the conclusion that, the multiplication being commutative, the amplitude modulations functions $M_C(\lambda)$ or $M_{NC}(\lambda)$ can be applied either before or after the backscattering process occurring in the atmosphere. Therefore, it follows that two experimental OCS-lidar configurations can be achieved:

- Amplitude Modulation at the Emission or AME-configuration, in which the broadband laser pulse is shaped before its emission in the atmosphere, as described in Chapters 3 and 4.
- Amplitude Modulation at the Reception or AMR-configuration, where the amplitude modulation functions are applied after the atmospheric backscattering process occurred.

These two experimental OCS-lidar configurations are detailed in the following Sections 5.2.1 and 5.2.2.

5.2.1 Amplitude modulation in the AME-configuration

a) The AME experimental set-up

In the AME-configuration, each laser pulse is spectrally shaped before the backscattering process by using an amplitude modulator, to be described in Section 5.2.1.c, alternatively generating the amplitude modulation functions $M_C(\lambda)$ and $M_{NC}(\lambda)$, as seen in Section 3.3.1, Figure 3.15. The OCS-lidar signals $P_C(r)$ and $P_{NC}(r)$ are alternatively measured since each laser pulse propagating into the atmosphere is specifically designed to be correlated or non-correlated with the atmospheric gas absorption cross-section. The two OCS-lidar signals are hence measured with a single detector D . The OCS-lidar signals are then sampled by a Transient Recorder (Licel, 12 bits, 40 MHz sample rate) in an alternative mode allowing to record the $P_C(r)$ and $P_{NC}(r)$ signals on two different memories (see Section 5.3.2).

The optical layout for the emission in the AME-configuration is presented in Figure 5.8. The signal and the idler emitted by the OPA have an orthogonal polarization. Since the idler pulse has a power spectral density not centered in the wavelength range of interest for the trace gas, a Glan Thompson polarizer is used to separate the idler from the signal. Moreover, depending on the instantaneous power emitted by the OPA, non-linear effects, such as Kerr self-focusing, can occur in the AOPDF birefringent crystal. In this case, a second Glan Thompson polarizer placed behind the first one can be used to control the transmitted power. The polarization of the signal is adjusted thanks to a half-wave plate to exactly match the AOPDF crystal optical axis. Then, the laser pulse is spatially stretched to reduce the volume power density as detailed in the following section. Once spectrally shaped by the AOPDF, the pulse goes through a 3X beam expander to reduce its divergence before being sent into the atmosphere.

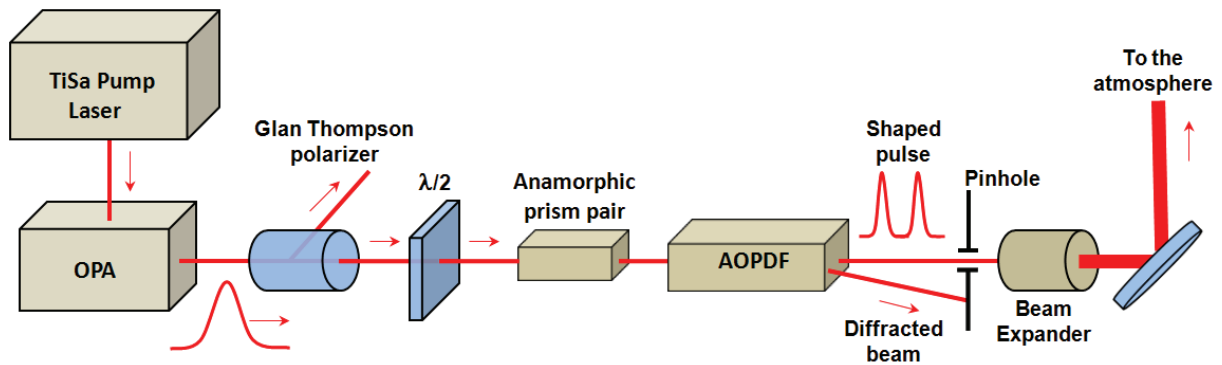


Fig. 5.8: Scheme of the optical component used in the AME-configuration.

b) Nonlinear effects and energy limitation

Since the emitted laser pulse has a 60 fs pulse duration with a typical energy of 1 mJ per pulse, the instantaneous power of the laser pulse reaches more than 16 GW. Therefore, nonlinear effects may occur in the tellurium dioxide crystal (TeO_2 or Paratellurite) of the AOPDF. The laser energy would generate white light in the crystal which reduces significantly its effective transmission, as well as decreasing the amplitude modulation quality. Moreover, at such energies, the Kerr effect [Melnichuk et al. 2010] may induce a change in the refractive index of the AOPDF crystal, which could cause an unwanted increase of the laser beam divergence before the laser pulse propagation in the atmosphere. These two effects (white light generation, Kerr effect) increase at higher input laser volume power densities, and in our case, for a 3 millimeters diameter beam section, we measured a threshold of 1 GW. This limitation due to the AOPDF is related to non-linear effects which occur in response to a too high intensity, therefore the energy threshold can be raised on the one hand, by increasing the pulse duration with a pulse stretcher leading to a lower instantaneous power, and on the other hand, by increasing the section of the laser beam to lower the volume power density. In order to do so, the pulse beam has been extended using an anamorphic prisms pair. Figure 5.9 shows a picture of the anamorphic prisms pair placed before the AOPDF.

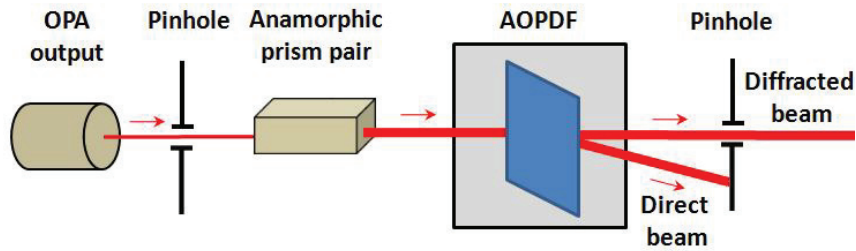
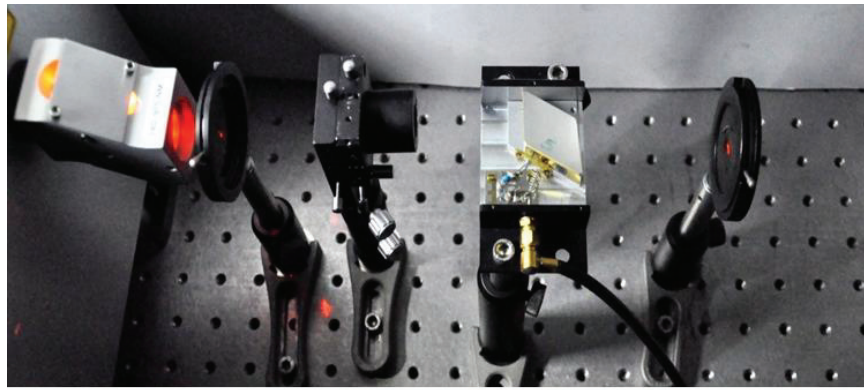


Fig. 5.9: Picture and layout of the anamorphic prism pair together with the AOPDF. From left to right, the OPA output, a pinhole, the 3X anamorphic prism pair, the AOPDF (uncovered showing the paratellurite crystal), and a pinhole.

Figure 5.10 presents the measured horizontal and vertical beam profiles showing the spatial broadening of the laser pulse on the horizontal axis after it went through the anamorphic prisms pair.

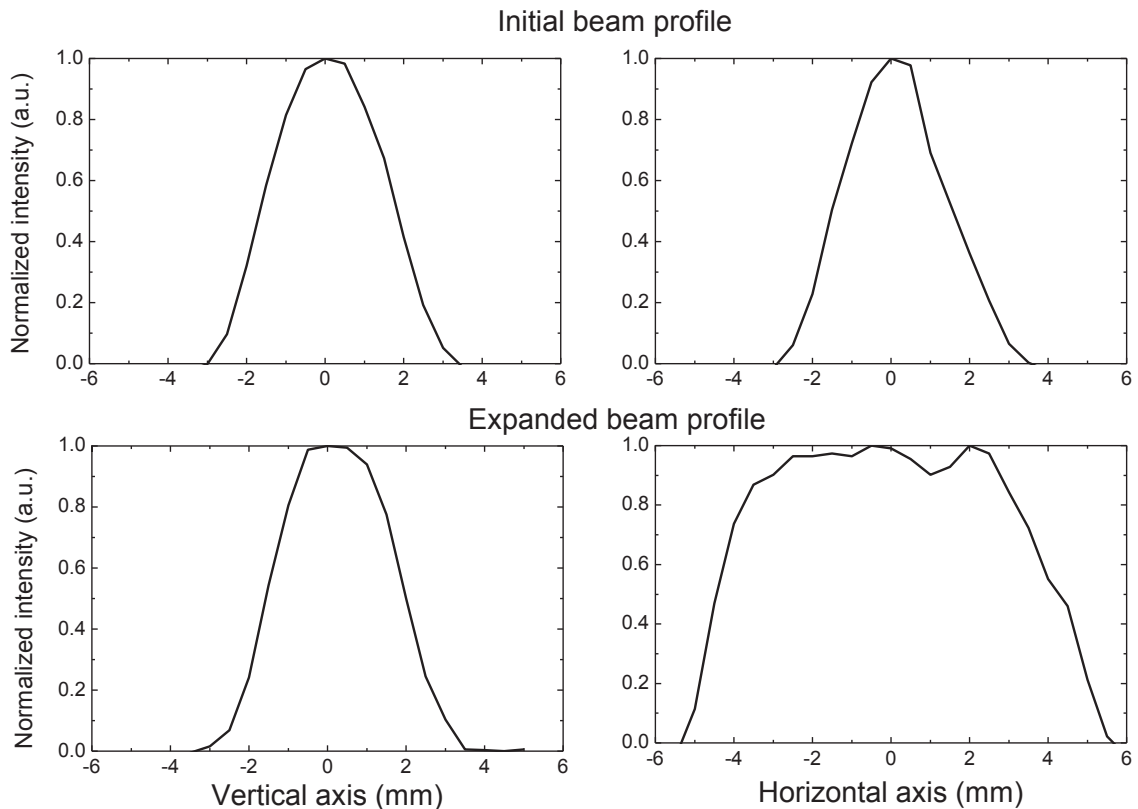


Fig. 5.10: Measurements of the vertical and horizontal beam profile of the OPA output beam before (top graphs) and after (bottom graphs) the anamorphic prism pair.

Stretching the pulse duration can also lower the volume power density. This can be performed by using two gratings which increase the pulse duration by a factor of 10^3 to 10^4 , as in the chirped pulse amplification presented in Section 5.1.1. Also, the use of an optical component having a high group velocity dispersion (GVD) can increase the pulse duration, though with less efficiency than a pair of gratings, although it requires almost no alignment since the laser pulse simply needs to be transmitted through the optical medium. For example, a SF68 glass has a GVD equal to $65 \text{ fs}^2/\text{mm}$, which leads, for 130 fs pulse and a 20 cm optical path way, to a 310 fs pulse. Bragg gratings are also a solution also used to perform CPA. The dispersion rate for such gratings reaches typically 50 ps per nanometers of the pulse spectral width.

c) The acousto optical programmable dispersive filter (AOPDF)

The amplitude modulation function $M_C(\lambda)$ and $M_{NC(\lambda)}$ are alternatively generated by an acousto optical programmable dispersive filter, called Dazzler and produced by Fastlite. It is a programmable coherent filter for femtosecond laser pulses based on the longitudinal acousto-optic interaction between a light pulse and a programmable acoustic waveform that describes the impulse response of the filter. Since the ratio between the speed of sound and light is in the order of 10^{-7} , coherent control of the optical pulses can be performed with electrical signals in the tens of megahertz range [Kaplan et al. 2004].

The AOPDF is based on the acousto-optics effect. This effect between an optical wave and an acoustic wave is mostly due to the change in the medium refraction index which occurs in the presence of the sound wave. Due to the alternation of high and low pressure zones, the medium acts as a diffraction grating. The light, when passing through the medium, behaves as if it was a regular diffraction grating. By controlling the amplitude, the frequency and the phase of the acoustic wave, a selected optical wavelength can be diffracted with a higher efficiency. The latter is related to the amplitude of the acoustic wave since it defined how strong the refractive index gradient is. As presented in Figure 5.11, when leaving the device, the diffracted beam and the direct beam are not collinear and have a 2.6° divergence angle and a 2 mm off-set.

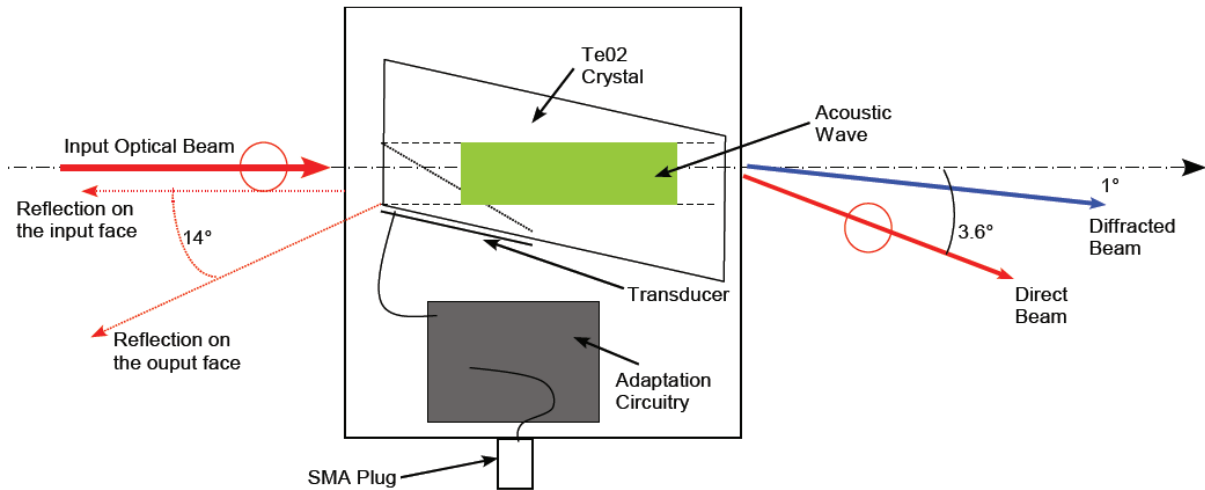


Fig. 5.11: Top view of the AOPDF presenting the input beam and output direct beam (red), the diffracted beam (blue) and the acoustic wave (green).

Figure 5.12 presents a schematic diagram of the AOPDF principle. The optical wave (blue) propagates along the fast axis of the birefringent crystal. In this example, the frequency of the acoustic wave established in the crystal (pink) decreases along the z-axis, so that the wavefront has the higher frequency. As a consequence, as it propagates through the crystal, short optical frequencies are diffracted on the slow axis before higher frequencies. Every optical frequency travels a certain distance before it encounters a phase matched spatial frequency in the acoustic grating. The pulse leaving the device by the slow axis will be made up of all the spectral components that have been diffracted at various positions. Since the velocities of the two modes are different, each optical frequency will see a different time delay, causing an increase of the pulse duration.

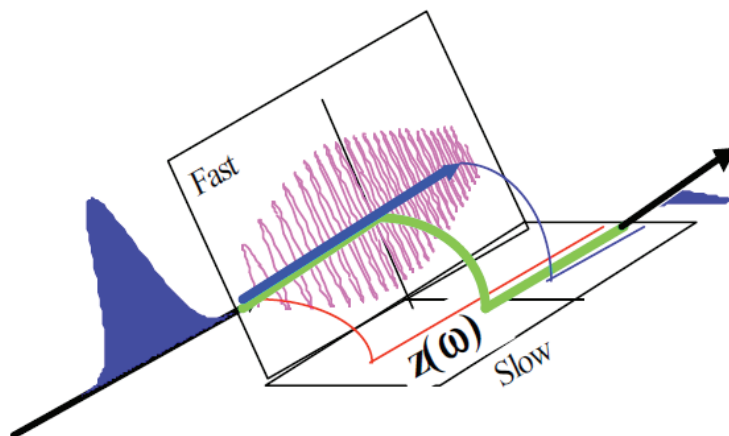


Fig. 5.12: Schematic diagram of the AOPDF, the electric field (dark blue) is transmitted on the fast axis of the crystal. When the phase matching occurs, the electric field is diffracted by the acoustic wave (pink). Each spectral component (red, green, blue) of the electric field is diffracted on the slow axis at various positions.

Table 5.2 presents the major Dazzler specifications.

Specifications	Visible	Near infrared
Spectral coverage	400 to 800 nm	1100 to 2200 nm
Spectral resolution	0.5 nm	1.1 nm
Maximum transmission	65 %	65 %
Maximum input beam size (height)	2.5 mm	2.5 mm
Maximum input beam size (length)	6 mm	6 mm
Maximum beam divergence	1 mrad	1 mrad

Table 5.2: AOPDF specifications.

5.2.2 Amplitude modulation in the AMR-configuration

a) AMR Experimental set-up

In the AMR-configuration, the optical correlation is achieved at the lidar receptor, as shown in Figure 5.13 where the experimental set-up in the AMR-configuration is presented. The AMR configuration is close to a low spectral resolution differential absorption spectroscopy scheme which uses a broadband laser source instead of a spectrally extended light source (white light continuum, spectroscopic lamp, natural light source) or a narrow band laser. In the AMR-experimental configuration, the broadband laser pulse with power density spectrum $P_0(\lambda)$ does not undergo any spectral modification before being sent into the atmosphere. The amplitude modulation is there operated once the photons are backscattered by the atmosphere.

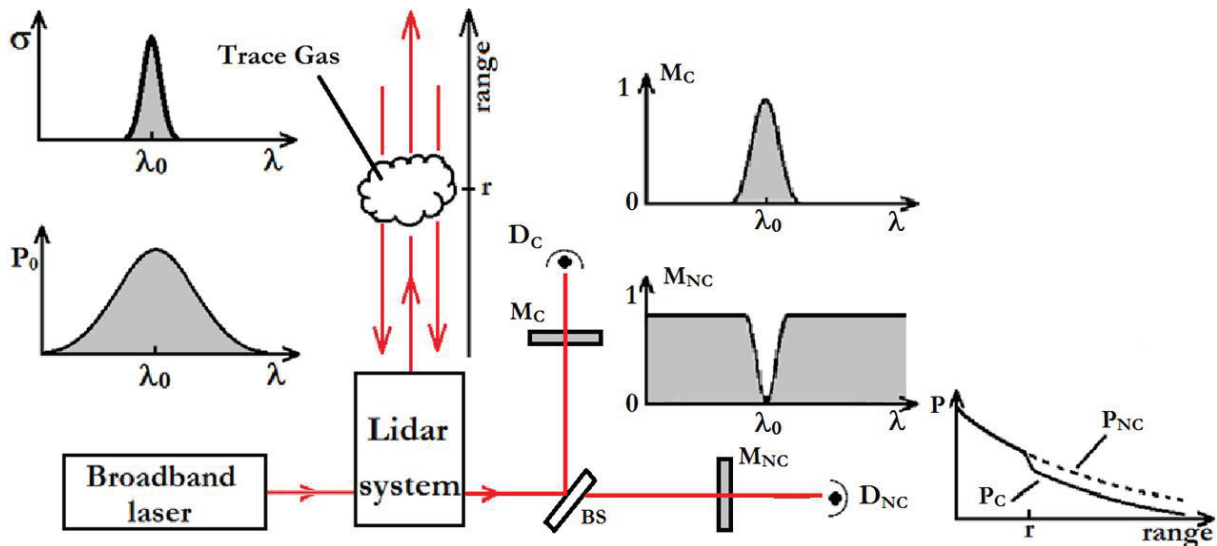


Fig. 5.13: OCS-lidar principle using AMR-configuration where the amplitude modulation functions are applied at the reception.

In this configuration, the amplitude modulations M_C and M_{NC} are performed by passive interference filters. An active amplitude modulator such as the AOPDF is not adapted due to the divergence of the backscattered light beam which is over the 1 mrad required by the AOPDF. In addition, due to the backscattering process, photons from the laser are received by the telescope during a few microseconds after the laser shot, yet the acoustic wave in the AOPDF crystal cannot be considered as stationary during this timeframe, as it is the case when considering a femtosecond pulse duration. As a consequence, the amplitude modulation would be performed only for a given altitude range.

The interference filter bandwidths and their transmission have been chosen by using the numerical simulation results presented in Section 4.4.1. The interference filters used in the water vapor experiments have been measured with a calibrated spectrograph. Figure 5.14 presents the transmission of two interference filters FB71010 and two filters FB72010 from Thorlabs. The difference between two interference filters supposedly similar underlines the need for accurately measuring the transmission of each filter.

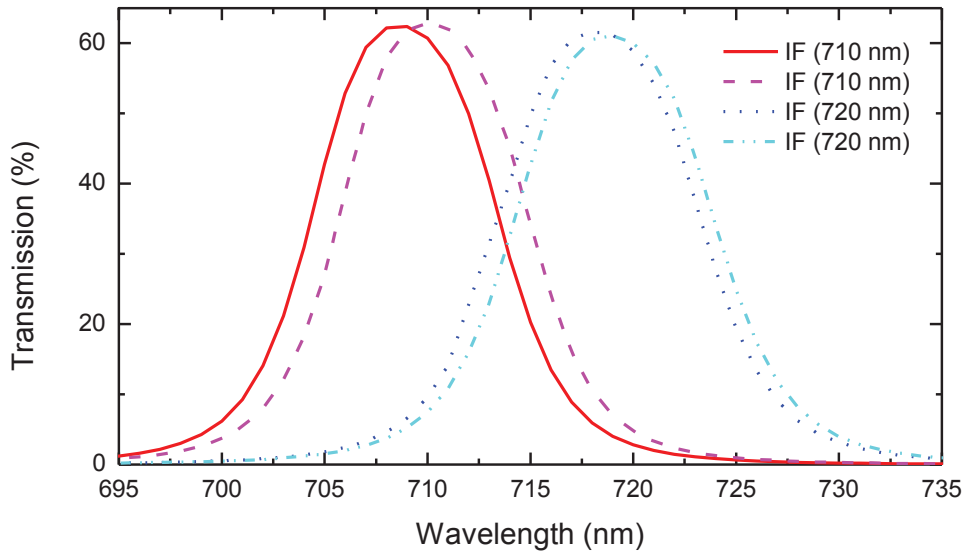


Fig. 5.14: Measured transmission of 2 FB71010 filters and 2 FB72010 from Thorlabs.

In the AMR-configuration, the OCS-lidar signals $P_C(r)$ and $P_{NC}(r)$ are measured thanks to two Hamamatsu photomultiplier tubes R7400-U20 (D_C and D_{NC}) placed on each detection channel. The resulting OCS-lidar signals are sampled with two transient recorders (Licel, 12 bit, 20 and 40 MHz sample rate).

Unlike the AME-configuration, where the amplitude modulation is performed at the emission, the laser pulse energy can here be higher and each laser pulse contributes to both $P_C(r)$ and $P_{NC}(r)$ OCS-lidar signals with only half intensity, since a 50/50 beam splitter is used. As the backscattered light is split into two different detection channels, any difference between the light collection efficiency, written $K(\lambda)$ in Chapter 3, of both channels would lead to a bias in the retrieved concentration. Similarly, the difference between the two overlap functions, written $O(r)$ in Chapter 3, has to be significantly lower than the difference in water vapor optical absorption undergone by the two OCS-lidar signals. Such alignment of both channels has been checked and is presented in Section 5.3.

Moreover, the optical efficiency $\eta(\lambda)$ introduced in OCS-lidar equation between the two channels may differ and cause systematic error on the retrieved concentration if considered as identical for the two detection channels. In order to avoid this difficulty, each optical component of each channel has been accurately specified. The transmission coefficient of the beam splitter at 45° has hence been measured with a UV-VIS-NIR spectrograph with less than 0.1 % error. The transmission coefficient exhibits a 5 % variation between 700 and 740 nm as shown in Figure 5.15. Secondly, the quantum efficiencies of both detectors have been

measured as a function of the wavelength: within our wavelength range, the two quantum efficiencies differ one to another up to 10 % as presented in Figure 4.8 (Section 4.1.4).

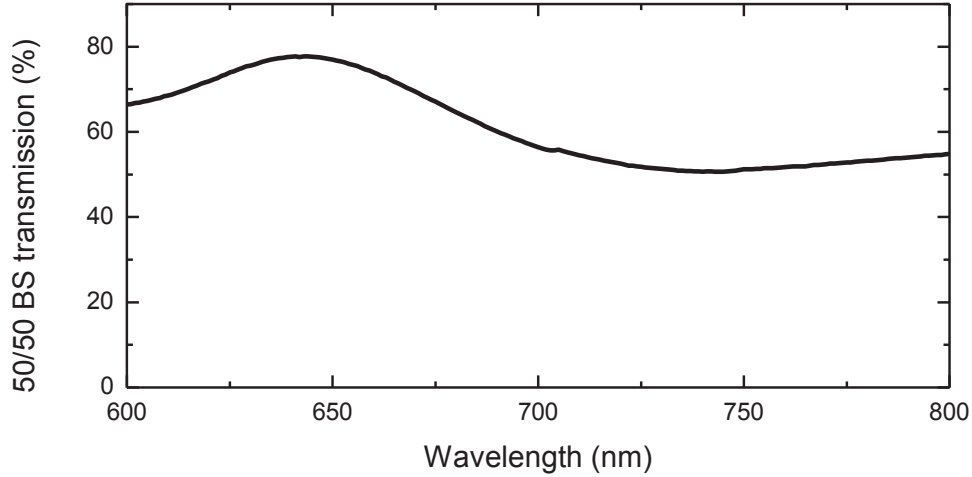


Fig. 5.15: Measured transmission of the 50/50 beam splitter between 600 and 800 nm.

b) The interference filters and angle of incidence

In the AMR-configuration, the amplitude modulation is performed by two interference filters which have been chosen thanks to the optimization procedure detailed in Section 4.4. An interference filter is composed of multiple thin layers of dielectric material having different refractive indices. Since they are based on interference, these filters are designed to be used with an angle of incidence (AOI) equal to 0° ; otherwise, the transmission band is shifted towards the shorter wavelengths. To achieve normal incidence, the incoming light is perfectly collimated and experiences no divergence at all. Since our methodology is based on the amplitude modulation introduced by the IF, this section is dedicated to the influence of the divergence of a normal light beam on the transmission of the filter.

The central wavelength of an interference filter λ_{IF} is governed by Equation (5.3).

$$\lambda_{IF}(\theta_{IF}) = \lambda_C \cdot \sqrt{1 - \frac{\sin^2 \theta_{IF}}{n_{IF}^2}} \quad (5.3)$$

where θ_{IF} is the angle of incidence of the incoming light, λ_C is the central wavelength at normal incidence (i.e. for $\theta_{IF} = 0^\circ$, $\lambda_{IF} = \lambda_C$), and n_{IF} is the filter effective refraction index.

Despite the lens making the light parallel, every light beam is not at normal incidence with respect to the IF. The worst case scenario is presented in Figure 5.16, where the maximum possible angle, or optical aperture, hereafter noted θ_{max} , reaches 6.7° for our optical layout.

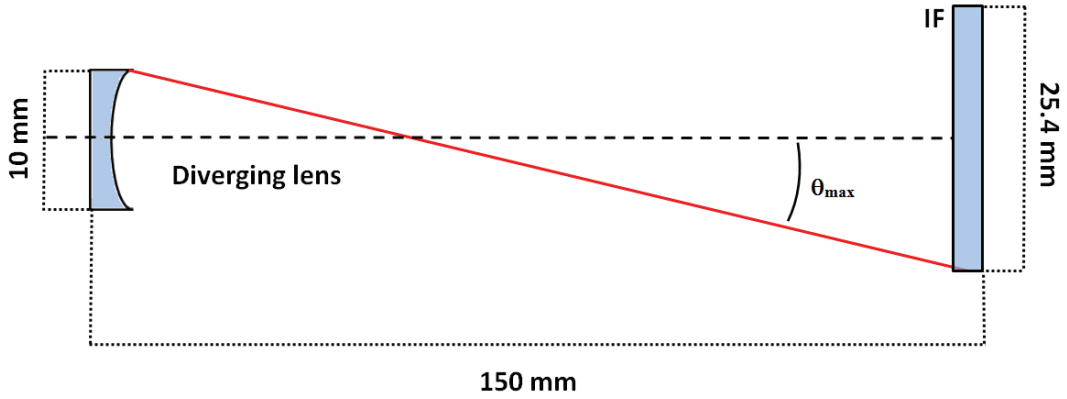


Fig. 5.16: Diagram showing the maximum angle of incidence θ_{max} considering the distance between the diverging lens and an IF. The 150 mm distance is due to the x,y,z mount of the divergence lens, the presence of the beam splitter (not displayed here) in between and the IF mount.

Using Equation (5.3), it is clear that the transmission can only be shifted towards shorter wavelengths, whatever the angle of incidence. In the case of a 6.7° angle, the central wavelength is shifted by 2.2 nanometers. Hence, a divergent light beam leads to an effective transmission of the filter which is broadened towards shorter wavelengths. We can consider the effective transmission $T_{eff}(\lambda)$ written as:

$$T_{eff}(\lambda) = \int_{-\theta_{max}}^{\theta_{max}} \psi(\theta_{IF}) \cdot T_{IF}(\lambda, \theta_{IF}) \cdot d\theta_{IF} \quad (5.4)$$

where $T_{IF}(\lambda, \theta_{IF})$ is the transmission of the interference filter as a function of the AOI. $\Psi(\theta_{IF})$ represents the probability density function for a light beam to reach the filter at angle θ_{IF} . More precisely, Figure 5.17 presents four different Ψ case studies. Figures 5.17a and b present the case of a Ψ -function for a beam with no divergence with an AOI of 0 and 1° respectively. Figure 5.17c represents a beam having an homogeneous probability density between $-\theta_{max}$ and θ_{max} at normal incidence. Finally, Figure 5.17d shows the Ψ -function for a beam with a Gaussian distribution limited by the maximum angle θ_{max} .

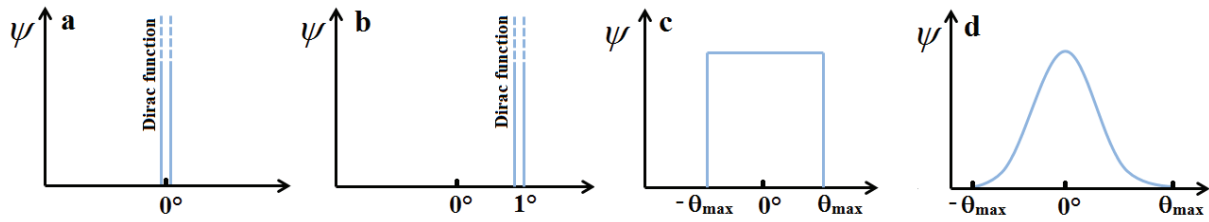


Fig. 5.17: Probability density function Ψ for a light beam to reach the IF as a function of the AOI.

Figure 5.18 shows the effective transmission using Equation (5.4) for a different set of Ψ and θ_{IF} -values. The effective transmission for a Gaussian Ψ limited by $\theta_{IF} = 6.7^\circ$ (red) is very close from the 0° transmission (black), the overlap between the two functions being 97 %. For a constant Ψ , limited by θ_{IF} (blue), the overlap drops down to 90 %. The effective transmissions for higher θ_{IF} values, 15° (pink) and 30° (green), have also been plotted showing the importance of considering this effect for non-collimated light.

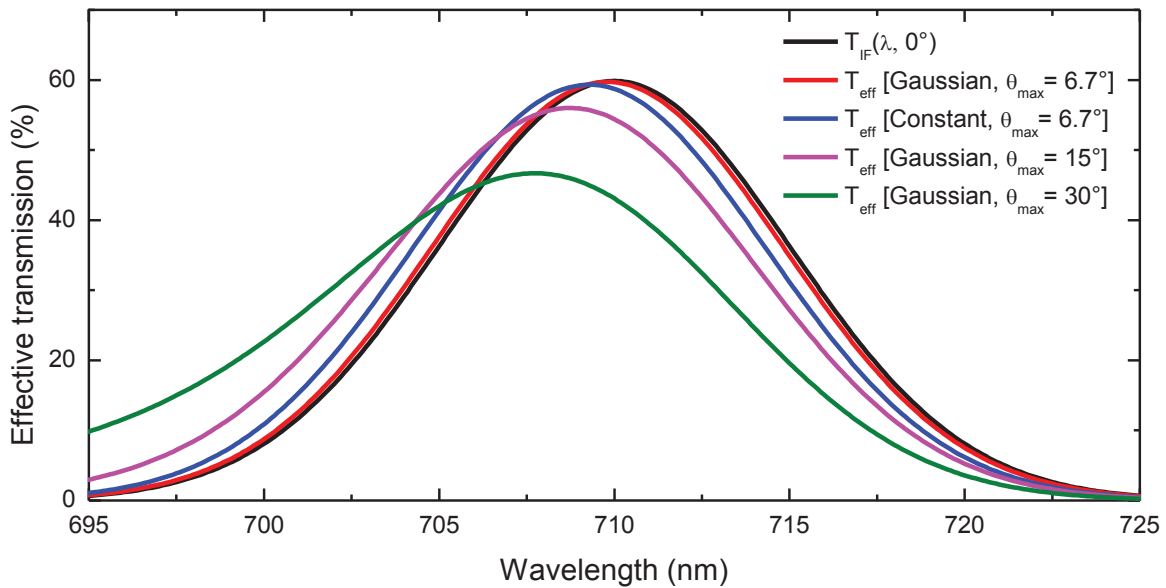


Fig. 5.18: Effective transmission for different probability density function Ψ . T_{IF} is the transmission of the IF for a normal beam with no divergence. $T_{eff}[\text{Gaussian}, \theta_{max} = 6.7^\circ / 15^\circ / 30^\circ]$ are the effective transmission for a beam with Ψ following a Gaussian distribution with the corresponding maximum angle θ_{max} , as represented in Figure 5.17d. $T_{eff}[\text{Gaussian}, \theta_{max} = 6.7^\circ]$ represents the effective transmission for a constant Ψ with $\theta_{max} = 6.7^\circ$ as in Figure 5.17c.

In our case, the probability density function Ψ is unknown and would vary a lot depending on the alignment of the lidar system, therefore Ψ has been assumed to be Gaussian as in Figure

5.17d. The influence of the light beam divergence turns out to be limited for $\theta_{IF} = 6.7^\circ$, but can be reduced by correcting the interferential filter transmission using Equation (5.4) so the beam divergence does not cause any bias.

5.3 The lidar detection system

This section presents the different parts of the detection system used in the OCS-lidar experiment, for both AME and AMR-configurations. Figure 5.19 shows a picture of the detection system gathering the telescope, the detector and the acquisition system.

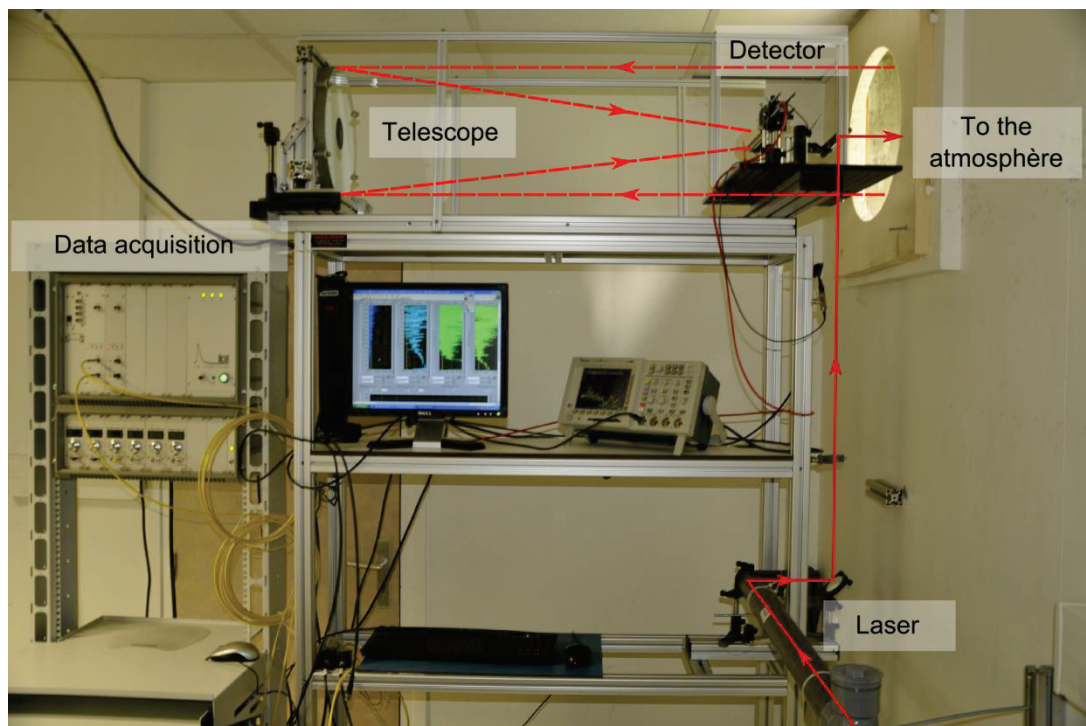


Fig. 5.19: Detection system of the lidar. The laser beam is sent into the atmosphere through mirrors (red full line). The backscattered light (red dash line) is focused by the telescope (uncovered on the picture) on the detector. The resulting signal is recorded by a transient recorder and displayed on the computer screen.

5.3.1 The telescope

Backscattered photons are collected with a 30 cm diameter $f/4$ Newtonian telescope, then focused on the light detector D. Figure 5.20 presents the telescope layout used for its construction. The optical axis of the primary mirror can be visualized thanks to the He-Ne

laser placed behind the primary mirror after the telescope has been aligned. This optical axis is reflected by the secondary mirror (SM), then passes through pinholes Ph1 and 2. Pinholes Ph3, 4, 5 and 6 are used for the alignment procedure. A -12 mm diverging lens (L1) is placed near the focal point of the primary mirror to make the beam parallel.

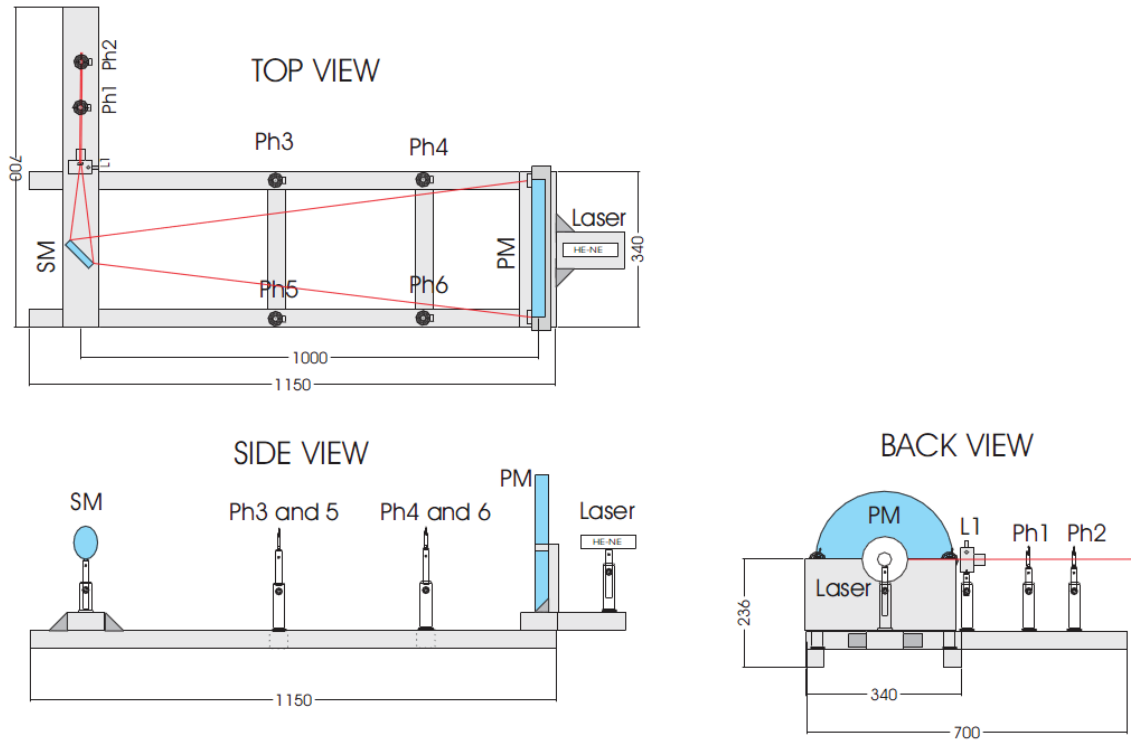


Fig. 5.20: Top, side and back view of the telescope layout (in mm).

Figure 5.21 shows a picture taken during the telescope alignment procedure. Three light beams, parallel to the primary mirror axis, are pointed to the edge of the mirror surface so that the telescope focal point can be properly localized, as well as the ideal SM position.



Fig. 5.21: The 30 cm diameter telescope during the alignment procedure.

5.3.2 The detection and the acquisition system

The optical layout of the detection system is different in the AME and AMR-configurations. In the AME-configuration, the backscattered light is first made parallel by a diverging lens (-12 mm) as presented in Figures 5.22 and 5.23, a possible interferential filter can be set to reduce the light background, then the light is focused on the detector surface (6 mm) through a converging lens (+ 40 mm).

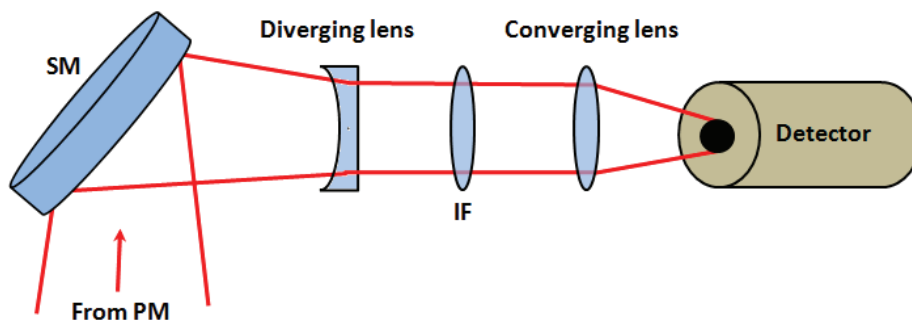


Fig. 5.22: Lidar detector in the AME-configuration.

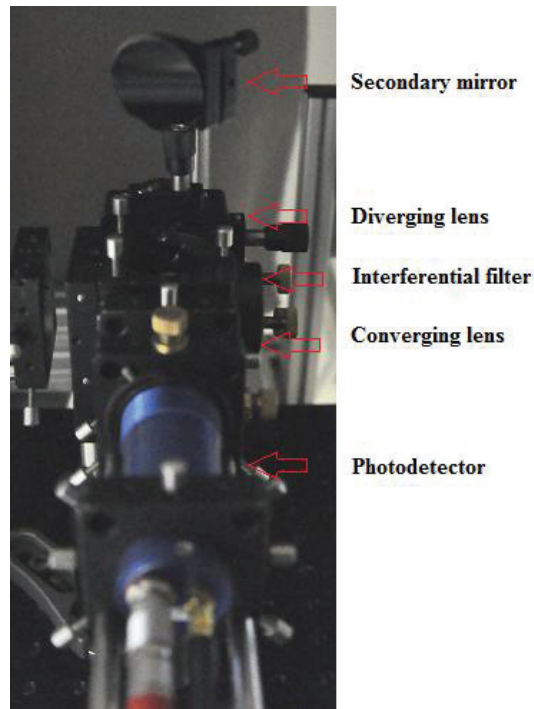


Fig. 5.23: Picture showing the secondary mirror (background), the diverging lens, the interference filter, the converging lens and the photomultiplier tube (forefront).

In the AMR-configuration, the backscattered light is collimated and then separated with a 50/50 beam splitter (Thorlabs BSW11) in two optical pathways (detection channels), as presented in Figure 5.24. On each detection channel, optical interference filters (IF) are used to achieve the optical correlation, the transmissions of these optical filters acting as the $M_C(\lambda)$ and $M_{NC}(\lambda)$ amplitude modulation functions.

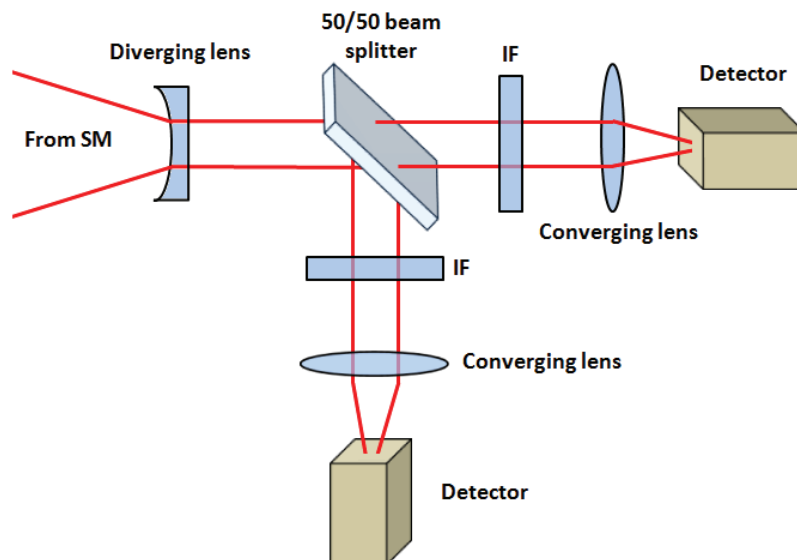


Fig. 5.24: Configuration of the detection system in the AMR-configuration. Once focused by the telescope, a diverging lens is used to paralyze the backscattered light before being split by 50/50 beam splitter. Each resulting channel is made of an interferential filter, a converging lens and a detector.

In the visible spectral range, the detection system is based on an Hamamatsu photomultiplier tube R7400-U20. The signal is then recorded by transient recorders (Licel). Table 5.3 presents its specifications.

Specifications	
Signal input	0 – 20 / 100 / 500 mV
A/D resolution	12 bits
Sampling rate	40 MHz
Summation memory	2 channels, 4094 acquisitions
Max repetition rate	300 Hz
Input impedance	50 Ω
Trigger	Optical
Trigger delay and jitter	25 \pm 7 ns

Table 5.3: Transient recorder specifications

Figure 5.25 presents how the trigger system is organized. The internal trigger of the femtosecond laser is used in both AME and AMR configuration.

In the AME-configuration, the AOPDF alternatively generates two different amplitude modulations, consequently the two memories of the transient recorder have to be triggered in order to either record the signal emanating from the correlated laser pulse or from the non-correlated one. The AOPDF generates a logical signal that is up when the correlated amplitude function is on, and down otherwise, as shown in Figure 5.25. Using a delay generator, the signal is changed in two logical signals at 500 Hz which are then converted in an optical pulse, used to trigger the two transient recorder memories. This procedure ensures that correlated and non-correlated OCS-lidar signals P_C and P_{NC} are sampled on two different memories.

In the case of the AMR-configuration, the triggering process is more straightforward, the laser trigger is transformed into two synchronized optical triggers sent to the transient recorders.

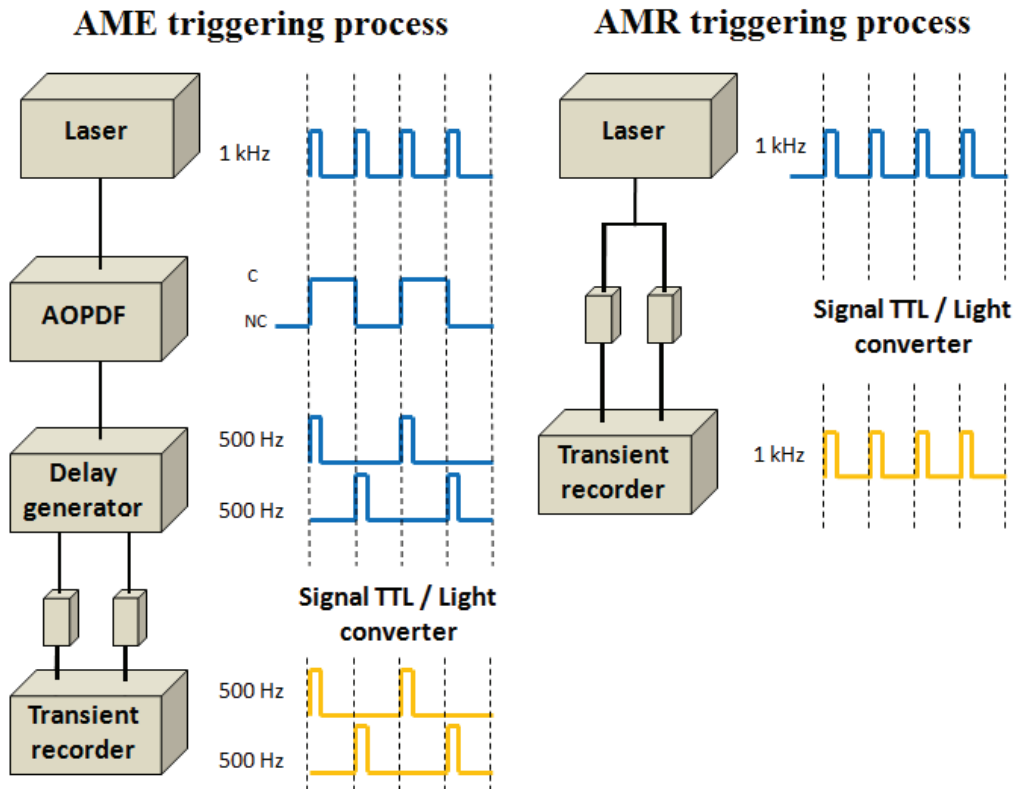


Fig. 5.25: Diagram of the triggering process for the AME and AMR-configuration.

5.4 Experimental results in the visible spectral range

In this section, the first experimental OCS-lidar signals are proposed in both the AME and AMR OCS-lidar configuration. As a case study, to achieve an experimental proof of the OCS-lidar methodology, we focus on the measurement of atmospheric water vapor concentrations in the visible spectral range in the troposphere. These first measurements have been performed during nighttime, at ground level, in the Lyon PBL. Range-resolved water vapor mixing-ratio measurements are presented and discussed in both configurations. The detection limit is also studied.

5.4.1 Water vapor mixing-ratio measurements in the AME-configuration

Before the OCS-lidar measurement itself, a control experiment is first performed to ensure that the two OCS-lidar signals probe the same atmospheric volume and do not undergo any range dependent bias. For that purpose, we first apply the same amplitude modulation on the

broadband laser pulse, i.e. $M_C(\lambda) = M_{NC}(\lambda)$. Under such circumstances, using Equation (3.14), it is clear that at a range r , $P_C(r)$ should be equal to $P_{NC}(r)$. Figure 5.26a shows the resulting range-corrected OCS-lidar signals, and the ratio of these two signals is displayed in Figure 5.26b with error bars, induced by the statistical fluctuations of the OCS-lidar signals.

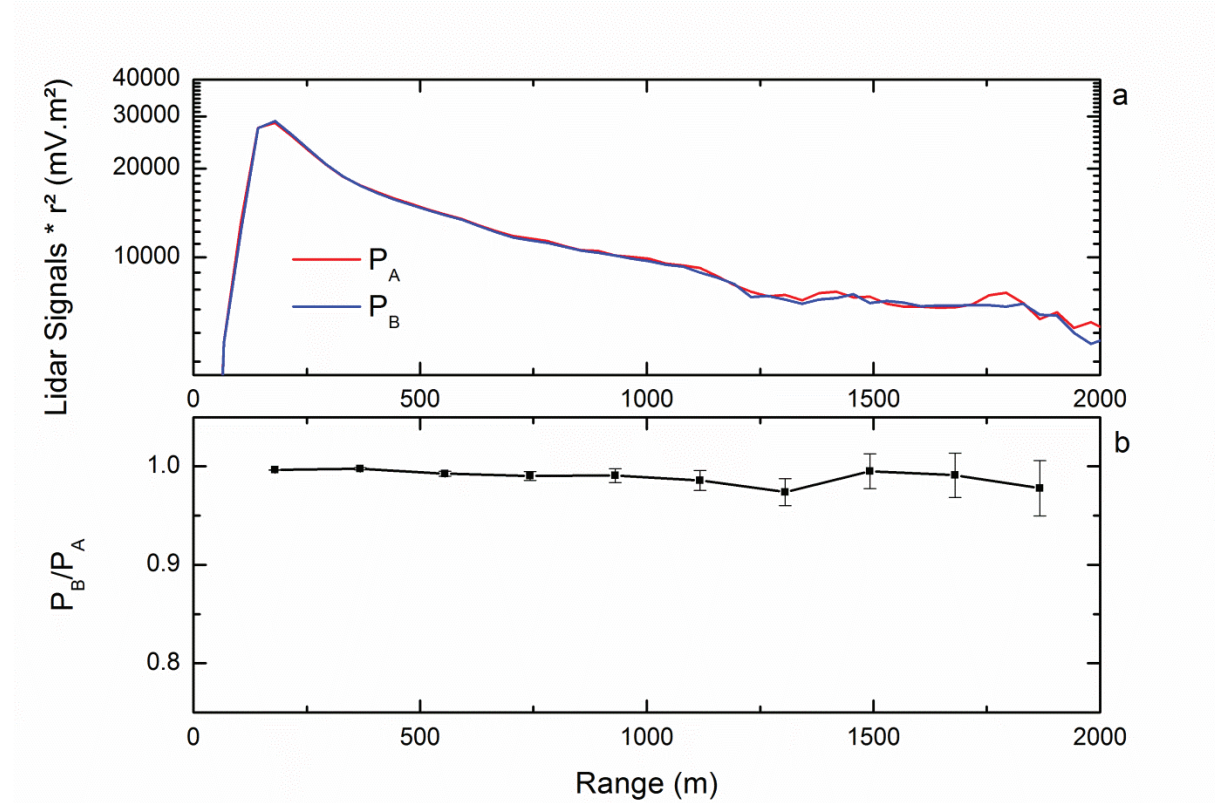


Fig. 5.26: Control bias experiment in the AME-configuration, performed at Lyon on December 19th 2012 at 19h UTC. (a) Range-corrected OCS-lidar signals P_A (blue) and P_B (red) sampled on the two channels A and B of the transient recorders with a 40 meters range resolution. (b) Ratio of both OCS-lidar signals with respective error bars, derived from the statistical fluctuations of the OCS-lidar signals for a ground level relative humidity and temperature are 85 % and 280 K respectively.

Then, the amplitude modulation functions derived in Section 3.2 have been applied to the broadband laser pulse to achieve the optical correlation. OCS-lidar signals $P_C(r)$ and $P_{NC}(r)$, presented in Figure 5.27a, have been acquired with a 1 kHz repetition rate over a time average of 5 minutes. The ratio P_C/P_{NC} , presented in Figure 5.27b, decreases with r as expected in a differential absorption measurement technique. Such a behavior reveals the water vapor content of the atmosphere, with a range-dependent water vapor mixing-ratio to be seen in Figure 5.27c. Error bars on the retrieved water vapor mixing ratios are evaluated thanks to the OCS-lidar numerical simulation based on the signal-to-noise ratio of experimental OCS-lidar signals. The mixing ratio detection limit is evaluated from this error bar taken at 2σ . This

approach leads to a range-dependent sensitivity equal to 3.10^5 ppm.m at a 2 kilometers range. The water vapor profile starts at $(9\,250 \pm 70)$ ppm ($RH = 93 \pm 1\%$) at a range of 260 meters, then strongly decreases down to $(2\,000 \pm 500)$ ppm ($RH = 20 \pm 5\%$) at a 1 200 meters range, and finally slightly varies up to $(4\,000 \pm 1200)$ ppm ($RH = 40 \pm 12\%$). At a 2 kilometers range, the mixing-ratio is $(3\,500 \pm 1400)$ ppm.

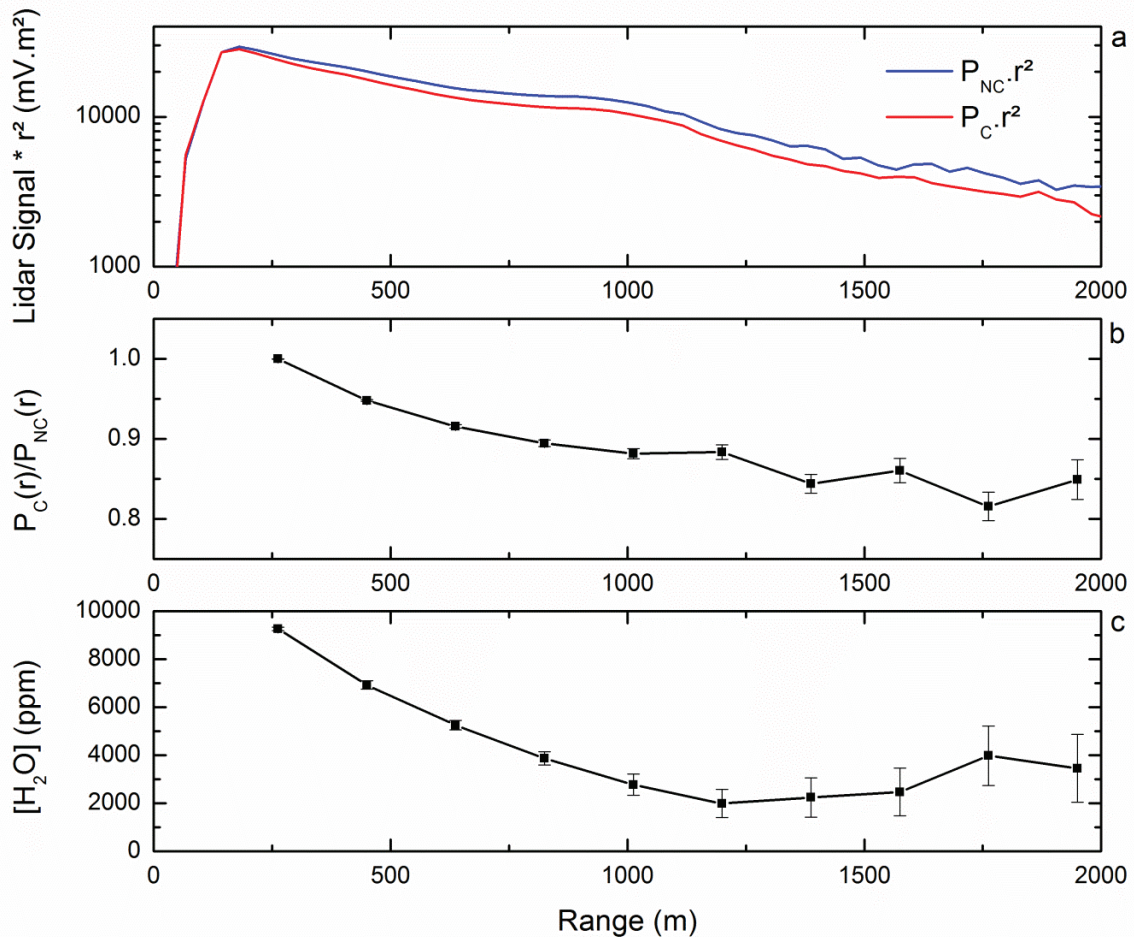


Fig. 5.27: OCS-lidar water vapor measurement in the AME-configuration performed at Lyon on December 19th 2012 at 19h UTC. (a) Range-corrected OCS-lidar signals, due to the water vapor presence $P_C(r)$ exhibits a higher extinction when compared to $P_{NC}(r)$. (b) The ratio P_C/P_{NC} is no longer constant with r , as it was in the control experiment. (c) Retrieved water vapor mixing-ratio profile obtained using the retrieval algorithm. The relative humidity observed with a standard hydrometer at ground level was equal to 85 % and the temperature was 280 K, corresponding to a water vapor mixing-ratio of 8400 ppm at ground level.

5.4.2 Water vapor mixing-ratio measurements in the AMR-configuration

Performing the bias control experiment corresponding to $M_C(\lambda) = M_{NC}(\lambda)$ is much more complex in the AMR-configuration since in this configuration, the detector is composed of two optical channels, as detailed in Section 5.2.2. To ensure that the correlated and the non-correlated channels are properly set, lidar measurements have been carried out without any interference filters, i.e. $M_C(\lambda) = M_{NC}(\lambda) = 1$. The corresponding range-corrected signals and their ratio are displayed in Figure 5.28, which is equivalent to Figure 5.26, but for the AMR-configuration.

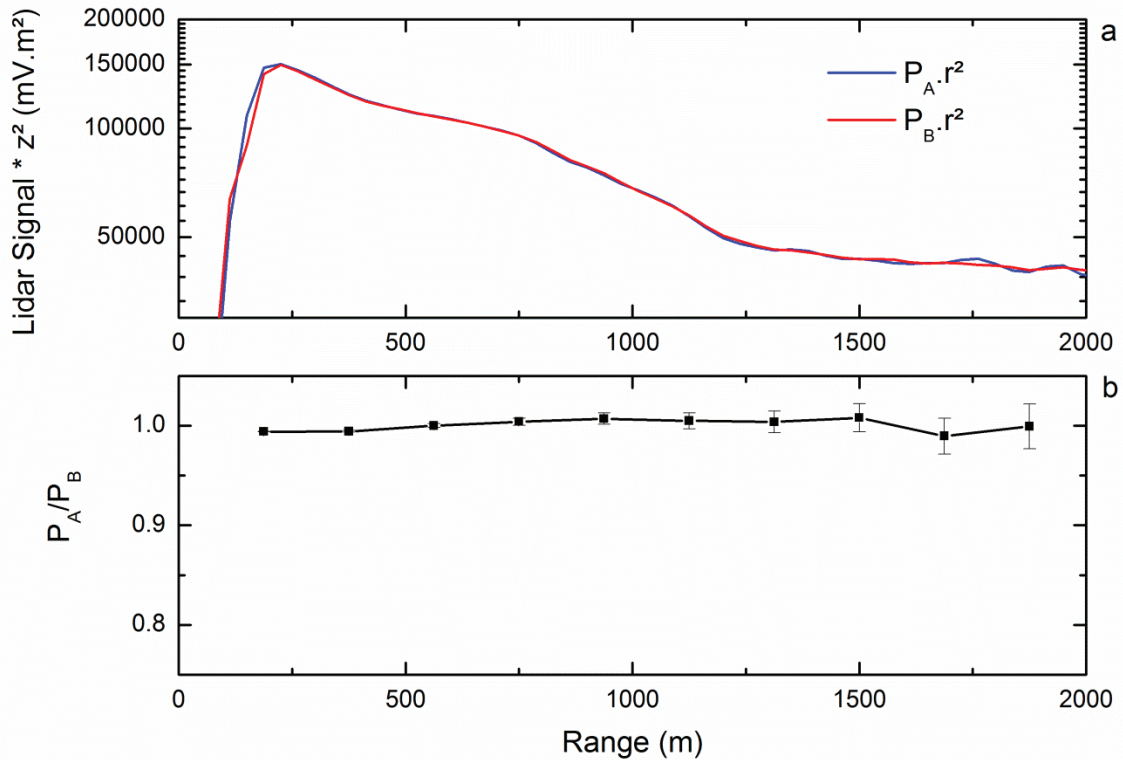


Fig. 5.28: Control bias experiment in the AMR-configuration, performed at Lyon on November 6th 2012 at 22h UTC. (a) Range-corrected OCS-lidar signals P_A (blue) and P_B (red) are obtained with two detection channels (A and B) with a 40 m range resolution. (b) Ratio of both OCS-lidar signals with respective error bars, derived from the statistical fluctuations of the OCS-lidar signals for a ground level relative humidity of 76 % and a 283 K temperature.

Then, the amplitude modulation functions have been applied to the broadband laser pulse to achieve the AMR-configuration, using the same measurement duration, location and pointing as those described for the AME-configuration. The amplitude modulations functions $M_C(\lambda)$ and $M_{NC}(\lambda)$ used in this experiment are identical to those displayed in Figure 4.5. The

corresponding OCS-lidar signals, the range-dependent P_C/P_{NC} ratio and the retrieved water vapor mixing-ratio profile are presented in Figure 5.29. As expected, the correlated signal $P_C(r)$ undergoes a higher extinction than the non-correlated signal $P_{NC}(r)$, and, consequently, the ratio $P_C(r)/P_{NC}(r)$ decreases with range r . Error bars retrieved from the Monte-Carlo numerical simulation lead to a sensitivity of $2 \cdot 10^5$ ppm.m at a 2 kilometers range. The retrieved water vapor mixing-ratio profile starts at $(7\,850 \pm 55)$ ppm ($RH = 64 \pm 0.5\%$) at a 260 meters range and drops around $(4\,000 \pm 300)$ ppm ($RH = 33 \pm 3\%$) from 500 to 1000 meters. It then reaches a minimum of $(1\,250 \pm 650)$ ppm ($RH = 10 \pm 5\%$) at a 1400 meters range before increasing after 1600 meters up to $(7\,500 \pm 1\,000)$ ppm.

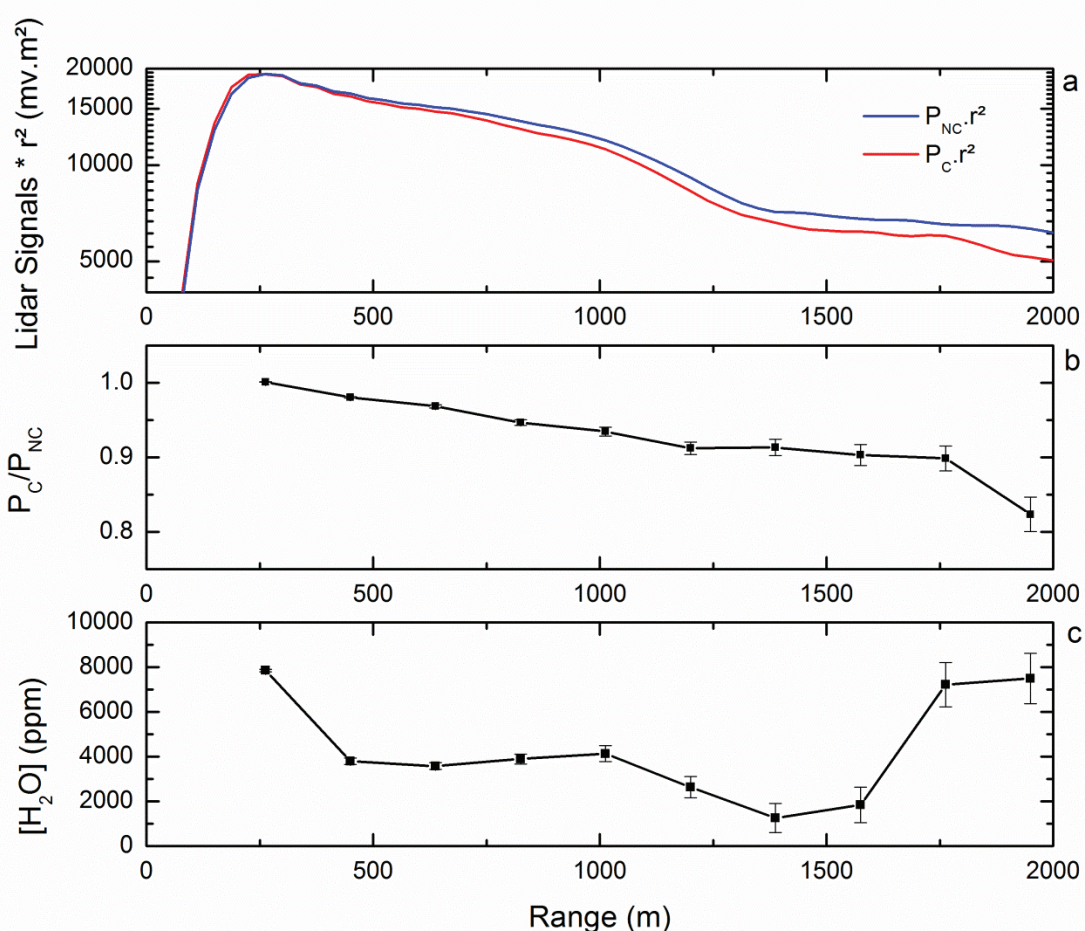


Fig. 5.29: OCS-lidar water vapor measurement in the AMR-configuration performed at Lyon on November 5th 2012 at 22h UTC. (a) Range-corrected OCS-lidar signals, due to the water vapor presence, $P_C(r)$ exhibits a higher extinction when compared to $P_{NC}(r)$. (b) The ratio P_C/P_{NC} is no longer constant with r , as it was in the control experiment. (c) Retrieved water vapor mixing-ratio profile obtained using the retrieval algorithm. Ground level relative humidity and temperature are respectively equal to 76 % and 283 K, corresponding to a water vapor mixing-ratio of 9200 ppm at ground level.

5.4.3 Discussion

In both configurations, sources of statistical signal fluctuations are due to shot noise, detection noise and background noise. These sources of noise limit the measurement range to a maximum of 2 kilometers. The signal-to-noise ratio depending on the range is, however, two times higher in the AMR than in the AME-configuration due to the AOPDF acceptance energy, limited to 30 micro-joules due to non-linear effects (see Section 5.2.1b).

The preliminary bias control experiment, operated by applying the same amplitude modulation functions, ensures that systematic errors are negligible when compared with the statistical fluctuations of the OCS-lidar signals. In both configurations, this control experiment also ensures that the signal acquisition process and trigger system are not a bias source. For the specific case of the AMR-configuration, this control experiment also helps to check that the two detection channels experience the same geometrical overlap function.

The two different experimental configurations AMR and AME achieve water vapor measurements in the PBL with the OCS-lidar methodology. The OCS-lidar signals taken two different days lead to water vapor mixing-ratios that are in the same range. Our measurements show water vapor mixing-ratios varying from 9 250 ppm (RH = 93 %) at a 250 meters range (corresponding to a 35 meters altitude), down to 1 250 ppm (RH = 10 %) at a range of 1 500 meters (corresponding to a 210 meters altitude). The water vapor mixing-ratio increases at a 1 800 meters range; this most likely corresponds to the water evaporation process above the 100 meters wide Rhône river.

These first experimental results show that the retrieved water vapor mixing-ratio profiles are comparable and in both cases, correspond to realistic relative humidity profiles described by a standard atmosphere. Moreover, near ground level, comparison between in-situ hydrometer at ground level and OCS-lidar measurements at the lower altitude (≈ 30 meters) shows similar concentrations values within 15 %. It shows that the OCS-lidar methodology is able to monitor water vapor mixing-ratios in the PBL. When comparing the main advantages / drawbacks of each configuration, it is clear that the AMR-configuration has a higher signal-to-noise due to the use of a higher laser energy. However, it should be noted that this configuration raises a much more complex detection set-up and that the corresponding sources of supplementary biases have to be checked. An accurate knowledge of the spectral

response of each optical component and a very accurate alignment of the two detection channels are hence required. In addition, the backscattered photons, once they have been collected by the telescope and made parallel with a lens, still exhibit a non-negligible divergence of around 5×10^{-2} radian, which may slightly broaden the interference filter transmissions towards shorter wavelengths, as detailed in Section 5.2.2b. Except for field measurements in which high temperature variations are involved, the modification of the spectral behavior of the interference filter due to temperature gradients should be negligible since the spectral drift due to temperature gradients is only equal to 0.025 nm per °C. In the AME-configuration, the sources of bias on the retrieved mixing-ratio are from that point of view minimized, since the emission and the reception are performed with the same equipment for both the correlated and the non-correlated signals. Despite the AOPDF limits the laser energy, it offers a great versatility: any amplitude modulation, including multiple transmission peaks or gaps, can be faithfully shaped within the spectral resolution of the AOPDF, equal to 0.5 nanometer in the visible spectral range (1.1 nanometers in the infrared spectral region).

5.5 Preliminary results in the infrared spectral range

At the time of writing, the OCS-lidar experiment in the infrared spectral range for measuring methane concentration profiles is under progress. Preliminary experiments have been achieved and are presented in this section. More precisely, the experimental set-up used in the infrared spectral range is described where a new telescope has been developed. Then, the first lidar signals obtained in the infrared spectral region are presented for two different laser sources. Finally, the first amplitude modulation operated in the infrared with an AOPDF are displayed and discussed.

5.5.1 Experimental set up for methane mixing ratios retrieval with OCS-lidar

Measurement of methane concentration by using the OCS-lidar methodology has been planned by using a methane source on the ground located at 200 m from the laser source. To

achieve these field measurements, a new telescope has been developed to perform lower range measurements. To obtain an overlap function that allows to efficiently collect the light backscattered above 100 meters range, an off-axis lidar using a 11 cm telescope with a shorter focal length (450 mm) has been designed, built and aligned. Figure 5.30 shows a picture of the telescope.

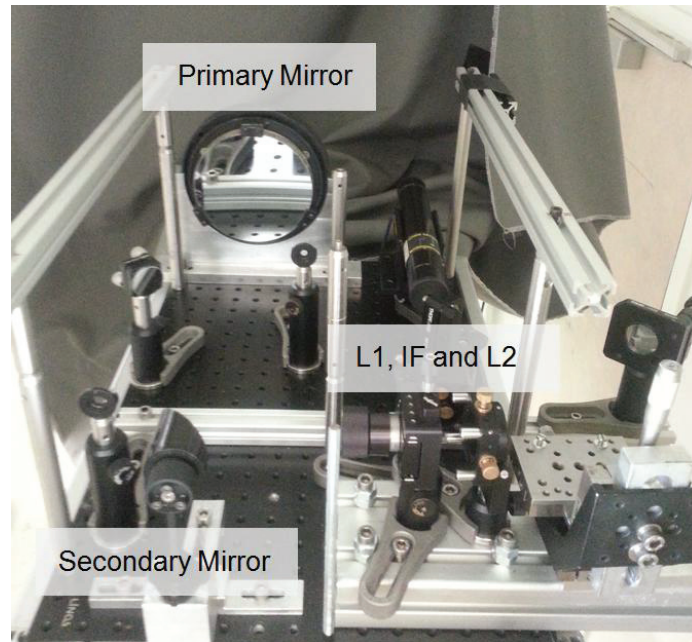


Fig. 5.30: Picture of the 11 cm diameter Newtonian telescope. L1 is the divergence lens used to make the backscattered light parallel, IF is the interference filter used to limit the influence of the background; finally L2 is a converging lens to focus the light on the InGaAs APD detector.

The optical layout of the infrared lidar is presented in Figure 5.31.

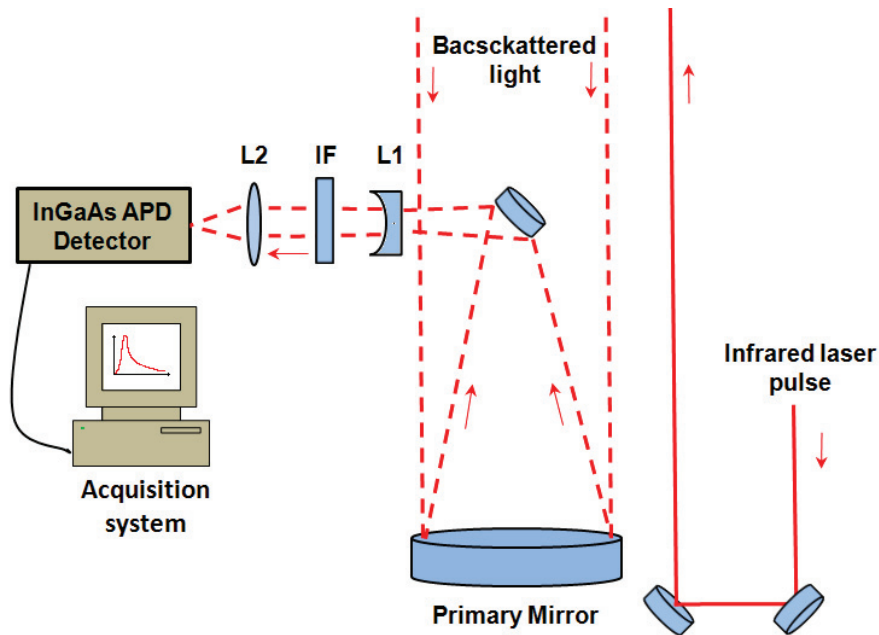


Fig. 5.31: Optical layout of the infrared lidar system developed for the measurement of methane using the OCS-lidar methodology.

5.5.2 First infrared lidar signals

In the infrared spectral range, many factors lead to a lower lidar signal. First, the molecular backscattering coefficient, following a $1/\lambda^4$ wavelength dependency, is greatly reduced when compared with the backscattering coefficient obtained in the visible spectral range, typically from 10^{-6} down to $10^{-8} \text{ m}^{-1} \cdot \text{sr}^{-1}$. The particle backscattering coefficient is also lower, with typical value around $10^{-7} \text{ m}^{-1} \cdot \text{sr}^{-1}$, which is around 10 times lower than in the visible spectral range. Moreover, the detector quantum efficiency and the response time of infrared detectors is not as high as for photomultiplier detectors used in the visible spectral range.

Hence, the alignment of a lidar system in the infrared with a micro joule laser pulse may turn out to be extremely complicated. Therefore, to overcome these difficulties, a Nd:YAG laser emitting at 1064 nm has been used to generate higher energy pulses, in the range of 90 mJ/pulse with a 10 Hz repetition rate.

Figure 5.32 presents the first lidar measurement operated at 1064 nm with a 0.3 nm bandwidth interference filter. The lidar signal is the result of 200 laser shots and is presented with a 3.75 m spatial resolution.

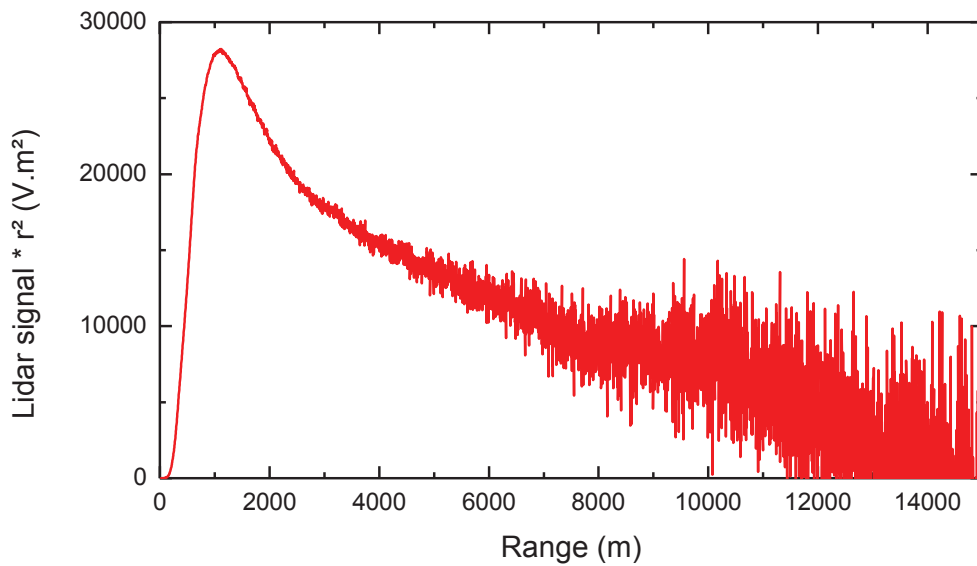


Fig. 5.32: Range corrected lidar signal at 1064 nm. The signal has been measured with an 11 cm telescope, 90 mJ/pulse and 200 laser shots.

Once the lidar system has been properly aligned thanks to the Nd:YAG laser, the first lidar measurements using the micro-joule energy femtosecond laser have been performed. Figure 5.33 presents the first measurement using the spectrally broadband laser source in the infrared spectral range at a 1.5 μm wavelength. The signal results from 400 000 laser shots with a 1 kHz repetition rate and 500 μJ per pulse and is shown in Figure 5.33.

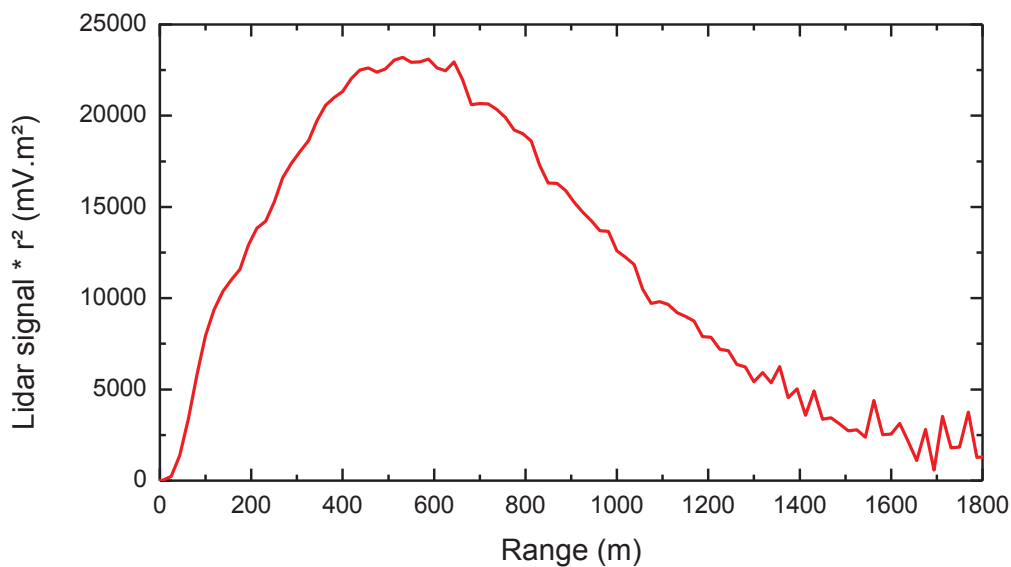


Fig. 5.33: Range corrected lidar signal at 1500 nm. The signal results of 400 000 laser shots with 500 μJ per pulse.

5.5.3 Amplitude modulation in the infrared spectral range

The first amplitude modulation functions have now been achieved on the femtosecond pulse at 1 500 nm. In order to evaluate the minimum spectral resolution and the maximum transmission of the device, preliminary measurements have been performed and are presented in this section.

Figure 5.34 presents the experimental setup used to achieve these measurements. The power density spectrum has been measured by using an infrared spectrometer based on an InGaAs linear array with an optical fiber to collect the light.

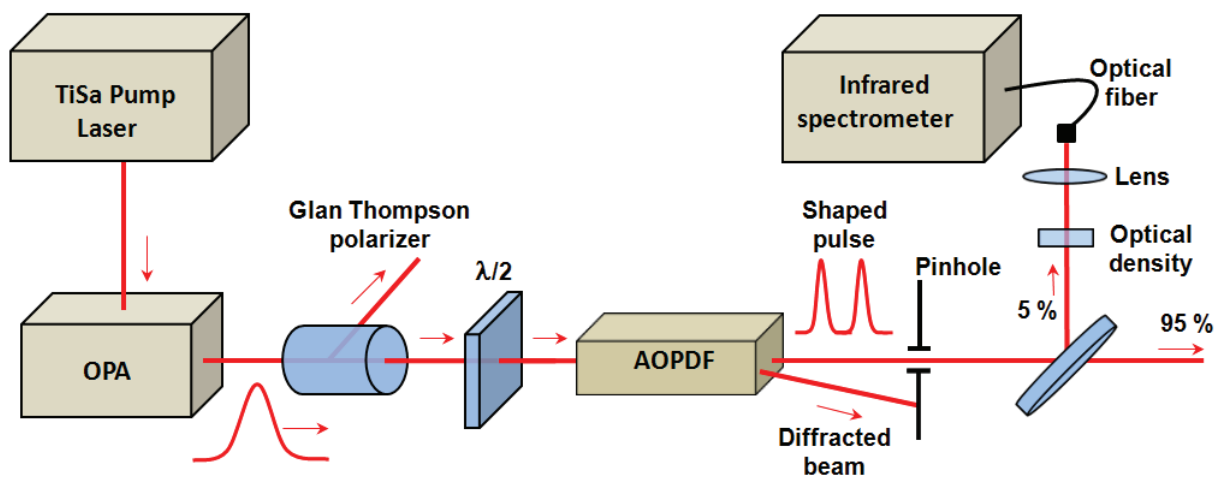


Fig. 5.34: Optical layout used to measure the power spectral density of the laser pulse after the amplitude modulation operated by the AOPDF.

To test the dazzler specifications in the infrared spectral range, measurements have been made to control the minimum spectral resolution, the minimum gap between two peaks in the modulations, and the maximum transmission or maximum extinction.

Figure 5.35 presents the power density spectrum of the initial laser pulse and the pulse once it has been modulated by the AOPDF. The latter has been programmed so that only two narrow peaks are transmitted. The minimum bandwidth of a transmission peak has been found around 1.1 nm with a transmission of 70 %. When programming a bandwidth below 1.1 nm, the transmission significantly drops without any significant change in the actual peak bandwidth. When the two peaks are too close, loss in the quality modulation appears. We found a minimum separation between the two central wavelength peaks of 4.6 nm.

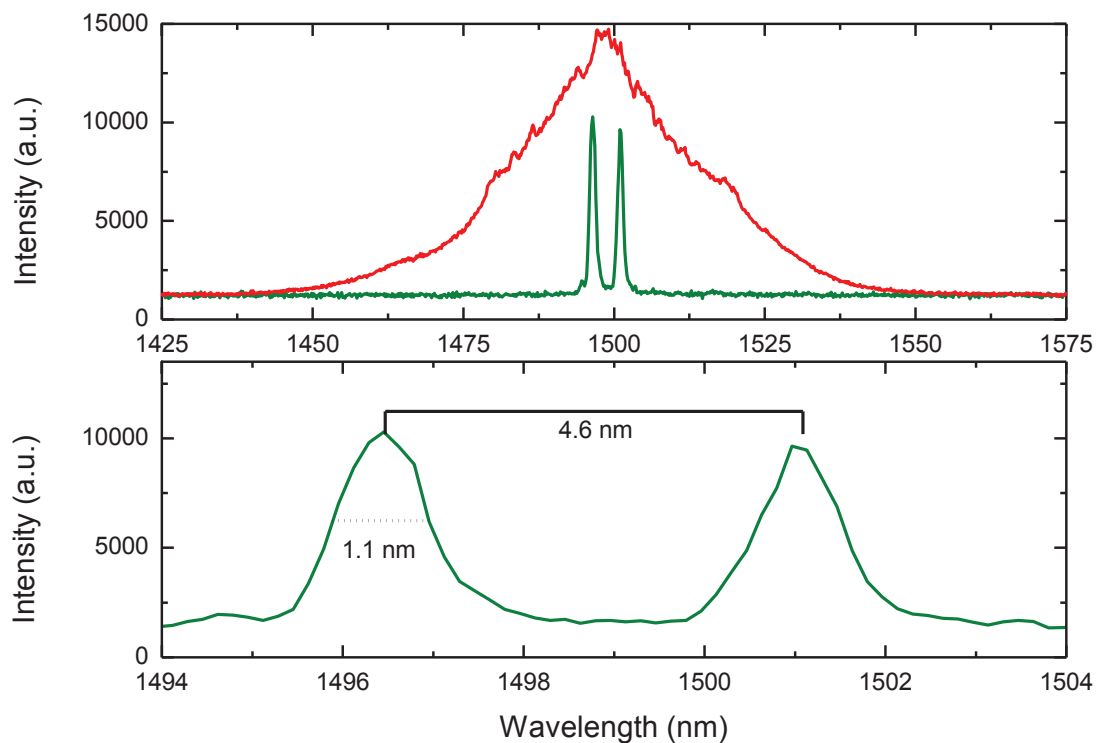


Fig. 5.35: Power density spectra of the initial laser pulse (red) and the modulated pulse after the AOPDF (green). The bottom graph shows a zoom on the power density spectrum of the modulated pulse. In this case, the AOPDF has been set so two peaks, as narrow and close to each other as possible without any loss in the amplitude modulation quality, are obtained.

The AOPDF can also be programmed to generate “holes” in the spectrum. There, most of the initial pulse is transmitted except a part of the spectrum that is diffracted. Figure 5.36 shows the power density spectrum when such amplitude modulation is applied. The two spectra presented there may look noisy. Actually, at the time of the measurement, the infrared spectrometer suffered from unexplained amplitude modulations. The most narrow transmission hole has been found to be around 2.5 nm, with a transmission of 15 %. The minimum transmission drops in the range of the percent when the extinction peak is broader than 2.5 nm.

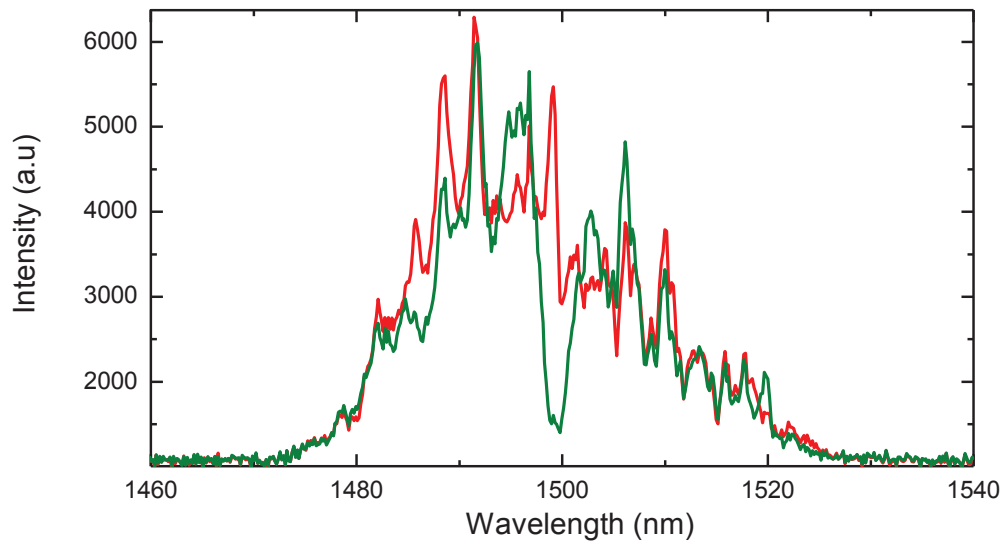


Fig. 5.36: Power density spectra of the initial laser pulse (red) and the modulated pulse (green). In this case, a transmission “hole” has been programmed on the AOPDF. At the time of measurement, strong amplitude modulations occurred on the infrared spectrometer, explaining the strong modulation on both spectra.

This chapter has presented the experimental aspect of this thesis. First, the experimental setup has been described. It is composed of a Ti-Sa femtosecond laser used to pump an OPA and the detection system based on a 30 cm diameter Newtonian telescope. Two different ways of applying the amplitude modulation functions are then described, on the one hand by using an active amplitude modulator to achieve the amplitude modulation on the laser pulse before it is sent in the atmosphere (AME-configuration), and on the other hand by filtering the backscattered light using passive interference filters on a two channels detection system (AMR-configuration).

Then, the first measurements using the OCS-lidar methodology are presented where water vapor profiles are retrieved in the planetary boundary layer up to 2 km range in the visible spectral range. The two different setups to apply the amplitude modulation have been tested and compared. In both the AME and AMR-configurations, the OCS-lidar methodology allows to retrieve range-resolved trace gas concentrations in the atmosphere.

The preliminary results regarding the measurement of methane concentrations in the infrared spectral range are also presented. First, measurements using a micro Joule infrared lidar are presented together with the first amplitude modulations in this spectral range. These first experimental results are very encouraging and should shortly lead to methane concentration profile measurements.

Chapter 6

Conclusion and outlook

This PhD thesis relates the work done on the development of a new optical methodology, called OCS-lidar, to evaluate the concentration of atmospheric trace gases. This methodology is based on the coupling of two existing technologies, a spectrally broadband lidar system and optical correlation spectroscopy (OCS), giving rise to the OCS-lidar methodology.

The main topic developed in this thesis is to study the feasibility and the sensitivity of this new methodology to remotely evaluate the range-resolved concentration profile of atmospheric trace gases. Since it is based on molecular absorption spectroscopy, an account on the interaction between light and molecules in the gas phase is given in Chapter 2, where the fundamental gas spectral absorption mechanisms are briefly presented with emphasis on the line shape profile and line strengths, including sensitivity to pressure and temperature variations. Hence, the major sources of line broadening are presented and their contributions are discussed, showing that spectrally-integrated optical measurements are weakly sensitive to pressure variations, which is new and very interesting for applications purposes. The end of the thesis being focused on either methane or water vapor measurements, the spectral properties of these two gases are detailed, on the basis of the HITRAN database, which is also introduced and used in this chapter.

Chapter 3 reviews the principle and the formalism on which the OCS-lidar methodology is based. As a first step, the historical background that led to the presented OCS-methodology is described, followed by the OCS-formalism. To illustrate the OCS-methodology, a brief numerical simulation for methane concentration measurements is presented. Then, the lidar technique is introduced: its principle and formalism are reviewed and extended to spectrally broadband light sources, such as femtosecond laser sources. The lidar system, designed, developed and implemented in the framework of this thesis is described. The first experimental measurements are compared with another lidar system during a Saharan dust episode. These results show that our new lidar system, based on a spectrally broadband laser, is operational. Finally, the coupling of the OCS-methodology with the broadband lidar is presented, together with the algorithm allowing the trace gas concentration retrieval. As detailed in Chapter 3, this thesis presents a new theoretical procedure to derive the trace gas concentration. In this new development, the trace gas concentration appears to be accessible by solving a third order polynomial equation, obtained from the ratio of the correlated and non-correlated OCS-lidar signals.

To test the ability of this new methodology to remotely monitor atmospheric traces gases, Chapter 4 presents the numerical model that has been developed to generate OCS-lidar signals for a realistic atmospheric trace gas concentration and a realistic set of lidar parameters, including random noise considerations. The case study of methane greenhouse gas, present in urban, agricultural and industrial areas, has been numerically treated in the infrared spectral range. Three different methane input profiles, corresponding to methane mixing ratio usually encountered in urban areas, are used to evaluate the statistical fluctuations on the retrieved methane mixing ratio. A similar study has been achieved in the visible spectral range, using in this case water vapor measurements. In particular, we functionalized the optical and electro-optical parts of the lidar device and took into account the different sources of noise (from the detector, the sky background radiation and the spectral and amplitude drifts from the laser source), by applying the statistical Monte-Carlo algorithm to produce a realistic OCS-lidar signal containing noise. Our numerical results on the methane case study show that methane background concentrations can be detected up to 1.5 kilometers with a 100 meters range resolution and with a relative error of 20 %. Moreover, the accuracy on the retrieved methane

mixing ratio can be improved by range averaging. For water vapor mixing ratio retrievals, our numerical results show that the sensitivity reaches 200 000 ppm.m at a 2 000 meters range, corresponding to a detection limit of 1 000 ppm with a 200 meters spatial resolution when using micro energy pulses.

The sources of possible systematic biases have also been studied through the OCS-lidar numerical model. In a first time, the bias due to the OCS-lidar algorithm has been evaluated, from there two different corrections have been proposed to significantly reduce this bias, leading in both cases to a relative concentration bias which is lower than 10^{-5} . Systematic errors due to possible temperature and pressure variations along the optical path are also studied. The OCS-lidar methodology presents a very low bias regarding pressure variations: within the troposphere, no significant bias should occur due to the pressure change. Temperature variations induce a stronger bias mostly due to the temperature dependence of the absorption line strength. It is clear that to retrieve the concentration of a trace gas with a high precision, the atmospheric temperature must be accurately known. As an example, for methane, a 10 K error on the temperature may lead to a 4 % systematic error on the retrieved methane concentration. Moreover, the bias due to the presence of possible interfering species has also been evaluated. When considering a standard composition of the atmosphere, only water vapor may significantly interfere with methane measurements, leading to a positive concentration bias. However, when the methane concentration reaches 10 ppm or more, the bias due to the presence of water vapor drops under 1 %.

Finally, the numerical model has been used to optimize the experimental parameters to decrease the statistical fluctuations on the retrieved concentration. The central wavelength of the laser as well as the amplitude modulator parameters can be adjusted by using an iterative procedure. Hence, based on the OCS-lidar numerical model, this section described how to properly choose the amplitude modulation functions used in the OCS-lidar methodology.

Chapter 5 experimentally demonstrates the ability of the OCS-lidar methodology to measure the water vapor content in the lower atmosphere. This is the first experimental achievement of the femtosecond broadband OCS-lidar methodology with a ground based micro-pulse lidar.

At first, the different components used in this experiment are described and their specifications, that have been measured and experimentally controlled, are given. The source is composed of the TiSa femtosecond laser used to pump an optical parametric amplifier. This laser source has been chosen to produce a spectrally stable light source emitting in the near

infrared spectral range tunable from 300 to 2 000 nanometers. Its energy, in the range of hundreds of micro-joule per pulse, fulfills the OCS-lidar signal to noise ratio requirement presented in [Thomas et al. 2012] and especially for water vapor measurements as presented in [Thomas et al. 2013]. The amplitude modulation has been operated by using either active or passive optical components. On the one hand, the active amplitude modulator, namely an acousto optical programmable dispersive filter (AOPDF), is presented. The spectral resolution is in the range of a nanometer and allows to easily control the amplitude modulation functions. However, the energy threshold limits the energy that can be used in the OCS-lidar experiments. On the other hand, the interference filters used for the passive amplitude modulation are specified. A numerical simulation is presented to control how the transmission of such interference filters behaves when the incident light beam has a large dispersion as it is the case in a telescope. The optical layout of the reception system, composed of a Newtonian telescope, interference filters, focusing lenses and an optical detector is also given. The acquisition system recording the signal emitted by the detector is composed of a transient record with a 40 MHz acquisition rate.

Then, the first experimental results are presented. It is shown that for experimentally achieving the OCS-lidar methodology, two experimental configurations are possible, namely the AME-configuration, where the amplitude modulation functions are applied before the backscattering process occurs (i.e. at the emission, AME stands for Amplitude Modulation at the Emission), and the AMR-configuration, where the modulation achieving the optical correlation spectroscopy is performed at the reception (AMR stands for Amplitude Modulation at the Reception). These two configurations have been presented and tested for water vapor mixing-ratio measurements. In the AME-configuration, we used an active AOPDF to achieve the amplitude modulation before the laser pulse be sent into the atmosphere while, in the AMR-experimental configuration, passive interference filters have been introduced in the lidar detector to achieve the spectral correlation.

These first OCS-lidar measurements exhibit water vapor mixing ratios varying from 1 000 to 10 000 ppm. The accuracy on the retrieved water vapor mixing ratios varies with the range r from the lidar receiver and with the water vapor content. In the AME-configuration, it reaches 40 % at a 2 kilometers range for a 3 500 ppm water vapor mixing ratio. In the AMR-configuration, this accuracy reaches 15 % at a 2 kilometers range for a 7 500 ppm water vapor mixing ratio.

Finally, the last section of Chapter 5 presents the preliminary results obtained in the infrared spectral region to retrieve range-resolved methane concentration profiles. Since the previous lidar system was operating in the visible range, preliminary tests have been performed to measure the infrared signal with an InGaAs APD. In order to counterbalance the low quantum efficiency of such detector (compared with photodiodes in the visible), a Nd:YAG laser emitting nanosecond laser pulses with 150 mJ at 1 064 nm wavelength has been used. This first experiment has provided an opportunity to optimize the lidar-setup in order to achieve infrared micro joule lidar measurement. First measurements using the broadband micro joule laser pulse at 1 500 nm are also presented in this section, with a range of 1 500 meters. In the meantime, amplitude modulation of broadband laser pulses in the infrared spectral region has been studied, the first measurement of laser pulse spectrally shaped by the AOPDF are presented and show a minimum spectral resolution of 1.1 nm.

At the time of writing, the prospects of this work on OCS-lidar experiments are numerous.

The accuracies on water vapor concentration measurements presented in Chapter 5, performed with a 250 meters range resolution, can be reached because measurements are done in the PBL where a high content of molecules and particle matter favors scattering processes. In the higher part of the atmosphere, where lower water vapor content and lower particle matter mixing-ratio are present, the OCS-lidar methodology could be applied but should be performed in the near infrared spectral range where water vapor absorption bands are stronger to balance the lower water vapor mixing-ratio.

In order to reduce the statistical error on the retrieved mixing ratio, the laser energy should be increased. This limitation due to the AOPDF is related to non-linear effects which occur in response to a too high intensity. Therefore, the energy threshold can be raised on the one hand, by increasing the pulse duration with a pulse stretcher leading to a lower instantaneous power, and on the other hand, by increasing the cross section of the laser beam to lower the intensity. More complex amplitude modulations can be operated with the AOPDF, for example, by combining more than two different amplitude modulation functions, multiple gases could be simultaneously monitored as long as they present sufficiently high absorption bands within the spectral width of the broadband laser source. In addition, this versatility would enable to greatly decrease the bias due to the possible presence of interfering gases, by adapting the amplitude modulation functions to reduce their extinctions.

In the infrared region, the difficulty rises from the energy threshold of the AOPDF, which makes the OCS-lidar signal harder to measure. However, most of these difficulties have been overcome and measurements of methane concentration profile are currently under progress. In conclusion, the OCS-lidar methodology offers great possibilities for atmospheric trace gases remote sensing. As it is brand new, many developments and improvements in terms of sensitivity and accuracy can be expected.

List of personal publications

David G., A. Miffre, B. Thomas, P. Rairoux, Sensitive and accurate dual wavelength UV-VIS polarization detector for optical remote sensing of tropospheric aerosols, *Appl. Phys. B*, 108, 197, (2012).

David G., B. Thomas, T. Nousiainen, A. Miffre, P. Rairoux, Retrieving simulated volcanic, desert dust, and sea-salt particle properties from two / three-component particle mixtures using UV-VIS polarization Lidar and T-matrix, *Atmos. Chem. Phys.*, 13, 6757, (2013a).

David G., B. Thomas, E. Coillet, A. Miffre, P. Rairoux, Polarization-resolved exact light backscattering by an ensemble of particles in air, *Opt. Express*, (accepted). (2013b).

Dupart Y., S. M. King, B. Nekat, A. Nowak, A. Wiedensohler, H. Herrmann, G. David, B. Thomas, A. Miffre, P. Rairoux, B. D'Anna, C. George, Mineral dust photochemistry induces nucleation events in the presence of SO₂, *Proceedings of the National Academy of Sciences of the United States of America*, doi: 10.1073/pnas.1212297109, (2012).

Miffre A., G. David, B. Thomas, P. Rairoux, Atmospheric non-spherical particles optical properties from UV-polarization Lidar and scattering matrix, *Geophys. Res. Lett.*, 38, L16804, (2011).

Miffre A., G. David, B. Thomas, M. Abou Chacra, P. Rairoux, Interpretation of accurate UV polarization lidar measurements: application to volcanic ash number concentration retrieval, *J. Atm. Ocean. Tech.*, 29, 558, (2012a).

Miffre A., G. David, B. Thomas, P. Rairoux, A.M. Fjaeraa, N.I. Kristiansen, A. Stohl, Volcanic aerosol optical properties and phase partitioning behavior after long-range advection characterized by UV-Lidar measurements, *Special Issue on the Eyjafjallajökull Icelandic Volcano*, *Atmos. Env.*, 48, 76, (2012b).

Thomas B., A. Miffre, G. David, J-P. Cariou, P. Rairoux, Remote sensing of trace gases with optical correlation spectroscopy and Lidar: Theoretical and numerical approach, *Appl. Phys. B*, 108, 689, (2012).

Thomas B., G. David, C. Anselmo, J-P. Cariou, A. Miffre and P. Rairoux, Remote sensing of atmospheric gases with optical correlation spectroscopy and lidar: first experimental result on water vapor profile measurements, *Appl. Phys. B*, doi: 10.1007/s00340-013-5468-4 (2013a).

Thomas B., G. David, C. Anselmo, E. Coillet, A. Miffre, J. P. Cariou, P. Rairoux, Remote sensing of methane with broadband laser and optical correlation spectroscopy on the Q-branch of the 2v₃ band, *Jour. Mol. Spectrom.*, doi: 10.1016/j.jms.2013.05.015, (2013b).

References

A

Abshire, J. B., H. Riris, G. R. Allan, S. R. Kawa, X. L. Sun, W. E. Hasselbrack, C. Weaver, M. R. Rodriguez, J. Mao, Measuring atmospheric CO₂ for the NASA ascends mission: the CO₂ laser sounder approach, 2012 IEEE international geoscience and remote sensing symposium (IGARSS) Book Series: IEEE International Symposium on Geoscience and Remote Sensing IGARSS Pages: 5665-5668 (2012).

Akhmanov S. A., V. A. Vysloukh, A. S. Chirkin, Optics of femtosecond laser pulses, American Institute of Physics, New York, (1992).

Anderson G., S. Clough, F. Kneizys, J. Chetwynd, E. Shettle, AFGL Atmospheric Constituent Profiles (0 – 120 km), Air Force Geophysics Laboratory, Environmental Research Paper No. 954. (1986).

Andrew E., J.A. Ogren, P. Bonasoni, A. Marinoni, E. Cuevas, S. Rodriguez, J.Y. Sun, D.A. Jaffe, E.V. Fischer, U. Baltensperger, E. Weingartner, M.C. Coen, S. Sharma, A.M. Macdonald, W.R. Leitch, N.H. Lin, P. Laj, T. Arsov, I. Kalapov, A. Jefferson, P. Sheridan, Climatology of Aerosol Radiative Properties in the Free Troposphere., Atmos. Res. 102, 365, (2011).

Ansmann, A., A. Petzold, K. Kandler, I. Tegen, M. Wendisch, D. Müller, B. Weinzierl, T. Müller, J. Heintzenberg, Saharan Mineral Dust Experiments SAMUM-1 and SAMUM-2: What have we learned?, Tellus Series B-Chemical And Physical Meteorology, 63, 403, doi: 10.1111/j.1600-0889.2011.00555.x, (2011).

Armstrong J. A., N. Bloembergen, J. Ducuing, P. S. Pershan, Interactions between light waves in nonlinear dielectric, Phys. Rev., 127, 1918 (1962).

B

Baduel C. , M.E. Monge, D. Voisin, J.L. Jaffrezo, C. George, I. El Haddad, N. Marchand, B. D'Anna, Oxidation of atmospheric humic like substances by ozone: A kinetic and structural analysis approach, Environ. Sci. Technol., 45, 5238 (2011).

Bandrauk A D., Y. Fujimura, R. J. Gordon, Laser Control and Manipulation of Molecules, 1st Ed., ISBN-10: 0841237867, (2002).

Banwell C. N., E. M. McCash, Fundamentals of molecular spectroscopy: 4th Ed. McGraw-Hill, London. ISBN:0-07-707976-0. (1994).

Bernath P. F., The spectroscopy of water vapour: Experiment, theory and applications, Phys. Chem. Chem. Phys., 4, 1501, doi: 10.1039/B200372D (2002).

Berner R. A., Z. Kothavala, GEOCARB III: A revised model of atmospheric CO₂ over Phanerozoic time. *American Journal of Science*, 304, 397, (2001).

Biémont E., *Spectroscopie moléculaire : structures moléculaires et analyse spectrale*, Bruxelles : De Boeck, ISBN 978-2-8041-5065-5, (2008).

Bohren C. F., D. R. Huffman, *Absorption and Scattering of Light by Small Particles*, doi: 10.1002/9783527618156, (2004).

Bond T. C., S. J. Doherty, D. W. Fahey, P. M. Forster, T. Berntsen, B. J. DeAngelo, M. G. Flanner, S. Ghan, B. Kärcher, D. Koch, S. Kinne, Y. Kondo, P. K. Quinn, M. C. Sarofim, M. G. Schultz, M. Schulz, C. Venkataraman, H. Zhang, S. Zhang, N. Bellouin, S. K. Guttikunda, P. K. Hopke, M. Z. Jacobson, J. W. Kaiser, Z. Klimont, U. Lohmann, J. P. Schwarz, D. Shindell, T. Storelvmo, S. G. Warren, C. S. Zender, Bounding the role of black carbon in the climate system: A scientific assessment, *Journal of Geophysical Research: Atmospheres*, 118, 5380, doi:10.1002/jgrd.50171, (2013).

Borg, L. A., R. E. Holz, D. D. Turner, Investigating cloud radar sensitivity to optically thin cirrus using collocated Raman lidar observations, *Geophysical Research Letters*, 38, doi: 10.1029/2010GL046365, (2011).

Brewer R. G, Coherent optical spectroscopy, *Bulletin of the American Physical Society*, 18, 1595, (1973).

Browell E. V., S. Ismail, B. E. Grossmann, Temperature sensitivity of differential absorption lidar measurements of water vapor in the 720-nm region, *Applied Optics*, 30, 1517, (1991).

Burlakov, V.D., S. I. Dolgii, A. P. Makeev, A. V. Nevzorov, O. A. Romanovskii, O. V. Kharchenko, A Differential-absorption lidar for ozone sensing in the upper atmosphere-lower stratosphere, *Instruments and Experimental Techniques*, 53, 886-889, doi: 10.1134/S0020441210060229, (2010).

C

Chambers A.K., M. Strosher, T. Wooton, J. Moncrieff, P. McCready, Direct measurement of fugitive emissions of hydrocarbons from a refinery, *J. Air Waste Manage. Assoc.*, 58, 1047, (2008).

Chambers P., *A Study of a Correlation Spectroscopy Gas Detection Method*, University of Southampton, (2005).

Champion J.-P., M. Loëte, G. Pierre, *Spectroscopy of the Earth's Atmosphere and Interstellar Medium, Spherical Top Spectra.*, K. N. Rao and A. Weber Editors, Academic Press, New York, 339-422, (1992).

Charlson R. J., J. E. Lovelock, M. O. Andreae, S. G. Warren, Oceanic phytoplankton, atmospheric sulphur, cloud albedo and climate, *Nature*, 326, 655, (1987).

Cheung A., W. Johnstone, D. Moodie, Detection of acetylene gas using optical correlation spectroscopy, *Proceedings OFS-17 International Conference*, (2005).

Cheung A., W. Johnstone, D. Moodie, Gas detection based on optical correlation spectroscopy using a single light source, *Measurement Science & Technology*, 17, 1107, (2006).

Clough S.A., Kneizys F.X., Davies R.W., Line shape and water vapor continuum, *Atmos. Res.*, 23, 229, (1989).

Clough S.A., The water vapor continuum and its role in remote sensing, in *Optical Remote Sensing of the Atmosphere*, OSA Technical Digest Series, Washington DC, 76-78, (1995).

Cogan A. J., H. Boesch, R. J. Parker, L. Feng, P. I. Palmer, J.-F. L. Blavier, N. M. Deutscher, R. Macatangay, J. Notholt, C. Roehl, T. Warneke, D. Wunch, Atmospheric carbon dioxide retrieved from the Greenhouse gases Observing SATellite (GOSAT): Comparison with ground-based TCCON observations and GEOS-Chem model calculations, *J. Geol. Res. Atm.* 117, doi:10.1029/2012JD018087, (2012).

Cohen A. J., H. Ross Anderson, B. Ostro, K. D. Pandey, M. Krzyzanowski, N. Künzli, K. Gutschmidt, A. Pope, I. Romieu, J. M. Samet, K. Smith, The Global burden of disease due to outdoor air pollution, *Journal of Toxicology and Environmental Health*, 68, 1301, (2005).

Cook G. E., Pulse compression-key to more efficient radar transmission, *IEEE Proc. IRE* 48, 310 (1960).

Cormier J. G., Hodges J.T., Drummond J.R., Infrared water vapor continuum absorption at atmospheric temperatures. *J. Chem. Phys.*, 122, 114309, (2005).

Cox P. M., R. A. Betts, C. D. Jones, S. A. Spall, I. J. Totterdell, Acceleration of global warming due to carbon-cycle feedbacks in a coupled climate model, *Nature*, 408, 184, doi: 10.1038/35041539, (2000).

D

Dakin J.P., M.J. Gunning, P. Chambers, Z.J. Xin, Detection of gases by correlation spectroscopy, *Sens. Actuators B*, 90, 124 (2003).

David G., A. Miffre, B. Thomas, P. Rairoux, Sensitive and accurate dual wavelength UV-VIS polarization detector for optical remote sensing of tropospheric aerosols, *Appl. Phys. B*, 108, 197, (2012).

David G., B. Thomas, T. Nousiainen, A. Miffre, P. Rairoux, Retrieving simulated volcanic, desert dust, and sea-salt particle properties from two / three-component particle mixtures using UV-VIS polarization Lidar and T-matrix, *Atmos. Chem. Phys.*, 13, 6757, (2013a).

David G., B. Thomas, E. Coillet, A. Miffre, P. Rairoux, Polarization-resolved exact light backscattering by an ensemble of particles in air, *Opt. Express*, (accepted). (2013b).

De Villiers A. R., G. Ancellet, J. Pelon, B. Quennehen, A. Scharwzenboeck, J.F. Gayet, K.S. Law, Airborne measurements of aerosol optical properties related to early spring transport of mid-latitude sources into the Arctic, *Atmos. Chem. Phys.*, 10, 5011-5030, (2010).

Delanoe J., A. Protat, O. Jourdan, J. Pelon, M. Papazzoni, R. Dupuy, J. F. Gayet, C. Jouan, Comparison of airborne in situ, airborne radar-lidar, and spaceborne radar-lidar retrievals of polar ice cloud properties sampled during the polarcat campaign, *J. Atmo. Ocea. Tech.*, 30, 57-73, (2013).

Delmas R., G. Mégie, V.-H Peuch, *Physique et chimie de l'atmosphère*, Belin, (2005).

Di Girolamo P., D. Summa, R. F. Lin, T. Maestri, R. Rizzi, G. Masiello, UV Raman lidar measurements of relative humidity for the characterization of cirrus cloud microphysical properties, *Atmospheric Chemistry and Physics*, 9, 8799, (2009).

Dmitriev V. G., G. G. Gurzadyan, D. N. Nikogosyan, *Handbook of Nonlinear Optical Crystals*, 3rd ed., Springer Series in Optical Sciences, Berlin, (1997).

Dobson G. M. B., Forty Years' research on atmospheric ozone at oxford: a history, *Applied Optics*, 7, 387, (1968).

Dupart Y., S. M. King, B. Nekat, A. Nowak, A. Wiedensohler, H. Herrmann, G. David, B. Thomas, A. Miffre, P. Rairoux, B. D'Anna, C. George, Mineral dust photochemistry induces nucleation events in the presence of SO₂, *Proceedings of the National Academy of Sciences of the United States of America*, doi: 10.1073/pnas.1212297109, (2012).

E

H. Edner, S. Svanberg, L. Uneus, W. Wendt, Gas-correlation lidar, *Opt. Lett.*, 9, 493, (1984).

EEA (European Environment Agency), Spatial assessment of PM₁₀ and ozone concentrations in Europe, 2009, doi: 10.2800/165, (2005).

Ehret G., C. Kiemle, M. Wirth, M.A. Amediek, A. Fix, S. Houweling, Space-borne remote sensing of CO₂, CH₄, and N₂O by integrated path differential absorption lidar: a sensitivity analysis, *Appl. Phys. B*, 90, 593, (2008).

Eisinger M., A. Richter, A. Ladstätter-Weißmayer, J. P. Burrows, DOAS zenith sky observations: BrO measurements over Bremen (53°N) 1993–1994, *J. Atm. Chem.*, 26, 93, (1997).

El Haddad I., N. Marchand, B. Temime-Roussel, H. Wortham, C. Piot, J.L. Besombes, C. Baduel, D. Voisin, A. Armengaud, J.L. Jaffrezo, Insights into the secondary fraction of the organic aerosol in a Mediterranean urban area: Marseille, *Atmos. Chem. Phys.*, 11, 2059, (2011).

Etheridge D. M., L. P. Steele, R. L. Langenfelds, R. J. Francey, J. M. Barnola, V. I. Morgan, Natural and anthropogenic changes in atmospheric CO₂ over the last 1000 years from air in Antarctic ice and firn, *Journal of Geophysical Research*, 101, 4115, doi: 10.1029/95JD03410, (1996).

Extermann J., P. Béjot, L. Bonacina, P. Billaud, J. Kasparian, J.-P. Wolf, Effects of atmospheric turbulence on remote optimal control experiments, *Appl. Phys. Lett.*, 92, 041103, (2008).

F

Favez O., I. El Haddad, C. Piot, A. Boreave, E. Abidi, N. Marchand, J.L. Jaffrezo, J.L. Besombes, M.B. Personnaz, J. Sciare, H. Wortham, C. George, B. D'Anna, Inter-comparison of source apportionment models for the estimation of wood burning aerosols during wintertime in an Alpine city (Grenoble, France), *Atmos. Chem. Phys.* 10, 5295, (2010).

G. Faye, J. Kasparian, R. Sauerbrey, Modifications to the lidar equation due to nonlinear propagation in air, *Applied Physics B*, 73, 157, (2001).

Fiocco G., L.D. Smullin, Detection of scattering layers in the upper atmosphere (60-140 km) by Optical Radar, *Nature*, 199, 1275, (1963).

A. Fix, G. Ehret, A. Hoffstadt, H. Klingenberg, C. Lemmerz, P. Mahnke, M. Ulbricht, M. Wirth, R. Wittig, W. Zirnig, The French-German climate monitoring initiative on global observations of atmospheric methane International Laser and Radar Conference 2004, 45, (2004).

Fletcher N. H., *The Physics of Rainclouds*, Cambridge University Press, (1966).

Frankenberg C., T. Warneke, A. Butz, F. Aben, I. Hase, P. Spietz, Pressure broadening in the 2v₃ band of methane and its implication on atmospheric retrievals, *Atmos. Chem. Phys.*, 8, 5061, (2008).

Frehlich R., Scanning doppler lidar for input into short-term wind power forecasts , *J. Atmo. Ocea. Tech.*, 30, 230-244, (2013).

Freudenthaler V., M. Esselborn, M. Wiegner, B. Heese, M. Tesche, A. Ansmann, D. Müller, D. Althausen, M. Wirth, A. Fix, G. Ehret, P. Knippertz, C. Toledano, J. Gasteiger, M. Garhammer, M. Seefeldner, Depolarization ratio profiling at several wavelengths in pure Saharan dust during SAMUM 2006, *Tellus B*, 61, 165, doi: 10.1111/j.1600-0889.2008.00396.x, (2009).

Frosch M., M. Bilde, P.F. DeCarlo, Z. Juranyi, T. Tritscher, J. Dommen, N.M. Donahue, M. Gysel, E. Weingartner, U. Baltensperger, Relating cloud condensation nuclei activity and oxidation level of α -pinene secondary organic aerosols, *J. Geophys. Res., Atmos.*, 116, D22212, doi: 10.1029/2011JD016401 (2011).

Fujii T., T. Fukuchi, Laser Remote Sensing, CRC Press Ed., (2005).

G

Gaudio P., M. Gelfusa and M. Richetta, Preliminary results of a lidar-dial integrated system for the automatic detection of atmospheric pollutants, Proceedings of SPIE, 8534, doi:10.1117/12.974537, (2012).

Gayet J. F., O. Crépel, J.F. Fournol, S. Oshchepkov, A new airborne polar Nephelometer for the measurements of optical and microphysical cloud properties. Part I: Theoretical design., Ann. Geophys., 15, 451, (1997).

Geiko P. P., V.E. Privalov, O.A. Romanovskii, O.V. Kharchenko, Application of frequency converters to femtosecond laser radiation for lidar monitoring of the atmosphere, Opt. Spectrosc., 108, 80, (2010).

Georgieva E. M., W. S. Heaps and W. Huang, New Broadband LIDAR for Greenhouse Carbon Dioxide Gas Sensing in the Earth's Atmosphere, Conference on Lidar Technologies Techniques and Measurements for Atmospheric Remote Sensing, Proceedings of SPIE, 8182, (2011).

Gheusi F., F. Ravetta, H. Delbarre, C. Tsamalis, A. Chevalier-Rosso; C. Leroy, P. Augustin, R. Delmas, G. Ancellet, G. Athier, P. Bouchou, B. Campistron, J.M. Cousin, M. Fourmentin, Y.Meyerfeld, Pic 2005, a field campaign to investigate low-tropospheric ozone variability in the Pyrenees, Atm. Res., 101, 640, (2011).

Ghotbi M., M. Ebrahim-Zadeh, V. Petrov, P. Tzankov, F. Noack, Efficient 1 kHz femtosecond optical parametric amplification in BIB3O6 pumped at 800 nm, Opt. Express, 14, 10621, (2006).

Gianini M. F. D., C. Piot, H. Herich, J. L. Besombes, J. L. Jaffrezo, C. Hueglin, Source apportionment of PM10, organic carbon and elemental carbon at Swiss sites: An intercomparison of different approaches, Science of the Total Environment, 454, 99, doi: 10.1016/j.scitotenv.2013.02.043, (2013).

Gibert F., I. Xueref-Remy, L. Joly, M. Schmidt, J. Cuesta, K. J. Davis, M. Ramonet, P. H. Flamant, B. Parvitte, V. Zeninari, A case study of CO₂, CO and particles content evolution in the suburban atmospheric boundary layer using a 2 μ m Doppler DIAL, a 1 μ m backscatter lidar and an array of in-situ sensors, Boundary-Layer Meteorology, 128, 381, doi: 10.1007/s10546-008-9296-8, (2008).

Gosz J. R., C. N. Dahm, P. G. Risser, Long-path FTIR measurement of atmospheric trace gas concentrations, Ecology, 69, 1326, doi: 10.2307/1941630, (1988).

Grandpierre A., On the origin of solar cycle periodicity, Astrophysics and Space Science, 243, 393, doi: 10.1007/BF00644709, (2004).

Griffiths A. D., S. D. Parkes, S. D. Chambers, M. F. McCabe, A. G. Williams, Improved mixing height monitoring through a combination of lidar and radon measurements, *Atmospheric Measurement Techniques*, 6, 207, doi: 10.5194/amt-6-207-2013, (2013).

Guan Z.G., P. Lundin, L. Mei, G. Somesfalean, S. Svanberg, Vertical Lidar sounding of air pollutants in a major chinese city, *Appl. Phys. B*, 101, 465, (2010).

Gunthe S. S., D. Rose, H. Su, R.M. Garland, P. Achtert, A. Nowak, A. Wiedensohler, M. Kuwata, N. Takegawa, Y. Kondo, M. Hu, M. Shao, T. Zhu, M.O. Andreae, U. Poschl, Cloud condensation nuclei (CCN) from fresh and aged air pollution in the megacity region of Beijing, *Atmos. Chem. Phys.* 11, 11023, (2011).

Guo M., X. Wang, J. Li, K. Yi, G. Zhong, H. Tani, Assessment of global carbon dioxide concentration using MODIS and GOSAT data, *Sensors*, 12, 16368, (2012).

H

Haywood J., O. Boucher, Estimates of the direct and indirect radiative forcing due to tropospheric aerosols: A review, *Rev. Geophys.* 38, 513, (2000).

Heimann M., Atmospheric science: Enigma of the recent methane budget, *Nature*, 476, 157, doi: 10.1038/476157a, (2011).

Henin S., Y. Petit, P. Rohwetter, K. Stelmazczyk, Z. Q. Hao, W. M. Nakaema, A. Vogel, T. Pohl, F. Schneider, J. Kasparian, K. Weber, L. Wöste, J.-P. Wolf, Field measurements suggest the mechanism of laser-assisted water condensation, *Nature communications*, 2, 456, doi: 10.1038/ncomms1462, (2011).

Herget W. F., J. A. Jahnke, D. E. Burch, D. A. Gryvnak, Infrared gas-filter correlation instrument for in situ measurement of gaseous pollutant concentrations, *Applied Optics*, 5, 1222, (1976).

Hodgkinson J., R. P. Tatam, Optical gas sensing: a review, *Meas. Sci. Technol.*, 24, doi:10.1088/0957-0233/24/1/012004, (2013).

Hollas J. M., *High Resolution Spectroscopy*: 2nd Ed. Wiley, England. ISBN:0-471-97421-8, (1998).

Howard R. M., *Principles of Random Signal Analysis and Low Noise Design: The power spectral Density and its Applications*, ed. John Wiley & Sons Inc, (2002).

Hsieh Y. L., S. S. Tsai, C. Y. Yang, Fine particulate air pollution and hospital admissions for congestive heart failure: a case-crossover study in Taipei, *Inhalation Toxicology*, 25, 455, doi: 10.3109/08958378.2013.804609, (2013).

Huang Y.K., M. E. Luvsan, E. Gombojav, C. Ochir, J. Bulgan, C. C. Chan, Land use patterns and SO₂ and NO₂ pollution in Ulaanbaatar, Mongolia, *Environmental Research*, 124, 1, doi: 10.1016/j.envres.2013.02.006, (2013).

I

Inaba H., Detection of atoms and molecules by Raman scattering and resonance fluorescence, *Laser Monitoring of the Atmosphere*, 1976, pp. 153-236.

IPCC, S. Solomon, D. Qin, M. Manning, Z. Chen, M. Marquis, K.B. Averyt, M. Tignor and H.L. Miller, *Climate Change 2007: The Physical Science Basis. Contribution of Working Group I to the Fourth Assessment Report of the Intergovernmental Panel on Climate Change*, Cambridge University Press ed., Cambridge United Kingdom and New York USA, (2007).

Ismail S., G. Koch, N. Abedin, T. Refaat, M. Rubio, U. Singh, Development of laser, detector, and receiver systems for an atmospheric CO₂ lidar profiling system, *IEEE Aerosp. Conf. Proc.*, 1, 1527, (2008).

Ismail S., R.A. Ferrare, E.V. Browell, S.A. Kooi, J.P. Dunion, G. Heymsfield, A. Notari, C.F. Butler, S. Burton, M. Fenn, T.N. Krishnamurti, M.K. Biswas, G. Chen, B. Anderson, LASE measurements of water vapor, aerosol, and cloud distributions in Saharan air layers and tropical disturbances., *J. Atmos. Sci.* 67, 1026, (2010).

J

Jacquinet-Husson N., L. Crepeau, R. Armante, C. Boutammine, A. Chédin, N.A. Scott, C. Crevoisier, V. Capelle, C. Boone, N. Poulet-Crovisier, A. Barbe, A. Campargue, D. Chris Benner, Y. Benilan, B. Bézard, V. Boudon, L.R. Brown, L.H. Coudert, A. Coustenis, V. Dana, V.M. Devi, S. Fally, A. Fayt, J.-M Flaud, A. Goldman, M. Herman, G.J. Harris, D. Jacquemart, A. Jolly, I. Kleiner, A. Kleinböhl, F. Kwabia-Tchana, N. Lavrentieva, N. Lacome, Li-Hong Xu, O.M. Lyulin, J.-Y. Mandin, A. Maki, S. Mikhailenko, C.E. Miller, T. Mishina, N. Moazzen-Ahmadi, H.S.P. Müller, A. Nikitin, J. Orphal, V. Perevalov, A. Perrin, D.T. Petkie, A. Predoi-Cross, C.P. Rinsland, J.J. Remedios, M. Rotger, M.A.H. Smith, K. Sung, S. Tashkun, J. Tennyson, R.A. Toth, A.-C. Vandaele, J. Vander Auwera, The 2009 edition of the GEISA spectroscopic database, *Journal of Quantitative Spectroscopy and Radiative Transfer*, 112, 2395, (2011).

K

Kacenenbogen M., M.A. Vaughan, J. Redemann, R.M. Hoff, R.R. Rogers, R.A. Ferrare, P.B. Russell, C.A. Hostetler, J.W. Hair, B. N. Holben, An accuracy assessment of the CALIOP/CALIPSO version 2/version 3 daytime aerosol extinction product based on a detailed multi-sensor, multi-platform case study, *Atmos. Chem. Phys.*, 11, 3981, (2011).

Kahnert M., T. Nousiainen, B. Veihelmann, Spherical and spheroidal model particles as an error source in aerosol climate forcing and radiance computations: A case study for feldspar aerosols., *J. Geophys. Res.*, 110, D18S13, (2005).

Kaiser W., *Ultrashort laser pulses and applications*, Berlin ; New York : Springer-Verlag, (1988).

Kaplan D., P. Tournois, Theory and performance of the acousto-optic programmable dispersive filter used for femtosecond laser pulse shaping, *J. Phys. IV France*, 12, 69, (2002).

Kaplan D., P. Tournois, Acousto-Optic Spectral Filtering of Femtosecond Laser Pulses, *Ultrafast Optics IV*, Springer, 105, (2004).

Karl T. R., K. E. Trenberth, Modern global climate change, *Science*, 302, 1719, doi: 10.1126/science.1090228, (2003).

Kasparian J., M. Rodriguez, G. Mejean, J. Yu, E. Salmon, H. Wille, R. Bourayou, S. Frey, Y. B. Andre, A. Mysyrowicz, R. Sauerbrey, J. P. Wolf, L. Woste, White-light filaments for atmospheric analysis, *Science*, 301, 61, doi: 10.1126/science.1085020, (2003).

Kasparian J., J. P. Wolf, Ultrafast laser spectroscopy and control of atmospheric aerosols, *Physical Chemistry Chemical Physics*, 14, 9291, doi: 10.1039/c2cp23576e, (2012a).

Kasparian J., P. Rohwetter, L. Woste, J.-P. Wolf, Laser-assisted water condensation in the atmosphere: a step towards modulating precipitation?, *J. Phys. D: Appl. Phys.*, 45, 293001, (2012b).

Kebabian P.L., K. D. Annen, T. A. Berkoff, A. Freedman, Nitrogen dioxide sensing using a novel gas correlation detector, *Measurement Science & Technology*, 11, 499, (2000).

Kiemle C., M. Quatrevalet, G. Ehret, A. Amediek, A. Fix, M. Wirth, Sensitivity studies for a space-based methane lidar mission, *Atmos. Meas. Tech.*, 4, 2195, (2011).

Klett J. D., Lidar inversion with variable backscatter extinction ratios, *Appl. Opt.*, 24, 1638 (1985).

Krekov G.M., M.M. Krekova, A.Y. Sukhanov, Estimation of the broadband lidar potential for remote sensing of the molecular atmosphere, *Atmo. Ocea. Opt*, 22, 346, (2009).

Kuang S., M. J. Newchurch, J. Burris, X. Liu, Ground-based lidar for atmospheric boundary layer ozone measurements, *Applied Optics*, 52, 3557, doi: 10.1364/AO.52.003557, (2013).

Kulmala M., T. Petäjä, T. Nieminen, M. Sipilä, H. E. Manninen, K. Lehtipalo, M. Dal Maso, P. P. Aalto, H. Junninen, P. Paasonen, I. Riipinen, K. E. J. Lehtinen, A. Laaksonen, V.-M Kerminen, Measurement of the nucleation of atmospheric aerosol particles, *Nature protocols*, 7, 1651, (2012).

Kulmala, M., J. Kontkanen, H. Junninen, K. Lehtipalo, H. E. Manninen, T. Nieminen, T. Petaja, M. Sipila, S. Schobesberger, P. Rantala, A. Franchin, T. Jokinen, E. Jarvinen, M. Aijala, J. Kangasluoma, J. Hakala, P. P. Aalto, P. Paasonen, J. Mikkila, J. Vanhanen, J. Aalto, H. Hakola, U. Makkonen, T. Ruuskanen, R. L. Mauldin, J. Duplissy, H. Vehkamäki, J. Back, A. Kortelainen, I. Riipinen, T. Kurten, M. V. Johnston, J. N. Smith, M. Ehn, T. F. Mentel, K. E. J. Lehtinen, A. Laaksonen, V. M. Kerminen,

D. R. Worsnop, Direct observations of atmospheric aerosol nucleation, *Science*, 339, 943, doi: 10.1126/science.1227385, (2013).

Kuprov R.Y., D. Buck, C. A. Pope, D. J. Eatough, J. C. Hansen, Design and characterization of a two-stage human subject exposure chamber, *Journal of the Air & Waste Management Association*, 61, 864, doi: 10.3155/1047-3289.61.8.864, (2011).

L

Lang-Yona M., Y. Rudich, E. Segre, E. Dinar, A. Abo-Riziq, Aerosol optical properties retrieved by continuous wave - cavity ring down aerosol spectrometer (CW-CRD-AS), *Anal. Chem.*, 81, 1762, (2009).

Légaré F., M. Naji, P. Lassonde, D. Comtois, V. Crozatier, T. Oksenhendler, H. Anis, J.-C. Kieffer, Pulse compression and shaping of broadband optical parametric amplifier laser source, *Optics Letters*, 33, (2008).

Lou X. T., G. Somesfalean, Z. G. Zhang, S. Svanberg, Sulfur dioxide measurements using an ultraviolet light-emitting diode in combination with gas correlation techniques, *Applied Physics B-Lasers and Optics*, 94, 699, doi: 10.1007/s00340-009-3399-x, (2009).

Lou X.T., G. Somesfalean, B. Chen, Y.G. Zhang, H.S. Wang, Z.G. Zhang, S.H. Wu, Y.K. Qin, Simultaneous detection of multiple-gas species by correlation spectroscopy using a multimode diode laser, *Opt. Lett.*, 35, 1749, (2010).

Lou X.T., C.T. Xu, S. Svanberg, G. Somesfalean, Multimode diode laser correlation spectroscopy using gas-filled porous materials for pathlength enhancement, *Appl. Phys. B*, 109, 453, (2012a).

Lou X.T., G. Somesfalean, S. Svanberg, Y.G. Zhang, S.H. Wu, Detection of elemental mercury by multimode diode laser correlation spectroscopy, *Opt. Exp.*, 20, 4927, (2012b).

M

Ma Q., R. H. Tipping, The averaged density matrix in the coordinate representation: Application to the calculation of the far-wing line shapes for H₂O, *J. Chem. Phys.*, 111, 5909, (1999).

Ma Q., R. H. Tipping, The frequency detuning correction and the asymmetry of line shapes: The far wings of H₂O-H₂O, *J. Chem. Phys.*, 116, 4102, (2002).

Mayer B., A. Kylling, Technical note: The libRadtran software package for radiative transfer calculations - description and examples of use, *Atmos. Chem. Phys.*, 5, 1855, doi: 10.5194/acp-5-1855-2005, (2005).

Marburger J. H., Self-focusing: Theory, *Prog. Quant. Electr.*, 4, 35, (1975).

McCormick P., L. W. Thomason, C. R. Trepte, Atmospheric effects of the Mt Pinatubo eruption, *Nature*, 373, 399, doi: 10.1038/373399a0, (1995).

Measures R. M., *Laser Remote Sensing, Fundamentals and Applications*, Krieger Ed., (1992).

Melnichuk M., L. T. Wood, Direct Kerr electro-optic effect in noncentrosymmetric materials, *Phys. Rev. A* 82 (2010).

Mei L., Z. G. Guan, H. J. Zhou, J. Lv, Z. R. Zhu, J. A. Cheng, F. J. Chen, C. Lofstedt, S. Svanberg, G. Somesfalean, Agricultural pest monitoring using fluorescence lidar techniques Feasibility study, *Applied Physics B, Lasers and Optics*, 106, 733, doi: 10.1007/s00340-011-4785-8, (2012).

Mejean G., J. Kasparian, J. Yu, S. Frey, E. Salmon, J.P. Wolf, Remote detection and identification of biological aerosols using a femtosecond terawatt lidar system, *Appl. Phys. B, Lasers Opt.*, 78, 535, (2004).

Miffre A., M. Abou Chacra, S. Geffroy, P. Rairoux, L. Souhac, R. J. Perkins, E. Frejafon, Aerosol load study in urban area by Lidar and numerical model, *Atmospheric Environment*, 44, 1152, doi: 10.1016/j.atmosenv.2009.12.031, (2010).

Miffre A., G. David, B. Thomas, P. Rairoux, Atmospheric non-spherical particles optical properties from UV-polarization Lidar and scattering matrix, *Geophys. Res. Lett.*, 38, L16804, (2011).

Miffre A., G. David, B. Thomas, M. Abou Chacra, P. Rairoux, Interpretation of Accurate UV Polarization Lidar Measurements: Application to Volcanic Ash Number Concentration Retrieval, *J. Atm. Ocean. Tech.*, 29, 558, (2012a).

Miffre A., G. David, B. Thomas, P. Rairoux, A.M. Fjaeraa, N.I. Kristiansen, A. Stohl, Volcanic aerosol optical properties and phase partitioning behavior after long-range advection characterized by UV-Lidar measurements, Special Issue on the Eyjafjallajökull Icelandic Volcano, *Atmos. Env.*, 48, 76, (2012b).

Miles R.B., W.R. Lempert, J.N. Forkey, *Laser Rayleigh scattering*, *Measurement Science and Technology*, 12, (2001).

Minato A, M.A. Joarder, S. Ozawa, M. Kadoya, N. Sugimoto, Development of a lidar system for measuring methane using a gas correlation method, *Jap. J. Appl. Phys.*, 38, 6130, (1999).

Mishchenko M.I., L.D. Travis, A.A. Lacis, *Scattering, Absorption and Emission of Light by Small Particles*, 3rd ed., Cambridge University Press, Cambridge, (2002).

Mlawer E. J., S. A. Clough, P. D. Brown, D. C. Tobin, Recent developments in the water vapor continuum, *Ninth ARM Science Team Meeting Proceedings*, (1999).

Mokdad A. H., J. S. Marks, D. F. Stroup, J. L. Gerberding, Actual causes of death in the United States, 2000, *J. Amer. Med. Assoc.*, 291, 1238, doi:10.1001/jama.291.10.1238, (2004).

N

Nakata M., I. Sano, S. Mukai, B. N. Holben, Spatial and temporal variations of atmospheric aerosol in Osaka, *Atmosphere*, 4, 157, doi: 10.3390/atmos4020157, (2013).

National Research Council, America's Climate Choices: Panel on Advancing the Science of Climate Change; National Research Council (2010), *Advancing the Science of Climate Change*, Washington, D.C.: The National Academies Press, ISBN 0-309-14588-0, (2010).

Nicolas M., M. Ndour, O. Ka, B. D'Anna, C. George, Photochemistry of atmospheric dust: ozone decomposition on illuminated titanium dioxide, *Environ. Sci. Technol.*, 43, 7437, (2009).

Nousiainen T., Optical modeling of mineral dust particles: a review, *J. Quant. Spectrosc. Radiat. Transf.*, 110, 1261, (2009).

O

Orphal J., Kelly Chance, Ultraviolet and visible absorption cross-sections for HITRAN, *Journal of Quantitative Spectroscopy & Radiative Transfer*, 82, 491, (2003).

P

Penchev S., V. Pencheva, S. Naboko, *Compte Rendus de l'Academie Bulgare des Sciences* 56, 669, (2012).

Pieniniemi K., Lassi U. Gas emission measurements with a FTIR gas analyzer - verification of the analysis method, SkyPro Conference, Clean Air Research at the University of Oulu, Oulu, Finland. (2010).

Pityn P. J., J. Anderson, Air sampling of mold spores by slit impactors: yield comparison *Journal of Environmental Science and Health Part a, Toxic/Hazardous Substances & Environmental Engineering*, 48, 1485, doi: 10.1080/10934529.2013.796817, (2013).

Plane J. M. C., C. F. Nien, Differential optical-absorption spectrometer for measuring atmospheric trace gases, *Review of Scientific Instruments*, 63, 1867, doi: 10.1063/1.1143296, (1992).

Platt U., M. Hausmann, Spectroscopic measurement of the free-radicals NO₃, BrO, IO, and OH in the troposphere, *Research on Chemical Intermediates*, 20, 557, doi: 10.1163/156856794X00450, (1994).

Pongrácz E., M. Hyvärinen, S. Pitkäaho, R. L. Keiski R. L., Clean air research at the University of Oulu, *Proceeding of the SkyPro conference*, University of Oulu, Finland, (2010).

R

Raaschou-Nielsen O., Z. J. Andersen, R. Beelen, E. Samoli, M. Stafoggia, G. Weinmayr, B. Hoffmann, P. Fischer, M. J. Nieuwenhuijsen, B. Brunekreef, W. W. Xun, K. Katsouyanni, K. Dimakopoulou, J. Sommar, B. Forsberg, L. Modig, A. Oudin, B. Oftedal, P. E. Schwarze, P. Nafstad, U. De Faire, N. L. Pedersen, C.-G. Östenson, L. Fratiglioni, J. Penell, M. Korek, G. Pershagen, K. T. Eriksen, M. Sørensen, A. Tjønneland, T. Ellermann, M. Eeftens, P. H. Peeters, K. Meliefste, M. Wang, B. Bueno-de-Mesquita, T. J Key, K. de Hoogh, H. Concin, G. Nagel, A. Vilier, S. Grioni, V. Krogh, M.-Y. Tsai, F. Ricceri, C. Sacerdote, C. Galassi, E. Migliore, A. Ranzi, G. Cesaroni, C. Badaloni, F. Forastiere, I. Tamayo, P. Amiano, M. Dorronsoro, A. Trichopoulou, C. Bamia, P. Vineis, G. Hoek, Air pollution and lung cancer incidence in 17 European cohorts: Prospective analyses from the European Study of Cohorts for Air Pollution Effects (ESCAPE), *The Lancet Oncology*, 14, 813, doi:10.1016/S1470-2045(13)70279-1, (2013).

Rairoux P., H. Schillinger, S. Niedermeier, M. Rodriguez, F. Ronneberger, R. Sauerbrey, B. Stein, D. Waite, C. Wedekind, H. Wille, L. Wöste, Remote sensing of the atmosphere using ultrashort laser pulses, *Appl. Phys. B*, 71, 573, (2000).

Reichardt J., A. Tsias, A. Behrendt, Optical properties of PSC Ia-enhanced at UV and visible wavelengths: Model and observations, *Geophys. Res. Lett.*, 27, 201, (2000).

Richter A., M. Eisinger, A. Ladstätter-Weißenmayer, J. P. Burrows, DOAS zenith sky observations. 2. Seasonal variation of BrO over Bremen (53°N) 1994–1995, *J. Atm. Chem.*, 32, 83, (1999).

Riris H., K. Numata, S. Li, S. Wu, A. Ramanathan, M. Dawsey, J. Mao, R. Kawa, J.B. Abshire, Airborne measurements of atmospheric methane column abundance using a pulsed integrated-path differential absorption lidar, *Appl. Opt.*, 51, 8296, (2012).

Robinson R., T. Gardiner, F. Innocenti, P. Woods, M. Coleman, Infrared differential absorption Lidar (DIAL) measurements of hydrocarbon emissions, *Journal of Environmental Monitoring*, 13, 2213, doi: 10.1039/c0em00312c, (2011).

Rothman L.S., I.E. Gordon, A. Barbe, D. ChrisBenner, P.F. Bernath, M. Birk, V. Boudon, L.R. Brown, A. Campargue, J.-P. Champion, K. Chance, L.H. Coudert, V. Dana, V.M. Devi, S. Fally, J.-M. Flaud, The HITRAN 2008 molecular spectroscopic database, *J. Quant. Spectrosc. Radiat. Transfer*, 110, 533, (2009).

S

Sandroni S, C. Cerutti, Long path measurements of atmospheric sulfur-dioxide by a Barringer cospec-3, *Atmospheric Environment*, 11, 1225, (1977).

Sasano Y., E.V. Browell, Light scattering characteristic of various aerosol types derived from multiple wavelength lidar observations, *Appl. Opt.*, 28, 1670, (1989).

Sassen K., J. Zhu, P. Webley, K. Dean, P. Cobb, Volcanic ash plume identification using polarization lidar: Augustine eruption, Alaska, *Geophysical Research Letters*, 34, L08803, doi: 10.1029/2006GL027237, (2007).

Schumann U., B. Weinzierl, O. Reitebuch, H. Schlager, A. Minikin, C. Forster, R. Baumann, T. Sailer, K. Graf, H. Mannstein, C. Voigt, S. Rahm, R. Simmet, M. Scheibe, M. Lichtenstern, P. Stock, H. Ruba, D. Schauble, A. Tafferer, M. Rautenhaus, T. Gerz, H. Ziereis, M. Krautstrunk, C. Mallaun, J. F. Gayet, K. Lieke, K. Kandler, M. Ebert, S. Weinbruch, A. Stohl, J. Gasteiger, S. Gross, V. Freudenthaler, M. Wiegner, A. Ansmann, M. Tesche, H. Olafsson, K. Sturm, Airborne observations of the Eyjafjalla volcano ash cloud over Europe during air space closure in April and May 2010, *Atmospheric Chemistry and Physics*, 11, 2245, doi: 10.5194/acp-11-2245-2011,(2011).

Seinfeld J., S. Pandis, *Atmospheric Chemistry and Physics: From Air Pollution to Climate Change* (2nd ed.). Hoboken, New Jersey: John Wiley & Sons, Inc. p. 97. ISBN 0-471-17816-0, (1998).

Schilt S., L. Thévenaz, P. Robeet, Wavelength modulation spectroscopy: combined frequency and intensity laser modulation, *Appl. Opt.*, 42, 6728, (2003).

Shakhova N., I. Semiletov, A. Salyuk, V. Yusupov, D. Kosmach, Ö. Gustafsson, Extensive methane venting to the atmosphere from sediments of the east siberian arctic shelf, *Science*, 327, 1246, (2010).

Shen Y.R., *The Principles of Nonlinear Optics*, Wiley-Interscience, ISBN 0-471-43080-3, (2003).

Shettle, E., Models of aerosols, clouds and precipitation for atmospheric propagation studies, in: *Atmospheric propagation in the UV, visible, IR and mm-region and related system aspects*, AGARD Conference Proceedings, 454, (1989).

South A.M., I.M. Povey, R.L. Jones, Broadband lidar measurements of tropospheric water vapor profiles, *J. Geophys. Res.* 103, 31191, (1998).

Spracklen D. V, B. Bonn, K. S. Carslaw, Boreal forests, aerosols and the impacts on clouds and climate, *Philosophical Transactions of the Royal Society A: Mathematical, Physical and Engineering Sciences*, 366, 4613, (2008).

Stepanov A. G., S. Henin, Y. Petit, L. Bonacina, J. Kasparian, J.-P. Wolf, Mobile source of high-energy single-cycle terahertz pulses, *Applied Physics B*, 101, 11, (2010).

Sugimoto N., I. Matsui, A. Shimizu, I. Uno, K. Asai, T. Endoh, T. Nakajima, Observation of dust and anthropogenic aerosol plumes in the Northwest Pacific with a two-wavelength polarization lidar on board the research vessel Mirai, *Geophys. Res. Lett.*, 29, 1901, doi: 10.1029/2002GL015112, (2002).

Sugimoto N., T. Nishizawa, A. Shimizu, H. Okamoto, Aerosol classification retrieval algorithms for EARTHCARE/ATLID, CALIPSO/CALIOP, and ground-based lidars, *Geoscience and Remote Sensing IGARSS*, 4111, (2011).

T

Tan H. S., W. S. Warren, Mid infrared pulse shaping by optical parametric amplification and its application to optical free induction decay measurement, *Optics Express*, 9, 1021, (2003).

Thomas B., A. Miffre, G. David, J-P. Cariou, P. Rairoux, Remote sensing of trace gases with optical correlation spectroscopy and Lidar: Theoretical and numerical approach, *Appl. Phys. B*, 108, 689, (2012).

Thomas B., G. David, C. Anselmo, J-P. Cariou, A. Miffre and P. Rairoux, Remote sensing of atmospheric gases with optical correlation spectroscopy and lidar: first experimental result on water vapor profile measurements, *Appl. Phys. B*, doi: 10.1007/s00340-013-5468-4 (2013a).

Thomas B., G. David, C. Anselmo, E. Coillet, A. Miffre, J. P. Cariou, P. Rairoux, Remote sensing of methane with broadband laser and optical correlation spectroscopy on the Q-branch of the $2\nu_3$ band, *Jour. Mol. Spectrom.*, doi: 10.1016/j.jms.2013.05.015, (2013b).

Trompeter W. J., S. K. Grange, P. K. Davy, T. Ancelet, Vertical and temporal variations of black carbon in New Zealand urban areas during winter, *Atmospheric Environment*, 75, 179, doi: 10.1016/j.atmosenv.2013.04.036, (2013).

Tvorogov S. D., L. I. Nesmelova, O. B. Rodimova, Model description of temperature dependence of the H₂O absorption in 8-14 microns atmospheric window, *Atmos. Ocean. Phys.*, 7, 802, (1994).

Tzankov P., M. Roth, Y. Kong, L. Xu, Z. Sartania, Spatio-temporal characterization of the signal pulse-shortening in type II optical parametric amplifier using BBO and BIBO crystals, *Technical Digest of Conference on Lasers and Electro-Optics*, 1365, (2008).

Twomey S., Pollution and the planetary albedo, *Atmos. Environ.*, 8, 1251, doi: 10.1016/0004-6981(74)90004-3, (1974).

V

Vargas-Rodríguez E., H.N. Rutt, Analytical method to find the optimal parameters for gas detectors based on correlation spectroscopy using a Fabry–Pérot interferometer, *Appl. Opt.*, 46, 21, (2007).

Veselovskii I., O. Dubovik, A. Kolgotin, T. Lapyonok, P. Di Girolamo, D. Summa, D.N. Whiteman, M. Mishchenko, D. Tanre, Application of randomly oriented spheroids for retrieval of dust particle parameters from multiwavelength lidar measurements, *J. Geophys. Res.*, 115, D21203, (2010).

Vigasin A. A., Weakly bound molecular complexes in the atmosphere, *Atmos. and Ocean Opt.*, 2, 907, (1989).

Vigasin A. A., Water vapor continuous absorption in various mixtures: possible role of weakly bound complexes, *Journal of Quantitative Spectroscopy and Radiative Transfer*, 64, 25, (2000).

Vinogradova A. A., E. I. Fedorova, I. B. Belikov, A. S. Ginzburg, N. F. Elansky, A. I. Skorokhod, Temporal variations in carbon dioxide and methane concentration under urban conditions, *Izvestiya Atmospheric and Oceanic Physics*, 43, 599, (2006).

X

Xu, H. L., G. Mejean, W. Liu, Y. Kamali, J. F. Daigle, A. Azarm, P. T. Simard, P. Mathieu, G. Roy, J. R. Simard, S. L. Chin, Remote detection of similar biological materials using femtosecond filament-induced breakdown spectroscopy, *Applied Physics B*, 87, 151, (2007).

W

Wagner G., A. Behrendt, V. Wulfmeyer, F. Spath, M. Schiller, High-power Ti:sapphire laser at 820 nm for scanning ground-based water-vapor differential absorption lidar, *Applied Optics*, 52, 2454, doi: 10.1364/AO.52.002454, (2013).

Ward T. V., H. H. Zwick, Gas cell correlation spectrometer: GASPEC T. V., *Applied Optics*, 14, 2896, (1975).

Weiner A.M., Femtosecond pulse shaping using spatial light modulators, *Rev. Sci. Instrum.*, 71, 5, (2000).

Weitkamp C., Lidar, Range-Resolved Optical Remote Sensing of the Atmosphere, Springer Ed., Berlin, New-York (2005).

Whiteman D. N., D. Venable, E. Landulfo, Comments on “Accuracy of Raman lidar water vapor calibration and its applicability to long-term measurements”, *Appl. Opt.*, 50, 2170, (2011).

Y

Yan Q., Hua D. X., Y. F. Wang, S. C. Li, F. Gao, Z. R. Zhou, L. Wang, C. X. Liu, S. Q. Zhang, Observations of the boundary layer structure and aerosol properties over Xi'an using an eye-safe Mie scattering Lidar, *Journal of Quantitative Spectroscopy and Radiative Transfer*, 122, 97, doi: 10.1016/j.jqsrt.2012.10.026 (2013).

Z

Zhao H. J., H. Z. Che, X. Y. Zhang, Y. J. Ma, Y. F. Wang, X. X. Wang, C. Liu, B. Hou, H. C. Che, Aerosol optical properties over urban and industrial region of Northeast China by using ground-based sun-photometer measurement, *Atmospheric Environment*, 75, 270, doi: 10.1016/j.atmosenv.2013.04.048, (2013).

